Electrochemical Supercapacitors for Energy Storage Applications

By

S. E. Rowlands BSc (Hons)

Thesis submitted in partial fulfilment for the degree of Doctor of Philosophy.

De Montfort University, Leicester

De Montfort University

July 2002

Declaration of originality

This is to certify that I am responsible for the work in this thesis, that the original work is my own unless otherwise acknowledged, that neither this thesis nor the original work contained herein has been submitted to this nor any other institution for a higher degree. The work was carried out in the Faculty of Applied Sciences at De Montfort University, Leicester and was supervised by Prof. R. J. Latham.

Signed :.....(Stephen E. Rowlands)
(Candidate)

Date : 29/10/2002

Signed :.....(Prof. R. J. Latham)
(Project supervisor)

Date : 29/10/2002

I fy Mam a'n Nhad.

Heb eu cymorth, ni fysai'r llyfr hon ym mhosib.

Diolch o'ng nghalon i'r ddau ohonnoch.

Acknowledgements

I would like to take this opportunity to thank all those who have made this research possible and fulfilling.

I would like to express my gratitude to Professor Roger Latham and Dr Walkeria Schlindwein for their support, guidance and encouragement throughout the last three years.

I would also like to thank the EPSRC for funding this work, Calgon and FMI composites for supplying carbon fabric and graphite paper respectively.

The help and advice given to me by Professor Sue Bayliss and Andy Mayne concerning the work carried out on porous silicon was invaluable and greatly appreciated, thank you both.

Thanks also to Norma Garrington for running the DSC samples, to Dave Bazley, Chris Warrington and Tony Woodford for their technical support.

And finally, to Victoria, Danny and Callum.

Abstract

Supercapacitor systems consisting of both liquid and solid polymer/gel electrolytes have been investigated. The liquid electrolytes were $LiClO_4$/PC and $TEABF_4$/PC (0.25M); the polymer/gel electrolyte was based on polyurethane (PU). A.c. conductivity measurements showed that the optimum composition of the gel electrolyte in thin film form was PU/PC(200%)/EC(200%)/$LiClO_4$(10%) and gave a conductivity of 6.22×10^{-3} S cm^{-1}.

DSC results indicated that when no plasticiser was added to the PU/$LiClO_4$ system, the conductivity followed a mechanism similar to that reported for Li^+ - PEO systems, i.e., cationic co-ordination to the ether oxygens of the PU backbone. On addition of plasticiser (EC/PC) forming a polymer/gel electrolyte, the conductivity mechanism of the system tended towards that of a liquid electrolyte, i.e., the cation co-ordinated to a greater extent with the ether oxygens of the PC and EC rather that the ether oxygens of the PU.

Supercapacitors consisting of activated carbon cloth (ACC) and graphite paper (GP) were initially characterised with $LiClO_4$/PC(0.25M) and $TEABF_4$/PC(0.25M) liquid electrolytes using a.c. impedance spectroscopy and cyclic voltammetry. The system ACC/$LiClO_4$/PC (0.25M) showed excellent capacitive characteristics giving a capacitance value of 3.2 F cm^{-2} relating to a specific capacitance of 160 F g^{-1}. The system GP/$LiClO_4$/PC (0.25M) gave a capacitance of 8 mF cm^{-2} relating to a specific capacitance of 0.30 F g^{-1}, hence demonstrating the increase in capacitance obtained by high surface area electrodes.

Solid state supercapacitor devices comprising of ACC/PU/PC/EC (200%) /$LiClO_4$ (10%) were characterised using a.c. impedance spectroscopy, cyclic voltammetry. and galvanostatic charge-discharge experiments. Capacitance values of 0.22 F cm^{-2} relating to a specific capacitance of 5.5 F g^{-1} were obtained and the cell retained 80% of the original capacity after 1000 galvanostatic charge-discharge cycles.

Carbon composite (CC) electrodes were constructed from a mixture carbon powder and the PU gel electrolyte. The optimum composition of the electrodes was found to be CC (100%) /PU electrolyte (200%)+200% added plasticiser solution (PC/EC [1:1]/ $LiClO_4$ [10%]). Supercapacitor cells constructed of the CC electrodes with the PU gel electrolyte, i.e., CC/PU/EC/PC (200%)/$LiClO_4$/(10%) were characterised as

described above. Capacitance values of 0.092 F cm^{-2} relating to a specific capacitance of 30.67 F g^{-1} were obtained and 75% of the original capacity was retained after 1000 charge-discharge cycles.

Porous silicon (PSi) electrodes were prepared by anodic and chemical-etch techniques. Supercapacitor cells were constructed and characterised using a.c. impedance spectroscopy and cyclic voltammetry.

It was found that sputtering a 300-Å layer of gold onto the PSi electrodes dramatically improved the capacitive characteristics. Capacitance values of 0.13 mF cm^{-2} relating to a specific capacity of 2.21 mF g^{-1} were obtained for anodically etched p-type silicon wafer electrodes with a $TEABF_4$/PC (0.25M) electrolyte. For the same electrodes with the PU gel electrolyte a capacitance of 29.5 μF cm^{-2} was obtained, relating to a specific capacitance of 0.50 mF g^{-1}. Devices constructed from PSi electrodes produced by chemical etching and gold-coated with $TEABF_4$/PC electrolyte, gave a capacitance of 0.6 mF cm^{-2}.

Chemical etched PSi was produced from thin layer silicon (~900 nm) which was vacuum deposited onto glass and coated with a 300-Å layer of gold. Devices with $TEABF_4$/PC and the PU gel electrolytes were characterised giving capacitance values of 0.64 mF cm^{-2}, relating to a specific capacitance of 2.82 F g^{-1} and 2.7 μF cm^{-2} relating to a specific capacitance of 10 mF g^{-1} respectively. The supercapacitor cell Au/PSi/ITO/glass /PU was galvanostatically charged and discharged cycles and retained 90% of the original capacitance after 1000 cycles.

Polypyrrole was galvanostatically grown onto PSi electrodes and cells ppyr/PSi/ PU/EC/PC/$LiClO_4$ were characterised. These cells showed poor capacitive characteristics and need to be investigated further.

Contents

Index

List of Figures

List of tables

List of Symbols

Å	Angstrom, ($1x10^{-10}$ m)
A	Area of an electrode
A^*	Pre exponential factor
α	Charge transfer coefficient
C	Capacitance/ F cm^{-2} or specific capacitance F g^{-1}
C_{dl}	Double layer capacitance/ F
Cp	Heat capacity / J mol^{-1} K^{-1}
C_ϕ	Pseudocapacitance / F
$C_{H_3O^+}$	Concentration of H_3O^+ / mol dm^{-3}
C^*	Concentration / mol dm^{-3}
C_o^*	Concentration of oxidised species / mol dm^{-3}
C_R^*	Concentration of reduced species / mol dm^{-3}
C_c	Capacitance for charging / F cm^{-2}
C_d	Discharge capacitance / F cm^{-2}
d	Thickness of electrolyte / m
E	Electrode potential/ V
E^θ	Standard electrode potential/ V
ε	Relative permitivity/ C^2 J^{-1} m^{-1}
ε_0	Permitivity of a vacuum ($8.85x10^{-12}$ C^2 J^{-1} m^{-1})
E_g	The band gap energy/ eV
E_f	The fermi energy level/ ev
E	External electric field/ eV
E_C	Energy of conduction band/ eV
E_V	Energy of valence band/ eV
e	Electronic charge, ($1.6022x10^{-19}$ C)
eV	Electron volt/ V
ΔE_a	Activation energy, (kJ mol^{-1})
η	Overpotential/ V
η	Coulombic efficiency

F	Faraday constant, (9.6485×10^4 C mol^{-1})
f(E)	Fermi-Dirac distribution function
f	a.c. frequency/ Hz
F	Force / N
G	Conductance / Ω^{-1} or Siemens / S
g_c	Density of states for the conduction band
g_v	Density of states for the valence band
h	Planck's constant, (6.6261×10^{-34} J s^{-1})
ħ	$\hbar = h/2\pi$, (1.0546×10^{-34} J s^{-1})
H	Enthalpy / J mol^{-1}
i	Current/ A, or current density/ A cm^{-2}
i_0	Exchange current density / A/cm^{-2}
i_C	Charging current / A
i_d	Discharge current / A
K_1	Electrochemical equilibrium constant for hydrogen chemisorption with charge transfer
χ	Degree of crystalinity
m_n^* and m_p^*	The carrier effective masses of the negative (electron) and positive (hole) carriers respectively
m_e	Mass of an electron (9.1094×10^{-31} kg)
μ	Chemical potential
μ_i	Mobility of charge carrier i
ν	Sweep rate of a voltammogram / V s^{-1}
n_e	Total electron concentration in the conduction band for the non-degenerate situation
n_i	Number of charge carrier i
n_d	Number density of the charge carriers, i.e. the number of charge carriers per unit volume
N	Number of atoms in a crystal
N_c and N_v	The effective density of the states in the conduction and valence band respectively
ω	Angular frequency / radians s^{-1}
ϕ	Phase angle / degrees

P	Pressure / N m^{-2}
p	The hole concentration in the valence band for the non-degenerate limit
q^*	Heat / J mol^{-1}
q	Charge/ C
r	radius of a circle / m
R	Gas constant, (8.3145 J K^{-1} mol^{-1})
R_b	Bulk resistance
R	Pyrrole monomer
R_F	Charge transfer resistance/ Ω
R_e	Electrolytic resistance /Ω
R_S	Separator resistance /Ω
$R^{+\bullet}$	Radical cation of pyrrole monomer
ρ	Resistivity / Ω cm
R_L	Limiting low frequency resistance / Ω
S	Entropy / J mol^{-1}
σ	Conductivity of a polymer film / S cm^{-1}
τ	Relaxation time / s
t	Time / s
T_g	Glass transition temperature
T_m	Melting temperature
T_c	Crystallisation temperature
T_F	Fusion temperature
t_D	Discharge time / s
t_C	Charge time / s
T	Temperature/ ^0K
θ_H	Surface coverage of hydrogen
V	Voltage/ V
X_c	The capacitive reactance
z	Number of electrons
Z	Electrical impedance /Ω
Z'	Real part of electrical impedance /Ω
Z"	Imaginary part of electrical impedance /Ω

Z_W	Warburg impedance /Ω

List of Abbreviations

ACC	Activated carbon cloth
CC	Carbon composite
CP	Carbon powder
EC	Ethylene carbonate
ECP	Electronically conducting polymer
EDLC	Electrical double layer capacitor
GP	Graphite paper
HF	Hydrofluoric acid
ITO	Indium tin oxide
$LiClO_4$	Lithium perchlorate
PC	Propylene carbonate
PSi	Porous silicon
$TEABF_4$	Tetraethylammoniumtetrafluoroborate
THF	Tetrahydrofuran

1. Introduction

1.1 Supercapacitors

There are two general classes of supercapacitor devices, namely the electrical double layer capacitor and the redox supercapacitor.

1.1.1 Electrical Double Layer Capacitors

Capacitors that store the energy within the electrochemical double-layer at the electrode/electrolyte interface are known under various names, which are trademarks or established colloquial names such as "electrical double-layer capacitors (EDLC)", "supercapacitors", "ultracapacitors", "power capacitors" or "power cache". "EDLC" is the name that describes the fundamental charge storage principle of such capacitors [1, 2].

EDLC's have been known in the energy storage community for many years with some of the first patents dating back to 1957 where an EDLC based on a high surface area carbon was reported by Becker [H.E. Becker, U.S. Patent 2 800 616 (to General Electric) 1957]. However, in the 1990's EDLC's became well known in their potential use for electric vehicles [3]. The EDLC was proposed to boost the battery or fuel cell in the hybrid electric vehicle to provide the necessary power for acceleration, and would be recharged under regenerative breaking. Several companies such as Maxwell technologies, EPCOS, NEC and Panasonic are developing EDLC devices. The general use for these device are boost components working in conjunction with batteries or the replacement of batteries for starting, lighting and ignition (SLI) for internal combustion engines.

The theory of the EDLC is described in more detail in chapter 2.1.

The capacitance C, of a capacitor is defined by the relation $C = q/V$ where V is the voltage difference between the plates associated with the accommodation of charge q on an area A of each plate. If C is not constant with changing potential, as is often the case with supercapacitors a differential capacitance is defined as

$C = dq/dv$. Equation 2.1, ($C = A\varepsilon\varepsilon_0/d$) describes the relationship between capacitance and geometrical dimensions of an EDLC. Thus, materials used for electrodes in EDLC devices are those which have a high surface area for example carbon powders, activated carbon fabrics and porous silicon, (porous silicon is described later in chapters 1.3 and 4.2 [4]. Electrochemical capacitors differ in their mode of energy storage from batteries. In the electrochemical charging of a cell exhibiting a Nernstian cell potential (or e.m.f) of V, V remains ideally constant, (practically moderately constant for many cell configurations except Li-intercalation ones and quite constant for 95% of discharge for $Li/SOCl_2$ primaries), during charge or discharge until all the reactant materials have been electrochemically consumed, i.e. oxidised and reduced or vice versa during discharge or recharge. For EDLC devices ideally no Faradaic processes occur.

1.1.2 Pseudocapacitance or Redox Supercapacitors

Redox supercapacitors are those which utilise a pseudocapacitance C_ϕ, associated with a Faradaic charge transfer. Conway reported some of the initial work in 1991 [5]. Pseudocapacitance arises in cases where Faradaic charge-transfer processes lead to passage of pockets of charge, q, that depend on potential, unlike ideal Nernstian processes where a singular, (ideally) constant electrode potential (e.g. metal/ metal-ion equilibrium), arises, independent of extent of reaction. Two types of pseudocapacitance can arise in electrochemical processes,

- Adsorption pseudocapacitance
- And redox pseudocapacitance.

Both usually meet the requirement of good reversibility characteristic of capacitor behaviour.

Adsorption Pseudocapacitance

Two-dimensional surface reactions give the best example of reversible processes associated with adsorption pseudocapacitance. This can be 10-100 times greater than the double-layer capacitance at the same electrode. Faradaic deposition and desorption of hydrogen (coverage θ) at a platinum electrode is an example of this phenomenon. The surface reaction equation for platinum in acidic conditions is:

$$Pt + H_3O^+ + e^- \underset{K\text{-}1}{\overset{k1}{\longleftrightarrow}} PtH_{ads} + H_2O \qquad \text{Equation 1.1}$$

For an equilibrium situation at any potential it can be shown that,

$$\frac{\theta_H}{1-\theta_H} = \frac{k_1 C_{H_3O^+}}{k_{-1}} \exp(-VF/RT) \qquad \text{Equation 1.2}$$

(V is negative for the cathodic direction of current), alternatively for θ_H,

$$\theta_H = \frac{K_1 C_{H_3O^+} \exp(-VF/RT)}{1 + K_1 C_{H_3O^+} \exp(-VF/RT)} \qquad \text{Equation 1.3}$$

Where $K_1 = k_1/k_{-1}$ and is the electrochemical equilibrium constant for hydrogen chemisorption with charge transfer as shown in equation 1.1.

On differentiating equation 1.3 the result gives a quantity having the significance of a pseudocapacitance $C_\phi = q_1 (d\theta_H/dv)$, where q_1 is the Faradaic charge required for deposition or desorption of a monolayer of hydrogen.

$q_1 \cong 210\mu C\ cm^{-2}$ for 1 atom of H/Pt atom in the surface ($\theta_H \rightarrow 1$), q_1 depends a little on crystallographic orientation of the surface planes exposed.

From equation 1.3 the result is:

$$\left(\frac{RT}{F}\right)\frac{C_\phi}{q_1} = \frac{K_1 C_{H_3O^+} \exp(-VF/RT)}{1 + K_1 C_{H_3O^+} \exp(-VF/RT)^2} \qquad \text{Equation 1.4}$$

For a single state C_ϕ has a large maximum value of ~2200μF cm^{-2}, i.e. about 100 times greater than the double-layer capacitance. For multi-state adsorption the value is diminished 5-10 times but extends over a wider potential range. C_ϕ is referred to as a pseudocapacitance since it arises from a Faradaic charge-transfer reaction and not from electrostatic charging which is the origin of double-layer capacitance.

Redox Pseudocapacitance

The potential of a redox system, ox $+ze^- \leftrightarrow$red, is given by the Nernst equation,

$$E = E^\theta + \frac{RT}{zF}\ln\frac{[ox]}{[red]} \qquad \text{Equation 1.5}$$

Or,

$$E = E^\theta + \frac{RT}{zF}\ln\frac{[ox]/[red]}{1 - [ox]/[red]} \qquad \text{Equation 1.6}$$

Since the concentrations or activities of the ox and red species can be represented as relative fractions [ox]/([ox]+[red]) and [red]/([ox]+[red]), so that the latter is 1-[ox]/([ox]+[red]), then ln [ox]/[red] ≡ ln (κ/(1- κ) is formally analogous to that of $\theta_H/(1-\theta_H)$, for electrochemical adsorption with charge transfer, in terms of coverage fraction θ (equation 1.2 in log form) that gives rise to adsorption pseudocapacitance C_ϕ, for coverage θ, analogous to [red]/([ox]+[red]) in equation 1.6. Thus a redox capacitance is analogous to an adsorption capacitance with charge transfer [4]. Practically, a redox capacitance can involve diffusion control if both "red" and "ox" are solution species. However this complication can be avoided by physically or chemically anchoring the redox species on a polymer at the electrode surface or by using an electroactive (sometimes known as an electronically conducting polymer, ECP) [6]. Since the charge q is determined by the total concentration [ox]+ [red] which can be quite large (e.g. for 1 M solution of a z=1 system, q=96.5 C cm^{-3}, the C_ϕ can be very large but only over a restricted potential range, ~120 mV).

The versatility of ECP's provides three different configurations of redox supercapacitor:

(i) Symmetric p-doped supercapacitor;
(ii) Unsymmetrical supercapacitor based on two different p-dopable ECP's that are dopable over different potential ranges;
(iii) Symmetric supercapacitor device using p- and n-doped ECP [7].

1.2 Electrolyte materials for Supercapacitor devices

The electrolyte material for supercapacitor devices may be a liquid or solid. The advantage of liquid electrolytes is that they are more efficient in their ability to penetrate into the active surface of an electrode but their use may lead to device corrosion and high rates of self-discharge. Solid polymer electrolytes are low in mass, yielding high power densities, and have good mechanical strength in thin films. The disadvantages are their relative inability for pore penetration and therefore poor contact area with the electrode surface. The most effective geometry for EDLC construction is to use a gel electrolyte, which may be regarded as an intermediate between a liquid and solid electrolyte. A gel consists of a salt dissolved in a polymer matrix containing a certain degree of plasticiser. The purpose of the plasticiser is to maximise the amorphous phase, which is responsible for ionic conductivity. Poly(ethyleneglycol) (PEG) and Poly(methylmethacrylate) (PMMA) have been previously studied for this purpose [8-12]. Chapter 3 deals with this topic in more detail and describes the use of polyurethane as a polymer/gel electrolyte, which was one of the primary aims of this study.

1.3 Porous silicon

Porous silicon (PSi), is produced by chemical or electrochemical etching of p- or n-type crystalline silicon. The electrochemical etch solution is usually a mixture of hydrofluoric acid (HF), ethanol and either water or deuterated water. The concentration of the etch solution together with the anodisation current density and the etch time govern the properties of the PSi layer. These properties include the porosity (*i.e.* the percentage coverage of pores over the wafer surface), the shape and depth of the pores. After the etching process the PSi is dried. This may be achieved by simply allowing solvent evaporation under atmospheric conditions, but this can lead to degradation of the structure due to microscale cracking of the surface. Other methods include drying under supercritical conditions or washing with a liquid of low surface tension, such as pentane. PSi has been used as an electrode material in a parallel plate capacitor using a chemically etched macroporous n-type silicon

PAGE

MISSING

IN

ORIGINAL

2 Supercapacitor Theory

As mentioned in the introduction (chapter 1.1), there are two general classes of supercapacitor devices, namely the electrical double layer capacitor (EDLC) and a capacitor that utilises a pseudocapacitance, see chapter 1.12.

The EDLC was first produced commercially, utilising an activated carbon fabric (ACF) with a sulphuric acid electrolyte, over 30 years ago by NEC under the brand name "Supercaps" [1]. Since then EDLC's have been extensively investigated due to their potential high power densities and cycle life. Applications include power backup for portable military and medical equipment, starting-lighting and ignition systems and in battery-capacitor hybrid devices for electric vehicle (EV) propulsion [2-8].

2.1 The Electrical Double Layer

At any interface between solid and ionic solutions a separation of ionic and or electronic charges occurs giving rise to the double layer [9-12], thus, double layer capacitance is electrostatic in origin and no faradic charge transfer occurs as does in secondary batteries. Therefore EDLC's may be compared with the conventional parallel plate capacitor where the capacitance 'C' is given by,

$$C = A\varepsilon\varepsilon_0/d \qquad \text{Equation 2 1}$$

Where d, is the separation distance of the parallel plates of area A, ε and ε_o are the permittivities of the separating material and of free space respectively. Typically values of 15-50 $\mu F\ cm^{-2}$ arise due to the double layer in aqueous electrolytes [9], which is considerably larger than conventional high dielectric-type capacitors. This may be attributed to the fact that the charge separation occurs over a distance of approximately 3-5Å [(1)] in the compact layer [9] and spanning up to 1000 Å in the diffuse layer [10-12], see figure 2.1, hence from equation 1 a small separation gives rise to a large capacitance. Also, since capacity is proportional to surface area, the utilisation of large surface area materials such as activated carbon fabric (a specific

[(1)] Å=$1x10^{-10}$ m

real area of 1000-2500 m^2 g^{-1}) and porous silicon (PSi,) (a specific real area of 200-800 m^2 g^{-1}, see chapter 4.1) may yield a theoretical capacitance of hundreds of F g^{-1}. Practically, for solid state devices however, values in the tens F g^{-1} are attainable due to the inaccessibility of the electrolyte to the entire electrode surface.

At any interface between two phases and particularly between an electrode and an electrolyte solution, there exists a segregation of positive and negative charge in a direction normal to the phase boundary. These charges may be associated in the form of dipolar molecules or polarised atoms, or they may be as free holes, electrons or ions. The charge segregation may occur through the preferential adsorption of either positive or negative ions at the interface, through the transfer of charge across the interface or through the deformation of polarisable molecules by the asymmetrical force field at the interface. The theory of the electrical double layer is concerned with the charge distribution and the electrical potentials that arise as a consequence of this charge separation. The study of the electrical double layer is concerned with the concept of the ideally polarised electrode, which may be defined as an electrode at which no charge transfer can occur, regardless of the potential imposed by an external voltage source. The equilibrium established at such an interface is not chemical as the two phases have no component in common, but is electrostatic as in a parallel plate capacitor, and may be described by equation 2.1. The simplest model was described by Helmoltz [10], who envisaged that the excess charge on a metal (electrode) would be neutralised by a monolayer of ions of opposite charge to that on the electrode phase. This concept of two layers of opposite charge is the origin of the term "electrical double layer", and although the situation is more complex, the original name remains. Figure 2.1 illustrates the double layer concept.

Gouy [11] and Chapman independently realised that in an electrolyte solution, the charges are free to move and are subject to thermal motion. They retained the concepts of the electrostatic theory (Debye-Huckel), to describe the coulombic electrode-counter ion interaction but, in addition, they allowed for the random motion of ions. The result being a diffuse layer of charge in which the concentration of counter ions is greatest next to the electrode surface and decreases progressively until a homogeneous distribution of ions pertains in the bulk electrolyte. However, the theory neglects the fact that the ions are not point charges and it was Stern [12]

who postulated that there was a plane of closest approach of the ions. This introduced the concept of hydrated sheaths around the ions; the outer and inner Helmoltz planes and the diffuse layer, which are illustrated in figure 1 below. This is the accepted model for the double layer today, [9-12, 13]. These theories were developed for aqueous solutions but the concept of the double layer is still valid for other liquid systems and polymer/gel electrolytes.

From equation 2.1 it can be seen that using high surface-area electrode materials such as activated carbon fibre may enhance the total capacitance of the double layer. Values of hundreds of farads per gram have been envisaged and tens of farads per gram attained [3]. Liquid electrolyte systems are subject to corrosion and high rates of self-discharge [14]. The solid state systems provide small-lightweight devices, but due to the solid polymer electrolyte being inefficient in pore penetration a gel electrolyte (see chapter3.2) offers the best combination of mechanical strength, pore penetration and ionic conductivity for these types of device.

An illustration of a supercapacitor cell is shown in figure 2.2.

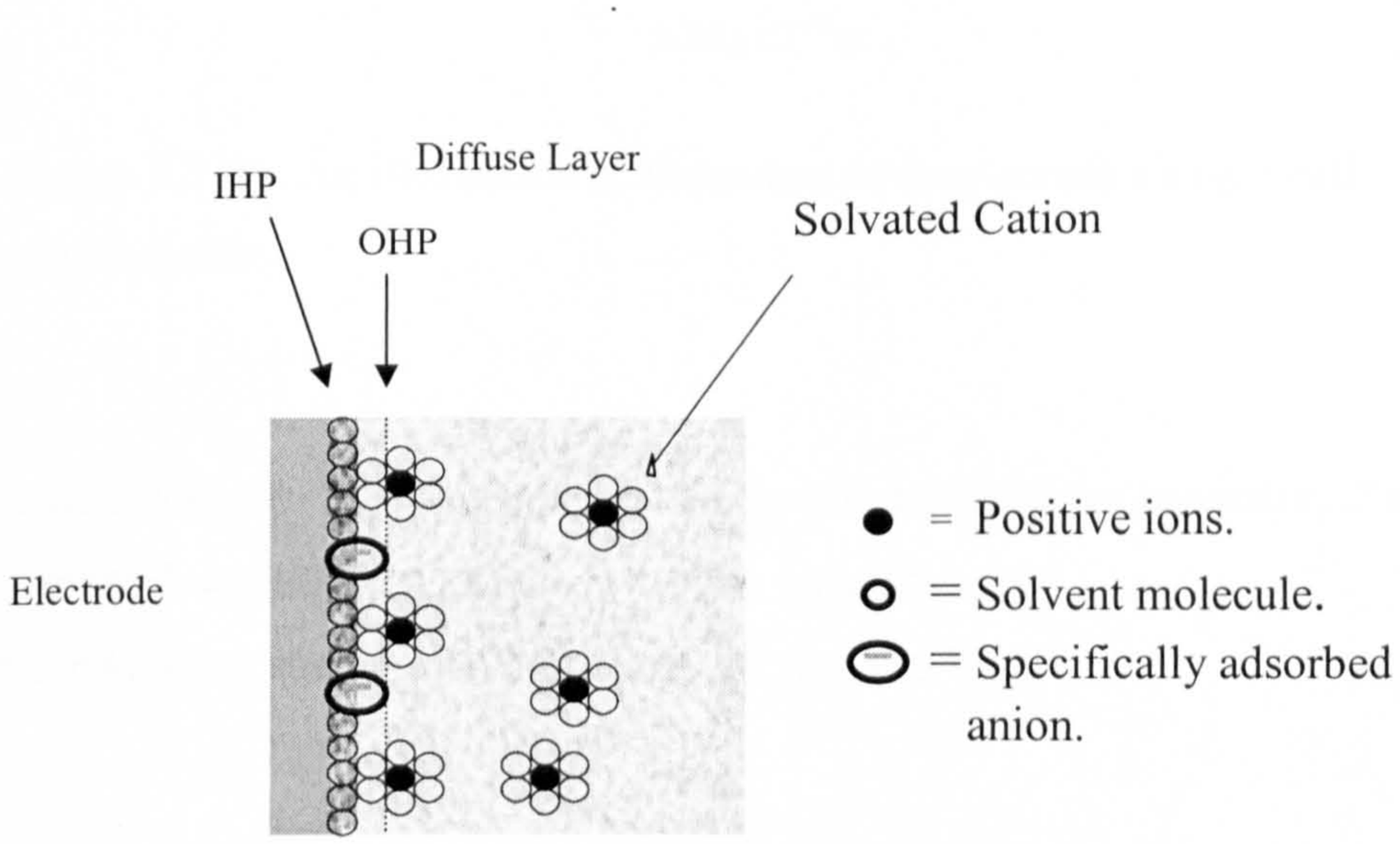

Figure 2.1 An illustration of the double layer of ions at an electrode/electrolyte interface.

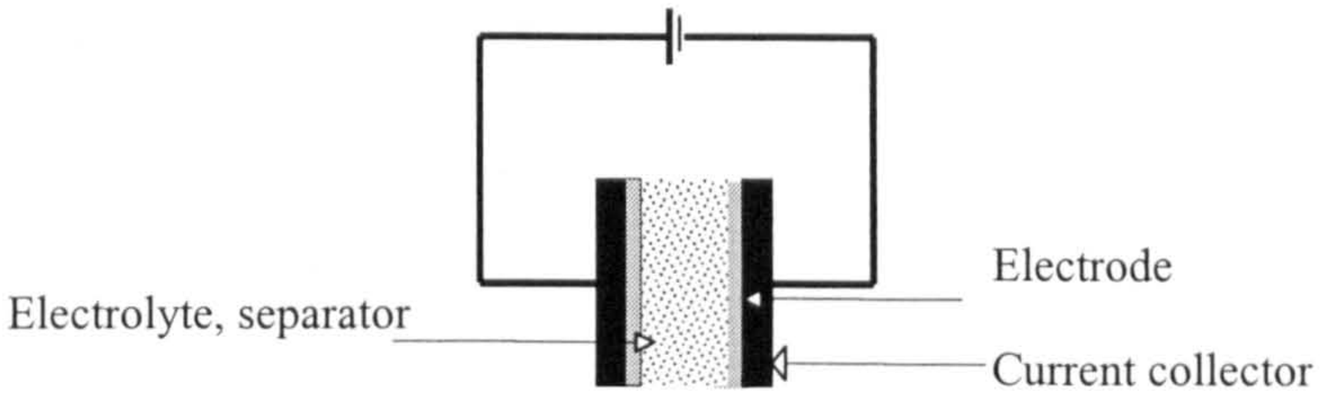

Figure 2.2 Schematic representation of a supercapacitor cell.

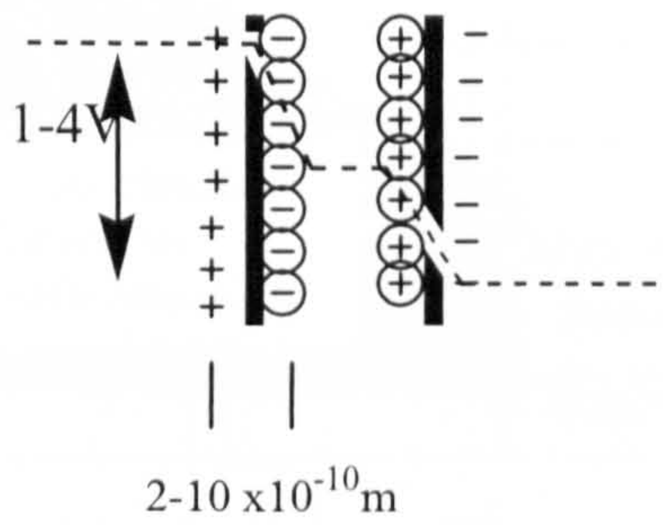

Figure 2.3 An illustration of the potential drop across a single cell supercapacitor.

Figure 2.3 shows the principle of a single-cell double-layer capacitor, illustrating the potential drop at the electrode/electrolyte interface.

The maximum energy stored in an EDLC is given by,

$$W=1/2\ C\ V_0^2 \qquad \text{Equation 2.2}$$

With a cell voltage V_0 of 1V (aqueous electrolyte) a specific energy of about 3.5 Wh/kg may be obtained, whereas using an organic electrolyte with a typical cell voltage of 2.3 V, 18 Wh/kg is achievable. These values are lower than those

achieved for batteries but much higher than those for conventional dielectric capacitors. A Ragone plot for dielectric capacitors, supercapacitors, batteries and fuel cells is shown in figure 2.4.

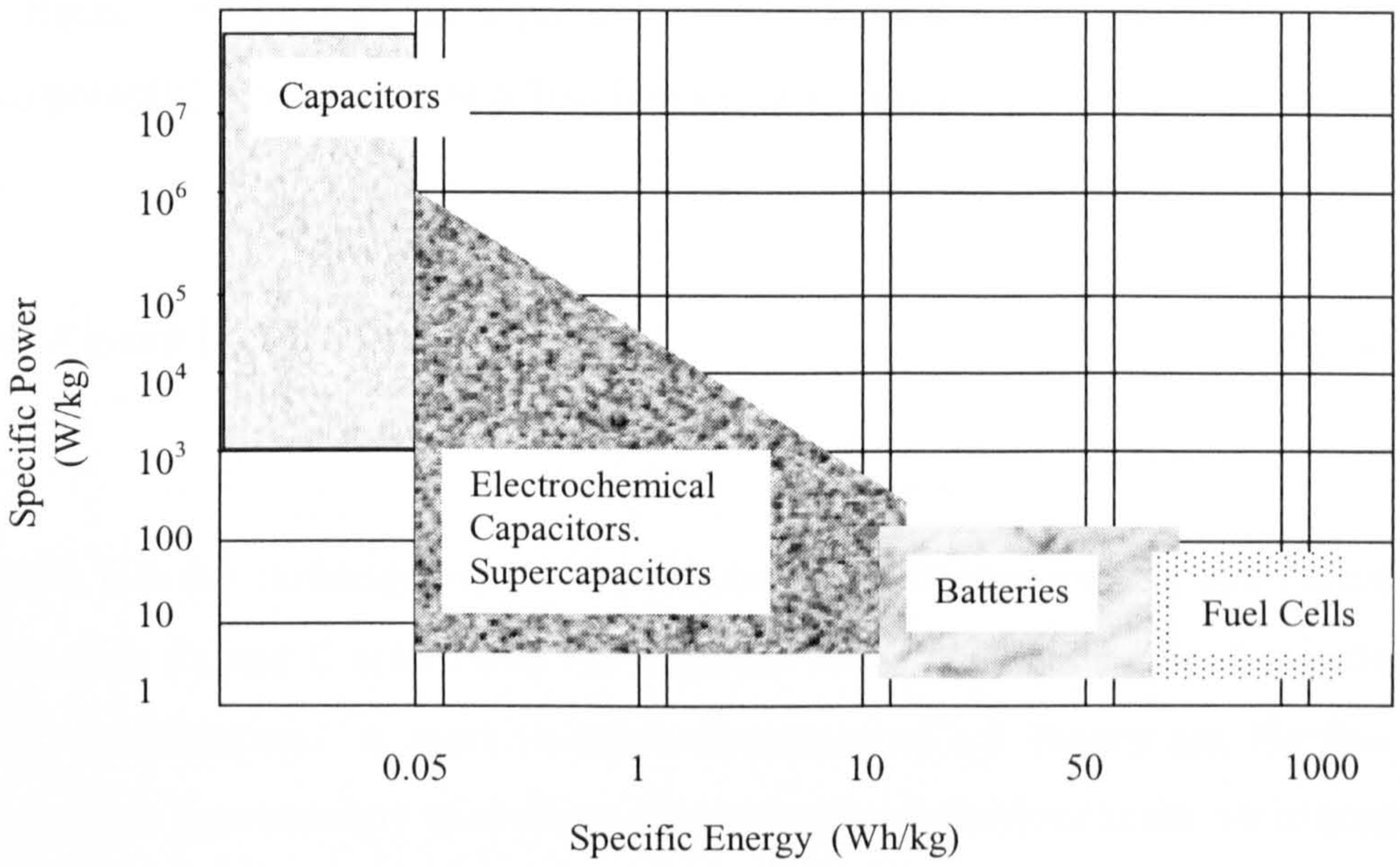

Figure 2.4 A Ragone plot for various electrical energy devices showing the position of supercapacitors. [15]

As mentioned earlier in this chapter, charge storage is mainly electrostatic in nature and, for this reason, charging/discharging is highly reversible and thousands of cycles are typically attainable with a given element of charge being able to be admitted or withdrawn at virtually the same potential [3]. Also, since C = q/v, an advantageous direct state-of-charge indication is given by the variation of voltage on charge or discharge, which is unlike the situation with many batteries. However, with carbon based EDLC's a small but significant "pseudocapacitance" (see below in figure 2.5) can also arise due to some electrochemical surface reactions on the carbon, e.g. reversible quinoid-type redox reactions or chemisorption processes involving partial charge transfer [3, 16].

An equivalent circuit can be used to represent the EDLC model, where the individual elements of the circuit mimic the current or potential modulation response of the actual interface. The simplest model is that of an ideally polarisable electrode as shown below in figure 2.5 (a), R_b is added to represent the solution or electrolyte resistance as shown in figure 2.5 (b). In practice, however, Faradaic leakage currents can arise depending on the electrode potential and solution composition, so circuit 2.5 (b) is modified to include a Faradaic resistance, R_F in parallel across C, as shown in figure 2.5 (c). R_F is usually inversely related to the electrode potential or overpotential η according to a Tafel-type relationship,

$$i(\eta) = i_0 \exp [-\alpha\eta F/RT] \qquad \text{Equation 2.3}$$

where, i_0 is the exchange current density and α the charge transfer coefficient. R_F in relation to R_b and C determines the response behaviour to changes of η with respect to a.c. modulation. A more in-depth discussion of a.c. theory and the use of a.c. impedance spectroscopy to evaluate supercapacitor behaviour is shown in chapter 5.

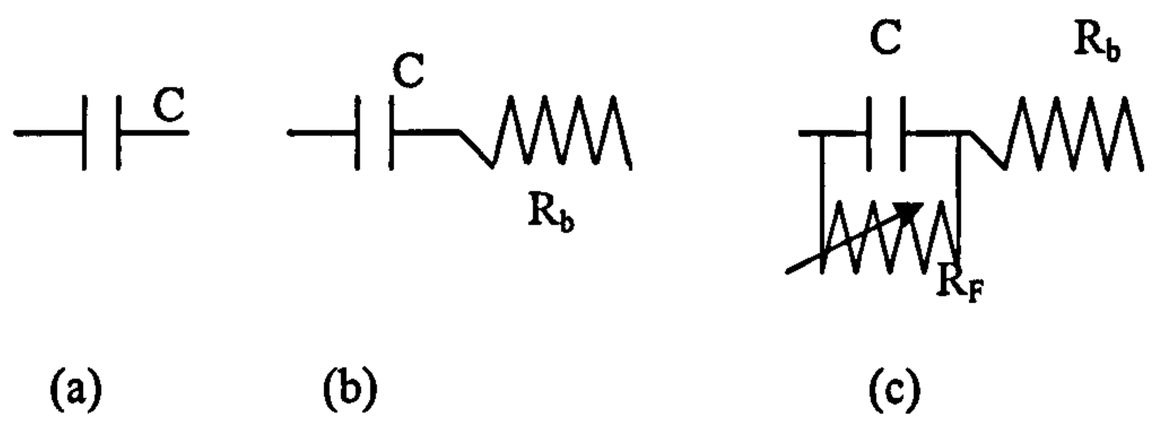

Figure 2.5 Equivalent circuit elements for (a) a capacitor, (b) a capacitor in series with a resistor for bulk electrolyte and (c) showing the inclusion of a Faradaic resistance in parallel with the capacitance.

2.2 Redox supercapacitors

For the redox capacitor the charge storage is similar to that of a secondary battery and in fact there is some debate whether these types of device should be classed as secondary batteries. However, the sketch of a Ragone plot for electrical energy storage devices (Figure 2.4) show that a redox supercapacitor falls into the electrochemical capacitor region.

As previously stated for an ideal EDLC, the charge is transferred into the double layer and there are no Faradaic reactions between the solid material and the electrolyte. In this case the capacitance (dq/dv) is a constant and independent of voltage. For devices that utilise pseudocapacitance, most of the charge is transferred at the surface or in the bulk near the surface of the solid electrode material. Hence, the interaction between the electrode and electrolyte involves Faradaic reactions, which in most cases can be described as charge transfer reactions. The charge transferred in these reactions is voltage-dependant resulting in the pseudocapacitance (C_ϕ=dq/dv) also being voltage dependant. Three types of electrochemical processes have been utilised in the development of supercapacitors using pseudocapacitance:-

- Surface adsorption of ions from the electrolyte.
- Redox reactions involving ions from the electrolyte.
- And the doping and undoping of electroactive polymer material in the electrode [17].

The first two processes are primarily surface mechanisms and are highly dependent on the surface area of the electrode material (as described in chapter 1.1.2), these types of pseudocapacitance were not directly used in this investigation. The third process involving the conducting polymer material is more of a bulk process and the specific capacitance of the material is much less dependent on the surface area, although relatively high surface area with micropores is required to distribute the ions to and from the electrodes in a cell. Thus the electrodes must have high electronic conductivity to distribute and collect the electronic current. The mechanisms of formation and conductivity of redox polymers, in particular polypyrrole, are discussed later in chapter 3.

2.3 Self-discharge

Supercapacitors can be used for storing electrical energy over a period of time ranging from seconds to several days [18]. The main factor determining energy storage time of a supercapacitor is its self-discharge rate. Self-discharge of a capacitor refers to the gradual decrease in the voltage across the capacitor, which occurs when the capacitor is left unconnected to either a charging circuit or an electrical load. In batteries, the self-discharge rate is very slow and the shelf life is measured in months and sometimes years. However supercapacitors have much higher rates of self-discharge. All capacitors slowly lose their charge, and hence, their stored energy.

Charged capacitors, like charged batteries are in a state of high free energy relative to that of the discharged state, so there is a pseudo-driving force for their self-discharge, as indicated in figure 2.6, if appropriate mechanisms are available for passage of Faradaic currents.

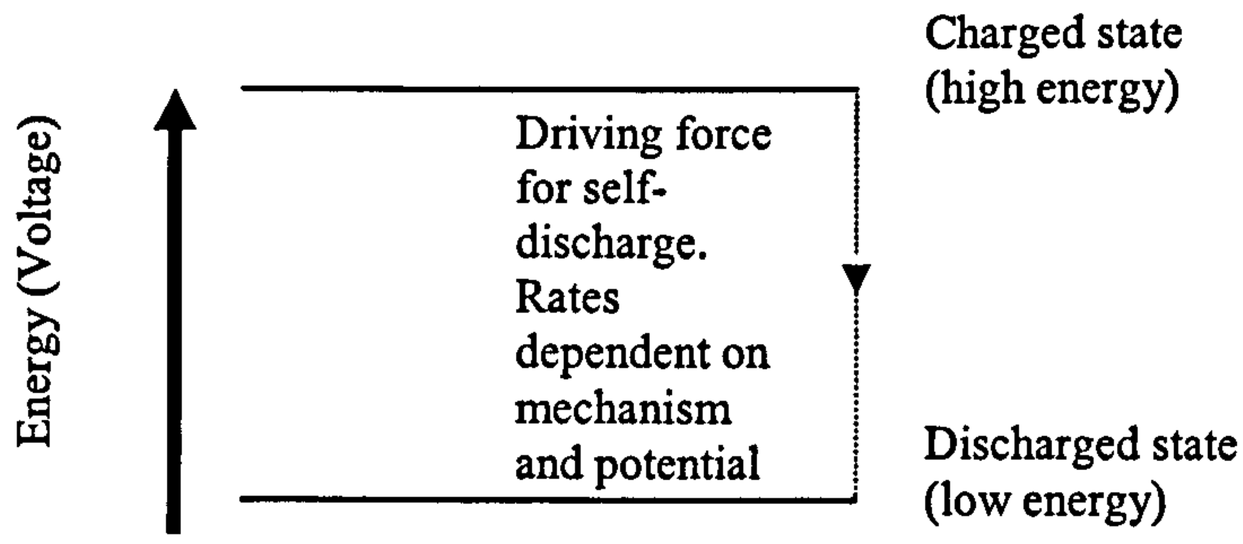

Figure 2.6 Diagram showing relative energy states for the charged and discharged state, illustrating the driving force for possible self-discharge of the supercapacitor [19].

2.3.1 Self-discharge mechanisms.

A capacitor or battery in the charged condition is in a state of high positive free energy relative to that of the discharged state, as shown in figure 2.6. Three kinds of self-discharge may then operate:-

i. If the capacitor has been overcharged beyond the respective decomposition potential limit of the electrolyte, then the self-discharge corresponds to the spontaneous decline of η, due to the overcharging current and arises because of continuing discharge across the double layer until $\eta \rightarrow 0$. The leakage process corresponds to a Faradaic charge-transfer reaction having a potential dependant Faradaic resistance R_F, operating in parallel across the double-layer capacitance, as shown in figure 2.5(c). The value of R_F increases with declining potential [19].
ii. If the materials from which the device is fabricated, (electrode or electrolyte) have impurities that are oxidisable or reducible within the working or charging potential range of the capacitor, then the capacitor may then be said to be non-blocking or non-polarisable. If the concentration of impurities is small then the self-discharge redox processes are diffusion controlled.
iii. If the capacitor or battery has internal ohmic leakage pathways, e.g. due to incomplete sealing of bi-polar electrodes or inter-electrode contacts, self-discharge will take place *via* a galvanic couple.

2.3.2 Self-discharge of double-layer type capacitors.

These have different self-discharge pathways to those of regular leaky capacitors because the EDLC consists of two interfacial capacitances separated by an electrolytic resistance R_b, plus a separator resistance R_S, if one is used, although solid polymer electrolytes behave as separators. The equivalent circuit is shown in figure 2.7.

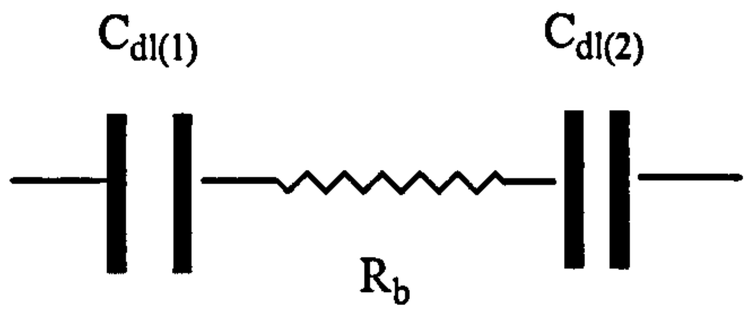

Figure 2.7 A simple equivalent circuit of an EDLC solid state cell without a separator.

Self-discharge processes can occur at either or both interphases of the double-layer capacitor depending on overcharge conditions or redox mechanisms. Thus it is possible for asymmetric self-discharge to occur, i.e. across one double layer or the other. The representative equivalent circuit would then have two Faradaic leakage resistances in parallel with the double-layer capacitances which will not necessarily have the same value, as shown in figure 2.8.

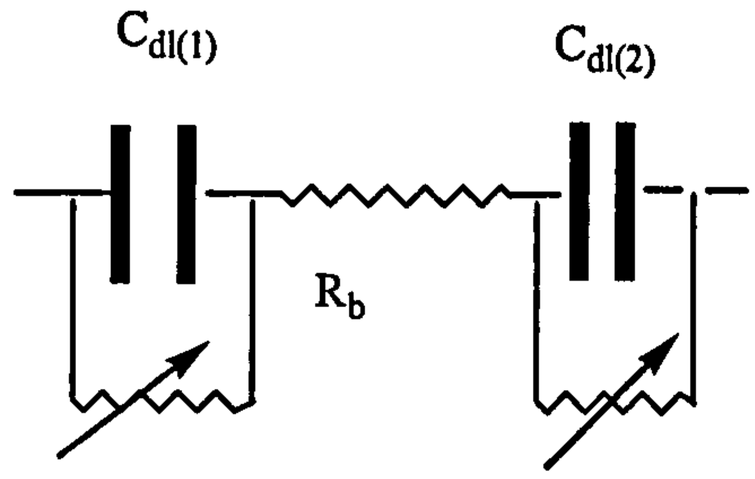

Figure 2.8 Equivalent circuit showing the faradaic leakage resistances across the double layer capacitances.

2.3.3 Temperature effects on self-discharge

Self-discharge is a rate process so it is affected by temperature according to known kinetic effects associated with activation energy, $\Delta E_a^{\pm}$ in an Arrhenius relation. Since $\Delta E_a^{\pm}$ is positive then self-discharge currents i(T) increase with temperature according to equation 2.4.

$$2.3 \log i(T) = 2.3 \log A^{*} - \Delta E_a^{\pm}/RT \qquad \text{Equation 2.4}$$

Thus log i(T) is a linear relation in 1/T, the slope of which gives $-\Delta E_a^{\pm}/R$.
For Faradaically controlled self-discharge processes, $\Delta E^{\pm}$ is in the order of 40-80 kJ mol^{-1}. For diffusion controlled, $\Delta E_a^{\pm}$ is around 16-20 kJ mol^{-1} corresponding to activated transfer of the depolarising impurity or redox species in the bulk of the "solution", towards the electrode surface. The important practical consequence of the temperature effect is that self-discharge of capacitors or batteries is much more of a serious problem at elevated temperatures. For a typical activation energy of 40 kJ mol^{-1}, the ratio of self-discharge currents at 70^0C compared with 0^0C is equal to 37 or $10^{1.56}$, a large increase. This is important practically since 70-100^0C is a normal operating temperature for an internal combustion engine and therefore the use of supercapacitors in hybrid vehicles might prove problematic. Clearly considerable effort needs to be taken in order to minimise rates of self-discharge in supercapacitor devices [19, 20].

The electrochemical techniques such as a.c. impedance spectroscopy, cyclic voltammetry and galvanostatic charge-discharge experiments used to characterise and asses capacitor performance are discussed later in chapter 5.

3. Conducting Polymer theory

An in-depth review of the formation mechanism of polypyrrole is presented. The reader may then be familiarised with the background theory of polypyrrole and the different parameters that govern the properties of the as grown film. This was considered essential for the future development of the polypyrrole investigation presented in chapter 8.6.

3.1 Electronically Conducting Polymers

The discovery of the metallic properties of $(SN)_X$ was enhanced by the demonstration by MacDiarmid, Heeger and Shirakawa *et al.* (1977-78) [1, 3] of the semiconducting and metallic properties of polyacelylene, for which they received the Nobel price for chemistry in 2000. Since the late seventies numerous materials of this nature have been reported, such as polythiophene, polyanniline and polypyrrole. These polymers have the ability to switch between insulating and conducting or (semiconducting) states [4, 5].

Polypyrrole was first synthesised in 1916 [6, 7[1]] by the oxidation of pyrrole with H_2O_2 to give an amorphous powder called pyrrole black. The electrochemical production of polypyrrole dates back to the work of Dall'Ollio [8[1]] who also obtained pyrrole black by the electrochemical oxidation of pyrrole in sulphuric acid on a platinum electrode. Since then there have been extensive and there are ongoing studies on the properties and uses of polypyrrole. In this study, polypyrrole was used as an electrode material in the preparation of redox supercapacitor devices. A brief discussion of some of the mechanistic pathways proposed by various groups on the electropolymerisation of pyrrole to polypyrrole is presented.

Polypyrrole forms as a semiconducting film on the working electrode (anode) in a cell containing a solution of the monomer when the appropriate potential is applied to the cell. The film as grown (*i.e.* before any electrochemical cycling) is in the oxidised form. Diaz and co-workers proposed the mechanism for polypyrrole growth as shown in chapter 3.1.1. [9, 10].

[1] References taken from reference 5

3.1.1 Polypyrrole growth mechanism

The electropolymerisation of pyrrole to polypyrrole may be split into the following steps:-

Initially an electron transfer occurs (E) followed by a series of chemical reactions (C) and subsequent electron transfer reactions. The term $E(CE)_n$ is generally used to describe this mechanistic pathway.

Oxidation of the pyrrole monomer "R" at the electrode surface forming the radical cation $R^{+\bullet}$, shown in figure 3.1.

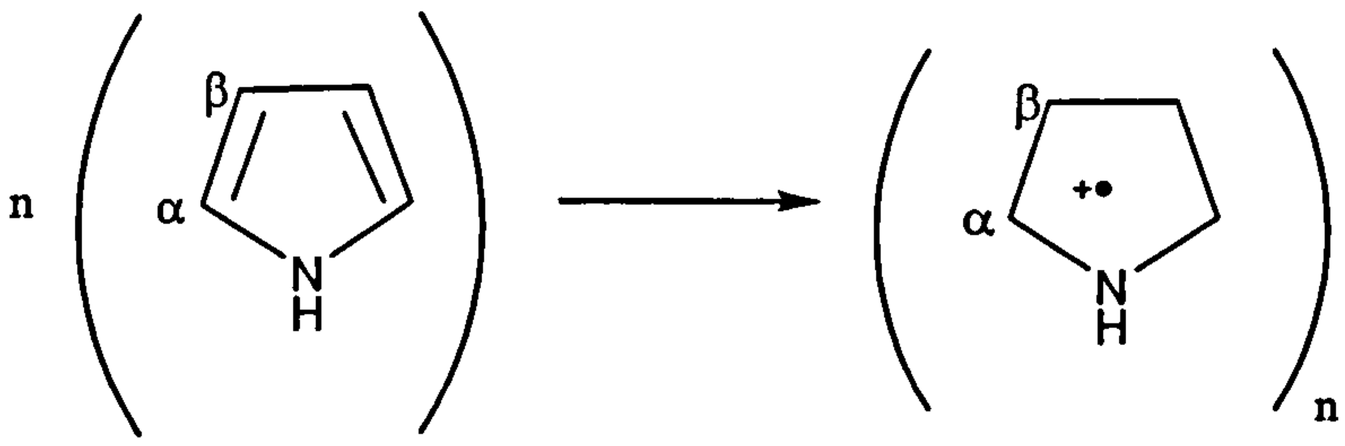

Figure 3.1 The oxidation of pyrrole monomer to the radical cation

The radical cation of figure 3.1 may be represented as four resonant structures as shown in figure 3.2.

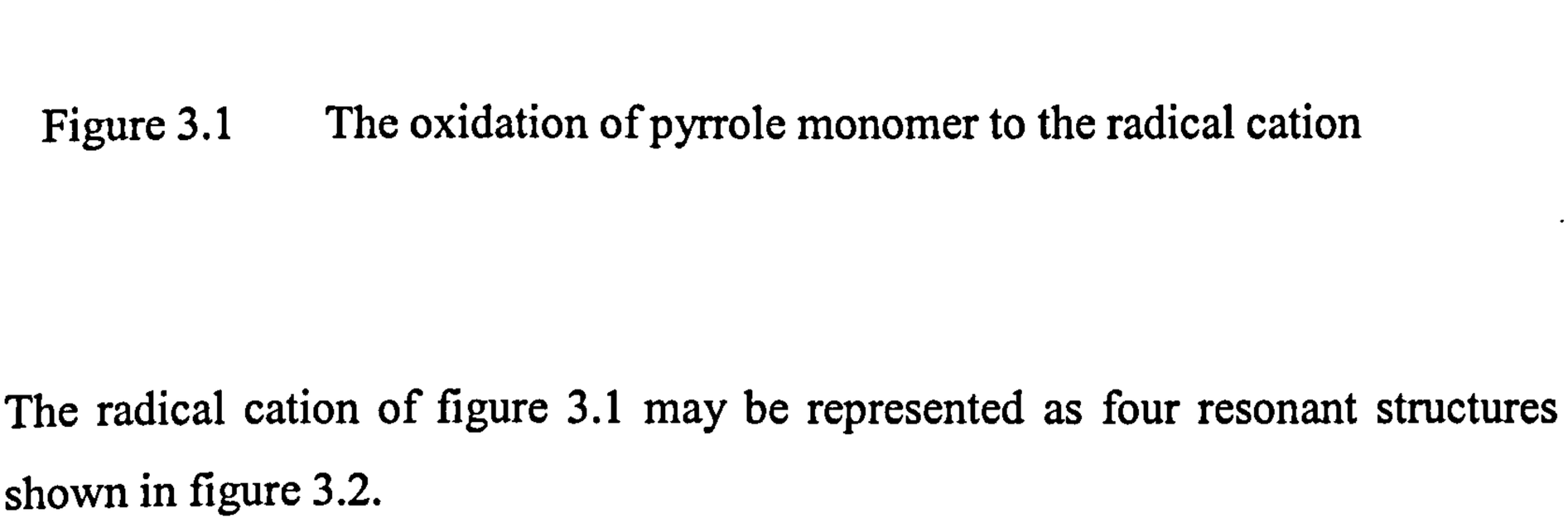

Figure 3.2 Four resonant structures of the pyrrole radical cation

The electron transfer reaction is faster than the diffusion of R in the solution at the electrode surface. Thus at the oxidation potential there is a high concentration of $R^{+\bullet}$ at the electrode surface, which is being continually fed by the diffusion of R. $R^{+\bullet}$ can undergo a number of different reactions depending on their reactivity:

When $R^{+\bullet}$ is relatively stable it has time to diffuse into the bulk solution and react to form soluble low molecular weight products. When $R^{+\bullet}$ is very unstable it can react rapidly at the electrode surface with the solvent or the anion also forming soluble low molecular weight products. Between these two extremities $R^{+\bullet}$ may undergo dimerization reactions.

The radical cation $R^{+\bullet}$ has a greater unpaired electron density at the α position and therefore dimerises *via* resonance form (iii), as shown in figure 3.2. The coupling of two radical cations in the α position results in the formation of a dihydromer dication, shown in figure 3.3 (v).

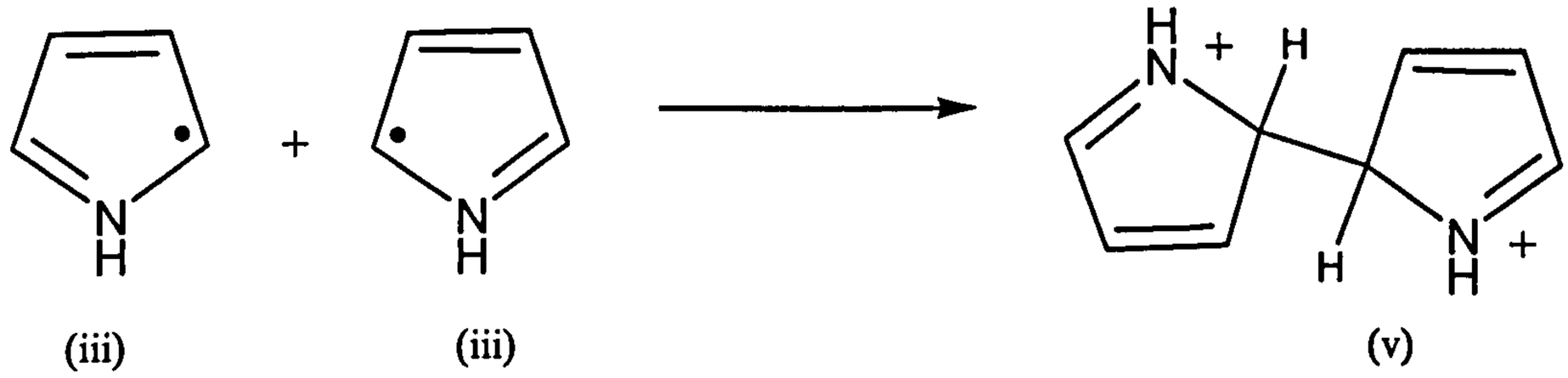

(iii) (iii) (v)

Figure 3.3 α-coupling of two radical cations forming a dihydromer dication

The loss of two protons forms the aromatic dimer as shown in figure 3.4.

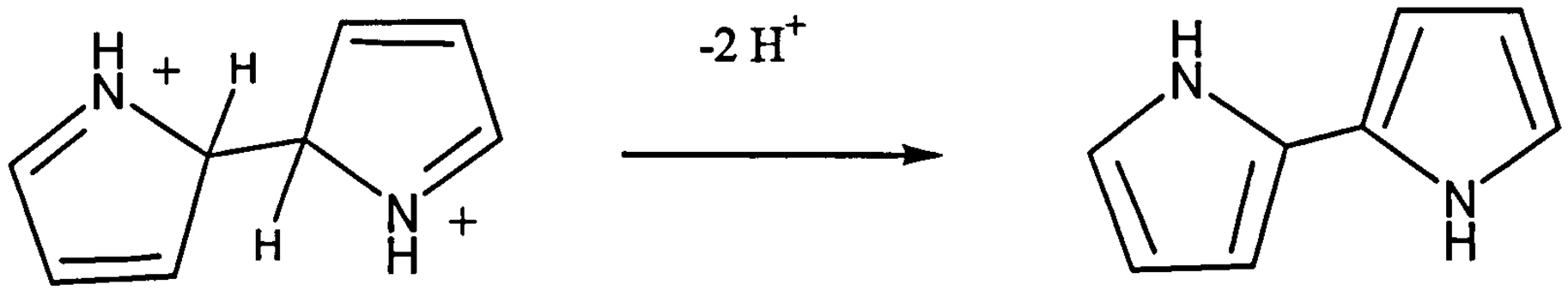

(v) (vi)

Figure 3.4 Formation of the aromatic dimer

The polymerisation follows the oxidation of the dimer (vi), as shown below in figure 3.5, into the radical cation (vii). Since the unpaired electron is now delocalised over two rings, the oxidation potential of (vi) is lower than the oxidation potential of the monomer. The dimer (vi) is therefore more easily oxidised at the applied potential (i.e. the oxidation potential of the monomer). Due to this stabilisation the dimer radical cation becomes less reactive than the monomer. The α position (position 2 or 2') is the most reactive and the resonance form (ix) is dominant over the others shown in figure 3.5.

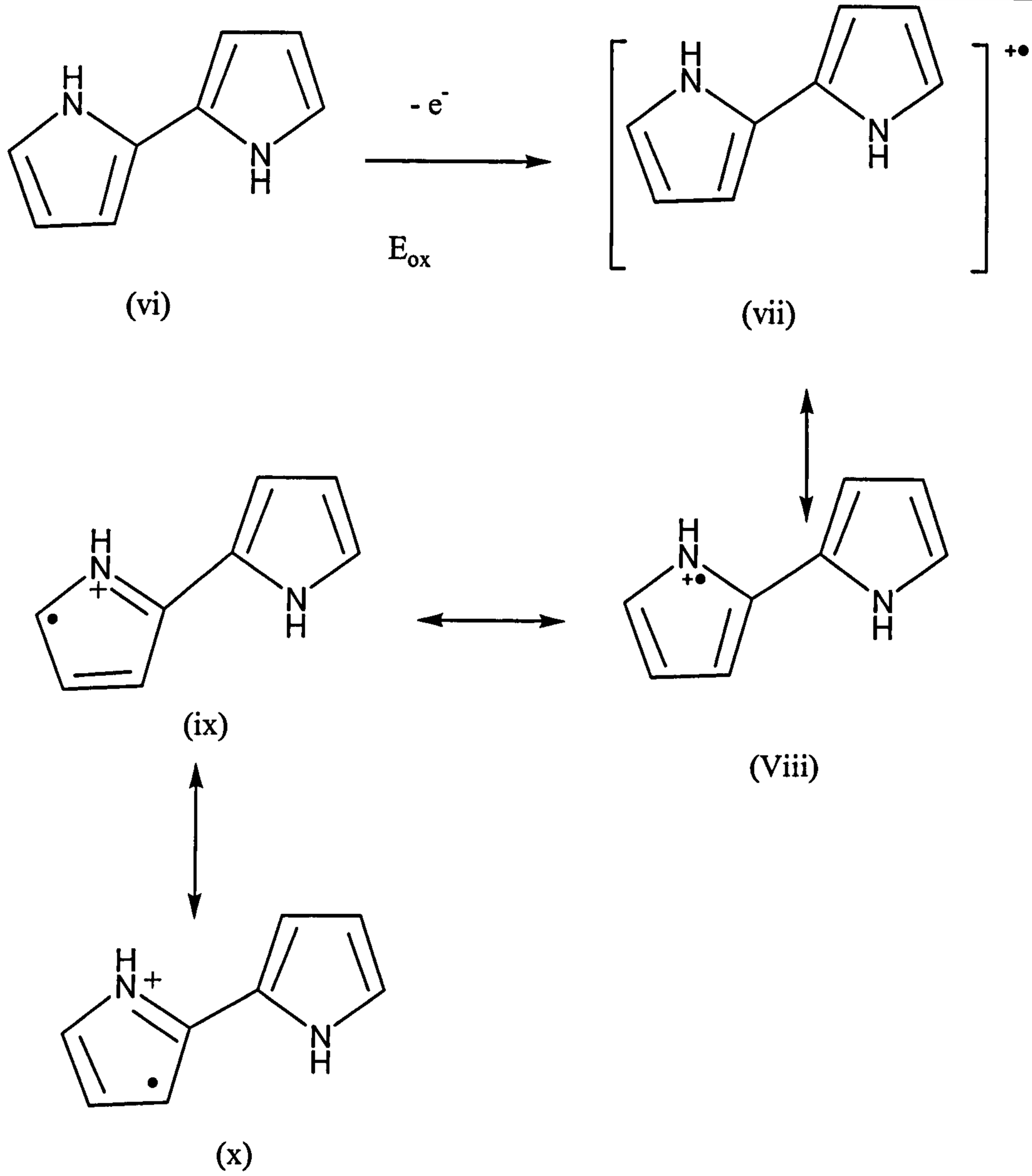

Figure 3.5 Oxidation of the aromatic dimer

The resonant form (ix) reacts at position 2 or 2' with a monomer radical cation (iii) to form a dimer trication (xi) that deprotonates to give the neutral trimer (xii) as shown in figure 3.6.

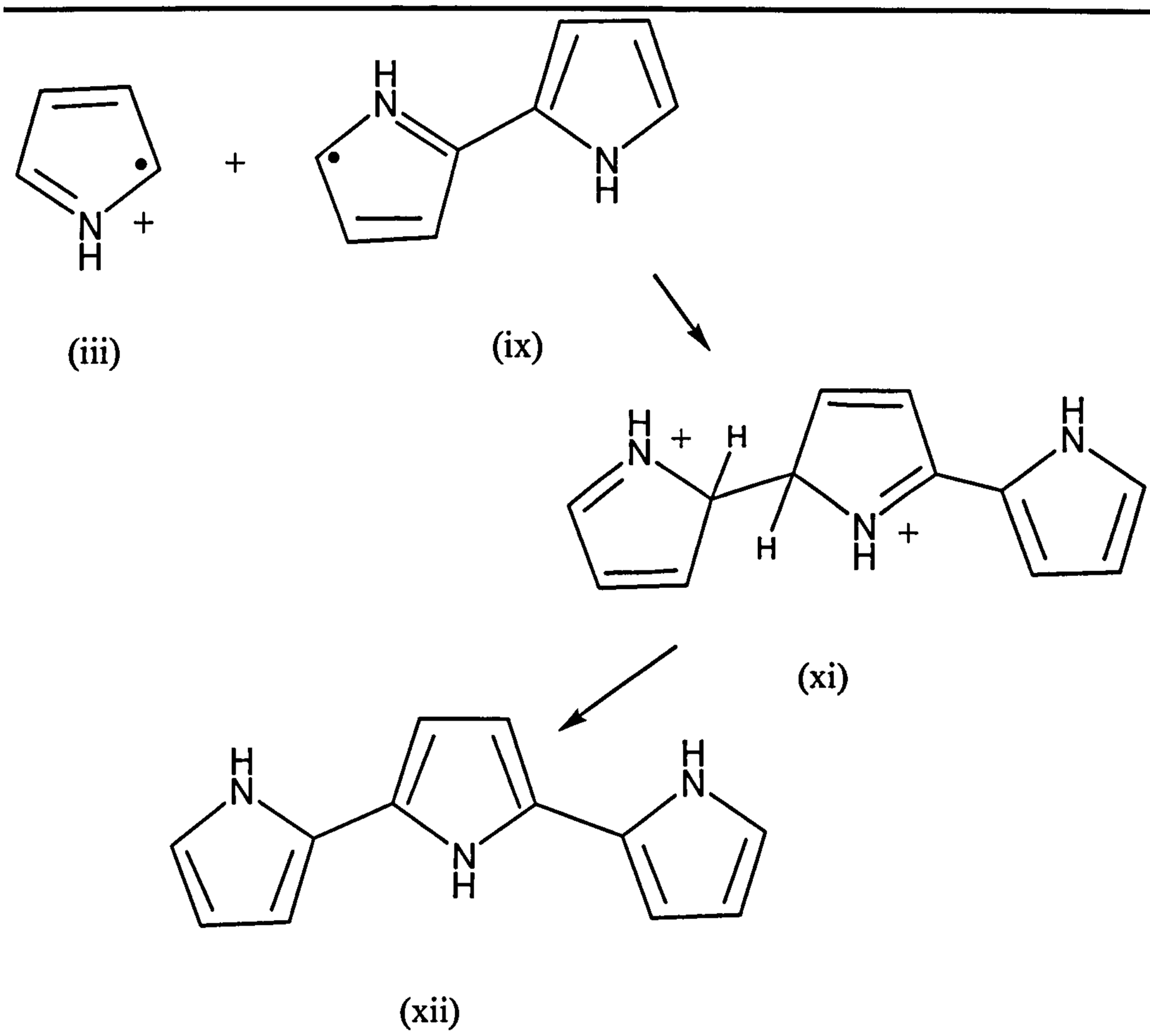

(iii) (ix) (xi) (xii)

Figure 3.6 Formation of the neutral trimer.

The electro-oxidation of (xii) results in the radical cation (xiii), shown in figure 3.7. The trimer (xii) may undergo coupling reactions in the α position (2-2') or the β position (3-3'), even though the β position is sterically hindered and due to the steric hindrance the α position will predominate. However, the oligomer chain, as well as the delocalisation of the unpaired electron, increases progressively and the α-coupling will no longer be the only possible coupling. The longer the chain the more the possibility of β-coupling.

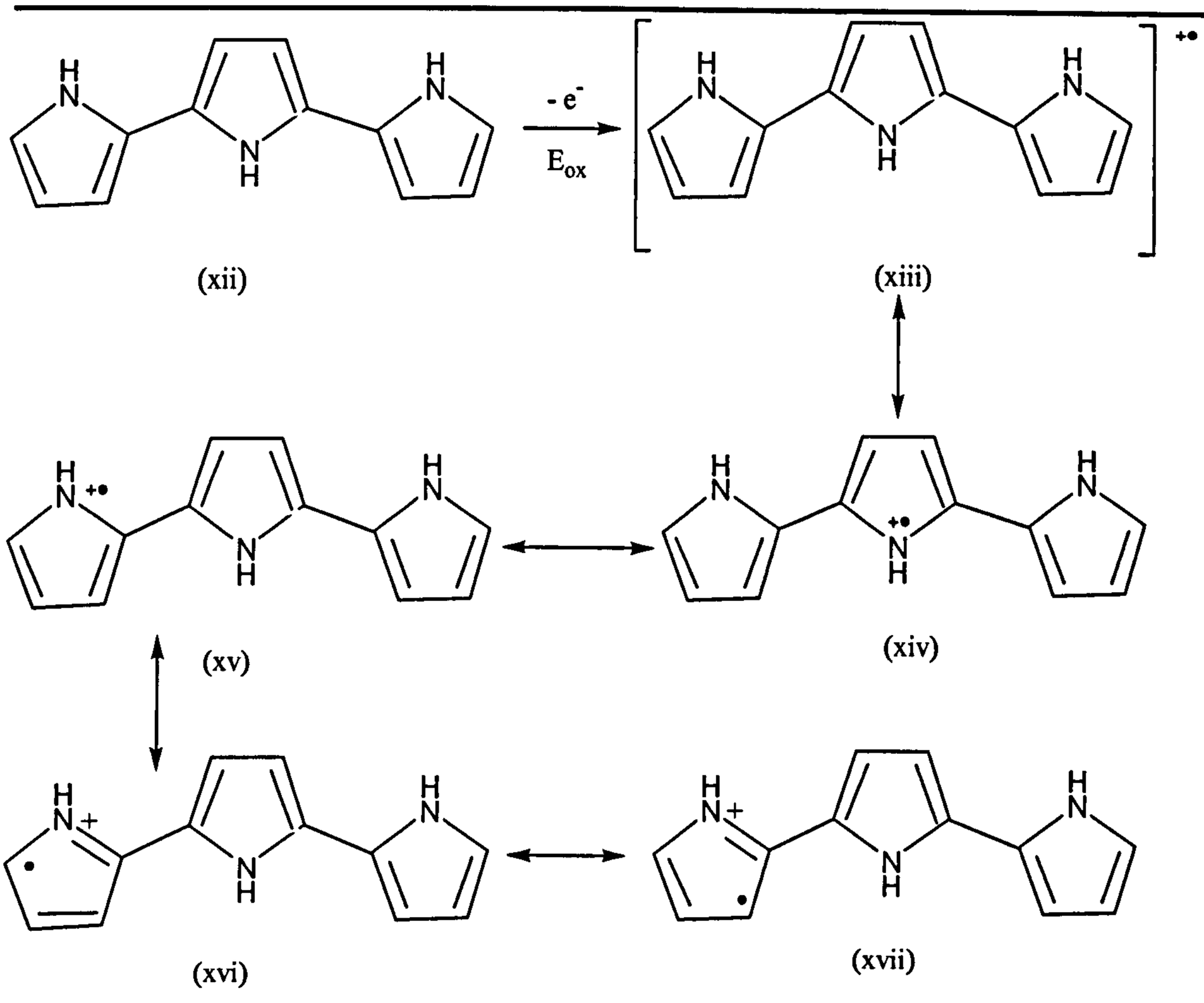

Figure 3.7 Formation of the radical cation trimer, showing the different resonant structures

The propagation continues *via* the same sequence i.e. oxidation, coupling, deprotonation, until the final polymer product is obtained. (Figure 3.8)

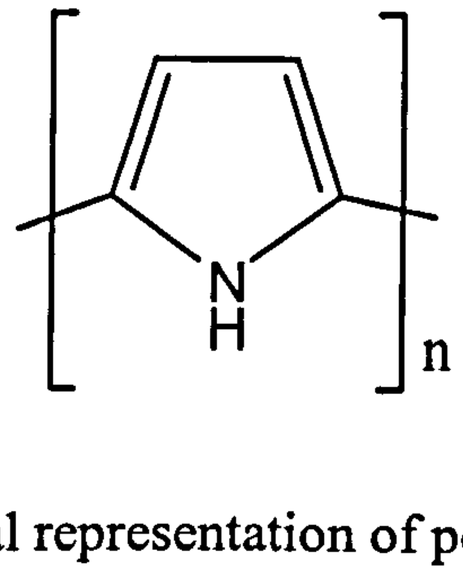

Figure 3.8 Structural representation of polypyrrole.

The electropolymerisation produces polypyrrole in its oxidised (doped) state, i.e. in its conducting form. The polymer chain carries a positive charge every 3-4 repeat units which is counterbalanced by the anion supplied by the electrolyte solution in which the monomer was electropolymerised.

This is represented in figure 3.9, where A^- is the electrolyte anion.

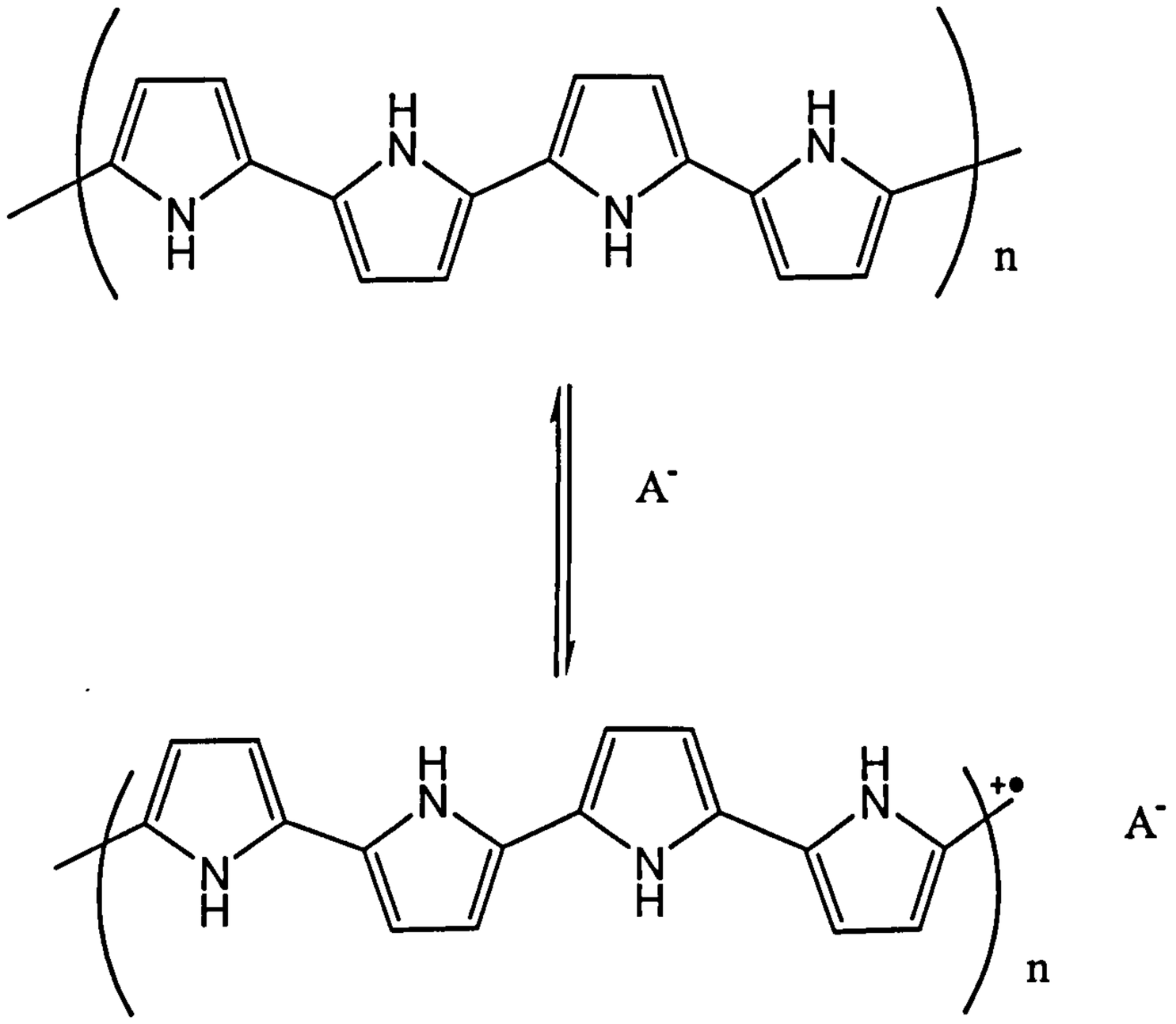

Figure 3.9 representation of polypyrrole in its oxidised state

The polypyrrole films obtained are approximately 65% polymer and 35% counteranion. The number of electrons per molecule is generally between 2 and 2.7, where 2 electrons are used in the film formation and the excess charge is consumed by the polymer oxidation. This number is usually in agreement with the number of anions found in the system.

There are several reasons why this mechanistic pathway is generally favoured:- Electron paramagnetic resonance (EPR) studies show the existence of a π-type radical. [11].

The elimination of protons from the α-position corresponds with a drop in pH of the solution during polymerisation.

The number of electrons consumed has been found to be 2.25-2.33, which is in agreement with this mechanism. Chronoabsorption studies have shown that the film grows linearly with respect to t and not to $t^{1/2}$. This observation shows that the rate determining step during the film growth is a coupling process and not the monomer diffusing towards the electrode [12].

However there are other proposed mechanisms for the formation of electropolymerised polypyrrole: -

- K.J. Kim *et al.* [13], who postulated that polymerisation is initiated by the loss of two electrons and a proton from a pyrrole molecule forms the active intermediate Py^+. A neutral Py molecule then dimerises Py^+ with the loss of a second proton. The growth then continues *via* the loss of two electrons and coupling. The polymer is then deposited in three stages:-
  i. Initially monomer absorption occurs.
  ii. The formation of the polymer and the nucleation of low molecular weight polypyrrole in solution.
  iii. Layer by layer growth.

- Pei *et al.* proposed that the initial polymerisation stage be in solution followed by polymer precipitation [14].
- Pelcher *et al* [15] have proposed a mechanism in which the radical cation reacts directly with a neutral molecule giving a cation dimer. The cation dimer then looses a second electron and two protons forming the neutral dimer. Sato *et al.* [16] have studied this coupling mechanism by comparison with the classical radical cation approach. They explained their experimental results by a coupling between the radical cation and a pyrrole monomer molecule, which corresponds to an aromatic substitution reaction of an electrophile. This mechanism, however has been challenged by Takakubo [17] who demonstrated by molecular orbital

calculations that the addition of a radical cation to a neutral molecule is symmetry forbidden and therefore would require a large activation energy.

- Finally, Reynolds *et al.* [18], studied polypyrrole polymerisation by electrochemical Quartz Crystal Microbalance (EQCM) in various aqueous electrolyte solutions. Under specific conditions with ClO_4^-, BF_4^-, PF_6^- electrolytes, three stages are observed during electropolymeristion. Where the number of electrons (n) is different. The first and second stages give n values of 1.60 and 0.12 respectively, whereas the third value gives n = 2.50. The third stage gives an n value, which corresponds to that of the Diaz mechanism. To explain the low n values and high rates of polymerisation in the first two stages, an electrochemically initiated chain polymerisation mechanism was proposed which starts the growth of the ppyr film. The reaction pathway is initiated by the formation of a monomer radical cation at the surface of the electrode followed by a rapid growth of the chain and a low n value. The obtained non-conjugated polymer becomes conjugated and takes on the form of the doped polypyrrole form by oxidation at the electrode. This mechanism is only valid in aqueous electrolytes and the ions mentioned above. The strong interaction between the water molecules and the radical cations, and the anions ability to achieve the initiation step enable this type of mechanism. The product of this type of mechanism have the ability to transport both anions and cations during electrochemical switching between the oxidised and reduced states, unlike the polymers produced by radical cation coupling which only transport the anion.

The final step in the mechanism is not clear and different hypotheses have been suggested. Diaz proposed that the reaction with water might quench the polymerisation (figure 3.10). Street believes that the growth of the polymer chain terminates because the radical cation becomes relatively unreactive towards chain propagation or because of steric hindrance at the chain ends.

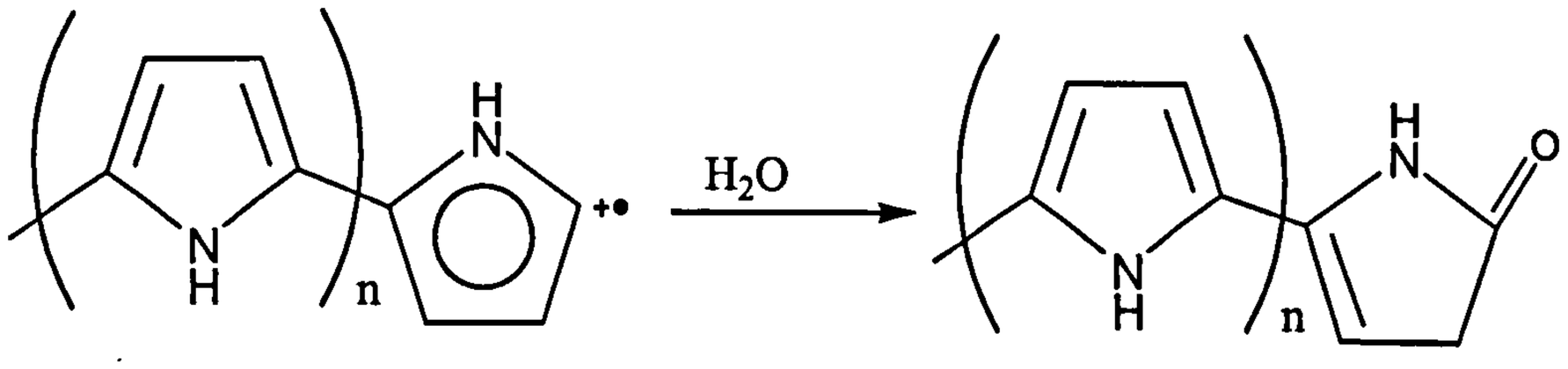

Figure 3.10 Termination of polypyrrole growth via a reaction with water.

3.1.2 Conductivity of polypyrrole

The potential cycling of the polymer, between the insulating and conducting forms, can be repeated many times without the loss of electroactivity of the film. The conductivity of the films grown from acetonitrile has been shown via conventional four point probe techniques to be 10-100 S cm^{-1} (cf. Copper metal, 10^6 S cm^{-1}) [4].

Diaz and colleagues [19], when faced with a new conducting material, had a choice of two possible conduction mechanisms, differentiated only by the parameter τ, the residence time, *i.e.* the time spent by a carrier on any particular site in the lattice. Thus, if τ is significantly shorter than the time over which the atoms in the lattice vibrate (phonon vibrations), then the carrier appears to move on an essentially rigid background and is termed "free". This is found in most simple metals.

In contrast, if τ is much longer than the time taken for lattice vibrations to occur, then the atoms of a particular site may relax around the occupying carrier. The carrier then cannot move as easily and must wait until the vibrations of the lattice provide a favourable pathway for it to escape to the next site. The carriers in this case are polarons (polar phonons) or bipolarons, as shown in figures 3.11(a) and 3.11(b) below. Thus the removal of an electron from the chain leaves behind a localised charged entity having finite conjugation length. Removal of a single charge results in a radical cation (a polaron) and removal of a second charge generates a bipolaron. Diaz measured the conductivity, σ, of a film as a function of temperature and found that it varies as:

$$\sigma \propto \exp [-a/T^{1/4}] \qquad \text{Equation 3.1}$$

Where 'a' is a constant. Equation 3.1 suggests a three-dimensional variable-range hopping mechanism, which is therefore not metallic in nature. The hopping species, polarons and bipolarons, are almost degenerate and coexist, with both contributing to the conductivity. At very low doping concentrations only polarons are generated. As the doping level increases, both carriers are produced until polaron recombination results in bipolarons being the dominant species in the highly oxidised polymer. The doping levels at which bipolarons start to be generated, and then polaron recombination commences, will depend on the exact relationship between the relative number of the two carriers at low and medium doping levels. This, in turn will be dependent on the average chain length of the polymer, or more precisely, the average conjugation length between defect or β-coupled monomer units, the distribution of conjugation lengths throughout the polymer and the size of polarons and bipolarons (figures 3.11(a) and (b)). Based on these considerations Hammet (1989) stressed the diverse nature of growth conditions as a possible explanation for the spread of results commonly obtained from the same conducting polymer grown in different laboratories.

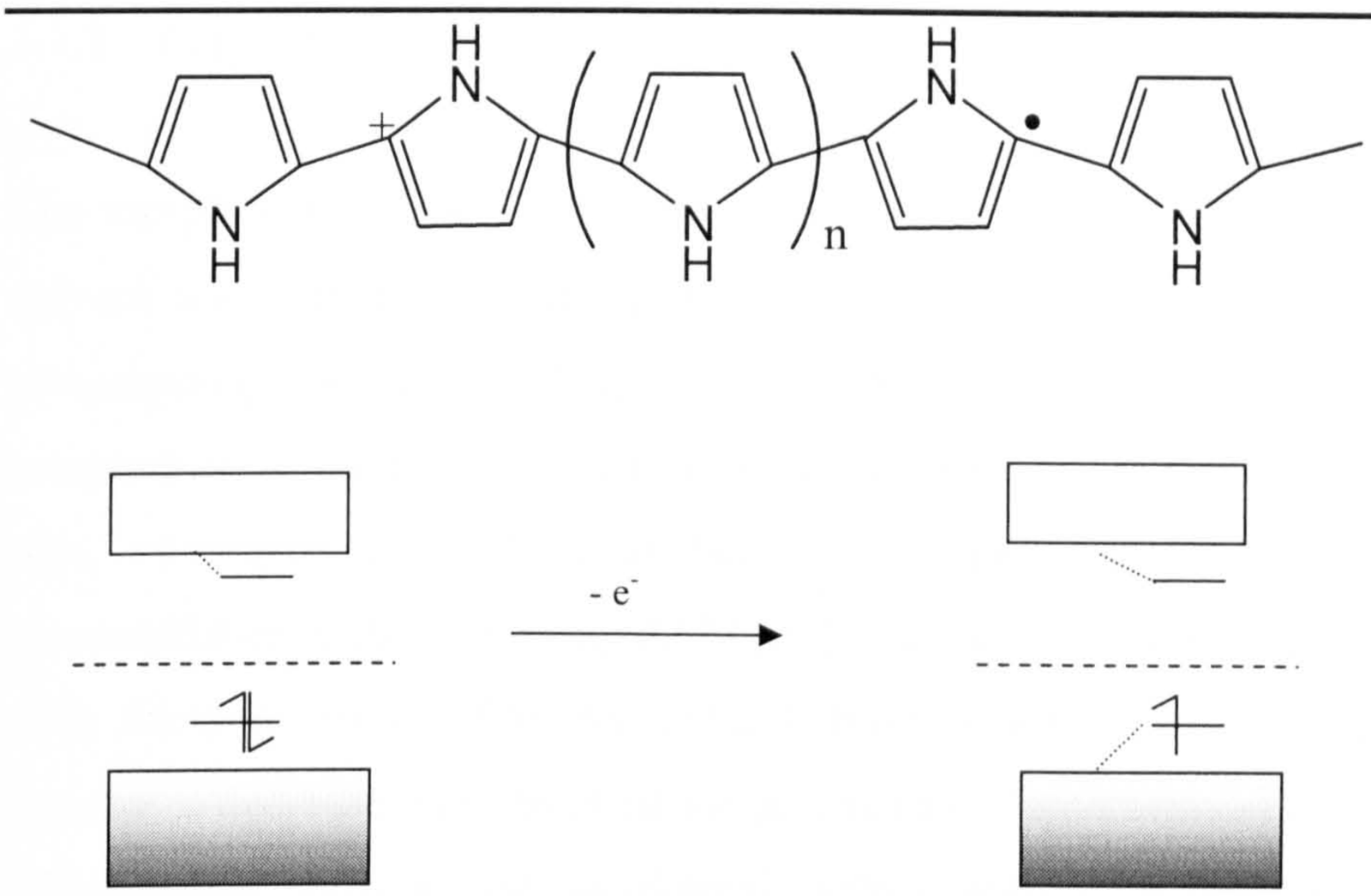

Figure 3.11 Electronic/band description of polypyrrole, illustrating polaron formation.

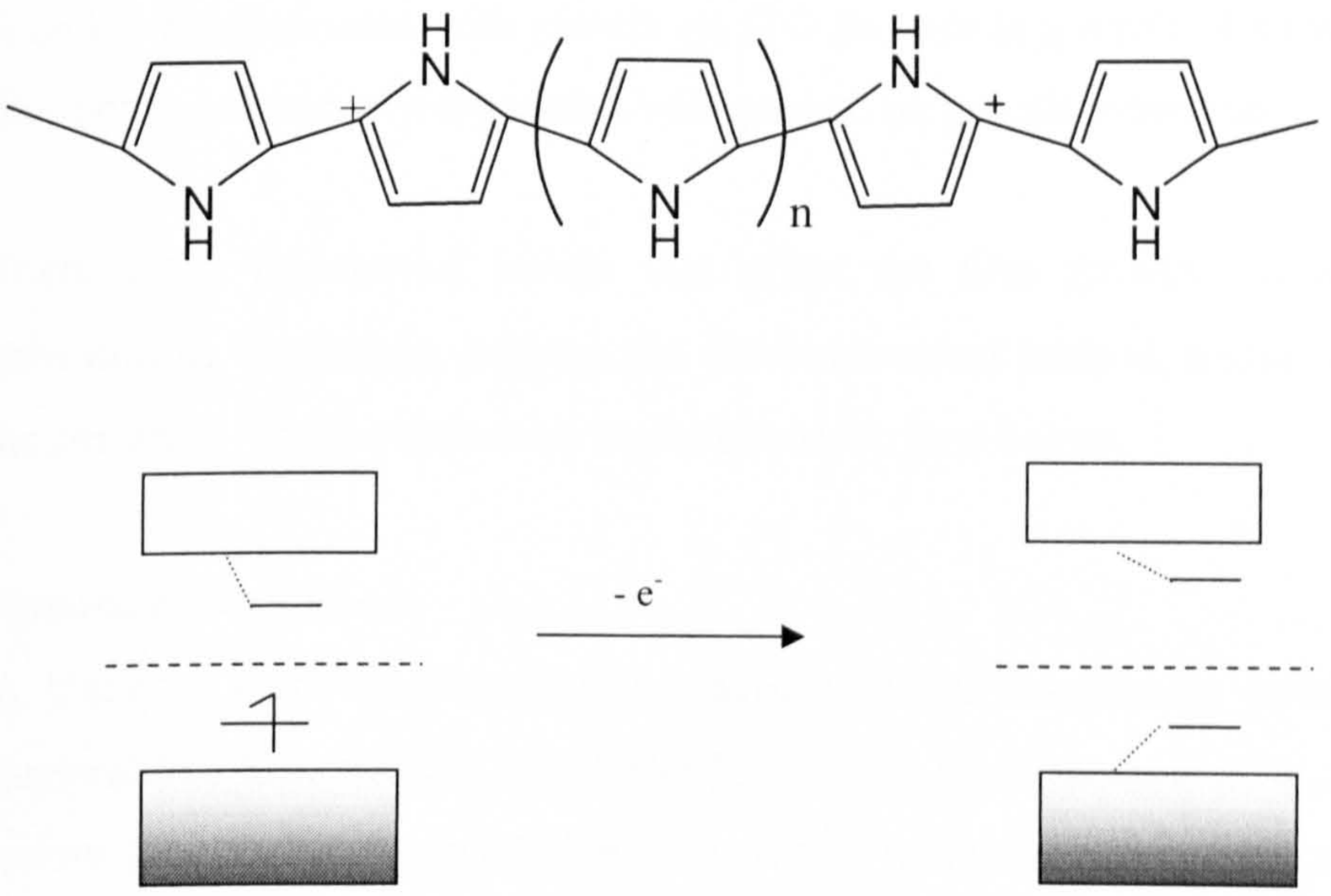

Figure 3.12 Electronic/band description of polypyrrole, illustrating Bipolaron formation.

3.1.3 Polypyrrole film morphology

The morphology of the polypyrrole film is influenced by variables such as dopant, solvent and applied potential [20]. A number of studies have been carried out investigating the relationships between these variables and morphology, since morphology of the film greatly affects the mechanical and electrical properties of the film. Compton *et al.* have studied the influence of dopant on the roughness characteristics of the film using AFM [21]. Surface roughness was found to increase with thickness of the film for chloride-based dopants and sulphate-doped films, whereas a decrease was observed for perchlorate. For thickness below 1000 nm the AFM results show a globular-shaped surface with little influence of the dopant nature. For thicker films, chloride-doped and perchlorate-doped films have "cauliflower" structures. An interesting point is that mainly two types of globules with different heights were noticed on the film surface and were found to be independent of film thickness and dopant nature. Miles *et al.* investigated the formation of wrinkles on the surface of films using *in situ* AFM [22]. These wrinkles may cause interfacial problems in practical devices. The wrinkles were found to be associated with growth on ITO and not as a result of handling. They are thought to be uniquely associated with growth on porous substrates.

There are a number of factors that affect the film growth, including monomer substitution, electrolyte, solvent, the electrochemical method, temperature and pH of the solution. These parameters are briefly described below.

Monomer substitution

In classical electropolymerisation, monomers are continually oxidised while the electroactive film forms at the electrode surface. Since the oxidation of the monomer occurs at a higher potential than that of the redox processes of the polymer, side reactions including crosslinking and/or overoxidation of the polymer may take place. A disadvantage of using pyrrole is the availability of β-sites for coupling. β-coupling leads to a conjugation break along the polymer backbone which results in an increase in the observed band gap and a decrease in conductivity. Substitution in the β-position, causes an increase in the crystalinity of the polymer. However, the

steric effect of β-substitution cannot be ignored, since 3,4-dimethyl pyrrole produces polymers with lower conductivities and lower mean conjugation length relative to pyrrole [23]. The substituents in position 3- or 4- of the pyrrole ring can also affect the electron density of the heterocycle. Mertz *et al.* [from 12] studied the effect of substitution in the 3,4-dimethoxypyrrole and showed that the electron donating effect of the methoxy groups results in a 350 mV decrease of the monomer oxidation potential. Thus, polymerisation exclusively proceeds *via* the α-positions and is likely to proceed without crosslinking and over-oxidation of the deposited polymer because of the lower potential required for the electropolymerisation. In order to substitute both the 3, 4- positions while avoiding steric interactions between repeat units of the polymer, Reynolds *et al* have studied the electropolymerisation of 3,4-alkylenedioxypyrrole monomers [24], resulting in a lower band gap polymer of 2.0 to 2.2 eV. Substitution in the 3, 4-positions by halogen atoms was found to result in a higher doping level compared to pyrrole [25]. The phenomenon is due to the greater charge delocalisation in the polyhalopyrroles because of the mesomeric effect of the halogen atoms. *N*-substituted pyrroles are known to exhibit a conductivity of three orders of magnitude lower than that of pyrrole as shown by Diaz *et al* for poly(*N*-methylpyrrole) [23]. These results were further confirmed by monitoring the conductivity of poly(3,4-dimethoxy-*N*-methylpyrrole) which was found to be three orders of magnitude lower than that of poly(3,4-dimethoxypyrrole) [26]. The larger the substituent on the nitrogen atom, the greater the steric interaction between repeat units, and the subsequent drop in conductivity. This drop in conductivity is due to the fact that the pyrrole units are not completely coplanar in the polymer, as demonstrated by the X-ray studies of Street on the α,α-substituted tetromer of *N*-methylpyrrole [12]. The influences of N-substitution on the electropolymerisation characteristics were examined by Waltman *et al* [12]. The polymer yield and the rate of oxidation were found to decrease as the size of the alkyl group increases. Bonding large substituents to the nitrogen atom or to the β-carbon stabilises the radical cation without stopping the polymerisation. If this intermediate is too stable it can diffuse into the solution and form soluble products, resulting in a lower yield and molecular weight. Some *N*-substituents inhibit the polymerisation due to their basicity, as observed for *N*-pyrrolidic pyrrole [27].

Electrolyte.

One important parameter affecting the physical characteristics and morphology of polypyrrole is the nature of the concentration of the dopant that represents 30% of the weight of the polymer film. The choice of an electrolyte is made by considering its solubility and its nucleophilicity. The anion oxidation potential should be higher than the monomer. The size of the anion controls the microstructure and porosity of the polymer, which determines the ability of the polymer to undergo an easier diffusion of the dopants during the redox process. The hydrophobic nature of the anion and the interactions between the polymer and the dopant are factors affecting microstructure and porosity. Kassim *et al* [from 12] have shown that in aqueous solution, the utilisation of a large aromatic sulphate anion, which is a surfactant, gives stable conducting polymers with better mechanical properties than when a perchlorate anion is used. Because of their hydrophobic interaction with water, one of the roles played by these organic anions is to orientate the polymer chain parallel to the electrode surface. This chain orientation increases the order in the polymer structure. The higher the basicity of the anion, the lower the conductivity of the polymer. This is due to the increase in the interactions of the positive charges of the polymer and the anions. Anion acidity leads to an increase in the conductivity of polypyrrole. On the other hand, anion nucleophilicity interferes with the reaction by increasing the formation of soluble products. The polymers of highest conductivity are produced when elevated electrolyte concentrations are used. The conductivity and tensile strength of the as-prepared nitrate doped polypyrrole films increased by *ca* 50-70% when the electrolyte concentration changed from 0.2 to 1M, no further improvement was observed for higher concentrations. The cationic influence associated with the anion is not negligible, it has been found that the larger the cation, the higher the conductivity of the polymer film.

Solvent

The solvent must minimise the nucleophilic reactions. Aprotic solvents appear to be the best for polypyrrole growth, acetonitrile being most common. In aqueous solutions high salt concentrations are necessary to give a polymer with the desired mechanical and conducting properties. Films prepared in ethanol and in aqueous and aprotic solvent mixtures have intermediate conductivities but good mechanical properties provided that the solutions contain dissociated mineral acids and not nucleophiles. In acetonitrile, an addition of a small amount of water has a big influence on the kinetics of the reaction and the properties of the polymer formed. This is due to the stabilisation of the radical cation intermediate by the water molecules, which have a larger polarity than the acetonitrile. Imanishi *et al* [from 12] have attempted to explain the strong influence of the solvent by drawing attention to its basicity and polarity. Film formation is influenced by the interactions between the solvent and the radical cation. The basicity of the solvent is the principal factor affecting the selectivity in polymer formation. But the solvent polarity will affect the strength of the interactions of the solvent and the electrolyte anions. Ko *et al* [from 12] have studied the morphology and film properties in aqueous and non-aqueous solutions (for acetonitrile). They have found that the films prepared in acetonitrile are more homogenous and are better conductors than polymers prepared in aqueous solution, which are more porous. The polymers prepared in aqueous solution undergo attack by water molecules during the reaction, which is responsible for their irregular morphology and weak properties. Unsworth *et al* have shown the absorption of oxygen gas formed during water oxidation is a source of surface defects in the polymer. Zhou and Heinze [from 12] have studied the "water effect" of polypyrrole growth. The favourable effect of water stems from its stronger basicity than pyrrole and therefore its ability to capture the protons released during the electropolymerisation, which prevents the formation of the trimer and thus avoids the passivation of the electrode. Other additives, such as methanol, ethanol and tetrahydrofuran which are more basic than pyrrole but not enough to deprotonate the intermediate radical cations have proved to be as effective as water.

pH

The pH has an influence on the reactivity and stability of the polypyrrole formed at the electrode. In general, protons are produced after each oxidation at the electrode which consequently increases the pH near the electrode. As shown by Unsworth *et al.* [from 12] the optimisation of the pH results in the formation of a uniform surface with very few defects. A low pH generally favours polymerisation. However, a very low pH will result in weak conductivity due to the acid catalysed formation of non-conjugated trimers, which further react to form a partly conjugated polypyrrole, or are incorporated into the film, or even diffuse into the solution. As a result, the films produced exhibit a lower conductivity. In acid solution insertion and deinsertion of the dopant is observed whereas in basic solution, the anion is replaced by hydroxy groups from the solution. Both phenomena are observed in neutral solution. The stability of pyrrole in an aqueous solution also depends on pH. Polypyrrole can undergo protonation and deprotonation processes. The polymer chain undergoes a deprotonation in basic solution (pK_a~9-11) which results in the modification of the electronic structure of the polymer. In strong acidic media (pK_a~2-4) a protonation process is observed. Consequently, conductivity decreases in basic solutions (10 S cm^{-1} at pH < 7 to 0.1 at pH 11). Zhou and Heinze [from 12] observed three types of polypyrrole under differing acidic media:-

- Regular polypyrrole in neutral and weak acidic acetonitrile (1% water).
- An unknown structure with a sharper more negative oxidation peak was found for 10^{-5} to 5 x 10^{-5} M HCl solutions in acetonitrile.
- Thirdly, in HCl concentrations above 10^{-4} M.

Electrochemical method

Otero and DeLarreta [from 12] have proposed that the choice of electrochemical polymerisation method influences morphology, appearance and adhesion of the polymer. A non-adhesive dendrite type polymer is formed when a constant current or potential is used. The film is poorly homogeneous and some electrolyte is present between the electrode surface and the film. Films produced from alternated polarisation are shinny black, very adhesive, and have a smooth and homogeneous surface. Zhou and Heinze [from 12] observed that the method controls the structural form of the electrodeposited polypyrrole. Classical polypyrrole polymerisation produces polypyrrole with a single oxidation wave (~ 0.1 V vs Ag/AgCl) followed by a broad plateau. However, cyclic voltammetry of polypyrrole films obtained by galvanostatic synthesis at extremely low current levels show an additional sharp oxidation peak at a much lower potential (-0.23 V vs AgCl). This is evidence of the structural diversity of polypyrrole. Experimental conditions have a significant impact on the properties of the resulting polymers and that changing a single variable such as acidity may induce a more profound change in the polymer characteristics than a change in applied potential.

Temperature

Electropolymerisation temperature has a substantial influence on the kinetics, conductivity, redox properties and the mechanical stability of the film. The average activation energy of the polymerisation process on Pt is between 15 – 20 kJ mol^{-1}. A decrease in redox properties is observed with increasing temperature. Generally, higher conductivities are obtained at lower temperatures, both in aqueous and propylene carbonate (PC) solutions. E.g. films prepared in PC at –20 ^{0}C have conductivities in the region of 300 S cm^{-1}, whereas at 20 ^{0}C 97 S cm^{-1} conductivities were obtained. Spectral analysis of the films prepared at lower temperatures show a more regular structure. At higher temperatures, side-reactions such as solvent discharge and nucleophilic attacks on polymeric radicals cause the formation of more structural defects, resulting in films of lower conductivity. However, Sato *et al* [from 12] have obtained highly conductive polypyrrole films (500 S cm^{-1}) at 10 ^{0}C.

This was obtained by optimising both polymerisation potential and temperature as both parameters have a large influence on the final properties of the film. However, films prepared at lower temperatures have a more rugged appearance and poorer adhesion than those prepared at higher temperatures [12].

From the above it was summarised that the following conditions were taken for the electrochemical growth of polypyrrole.

- The solvent must minimise nucleophilic reactions and aprotic solvents appear to be the best for polypyrrole growth. Acetonitrile is the most common choice.
- A large cation improves mechanical strength and conductivity of the film.
- Electrolyte concentrations of up to 1M have seen improvements in conductivity and tensile strength of the as grown polypyrrole film.

Considering these points, 1M $TBABF_4$/ACN was used as the support electrolyte. The final monomer solution was $TBABF_4$/ACN (1M)/Pyrrole (0.01M) as presented in chapter 8.6.

3.2 Ionically Conducting Polymers

It has been nearly 30 years since the first report by P. V. Wright of the conducting properties of "solvent free" poly(ethylene oxide) PEO-salt systems and in 1978 M. B. Armand highlighted the potential of these materials as solid polymer electrolytes. [28]. Rapid growth in the development of polymer electrolytes has taken place since this early pioneering work. The driving force behind this work being the practical advantages of solid, flexible and lightweight electrolytes for energy storage devices such as lithium ion batteries and supercapacitors, over their liquid counterparts. These advantages include:-

- Lower rates of self-discharge
- No corrosive liquids to react with device seals and containers.
- Polymers may be manufactured into thin films, hence improving energy densities, and be moulded into any shape required.
- Polymer electrolytes may act as electrode separators, therefore an inert porous separator is not required.
- Since technology for thin film manufacture is already commonplace the cost of manufacturing devices will kept to a minimum.

One major disadvantage with solid electrolytes however is the reduced contact area with porous electrodes compared with liquid electrolytes thus giving rise to a lower capacity than theoretically possible.

There are two main groups of solid electrolytes discussed in this thesis:-

- "Solvent free" polymer electrolytes.
- Gel electrolytes

As the name suggests the former type of electrolyte consists only of a salt dissolved in a polymer. The polymer is chosen so that it has an available ether oxygen for co-ordination with the cation of the salt, (for conduction mechanism see section 3.2.1 below), e.g. PEO, Polyurethane (PU). Conductivities of $>10^{-5}$ S cm^{-1} (a value generally accepted to be the threshold conductivity for a practical device [28]) have been reported for systems using $NaClO_4$ with PU [29] and $LiClO_4$ with PEO [28]. See figure3.13.

For gel electrolytes, the polymer is used primarily as an inert host matrix where a low molecular weight polymer such as poly(ethyleneglycol) PEG, propylene

carbonate (PC) or ethylene carbonate (EC) is dissolved in it. This type of electrolyte may be looked upon as a liquid electrolyte in the manner in which the ions are transported, supported within a polymer matrix, e.g. Polyvinylidenefluoride-hexafluoropropylene (PVdF-HFP), co-polymer hosting a PC/EC-salt solution.

The ions are then transported as solvated sheaths within the matrix. See section 3.2.2.

It is important to recognise the difference between these two types of ionic conducting systems. A gel electrolyte cannot be regarded as a true polymer electrolyte since it has liquid-like conduction properties.

Akihiro Noda and co-workers have reported highly conductive polymer electrolytes, (conductivities in the order of $2x10^{-2}$ and $3x10^{-3}$ S cm^{-1} at 30^0C), utilising the polymerisation of vinyl monomers in room temperature molten salts [30]. P.V. Wright and co-workers have reported conductivities of Langmuir-Blodgett (LB) film electrolytes of $6x10^{-4}$ to $8x10^{-3}$ S cm^{-1} [31]. This group have also reported a solvent-free low-dimensional polymer electrolyte blend, yielding DC and a.c. conductivities of up to 10^{-3} S cm^{-1} [32].

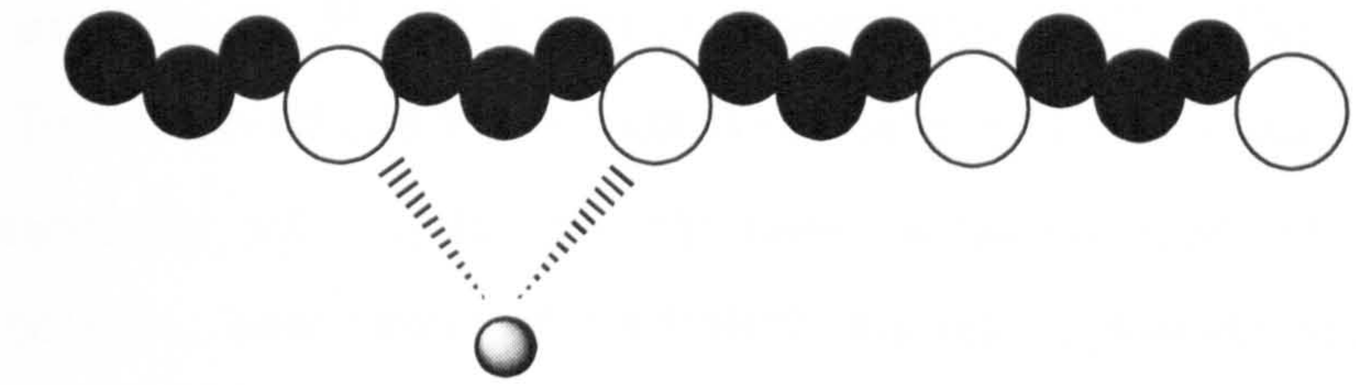

Where,

Oxygen

Polymer backbone

Cation

Figure 3.13 Representation of a polymer electrolyte

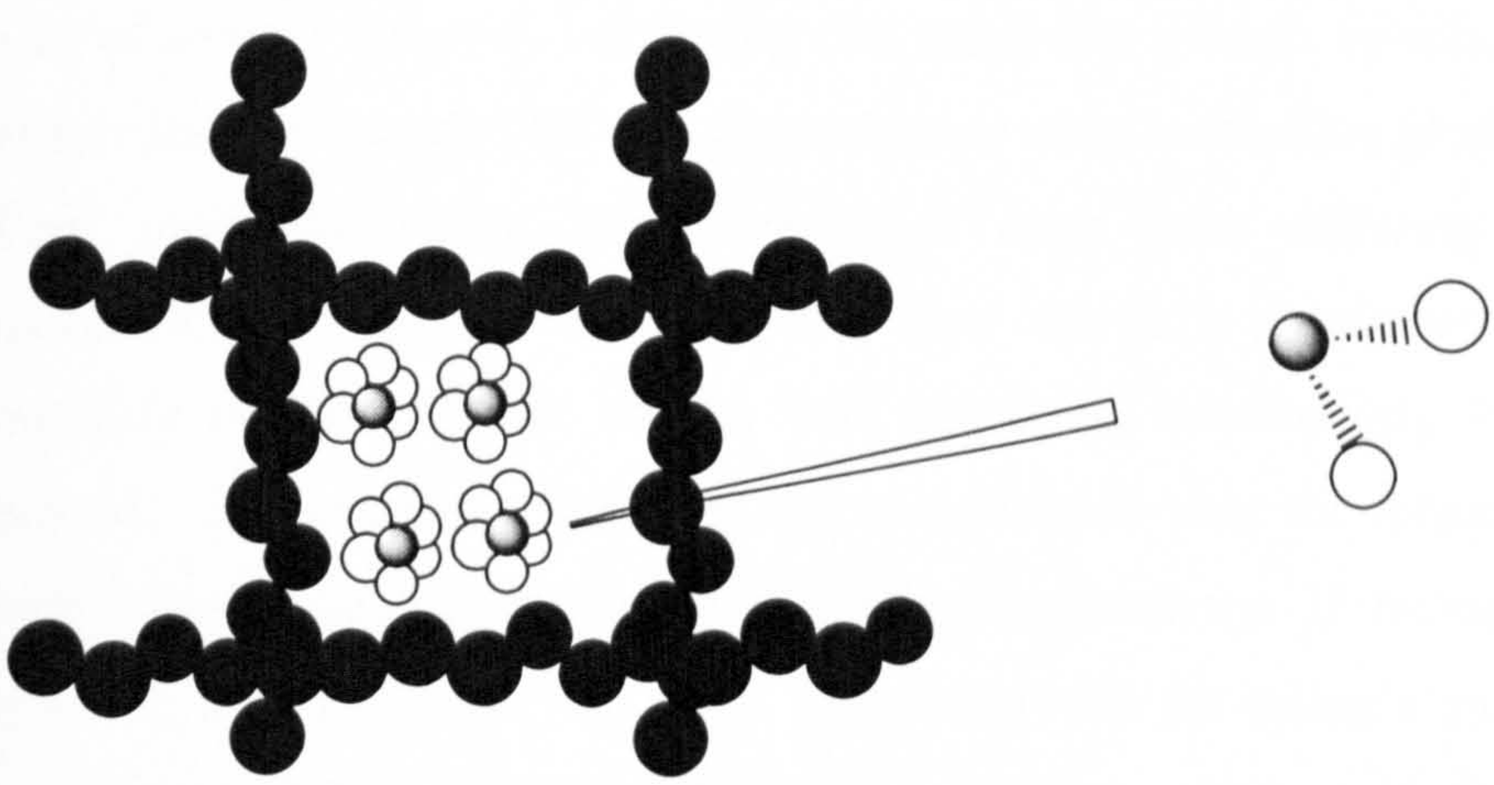

Solvated ion

Polymer matrix

Ether oxgen of PC or EC

Figure 3.14 Representation of a gel electrolyte.

3.2.1 Preparation of Polymer and gel electrolyte films

The two most common procedures are solvent and melt cast techniques.

Solvent casting involves preparing a solution of the salt and polymer in a suitable solvent, e.g. PU-$LiClO_4$ in tetrahydrofuran (THF). The solution is poured into a Teflon mould and the solvent is removed by slow evaporation. The film, which is normally between 10 and 50μ thick, is heated under vacuum to remove residual solvent. Some polymer electrolytes are semicrystalline and induced crystal growth may occur due to the nature of the solvent, the rate of solvent removal and by residual solvent, which may act as a nucleation site for spherulite growth or as a plasticiser. The latter case poses a further problem since the residual solvent may evaporate during the working lifetime of the electrolyte film, hence decreasing the apparent conductivity on evaporation. The drying temperature also affects spherulite growth. Higher temperatures may induce high-melting spherulite formation. It can be seen therefore that consistency in film preparation is vital in obtaining reproducible data. Neat [33] examined the effects of casting from solvents in PEO-$LiCF_3SO_3$ and $LiClO_4$ systems. He reported that the morphology was independent of rate of solvent removal, suggesting that spherulite growth be initiated after solvent evaporation, although THF-cast films showed some crystalline phases.

Low molecular-weight trace impurities may have differing effects on the morphology of the electrolyte. They may act as a plasticiser and increase the mobility of the polymer chains, thus enhancing conductivity [see section 3.2.2 below]. The impurities may also act as nucleation sites for spherulite growth, thus increasing crystalinity and hence decreasing conductivity. If the impurity is polar, as is water, it may bond to the cation, interfering with the cation's interaction with and transference between the co-ordinating sites of the polymer. Hydration may restrict the mobility of the cation by forming a tight sheath around the ion, competing with the polymer chain co-ordination sites and effectively reducing the number of cations participating in charge transport. Hydrogen bonding to the anion and the ether oxygens on the backbone may also contribute to this effect.

A grinding/ hot press technique was developed to overcome the solvent problem. This involves grinding the polymer to a fine powder under liquid nitrogen temperatures and thoroughly mixing the powder with a salt, the resulting homogeneous mixture is then heated and pressed into a thin film.

3.2.2 Conductivity in polymer electrolytes

Both anions and cations contribute to ionic conduction. For the polymer electrolyte group the conduction mechanism is thought to be that of the cation hopping along and between the polymer chains. The cation co-ordinates to the oxygen on the polymer backbone with successive breaking and reforming of these co-ordination bonds, thus affording ionic transport, see figure 3.15.

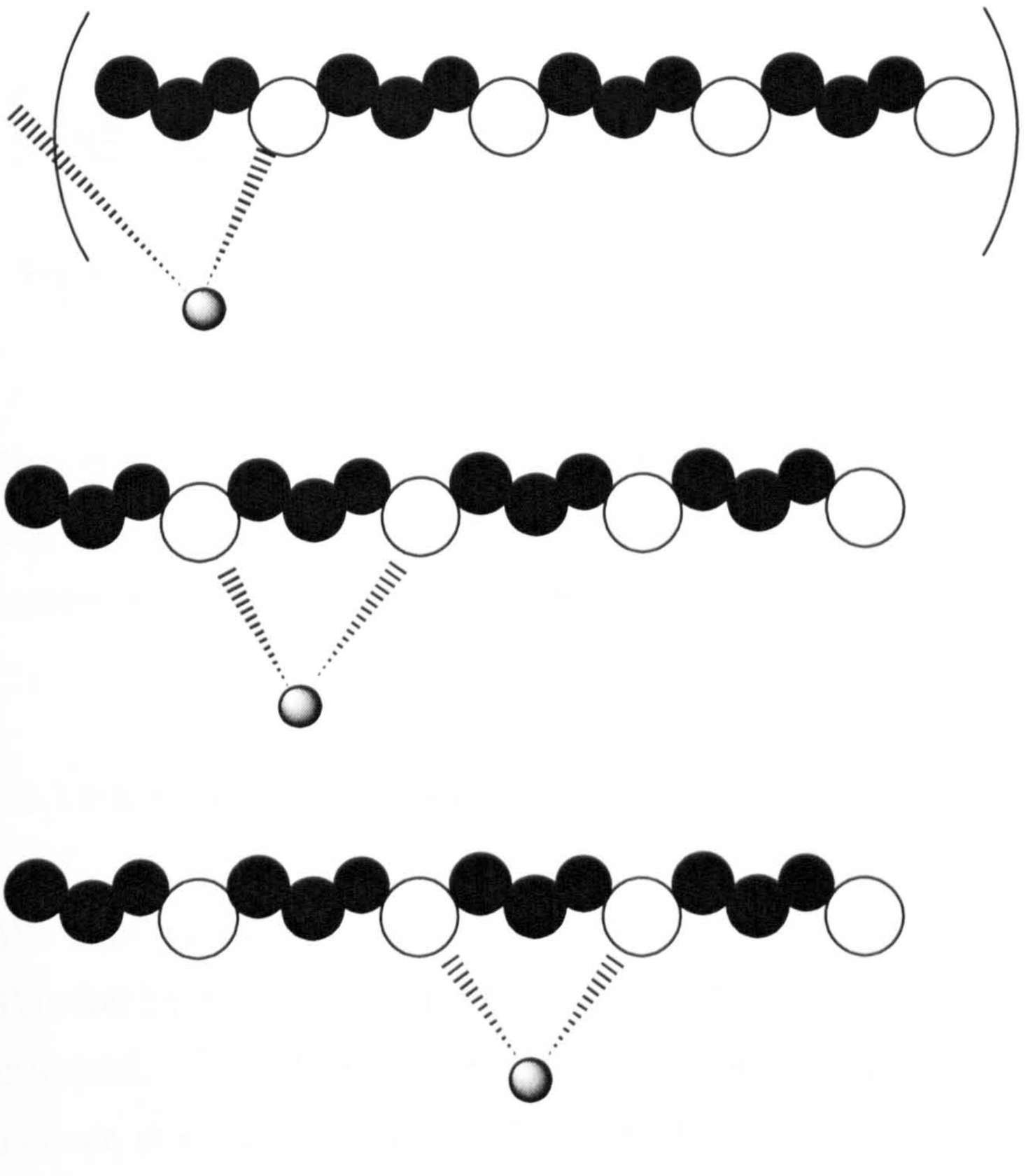

Figure 3.15 Illustration of ionic transport along a polymer backbone e.g. Li^+ with PEO.

Segmental motion of the polymer chain plays an important role in ionic conduction since the ions hop from chain to chain, giving rise to three dimensional ionic mobility figure 3.16. The conductivity of these types of electrolytes occurs in the

amorphous phase of the polymer. It is therefore important for a polymer to have a low glass transition temperature T_g since segmental motion is far greater above this temperature.

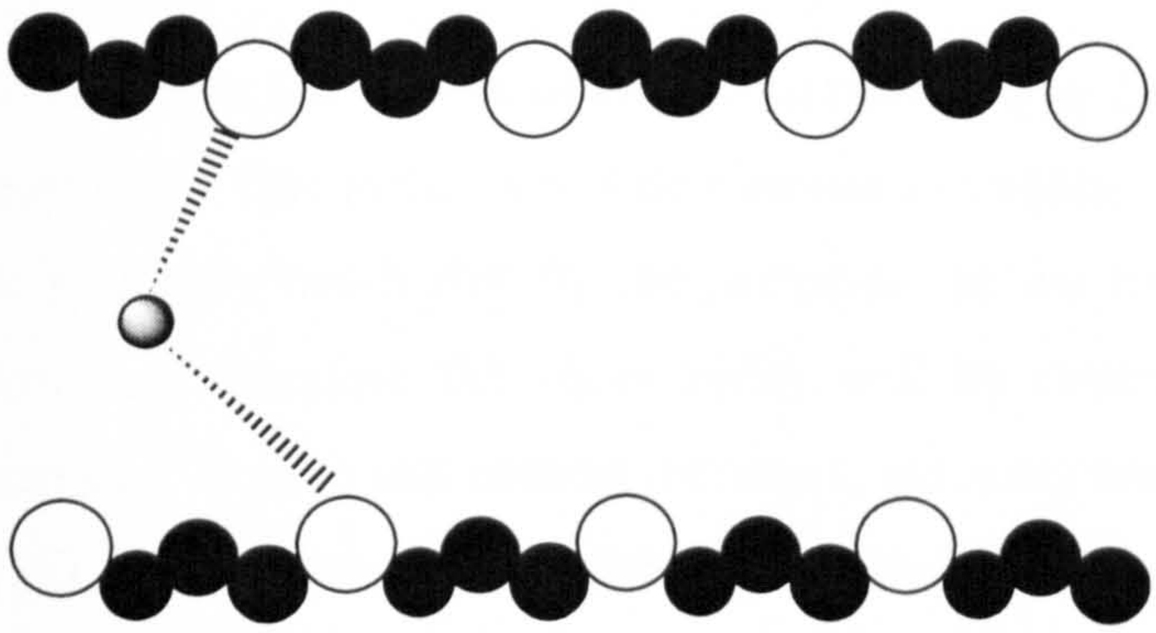

Figure 3.16 Illustration of 3-dimensional hopping of ions.

Two criteria significantly effect the conductivity of a polymer electrolyte, i.e. the degree of crystalinity χ, and the salt concentration C*, although the nature of the salt and the type of polymer have an important contribution.

3.2.2.1 Effect of salt concentration

The ionic mobility is closely related to the relaxation modes of the polymer host. This can be seen in the increase of T_g of polymeric systems as salt concentration is increased. The reduction in segmental motion may be attributed to the effects of an increase in intramolecular and intermolecular co-ordinations between co-ordination sites on the same or different polymer chains caused by the ions acting as transient crosslinks [34]. As shown in figure 3.17. As well as conductivity reductions caused by the stiffening of the matrix, the availability of vacant co-ordinating sites is greatly reduced at high salt concentrations. Also strong ion-ion interactions in systems of low permitivity such as polyethers are probable and therefore ion migration is likely to involve the co-operative motion of several ions. The conductivity of a homogeneous polymer electrolyte phase may be given as: -

$$\sigma\ (T) = \sum_{i}\ n_i q_i \mu_i \qquad \text{Equation 3.2}$$

Where n_i is the number of charge carriers of type *i*, q_i is the charge on each, μ_i is the mobility. This includes mobile charged aggregates. At low salt content the mobility is relatively unaffected by concentration, as the transient crosslink density will be low and therefore the conductivity will be controlled by the number of charge carriers. As the salt content increases, ion pairs and mobile higher aggregates form [35], which then form higher, less mobile clusters and may also act as transient crosslinking species, as shown in figure 3.17.

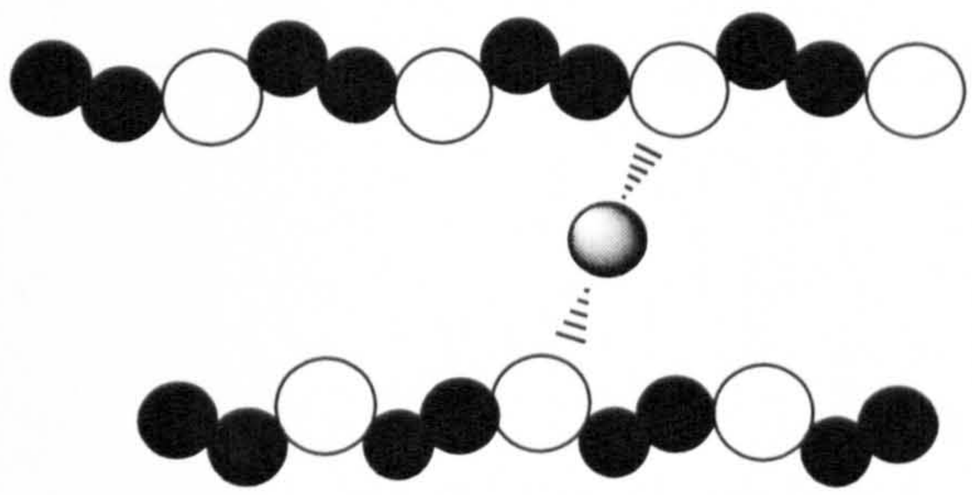

Figure 3.17 Illustration of a transient crosslink.

3.2.2.2 Effect of pressure

Armstrong *et al.* [36] found that the bulk conductivity of a $PEO_{4.5}$ $LiCF_3SO_3$ electrolyte decreased with increasing pressure over the range 60 to 300 MPa. When a cell was held at a constant pressure and temperature, the conductivity fell with time. These effects were attributed to some structural change at higher pressures and may involve increased crystallisation [37]. Since the contact between electrode and electrolyte is critical for supercapacitors it is sometimes required to hold the cell under pressure (0.3 to$2*10^6$ N m^{-2}) [38], therefore a compromise must be reached.

In gel systems the ionic transport takes place through an interconnected system of pores and cavities (typically in the micrometer range) in which the electrolyte solution can flow [39]. When using "solvent free" polymer electrolytes their conductivity may be enhanced by the addition of plasticiser, by effectively lowering the T_g of the system and increasing chain mobility. Thus an intermediate system between "true" polymer electrolytes and a gel electrolyte is formed. Differential scanning calorimetry, DSC, experiments on PU/PC/EC-salt systems suggest a major contribution to the conductivity from cation oxygen interaction and on increasing plasticiser concentration a greater contribution from ionic transport within the PC/EC "solution" to the overall conductivity [See chapter 6].

4 Porous Silicon

4.1 Semiconductor Theory

Generally materials may be separated into three categories according to their electrical conductivity, i.e. insulators, conductors and semiconductors. Figure 4.1 shows the band gap pattern for all three states.

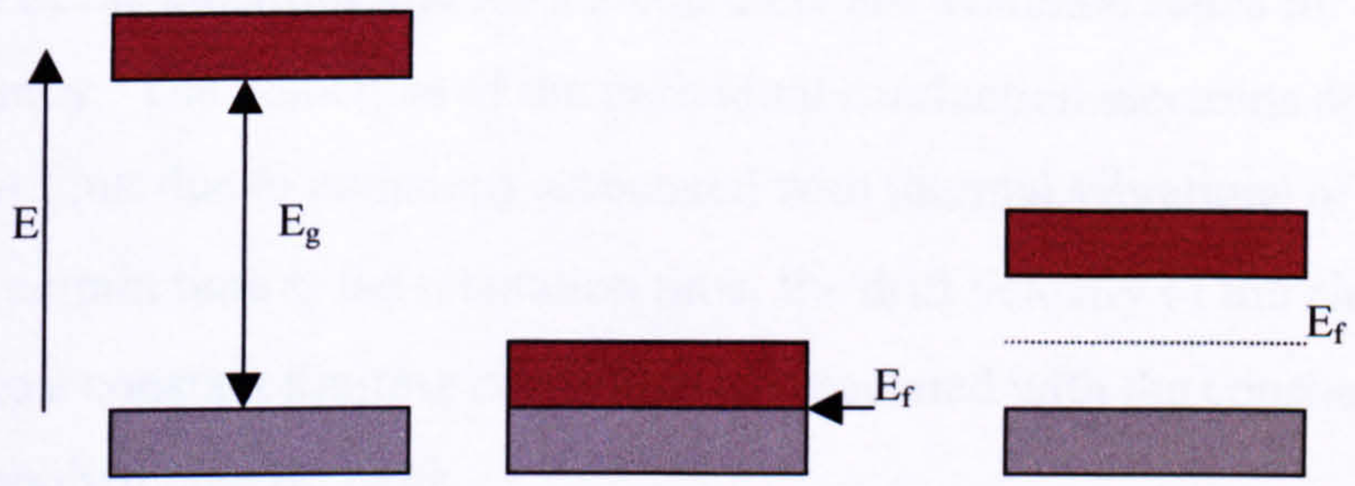

Figure 4.1. Idealised energy band gap pattern for an insulator, conductor and semiconductor at absolute zero.

Valence band, i.e. the highest energy states of the bonding electrons

Conduction band

E_g is the band gap energy (i.e. forbidden energy states for electrons or holes)
E_f is the fermi energy level.

An insulator maybe defined as being a material through which mobile charge carriers cannot flow as a directed drift current. If an external electric field **E** is applied to an insulator, a force of –e**E** is exerted on each electron, where –e is the electronic charge. This causes a change in the electron energy, thus the electron must move to

a different energy level within the material. For an insulator the Pauli exclusion principle forbids the movement of electrons since all other states are occupied. There are available states within the conduction band, but the electrons must have sufficient energy to jump the band gap. For diamond this value is 5.4 eV[(2)] and neither thermal excitation nor an external electric field can supply sufficient energy to cross this barrier [1].

As previously mentioned a force of $-e\mathbf{E}$ is exerted on each electron on the application of an external electric field. This force during time Δt, causes a change in energy of the electrons and for a metal there are available states for electron occupancy. The velocities of the individual conduction electrons do not increase without limit due to collisions associated with thermal vibrations of the lattice. Thus after a certain time τ, the relaxation time, the drift velocity of the electrons slows down to a constant limiting rate which is associated with the constant current set up by an applied electric field.

A useful term for quantifying the nature of conductivity of a material is its resistivity ρ, which is given by equation 4.1.

$$\rho = \frac{m_e}{n_d \tau e^2} \qquad \text{Equation 4.1}$$

where, m_e is the mass of an electron and n_d is the number density of the charge carriers, i.e. the number of charge carriers per unit volume.

A semiconductor is similar to an insulator with a much smaller band gap, typically for silicon 1.1 eV. This means that there is a possibility for electrons in the valence band to have sufficient energy to jump into the conduction band [2].

Crystal growth and device processing involve temperatures high enough to allow intrinsic point defects such as vacancies and self-interstitials to migrate rapidly and to react with extrinsic point defects such as dopants and impurities. Some typical examples are show in figure 4.2 below. In contrast to metals, charge effects in

(2) $1eV = 4.45*10^{-26}$ kWh and $1.602*10^{-19}$ J

semiconductors play a major role for point defects and may strongly influence their thermal equilibrium concentrations. Intrinsic point defects are defects of atomic dimensions not involving any foreign atoms. The most basic and simple intrinsic point defects are vacancies and self-interstitials for an element such as silicon.

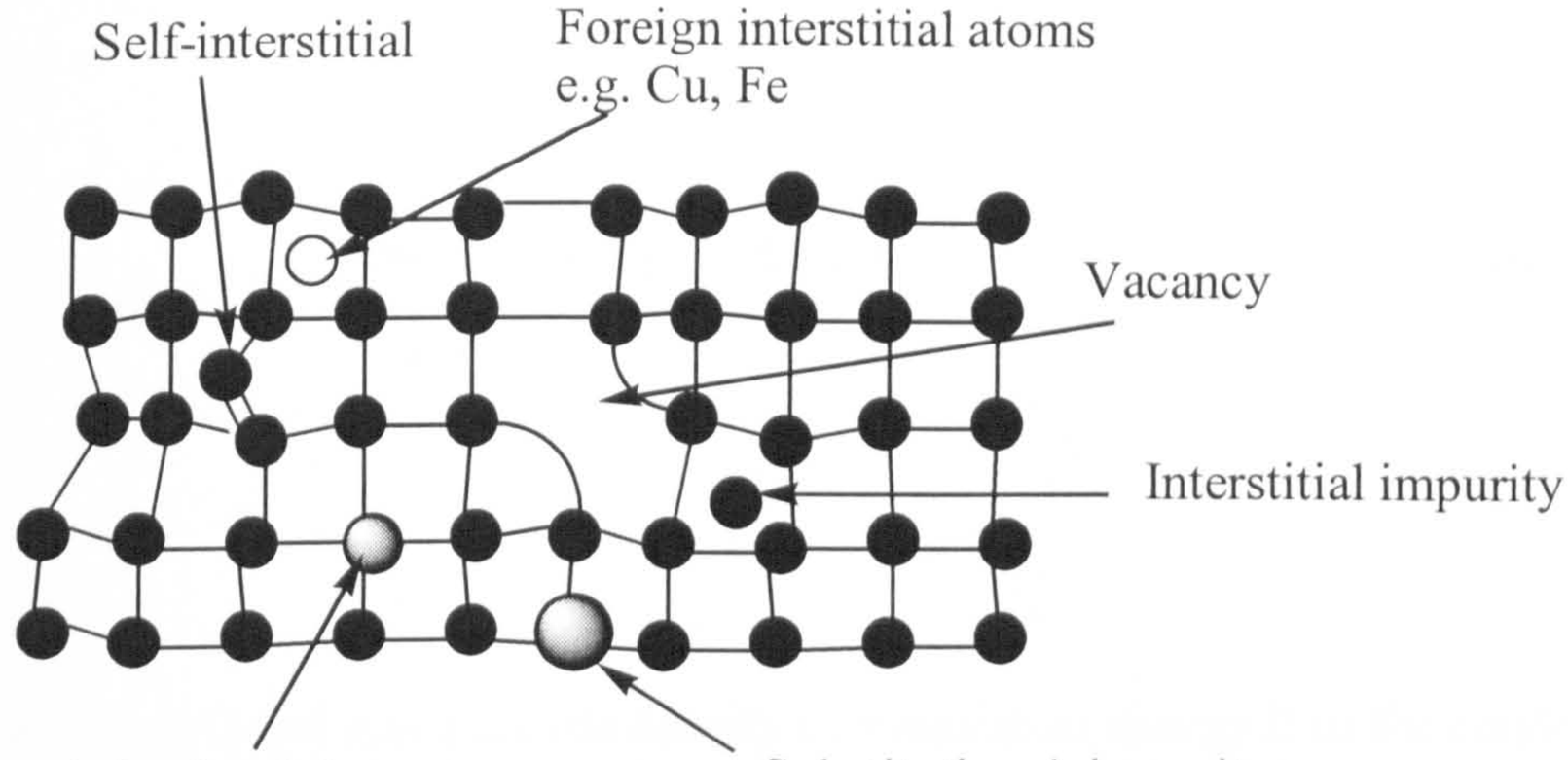

Figure 4.2 Schematic 2D representation of various types of intrinsic and extrinsic point defects in a silicon crystal. [3].

4.1.1 Density of states

According to the energy band model [4], the total number of allowed states in each band is four times the number of atoms (4**N**) in the crystal. The number of states at any given energy in the conduction and valence band, i.e. the energy distribution of states, or density of states, is an essential component in determining carrier distributions and concentrations. To determine the density of states it is necessary to perform an analysis based on quantum-mechanical considerations. The results of the analysis may be summarised as follows

$$g_C(E) = \frac{m_n^* \sqrt{2m_n^*(E - E_C)}}{\pi^2 \hbar^3}; \quad E \geq E_C \qquad \text{Equation 4.2}$$

$$g_C(E) = \frac{m_p^* \sqrt{2m_p^*(E_V - E)}}{\pi^2 \hbar^3}; \quad E_V \geq E \qquad \text{Equation 4.3}$$

where, $g_c(E)$ and $g_v(E)$ are the density of states at an energy E in the conduction and valence bands, respectively. The differences between $g_c(E)$ and $g_v(E)$ in practice arise due to the differences in the carrier effective masses ($m_n^* \neq m_p^*$). The density of states in the conduction and valence bands per unit volume lying in the range E and E+dE (if $E \geq E_C$ and $E_V \geq E$) are given by the expressions

$g_c(E)dE$,

and

$g_v(E)dE$, respectively.

4.1.2 Carrier Density

The number density of electrons and holes in their respective bands is a crucial quantity for understanding the properties of semiconductors. This density is equal to the product of the density of states available for occupancy in a particular band, and the probability that a state is occupied [5]. For a non-degenerate semiconductor, this leads to the important relationship known as the law of mass action, which states that

the product of electron density in the conduction band and the hole density in the valence band for a given semiconductor at a particular temperature is a constant ($n.p= n_i^2$), irrespective of whether it is an intrinsic ($n = p = n_i$) or an extrinsic ($n \neq p$) semiconductor. Thus if the density of electrons in the conduction band is increased by doping the semiconductor with donor impurities, then the density of holes in the valence band will decrease. The total electron concentration in the conduction band for the non-degenerate situation is given by,

$$n_e = \int_{E_g}^{\infty} g_C(E) f(E) dE = \frac{1}{2\pi^2}\left[\frac{2m_C}{\hbar^2}\right]^{3/2} \int_{E_g}^{\infty} \frac{(E-E_g)^{3/2} dE}{1+\exp[(E-E_g)/kT]} \qquad \text{Equation .4.4}$$

where $g_c(E)$ is the number density of the available states in the conduction band, $f(E)$ the Fermi-Dirac distribution function, the probability that the electron has an energy, E, m_c and m_v the effective masses of the electrons in the conduction band and holes in the valence band respectively. Similarly, the hole concentration in the valence band for the non-degenerate limit is given by the following expression,

$$p = \int_{-\infty}^{0} g_V(E)[1 - f(E)]dE = \frac{1}{2\pi^2}\left[\frac{2m_V}{\hbar^2}\right]^{3/2} \int_{-\infty}^{0} (-E)^{1/2} \exp\left(\frac{E-E_g}{kT}\right) \qquad \text{Equation 4.5}$$

Finally for the reference of zero energy taken at the top of the valence band, equations 4.4 and 4.5 can be rewritten for electron concentration in the conduction band and hole concentration in the valence band;

$$n_e = N_C \exp\left[\frac{(E_f - E_g)}{kT}\right]$$ Equation 4.6

$$p = N_V \exp\left(\frac{-E_f}{kT}\right)$$ Equation 4.7

where, N_c and N_v are the effective density of the states in the conduction and valence band respectively.

Figure 4.3 shows the band structure of a semiconductor, illustrating the density of states, the occupancy and the carrier density within the valence and conduction bands.

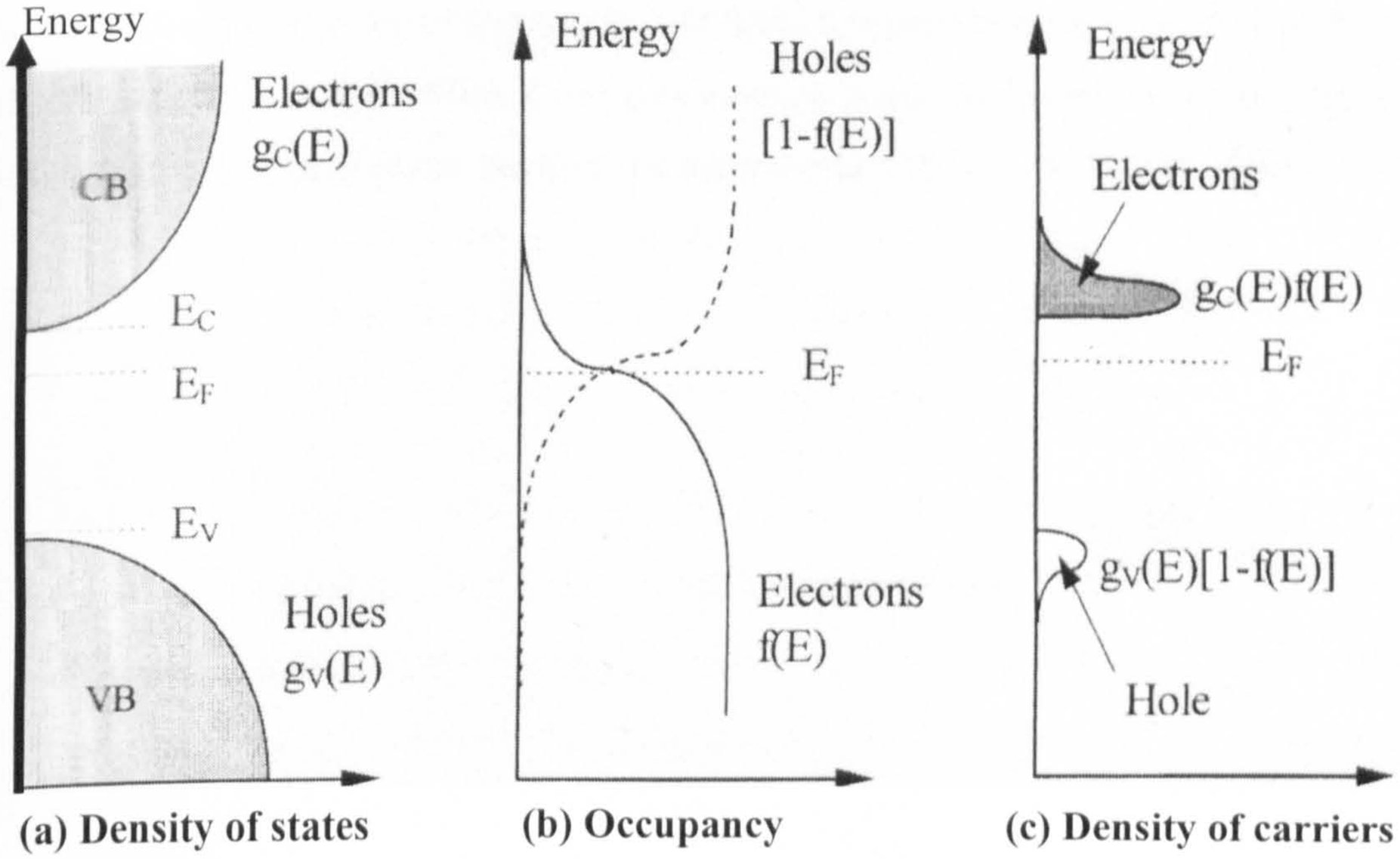

(a) Density of states **(b) Occupancy** **(c) Density of carriers**

Figure 4.3 Schematic diagrams showing n-type (donor doped) semiconductor band structure; 9(a) Density of states, (b) Fermi distribution of electrons and holes for T>0 K, (c) The carrier concentrations for T>0 K. [6].

4.1.3 Electron States

A description of electron energy states in a solid and their distribution functions among these states necessitates an understanding of the electronic properties of semiconductors. The total energy of electrons in a solid consists of their potential and their kinetic energies. Close to the nucleus the potential energy, arising from the interaction between the electron and the nuclei, is effectively that of the isolated atom. This results in a deep well. Between the nuclei, it is made up of contributions from many atoms and is not so deep. Core electrons are tightly bound in the well and it is essential that their energies be the same as that for an isolated atom. These electrons are strongly localised and are only slightly influenced by the other atoms in the solid. The electrons in the outermost shell, the valence electrons, are bound to a much less extent (typically of about an electron-volt for semiconductors) and are much less localised, spreading out into the region between atoms. Therefore the energy states of these electrons will be strongly affected by the presence of other atoms in the solid. At T=0 K in a pure semiconductor these electrons are in the highest occupied valence energy states. At finite temperatures they can, however, absorb sufficient energy to break free of a valence bond. Such electrons are mobile and free to move throughout the body of the material [7].

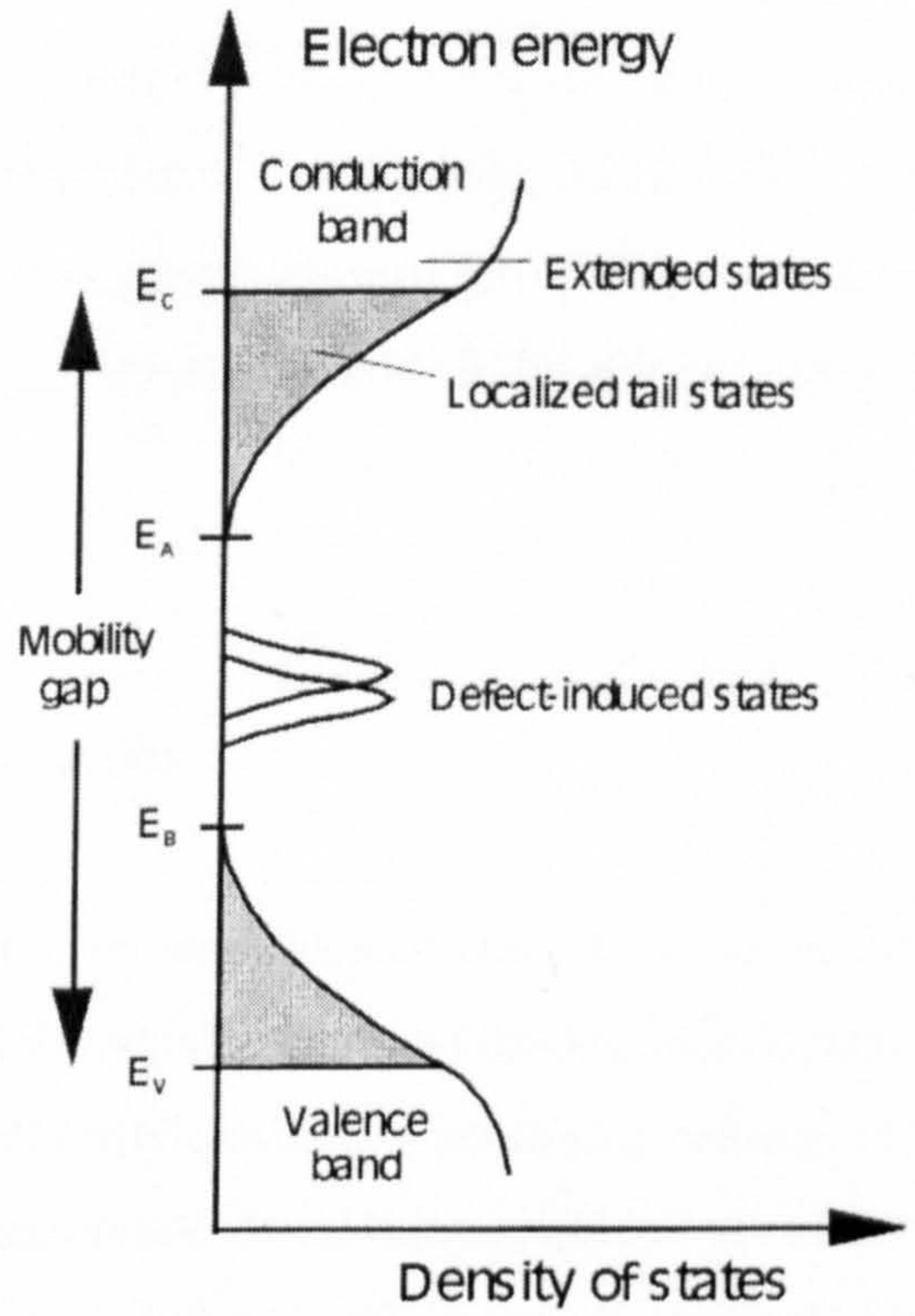

Figure 4.4 Density of states in an amorphous semiconductor, illustrating extended states, localised tail states and defect-induced gap states [8].

On the other hand, electron states in amorphous semiconductors [6] are characterised by the absence of long range order. However the concept of the density of states is still valid as is the possibility of a gap between the density of valence and conduction states. Like crystalline semiconductors, amorphous materials will have extended electronic states through which electrons and holes can move freely, (the mean free path will be much lower than for crystalline semiconductors). The disorder creates an effect, when the disorder is sufficiently high the resulting fluctuations in the atomic potential may cause charge carriers to be confined or localised, resulting in a tailing of the density states function, as shown in figure 4.4. The values of E_c and E_v

represent the boundary between extended and localised states and the energy difference is said to be the *mobility gap*. States within this gap arise due to defects, i.e. dangling bonds and voids in the structure. In sputtered amorphous silicon the density of these states is in the order of 10^{20} cm^{-3}. This value may be reduced to 10^{16} cm^{-3} by incorporating hydrogen into the material during deposition, since hydrogen reacts with the dangling bonds on the silicon thus, passivating them.

4.1.4 Dislocations

Dislocations in semiconductor materials act as electrically active defects. These may be structural dopants (acceptors and/or donors), recombination centres reducing the lifetime of minority carriers, or scattering centres. At low temperatures dislocations are linear conductors. In addition to this direct effect on carrier density, lifetime and mobility there are indirect influences. Electrically charged dislocations are surrounded by a screening space charge which causes local band bending and therefore may change the charge state of point defects in this region.

4.1.5 Impurities

Semiconductor electrical properties are effected by impurities. These impurities are said to be either shallow or deep. A shallow impurity has a high probability of undergoing thermal ionisation. A deep one a much lesser chance. For this reason shallow impurities are deliberately added to a semiconductor to improve its electrical conductivity, e.g. Boron is added to silicon to create p-type silicon. Deep level impurities can act as traps or centres for the recombination of mobile carriers and modify the action of the semiconductor [9].

4.2. Porous Silicon Theory

Introduction

Porous silicon (PSi) is rapidly becoming an increasingly important and versatile electronic material in today's fabrication technology. Its reactive porous nature allows for the selective formation of unique electronic components and mechanical nanostructures. PSi is not a new material. It was first reported over 30 years ago during the electropolishing of silicon in aqueous hydrofluoric acid (HF) [10], and has since been studied extensively [11-15].

Porous silicon, due to its high surface area and its ease of incorporation into modern integrated circuit technology is therefore a potential candidate as an electrode material in capacitors and supercapacitors. For example, Lehmann and co-workers (1995) produced a parallel plate capacitor using an oxide-nitride-oxide dielectric sandwich and PSi electrodes [16].

4.2.1 Formation Mechanisms

There are two general methods for PSi manufacture, chemical or stain etching and electrochemical anodisation.

4.2.1.1 Electrochemically Produced PSi

Despite the high degree of interest in PSi, the basic formation mechanisms and even some of the simplest material properties of PSi are still in dispute. Smith and Collins said of the different groups that study PSi, "that they are either unaware of, or simply don't believe each others work". It is generally accepted that holes are required in the initial oxidation steps for both electropolishing and pore formation. This means that for n-type substrates, significant dissolution only occurs under illumination, high fields or other hole generating mechanisms. Intermediate conduction band processes or electron injections have been suggested [17], but not yet proved. An example of

this occurs in the photocurrents of n-type material. Under illumination n-type photocurrents can be as high as 3 times greater than for p-type material. Every photogenerated hole allows the dissolution of one Si atom thus leaving 3 Si valence electrons to be injected into the conduction band structure [17]. In the past, virtually all studies for PSi formation have been limited to an electrochemical characterisation of its i-V relationships, with the Schottky diode model of the semiconductor/electrolyte interface playing a predominant role. Although other techniques for PSi study have been developed the main understanding comes from i-V relationships. A typical i-V relationship, illustrating the regions of pore formation and electropolishing, is shown in figure 4.5

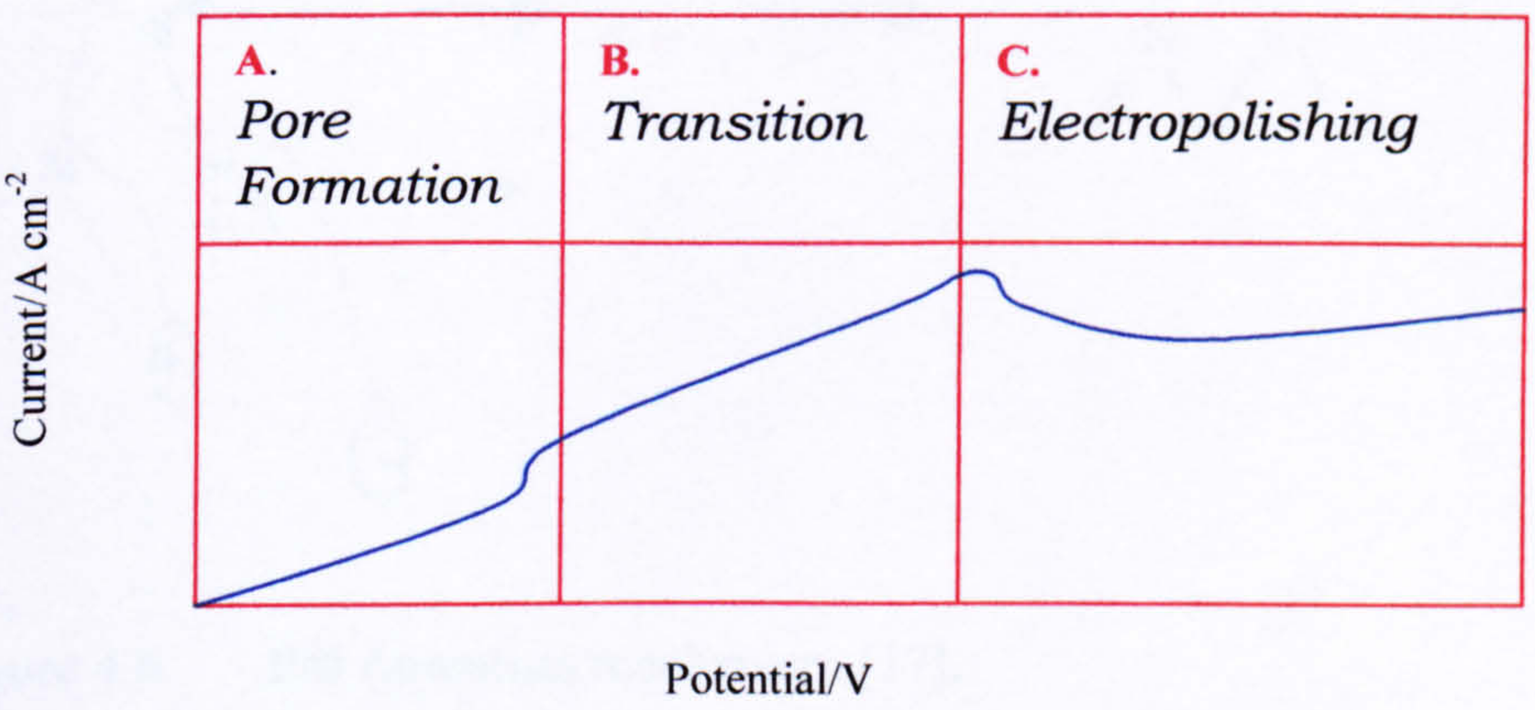

Figure 4.5 A schematic representation of the current voltage plot for electrochemical etching of silicon [17].

During pore formation in the Tafel region (region A in figure 4.5), hydrogen gas evolves in a 2:1 atomic ratio to silicon [18], diminishes in the transition region and disappears in the electropolishing region. Current efficiencies have been measured at approximately two e^- per dissolved Si atom during pore formation and four e^- per atom during the electropolishing regime. Regardless of which occurs the stable end product for Si in HF is H_2SiF_6, which appears in some ionised form depending on pH and concentration of the etch solution. Thus, mechanistically during pore formation, only two of the four Si electrons or holes are available for direct interfacial charge

transfer leaving the remaining two to undergo a corrosive hydrogen gas liberation. In contrast all four Si electrons are electrochemically active for electropolishing, hence a different reaction pathway exists between pore formation and electropolishing. Lehmann and Gosele [19] have presented an entirely surface bound oxidation scheme with hole capture and subsequent electron injection to produce the divalent Si oxidation state shown in figure 4.6.

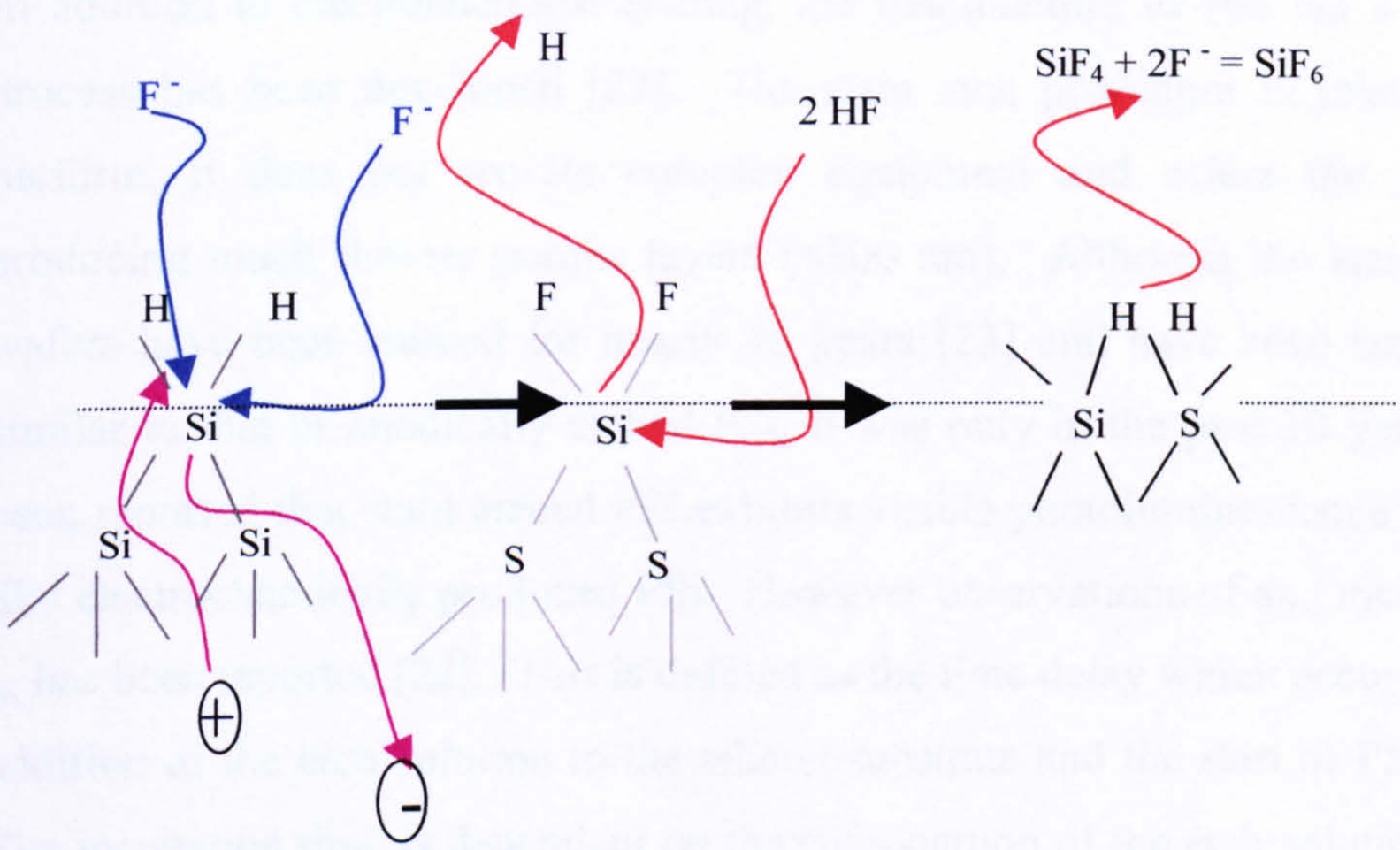

Figure 4.6 PSi formation mechanism [17].

According to figure 4.6, the silicon surface continuously vacillates between fluoride and hydride coverage at each pair of electron/hole exchanges. Recent x-ray photoelectron spectroscopy (XPS), studies have shown surface fluoride coverage of approximately 2.6×10^{14} atoms cm^{-2} [20], thus providing evidence that Si-F formation in HF is an important mechanistic step in PSi formation. However, the concentration of fluoride decreases rapidly on exposure to water. An essential proposition of Lehmann *et. al.* [20], is that silicon hydride bonds passivate the silicon surface unless there is a hole available. If the applied potential is released during pore formation, hydrogen gas continues to evolve from the PSi surface for a considerable length of time after release of the potential, lending further support to surface hydride coverage. Also, *in* and *ex-situ* spectroscopic studies confirmed the presence of Si-H

bond during PSi formation [20]. The present consensus is that hydrogen exists as two, possibly three forms, namely, Si-H, Si-H_2 and Si-H_3. The surface coverage of the di-hydride form increases with increasing anodic potential thus passivating the surface until at some critical current density electropolishing occurs [21].

4.2.1.2 Stain Etched PSi

In addition to electrochemical etching, the manufacture of PSi *via* a stain etching process has been developed [22]. The stain etch procedure is relatively easy to perform, it does not require complex equipment and offers the possibility of producing much thinner porous layers (<100 nm). Although the stain films on Si wafers have been studied for nearly 40 years [23] and have been suggested to be similar to that of anodically etched PSi, it was only in the past 10 years that it has been reported that stain etched PSi exhibits visible photoluminescence (PL) [22, 24] like electrochemically produced PSi. However observations of an "incubation" time t_i, has been reported [22]. .This is defined as the time delay which occurs between the addition of the etch solution to the silicon substrate and the start of PSi production. The incubation time is dependant on the composition of the etch solution the type of dopant and the resistivity of the silicon substrate [25]. Incubation times of 60-800 s have been reported [26]. Its value increases with resistivity for p-type silicon and decreases for n-type silicon, t_i for n-type is higher [25].

Dimova *et al* [26] have proposed a PSi formation mechanism which is based on previous studies of stain etching of silicon [27]. The chemical etching of semiconductors can be considered as a localised electrochemical process. Microscopically local anode and cathode sites form on the etched surface with local cell currents flowing between the sites during the etch. Therefore, the chemical etching mechanism should incorporate sources of excess holes and electrons in order to describe the charge transfer between electrodes. The reaction at the local anode consists mainly of the dissolution of silicon. The reaction at the local cathode is a complicated reduction of HNO_3, which causes holes to be injected into the silicon. The proposed reactions at the local anode and cathode are as follows,

<u>Cathode:</u> $HNO_3 + 3H^+ \rightarrow NO + 2H_2O + 3h^+$ Equation 4.8

<u>Anode:</u> (i) $Si + 2H_2O + nh^+ \rightarrow SiO_2 + 4H^+ + (4-n)\ e^-$

(ii) $SiO_2 + 6HF \rightarrow H_2SiF_6 + 2H_2O$ Equation 4.9

where n is the average number of holes required to dissociate 1 Si atom.

Dimova [26] reports that PSi formation involves the generation of HNO_2 from HNO_3 as a rate-determining step during the initial stages of the chemical reaction. Sarathay *et al* [22] proposed adding $NaNO_2$ to H_2SO_4 to evolve NO_2 gas. This mixture would be combined with HF to form an etch solution which permits the PSi formation without delay.

Dimova [26] proposed an alternative method to start the cathodic reaction utilising a thin film of Al deposited onto the Si surface. This generates H^+ ions and gives the following reaction,

$Al + 3HNO_3 \rightarrow Al(NO_3)_3 + 3H^+$ Equation 4.10

After dissolution of the Al film and the evolution of H^+ (which occurs for 15-20 s) the cathodic reaction is started which initiates oxidation of the Si. The SiO_2 subsequently reacts with HF to form water soluble H_2SiF_6 (equation 4.9ii), hence silicon is etched at the local anode. As a result thin (1000Å) PSi films showing visible PL are prepared on the Si substrates with different types of doping and resistivity. If the Al film is deposited through a mask with a desired configuration, a selective area of PSi is obtained.

4.2.2 Pore Morphology

A pore is defined as an etch pit whose depth exceeds its width. Most PSi layers are a few microns deep and individual pores are closed at one end, as shown in figure 4.7(a) and (b). There is some degree of interconnection in most layers as shown in figure 4.7(c), whereas 4.7(d) shows closed porosity and is caused by thermally induced reconstruction of the pore network. This is kept to a minimum by avoiding heating the PSi in any drying process. Either extended anodisation or the Turner lift-off technique can obtain pores open at both ends. In the latter case the current density is ramped high enough to go into the electropolishing mode, which results in the detachment of the porous layer, leaving free-standing PSi, in the order of 5-50 microns thick.

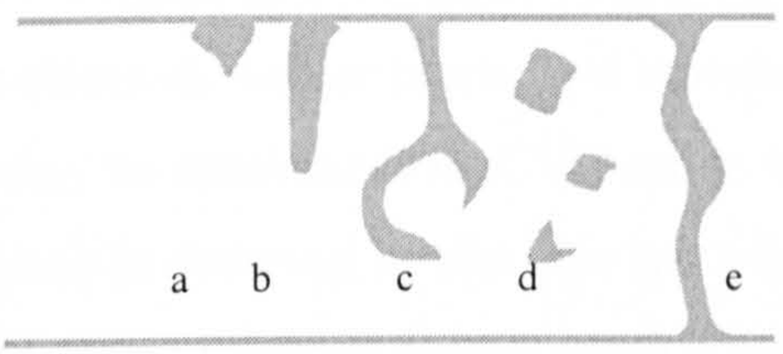

Figure 4.7 Schematic view of different pore shapes found in PSi.

IUPAC guidelines for pore size states that those less than 2 nm are microporous, 2-50 nm mesoporous and above 50 nm are macroporous. The vast majority of PSi studied to date is mesoporous. Microporous material is limited to anodisation in highly concentrated HF. The maximum pore width reported to date is by Lehman who produced a 10-micron wide pore from a 40 Ω cm n-type substrate.

The most common shape of a pore is that of the cylindrical one. Crystallographic orientations effect pore shape, for example anodisation of a 100 orientated wafer can generate pores of square cross-section whereas 111 wafers exhibit pyramidal shapes. For the preparation of PSi see chapter 8.

5. Electrochemical Techniques

5.1 Cyclic Voltammetry

Over the past thirty years potential step techniques, such as cyclic voltammetry (CV) and linear sweep voltammetry (LSV), have been applied to an increasing range of systems and at the same time mathematical techniques have progressed to enable kinetic parameters to be determined for a wide variety of mechanisms. It is, however in preliminary mechanistic studies that CV is most useful [1]. When investigating capacitor behaviour CV gives an excellent indication of true double layer capacity (i.e. no faradic processes occurring), since, for an ideal capacitor a rectangular shaped voltammogram is obtained as illustrated in figure 5.1. Practically, however, deviations from ideality occur giving a slightly rounded rectangular shape as shown by the red trace in figure 5.2. Nevertheless, parameters such as the stable potential window of the electrode and or electrolyte material along with that of the complete capacitor cell may be obtained from CV data, as shown in figure 5.2. In this example since a redox peak is observed on the blue trace between the potential of 1-1.5 V it may be concluded that the working potential window for this system is +1 to –1 V. At high negative potential values an increase in the negative current is observed. This phenomena is characteristic of overpotential induced self-discharge of the capacitor cell, thus giving further evidence of the stable potential window.

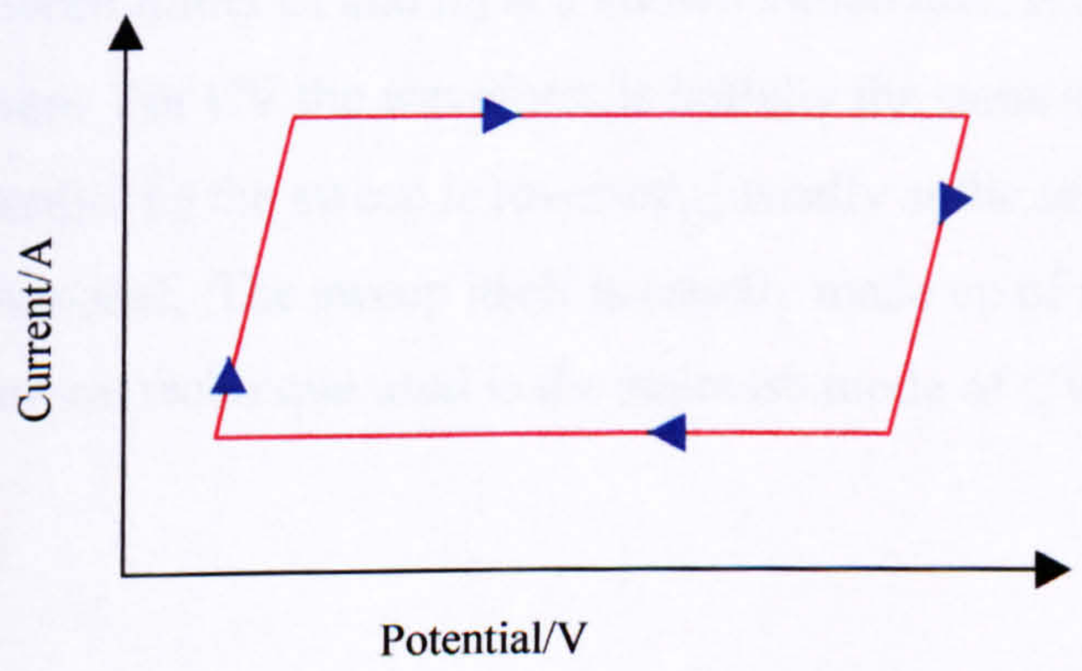

Figure 5.1 Cyclic voltammogram for an ideal capacitor

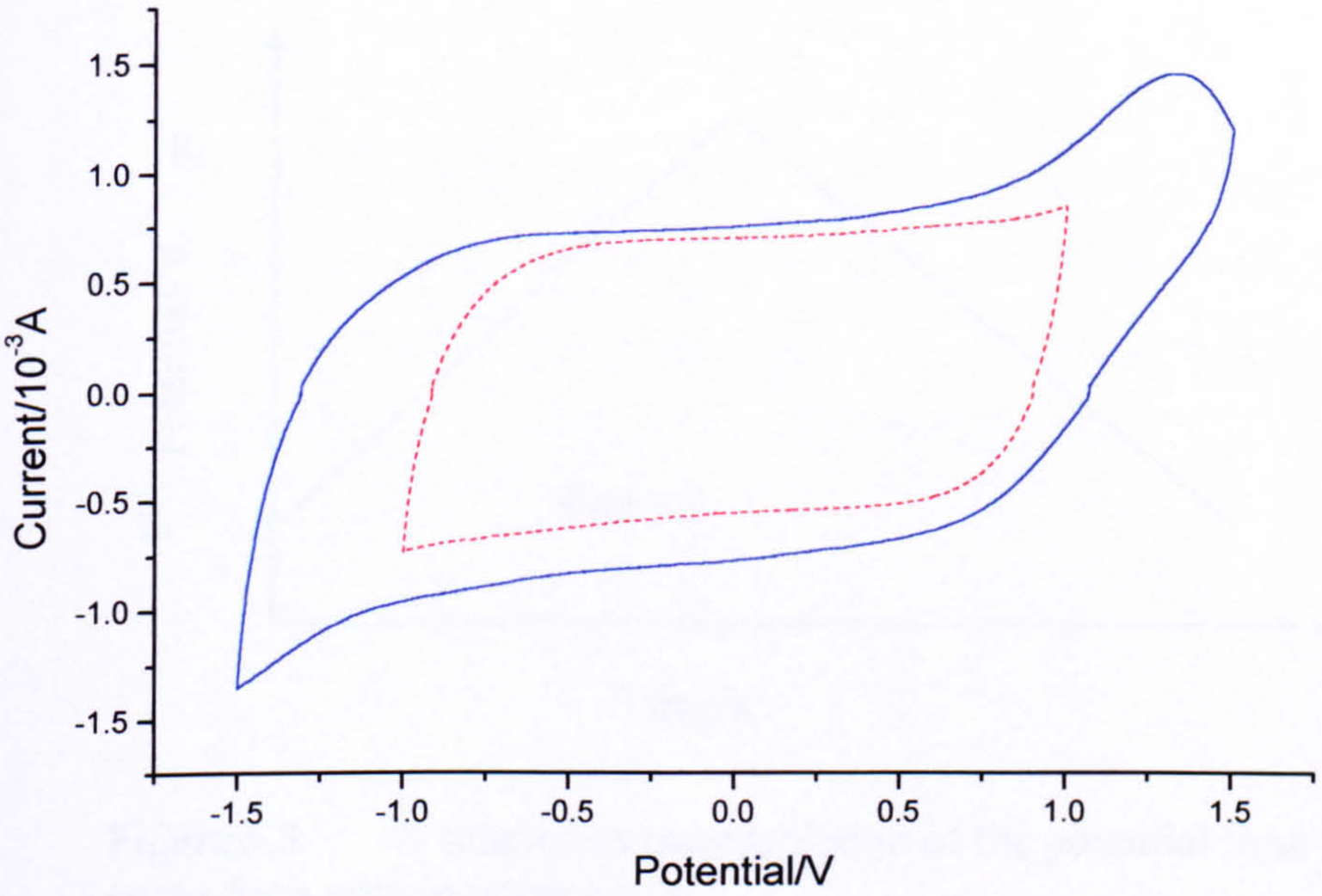

Figure 5.2 A typical CV showing the working potential of a practical supercapacitor cell. 1 mV s^{-1} vs a floating potential.

The potential-time waveforms used for sweep measurements are shown in figure 5.3. The simplest of these techniques is LSV, and this involves sweeping the potential between limits E_1 and E_2 at a known sweep rate, ν, before halting the potential sweep. For CV the waveform is initially the same as in LSV, but on reaching the potential E_2 the sweep is reversed, (usually at the same scan rate), rather than terminated. The sweep itself is usually made up of many potential steps and a common technique used is the staircase mode of CV.

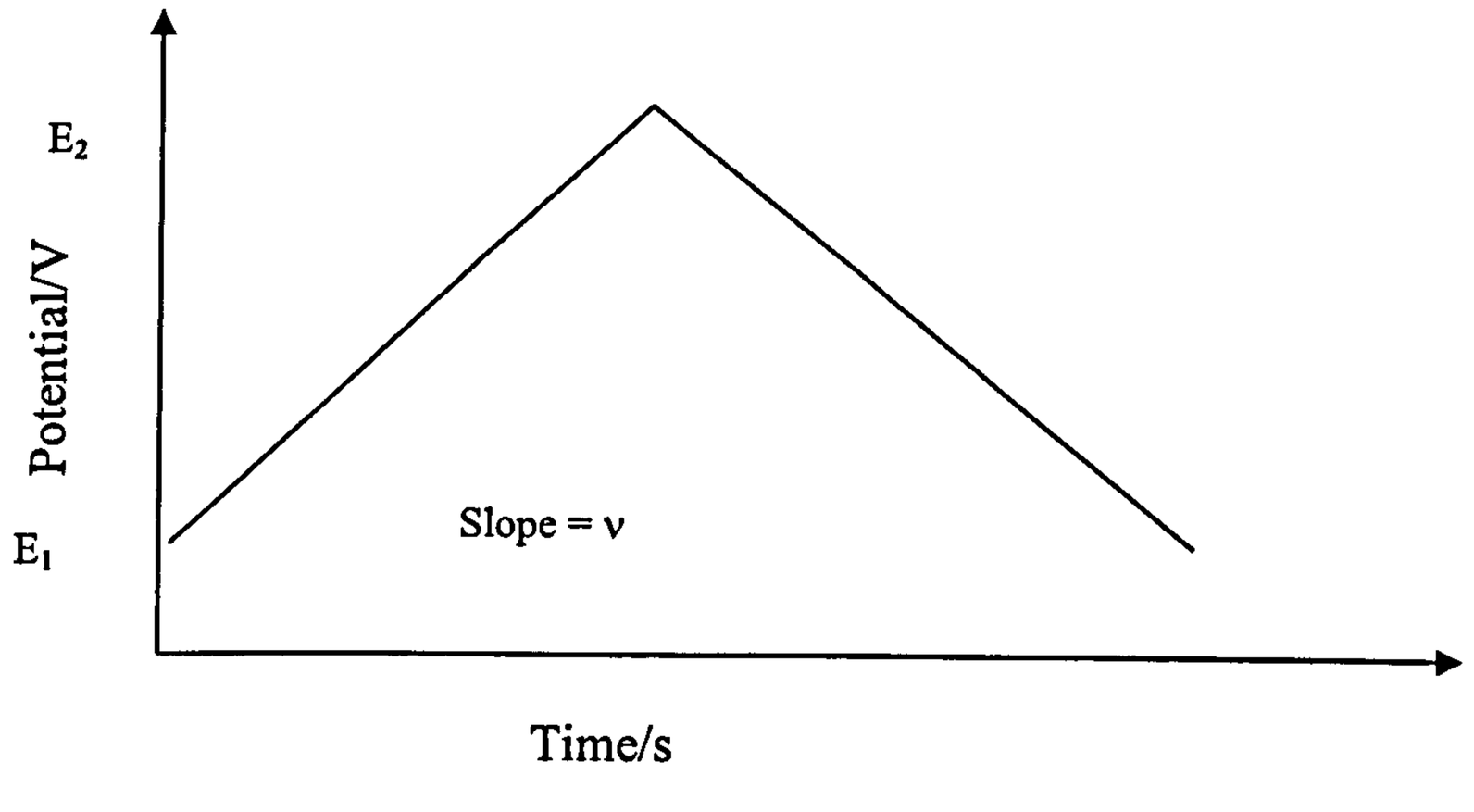

Figure 5.3 A schematic representation of the potential time curve for a voltammetric cycle.

In both LSV and CV experiments, the cell current is recorded as a function of applied potential (the potential axis is also the time axis). The sweep rates used in conventional electrochemical capacitor analysis ranges from 1 to 500 mV s^{-1}. The capacitance of a cell may be evaluated from the following relationship:

$$C = i\frac{dt}{dV(t)} \qquad \text{Equation 5.1}$$

Since,

$$i(t) = C\frac{dV(t)}{dt}$$ Equation 5.2

However, this equation represents the infinite time or steady state limit and is not obeyed at voltages just after commencement of the cycle and just after the voltage bias is reversed. For an RC circuit, this departure depends on the relative magnitude of the RC time constant compared to the time from the start of the experiment [2] and the equation for the forward branch is,

$$I(t) = C\frac{dV(t)}{dt}\left[1-\exp\left(\frac{-t}{RC}\right)\right]$$ Equation 5.3

Therefore equation 5.1 is only used to determine the capacity of a device at when the potential is at 0V, i.e. at a steady state. Alternatively, equation 5.1 may be written as

$$C = \frac{i(0V)}{\nu}$$ Equation 5.4

where ν is the sweep rate of the voltammogram.

5.2 A.C. Impedance Spectroscopy.

The perturbations associated with potential steps and sweeps (as in voltammetric methods) are usually of large amplitude and drive the working electrode far from equilibrium. Another approach is to perturb the cell using an alternating (usually sinusoidal) signal of small amplitude (~ 10 mV r m s) and observe the manner in which the system follows the perturbation at steady state. A major advantage with this a.c. spectroscopic technique is that the response may be theoretically treated via linearised current-potential (i-V) characteristics. This leads to important modelling simplifications in matters relating to diffusion and charge/ion transport kinetics. Detailed knowledge of i-V relationships over a wide range of overpotential is not needed. High precision measurements are possible because of the steady state nature of the response and the intrinsic multiplexing (data-averaging) capability. Multiplex data methods such as fast Fourier transform (FFT) have been profitably employed in the acquisition and analysis of a.c. impedance spectroscopic data [3].

The parameter (electrical) impedance, Z, is the a.c. analogue of resistance, R, for d.c. circuits and expresses the relationship between a sinusoidal signal and the corresponding response:

$$V = E \sin(\omega t) \qquad \text{Equation 5.5}$$

$$i = I \sin(\omega t + \phi) \qquad \text{Equation 5.6}$$

$$Z = V/i \qquad \text{Equation 5.7}$$

The phase angle, ϕ, is negative for capacitive circuits and is -90^0 for a "pure" capacitor. The impedance, then, is a vector quantity and both polar and rectangular co-ordinates may be employed to denote a vector. In the latter format, *Z* is given by $R - jX_c$, where $j = (-1)^{1/2}$ and X_c is termed the capacitive reactance (equal to $1/\omega C$, $\omega = 2\pi f$, where f is the a.c. frequency in Hz). Simply put, X_c is a frequency-sensitive "variable" resistor that switches from ∞ when $\omega \rightarrow 0$ (d.c.) to 0 when $\omega \rightarrow \infty$ (high

frequency). The magnitude of Z ($|Z|$) is $(R^2 + X_c^2)^{1/2}$, and the phase angle is given by,

$$\tan \phi = X_c/R = (\omega RC)^{1/2} \qquad \text{Equation 5.8}$$

In polar co-ordinates, Z may be written in Euler form as,

$$Z = |Z| e^{j\phi} \qquad \text{Equation 5.9}$$

Separation of the impedance components into "real" and "imaginary" components is a bookkeeping measure and simply embodies the fact that there is a phase lag between the applied signal and the measured response. For d.c. circuits this phase lag is obviously absent. Thus the system response can be modelled in terms of complex plane impedance plots and the expected response from a purely resistive circuit is distributed along the abscissa. On the other hand a pure capacitor will manifest a response along the ordinate (in the negative direction). Intermediate values of ϕ are expected for other RC circuits. These responses are illustrated in figure 5.4.

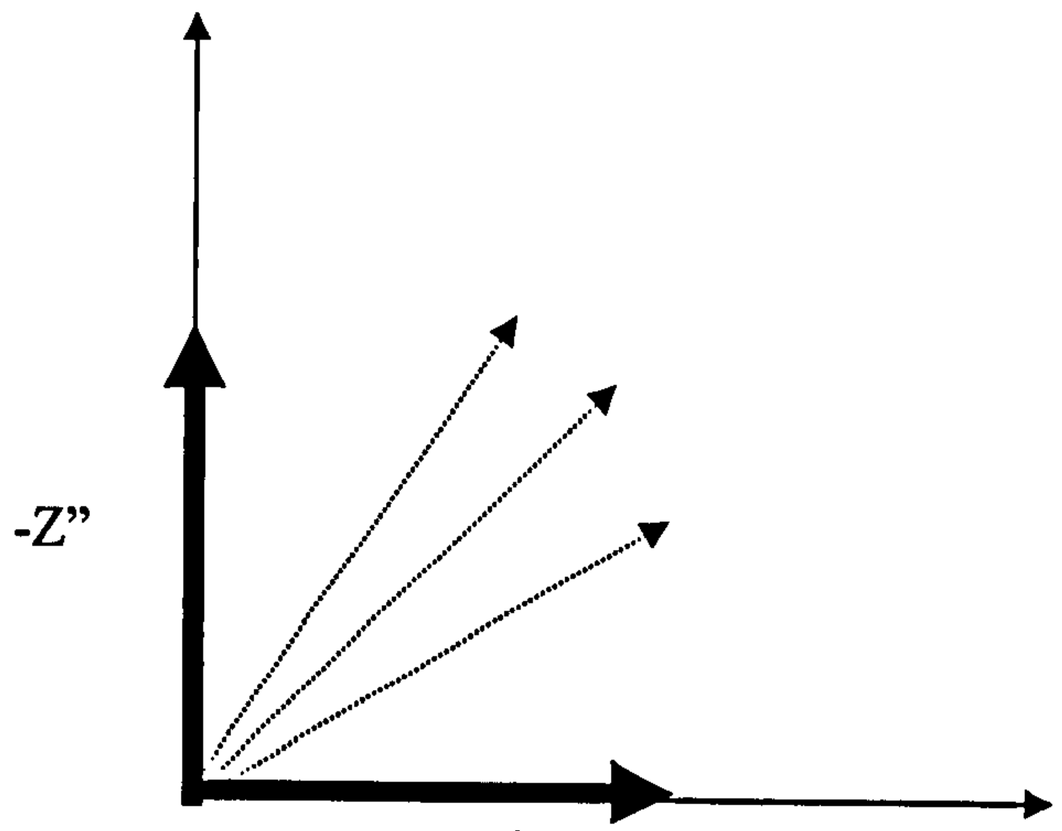

Figure 5.4 Illustration of complex plane responses for RC circuits with differing values of ϕ.

Representative complex plane plots for various RC circuits including one with multiple relaxation times are shown below in figure 5.5 (a)-(c).

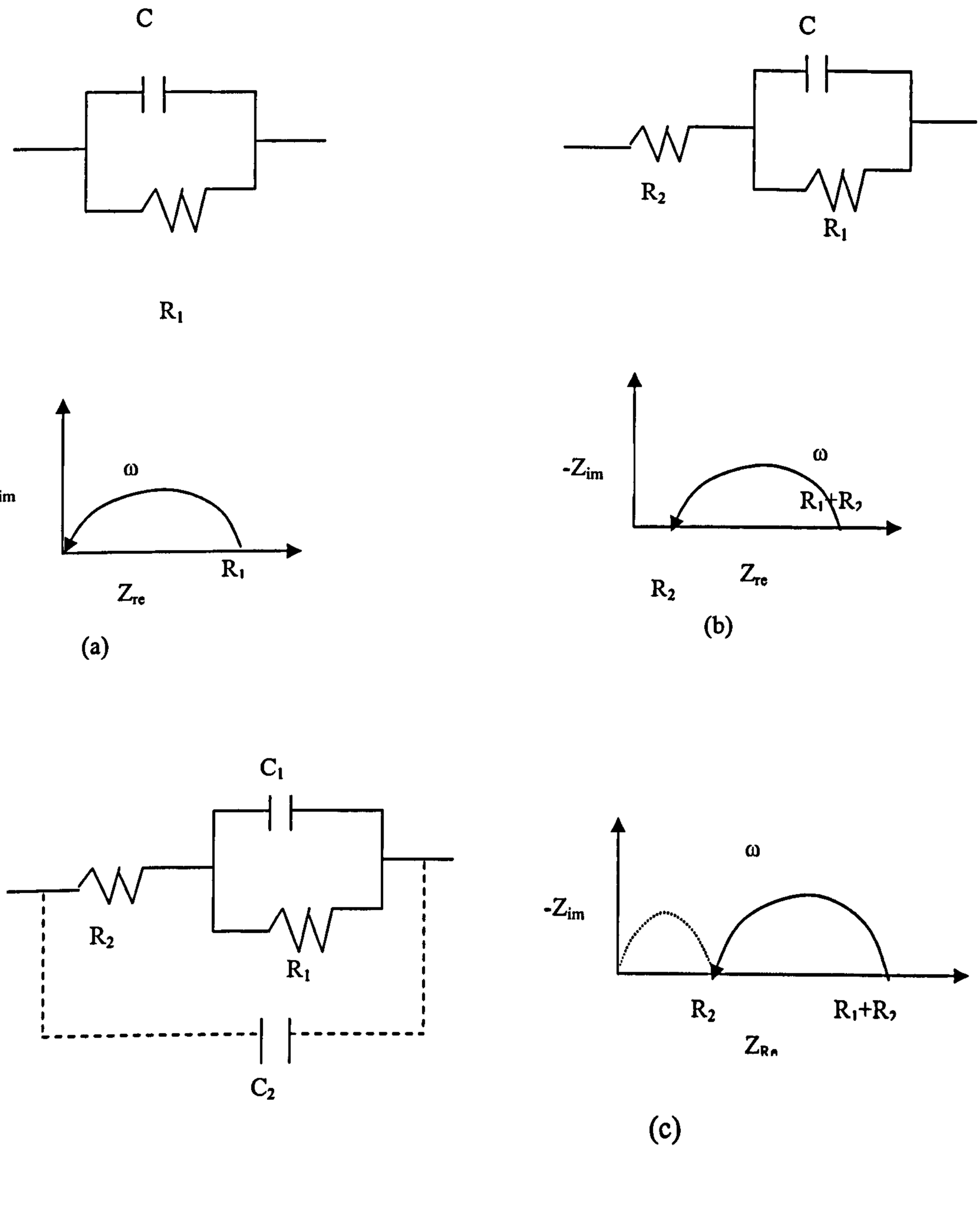

Figure 5.5 (a)-(c) RC circuits with their corresponding complex plane responses. Figure 5.5(c) shows multiple relaxation times.

The complex plane plot is also known as Nyquist, Argand, or Cole-Cole plot and these terms should be regarded as synonymous. A physiochemical system that can be represented by an electrical circuit is said to be modelled by an *equivalent circuit* with the implication that each of the circuit components can be associated with a portion or process in the test system.

A typical equivalent circuit for electrochemical systems is the Randles circuit shown in figures 5.6 and 5.7. This circuit is the same as the one in figure 5.5 with the addition of a diffusional impedance termed the "Warburg impedance", Z_W. Z_W, unlike other elements of the circuit is frequency dependent:

$$Z_W = \sigma (\omega)^{-1/2} - j (\sigma \omega)^{-1/2} \qquad \text{Equation 5.10}$$

where

$$\sigma = RT/ n^2 F^2 A (2D)^{1/2} [(C_o^*)^{-1} + (C_R^*)^{-1}] \qquad \text{Equation 5.11}$$

N.B. diffusional (random walk or stochastic) phenomena manifest themselves as a square root relationship, such as, $t^{-1/2}$ (potential step), $\nu^{1/2}$ (potential sweep), or $\omega^{1/2}$ (small amplitude a.c. perturbation).

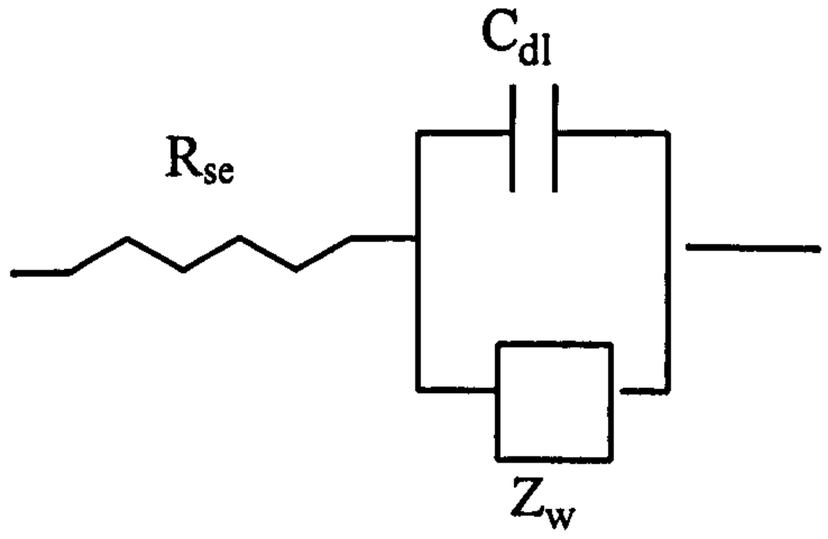

Figure 5.6 Randles equivalent circuit of a supercapacitor cell.

R_{se} and C_{dl} are the series resistance and the double layer capacitance respectively and R_F is the charge transfer resistance.

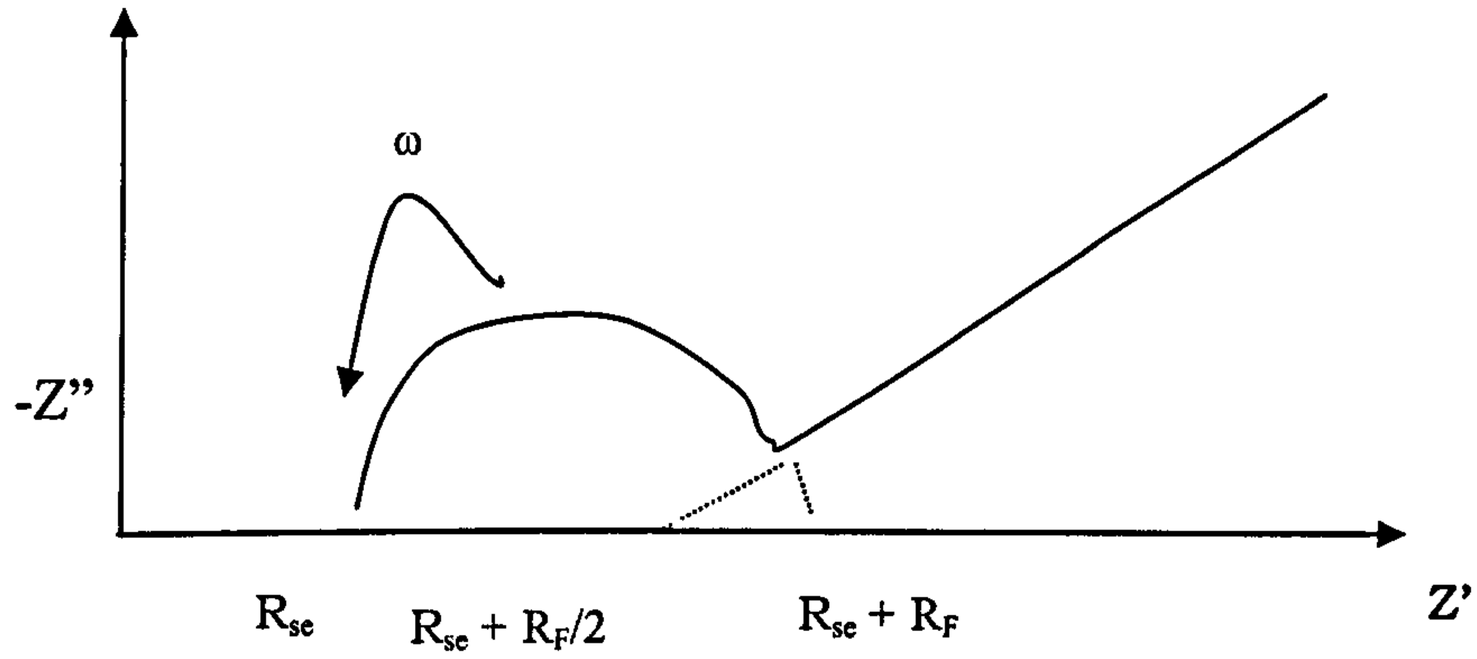

Figure 5.7 Illustration of the complex plane response expected from a supercapacitor cell, showing the bulk resistance, charge transfer resistance.

Experimentally, a device to separate the system response into real and imaginary components is required. One such phase-sensitive detector is the lock-in amplifier. The classical approach based on the use of various types of a.c. bridge circuits has been surpassed by more dynamic and user friendly approaches. Methodologies based on noise, correlation and time domain analysis have all been profitably employed in a.c. impedance spectroscopy and many of these approaches have been used in commercially available instruments [4-7].

Complexities associated with simple equivalent circuits previously mentioned include phenomena associated with depressed arcs and constant phase angles, [1], porous electrodes and electrodes with rough surfaces [2-4], pseudoinduction behaviour associated with electrosorbed intermediates [5] and non-idealities associated with (polymer) coatings on electrode surfaces. This latter aspect may be discussed as follows:

The boundary conditions for Warburg impedance, Z_W, previously discussed, were such that semi-infinite diffusion prevails. However, diffusion in these cases is bounded and is restricted to a thin layer of thickness, d. This problem has been independently addressed by three groups [6-8], and leads to the same conclusion, namely, that the phase angle begins to increase at very low frequencies due to the onset of finite length effects. Figure 5.8 illustrates the complex plane response in this instance.

The low frequency impedance in this case is given by the expression,

$$Z = RT/ j \omega n^2 F^2 C^* d \qquad \text{Equation 5.12}$$

With the redox capacity of the film being,

$$C_L = n^2 F^2 C^* d / RT \qquad \text{Equation 5.13}$$

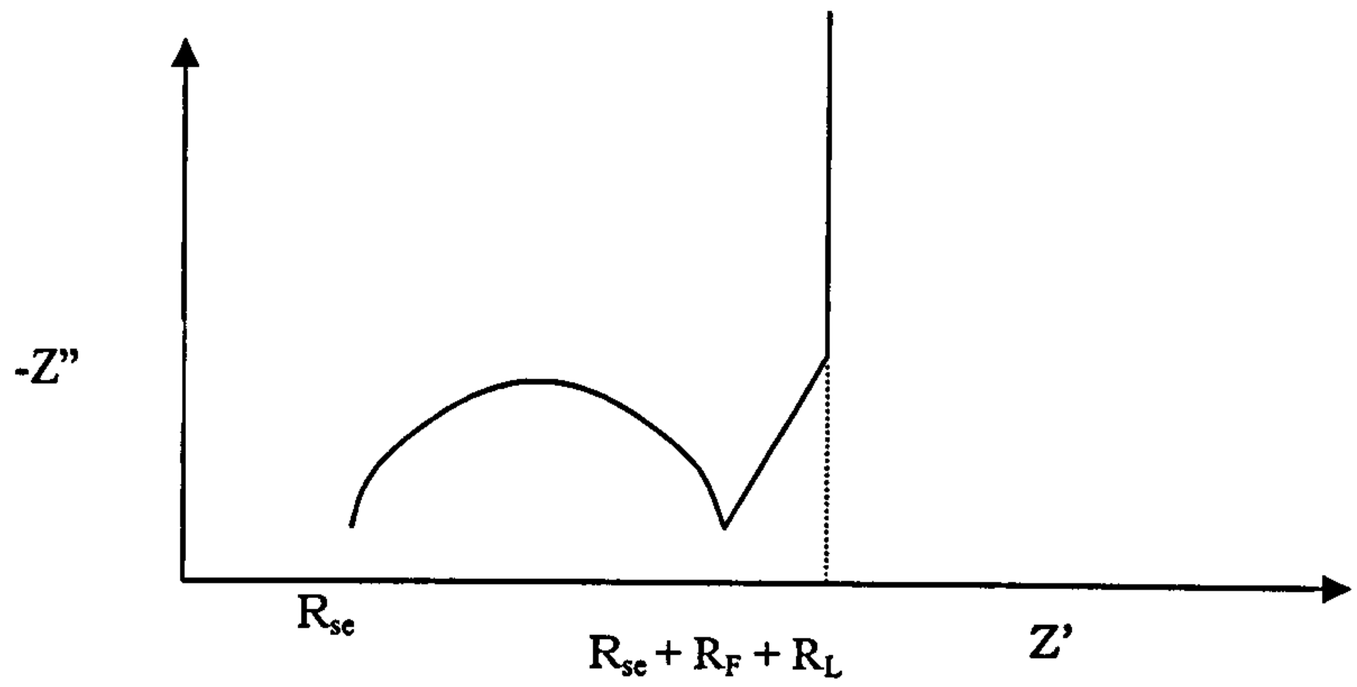

Figure 5.8 Complex plane response for an RC circuit showing the limiting low frequency resistance, R_L.

The limiting (low frequency) resistance, R_L, is obtained from the intercept of the plot with the real axis, as shown in figure 5.8. In real systems, however, the semi-circle is not centred on the real axis (i.e. depressed arc phenomenon) nor is the capacitive branch parallel to the imaginary axis. The microscopic origins of these effects is not fully understood but are believed to be related to surface inhomogeneities and roughness effects. Therefore real systems do not show a phase angle of -90^0 i.e. that of a pure capacitor.

The double layer capacitance is measured at low the frequency region and is given by,

$$C_{dl} = - (-Z'' \omega)^{-1} \qquad \text{Equation 5.14}$$

Where $\omega = 2\pi f$

When using a.c. impedance spectroscopy to analyse supercapacitor cells the frequency was swept from 65 kHz to either 1 or 10 mHz.

By convention the capacitance was then calculated at either 1 or 10 mHz using equation 5.14.

5.3 Galvanostatic charge-discharge

In previous sections, (5.1 cyclic voltammetry and 5.2 impedance spectroscopy), methods of determining capacitive characteristics have been described. A third and equally important supercapacitor characteristic is its behaviour under charging and discharging at constant current. This is particularly important for multiple cycling, since the ultimate goal is to produce a supercapacitor device with a service life of many thousands of cycles.

This method involves applying a constant current to a device until a pre-set value of voltage or power is attained. The polarity is then reversed until the original value is attained as shown schematically in figure 5.9.

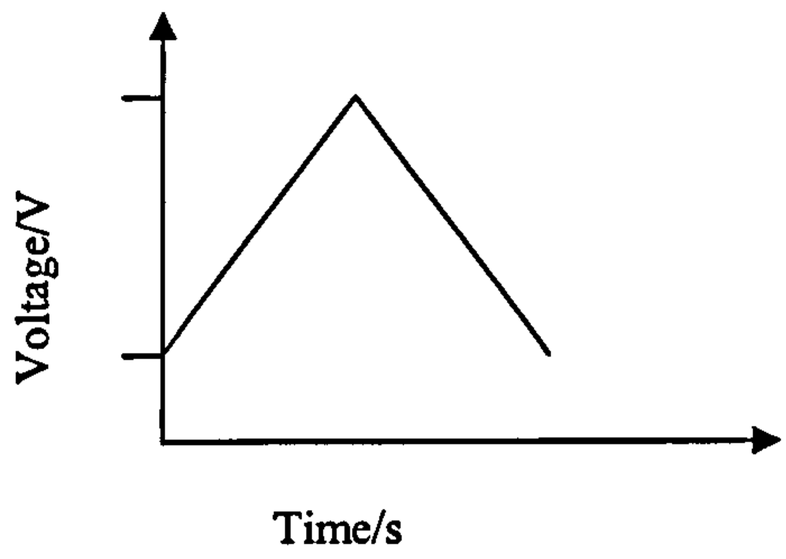

Figure 5.9 A schematic representation of a voltage time curve for galvanostatic cycling

This technique is commonly used in conjunction with a.c impedance spectroscopy to determine the efficiency and the ability of a supercapacitor device to withstand galvanostatic cycling. Parameters such as discharge capacity and coulombic efficiency of the device may also be attained from this technique.

$$C_d = \frac{i_d}{dV(t)/dt}$$ Equation 5.15

where, C_d is the discharge capacitance, i_d is the discharge current, dV the difference between the potential limits and dt the time taken to discharge between the specified potential limits. The corresponding capacitance for charging C_c

The coulombic efficiency η, is given by,

$$\eta = \frac{Cd}{Cc} * 100\%$$ Equation 5.16

Therefore,

$$\eta = \frac{idt_D}{ictc} * 100\%$$ Equation 5.17

Where, t_D and t_C are the discharge and charge times respectively. And i_d and i_C are the charging and discharging currents respectively [8]

Figure 5.10 shows a photograph of the charge-discharge equipment.

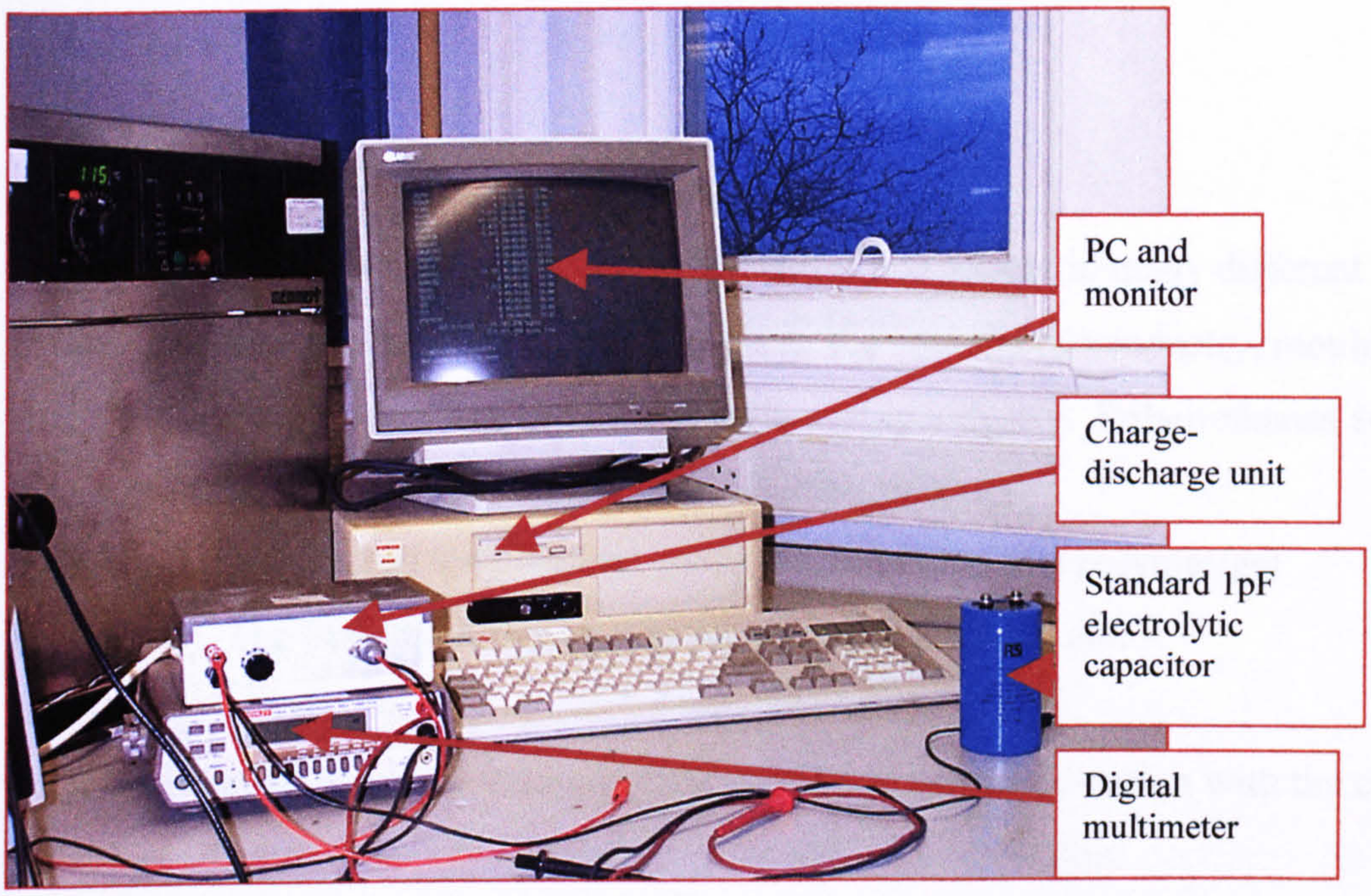

Figure 5.10 Photograph of the galvanostatic charge-discharge apparatus

6. Polyurethane Electrolyte

6.1 Introduction

Polyurethanes play a vital role in many industries and appear in many different forms. Applications involve rigid insulation in the construction industry, moulded dashboards and bumpers in the motor manufacturing industry. Polyurethanes are also used to manufacture shoe soles in the fashion industry.

This study has explored the potential use of polyurethane as a polymer/gel electrolyte. The basic requirements for a polymer electrolyte are: -

1. That it has an electron-donating group available for co-ordination with the cation.
2. It has adequate mechanical properties for thin film formation.

Polyurethane is said to have both hard and soft regions [1]. See figure 6.3. It is the soft regions that have the ether oxygen atoms responsible for potential cationic conductivity as in 1 above, and the hard regions give the polymer its mechanical stability. The origins of these so-called hard and soft regions may be better understood by studying the reaction sequence for the manufacture of a polyurethane polymer, as shown in figure 6.1. The soft regions are denoted by R in figure 6.1 and are aliphatic chains with structures that minimise the possibility of crystallisation in this region. R' denotes the hard region and is made up of aromatic groups. The aromatic substituents on the polymer chain have the effect of locking the chain and hence minimising segmental motion.

Polyurethanes are addition polymers formed by the reaction of di- or poly-isocyanates with polyols as shown in figure 6.1.

Polyol + Diisocyanate ⟶ Polyurethane

OH-R-OH + OCN-R'-NCO ⟶

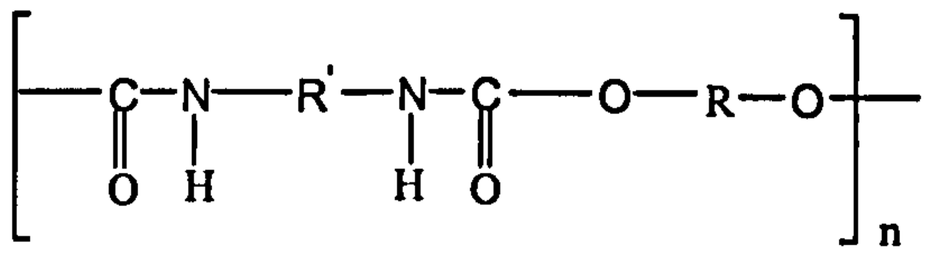

Figure 6.1 The basic reaction sequence of a polyol and diisocyanate yielding a polyurethane.

The reaction is exothermic and the heat evolved is used to vaporise a blowing agent for the manufacture of rigid polyurethane foams.

The polymerisation rate depends upon the structure of the polyol and the diisocyanate. Aliphatic polyols with primary hydroxyl end-groups are the most reactive, reacting approximately ten times faster than with secondary hydroxyl end-groups. Phenols react with isocyanates more slowly and the resulting urethane link is easily broken yielding the original isocyanate and phenol. This reversible reaction is used to manufacture 'blocked' isocyanates, which are activated on heating. The term polyurethane is used to describe any polymer that has been chain extended by a reaction with di- or poly-isocyanate. The isocyanate group (-NCO) can react with any compound containing active hydrogen atoms.

Isocyanates also react with water yielding a substituted urea and carbon dioxide and the CO_2 provides the principal source of gas for blowing in the manufacture of low-density flexible foams. It is extremely important however, to exclude any water moisture from the reaction when producing solid (non-foam) polyurethane.

Although the pKa value of polyols are higher than that for water and hence are more reactive towards isocyanates, the presence of water will give rise to a side reaction

and cause foaming of the final polyurethane product. The initial product of the reaction of isocyanate with water is a substituted carbamic acid, which breaks down into an amine and CO_2. The amine then undergoes further reaction with the isocyanate to yield the substituted urea, as shown in figure 6.2 below.

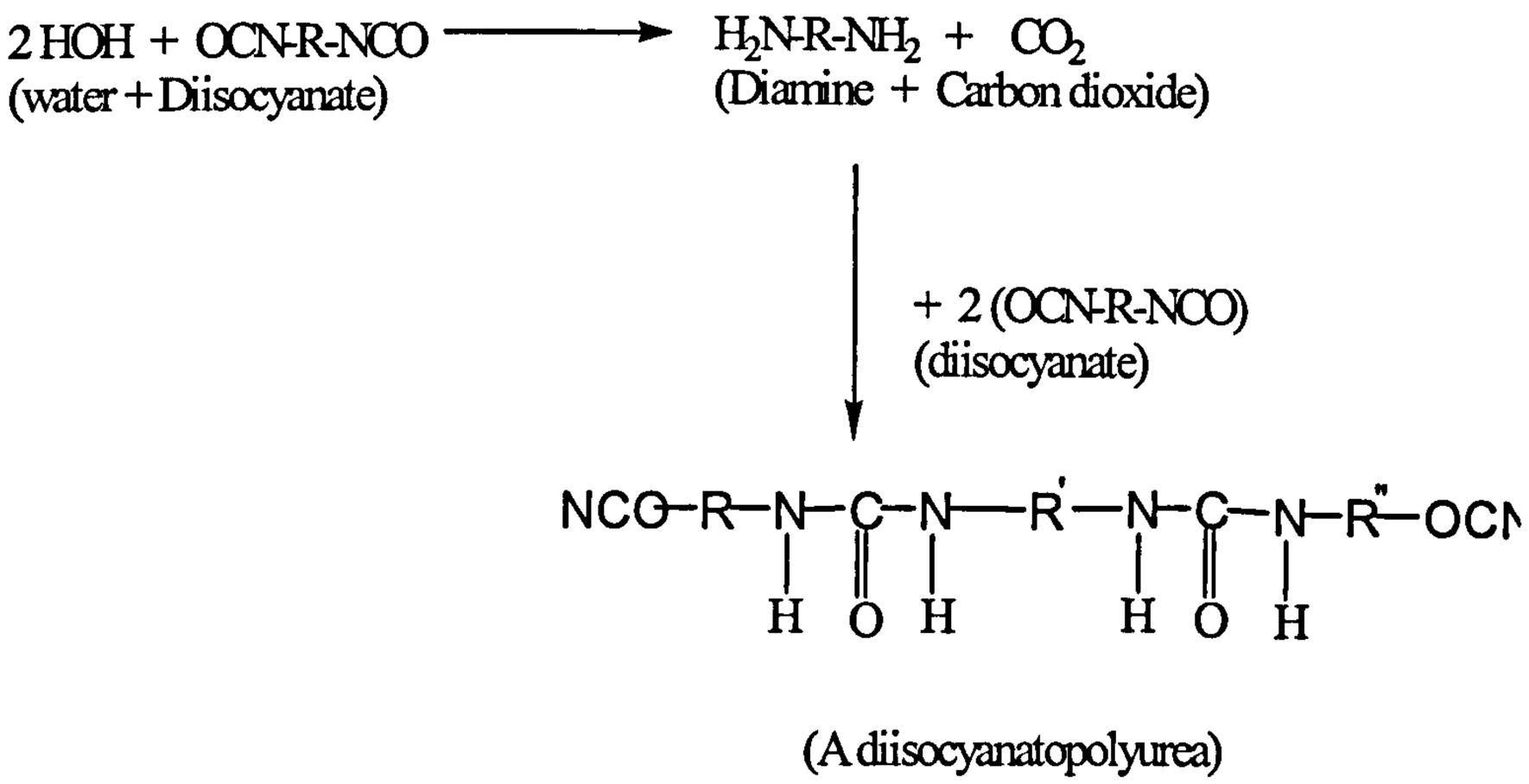

Figure 6.2 Reaction of water with diisocyanate

The reaction of isocyanates with amines is also important in the manufacture of polyurethanes. Diamines are used as chain extending and curing agents in polyurethane manufacture. The effect of diamine addition is to increase the reactivity of the reaction mixture and the resulting polyurea segments in the polymer increase the potential for both primary and or hydrogen bonded cross-links. The reaction of isocyanates with a primary amine is between 100 and 1000 times faster than that of the reaction of isocyanate with polyols.

The reactivity of amines increases with their basicity, aliphatic amines being more reactive than aromatic amines. Tertiary amines do not react with isocyanates because they posses no active hydrogen.

The molecular structure of polyurethane polymers varies from rigid cross-linked polymers to linear, highly extensible elastomers as shown schematically in figures 6.3 (a)-(c).

Figure 6.3-(a) soft, high elongation elastomers. Relaxed

Figure 6.3-(b) soft, high elongation elastomers. Stretched

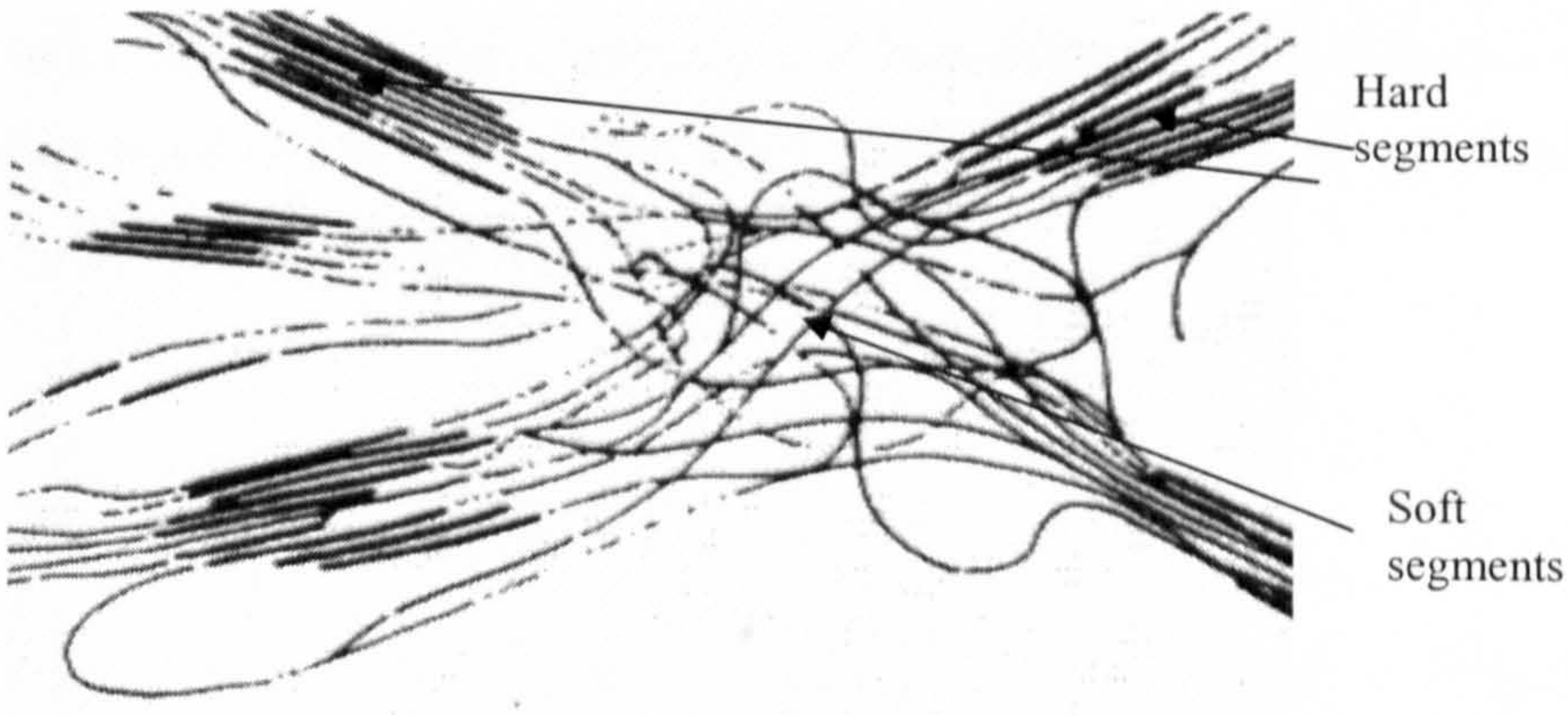

Figure 6.3-(c) high modulus elastomers, flexible foams; polymers with a segregated domain structure

Many elastomers have segmented structures consisting of long flexible chains (e.g. polyethers or polyesters) joined by relatively rigid aromatic polyurethane- polyurea segments. Their properties depend largely upon secondary or hydrogen bonding of polar groups within the polymer chains. Hydrogen bonding occurs readily between –NH groups (proton donors) and the carbonyl groups (electron donors) of the urethane and urea linkages. Hydrogen bonds are also formed between the NH-groups of the urethane and urea linkages and the carbonyl oxygen atoms of the polyester chains. The ether oxygens of the polyether chains also tend to align by hydrogen bonding with the NH-groups, but these bonds are much weaker and more labile than those formed with carbonyl oxygen atoms. The hard segments, especially the stiff polyurea hard segments, show strong secondary bonding and tend to agglomerate into hard segment domains in structures having long flexible chains. A major contribution to the hard segments is due to the alkyl and aryl groups of the polyurethane (shown by R, R' and R" in figure 6.2) particularly when they are sterically bulky.

The type of polyurethane that was utilised in this study as a polymer electrolyte is the type shown in figure 6.3-(c) above. The soft domains provide an ether oxygen atom for cation co-ordination and chain mobility, and hence ionic conductivity in a manner similar to that found polyethylene oxide PEO. The hard segments then provide the mechanical stability of the thin films.

6.2 Electrolyte Preparation

The polyurethane (Desmopan 385, supplied by Bayer) electrolyte was prepared by the solvent cast method [2].

This method involves dissolving the electrolyte components in a suitable solvent. The polymer electrolyte consisted of polyurethane and lithium perchlorate, 9$LiClO_4$), (Aldrich; 99.99% pure). The gel electrolytes contained the same constituents as above with added plasticiser. The plasticiser used was a mixture of ethylene carbonate (EC), (Aldrich; 99.99% pure) and propylene carbonate (PC), (Aldrich; 99.99% analytical grade, dried and sealed over nitrogen), in a 1:1 weight for weight ratio.

The chosen solvent was tetrahydrofuran THF, (Aldrich, 99.99% pure, analytical grade, dried and sealed over nitrogen).

The polyurethane/salt solution was stirred for 12 hours to ensure homogeneity. For the gel electrolytes, the PC and EC mixture was added and stirred for a further 12 hours.

The resulting homogenous, viscous solution was carefully poured into a glass-ring mould with a Teflon base as shown in figure 6.4, ensuring no air bubbles were introduced into the solution. The THF was left to evaporate at room temperature for 24 hours leaving a thin film polymer or gel electrolyte of approximately 460 μm thick. The films were then dried in a vacuum oven at 25°C for 12 hours in an attempt to extract all the THF from the electrolyte film.

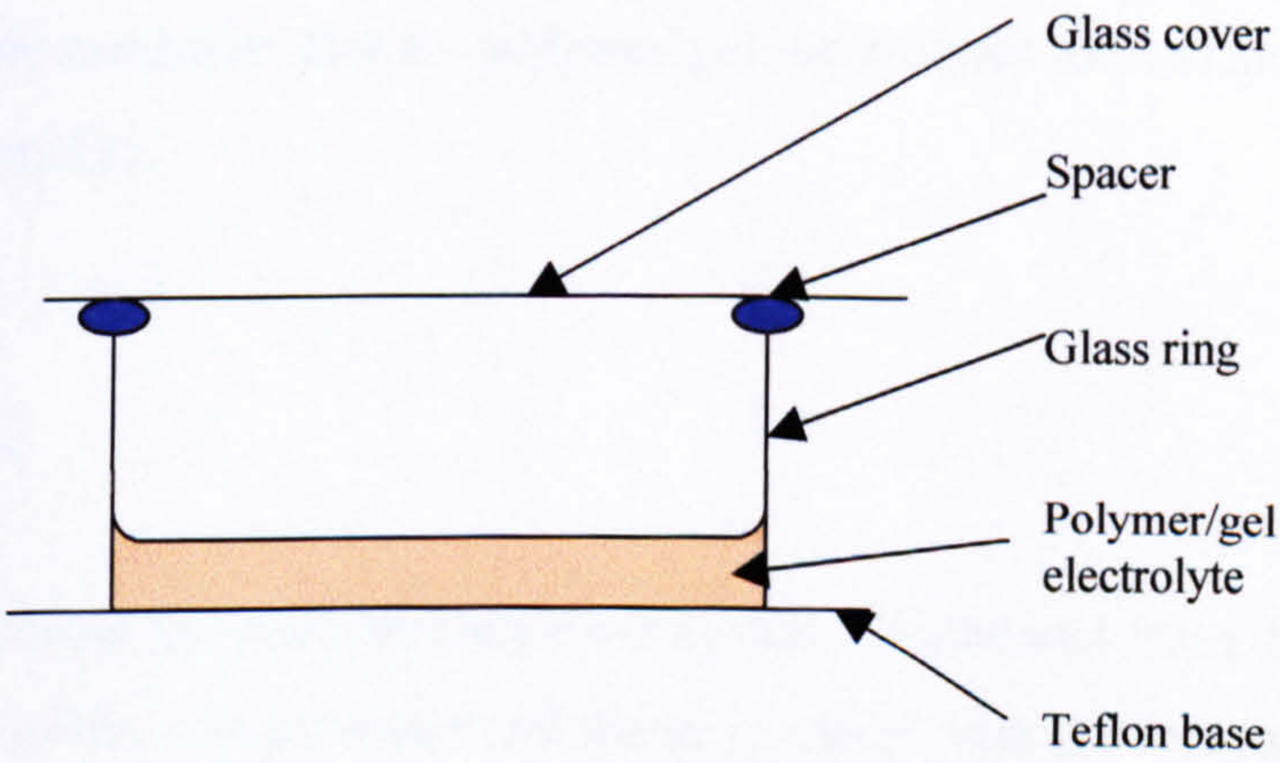

Figure 6.4 A schematic representation of the solvent casting mould.

6.3 Conductivity measurements

The conductivity of a polymer/gel electrolyte is its single most important parameter and the optimisation of the conductivity is therefore equally important in supercapacitor technology. This section reports the methodology by which the conductivity was optimised for the PU electrolyte.

6.3.1 Introduction

The conductance, G, is the reciprocal of the resistance, R, and is measured in Siemens, S; this unit is identical to the reciprocal ohm, Ω^{-1}. The conductance varies inversely with sample thickness (path length), d, and directly with sample area, A, and it is therefore conventional to characterise polymer electrolytes by the proportionality constant or conductivity, σ, as shown in equation 6.1 below [3].

$$G = \frac{\sigma A}{d} \qquad \text{Equation 6.1}$$

Rearranging and substituting for $G=1/R_b$, equation 6.2 is the expression used to calculate the conductivity of an electrolyte. The conductivity is normally expressed in S cm^{-1}, sometimes written as $(\Omega\ cm)^{-1}$. Typically values of 10^{-2}-10^{-4} S cm^{-1} are acceptable conductivities for polymer/gel electrolytes used in supercapacitor technology [3].

$$\sigma = \frac{d}{R_b A} \qquad \text{Equation 6.2}$$

By convention the bulk resistance of the cell is measured from the midpoint between intercept of the vertical spike and the semi-circle with the real axis of the complex plane impedance plot. When a semi-circle is not evident the intercept from the spike alone is used.

6.3.2 Experimental

The bulk resistance of the polymer electrolytes was measured using a.c. impedance spectroscopy, see chapter 5.2. A Solatron 1260-frequency response analyser coupled to a Solatron 1286 electrochemical interface was used to obtain an impedance spectrum, a photograph of the equipment may be seen in figure 6.6. An a.c. amplitude of 10 mV r.m.s. was used with a frequency range of 65 kHz to 0.1 Hz. The frequency response conformed with that expected for a polymer electrolyte and the bulk resistance R_b was then determined for each sample by interpolating the vertical spike in the complex plane to intersect the real axis.

A brass cell, as shown in figure 6.4, was designed and manufactured within the solid state electrochemistry research group and used to obtain the impedance spectra,

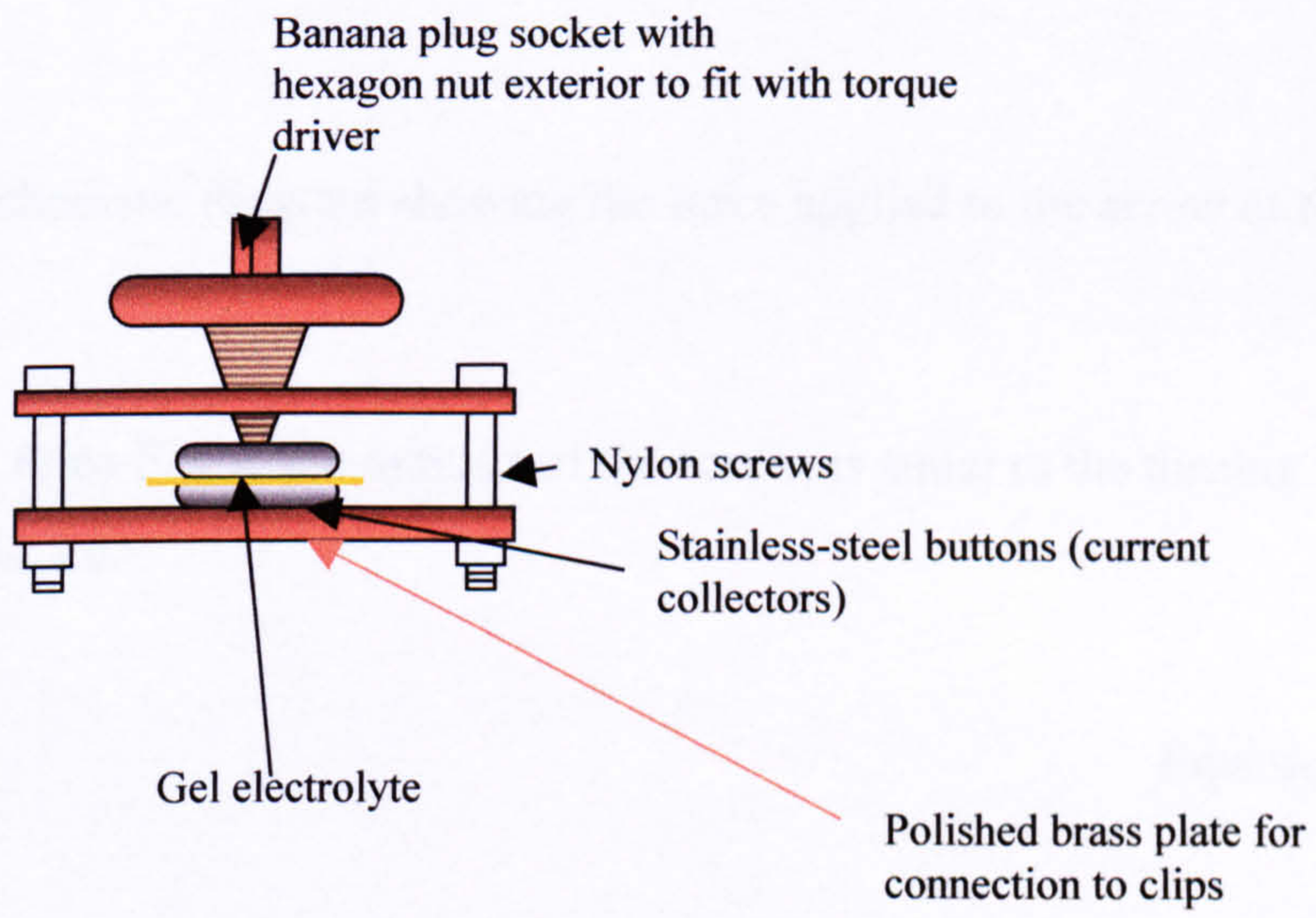

Figure 6.5 Schematic representation of a supercapacitor test cell

A torque driver was used to supply a constant turning force and to ensure reproducibility between the four different systems investigated.
An applied torque of 60 cN m was found to be a sufficient turning force to ensure a good contact between the polymer electrolyte and the current collector without

damaging the electrolyte film. A turning force of 60 cN m equates to a pressure of 1600 kN m^{-2} on the electrolyte.

Since,

60 cN = 0.6 N applied at a distance of 1 meter and,

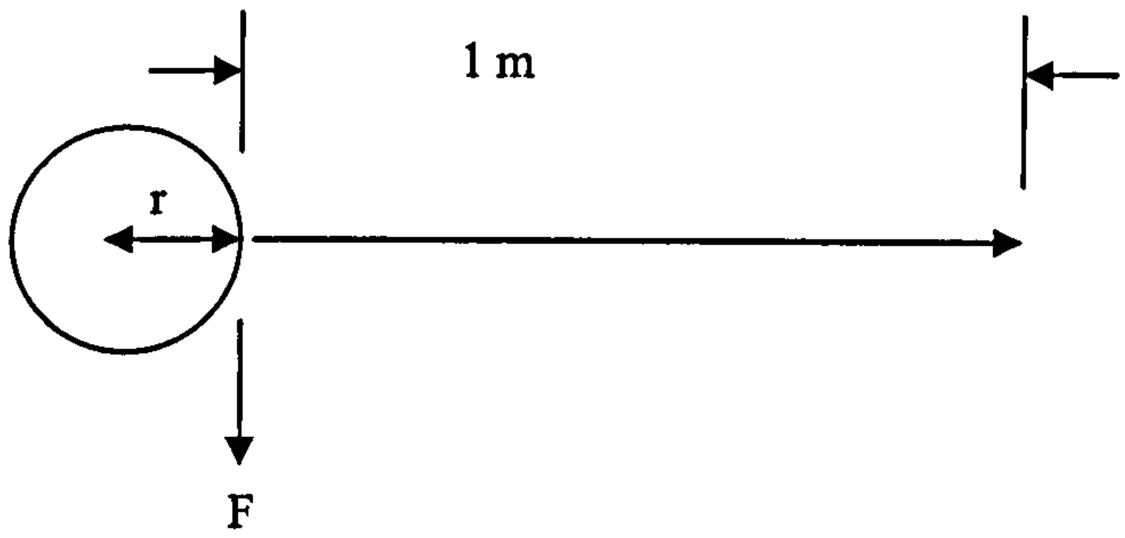

Figure 6.6 Schematic diagram showing the force applied to the screw of the test cell

The product of the force F, and the radius r of the screw, is equal to the turning force applied to the screw, i.e.

$$F = \frac{0.6x1}{r}$$ Equation 6.3

Where $r=3x10^{-3}m$

Therefore, F=200 N, and

Pressure P=F/A,

Where A is the area over which the pressure is applied,

Then, $P = 200/1.25*10^{-4}$ Nm^{-2}

Hence, P = 1600 kNm^{-2}

1286 Electrochemical Interface

1260 Frequency response analyser, FRA

Figure 6.7 Photograph of the Solatron 1260 FRA and the 1286 Electrochemical Interface used to measure the impedance of the test polymer.

6.3.3 Variation of the salt concentration

Four compositions of polymer electrolytes based on the percentage by mass of the salt were prepared using the solvent cast technique, see chapter 6.2. The percentage salt was varied from 5% to 50% by weight of PU, as shown in the captions of figures 6.8 and 6.9

Figures 6.8 and 6.9 show the complex plane impedance plots of the four-polymer electrolytes investigated.

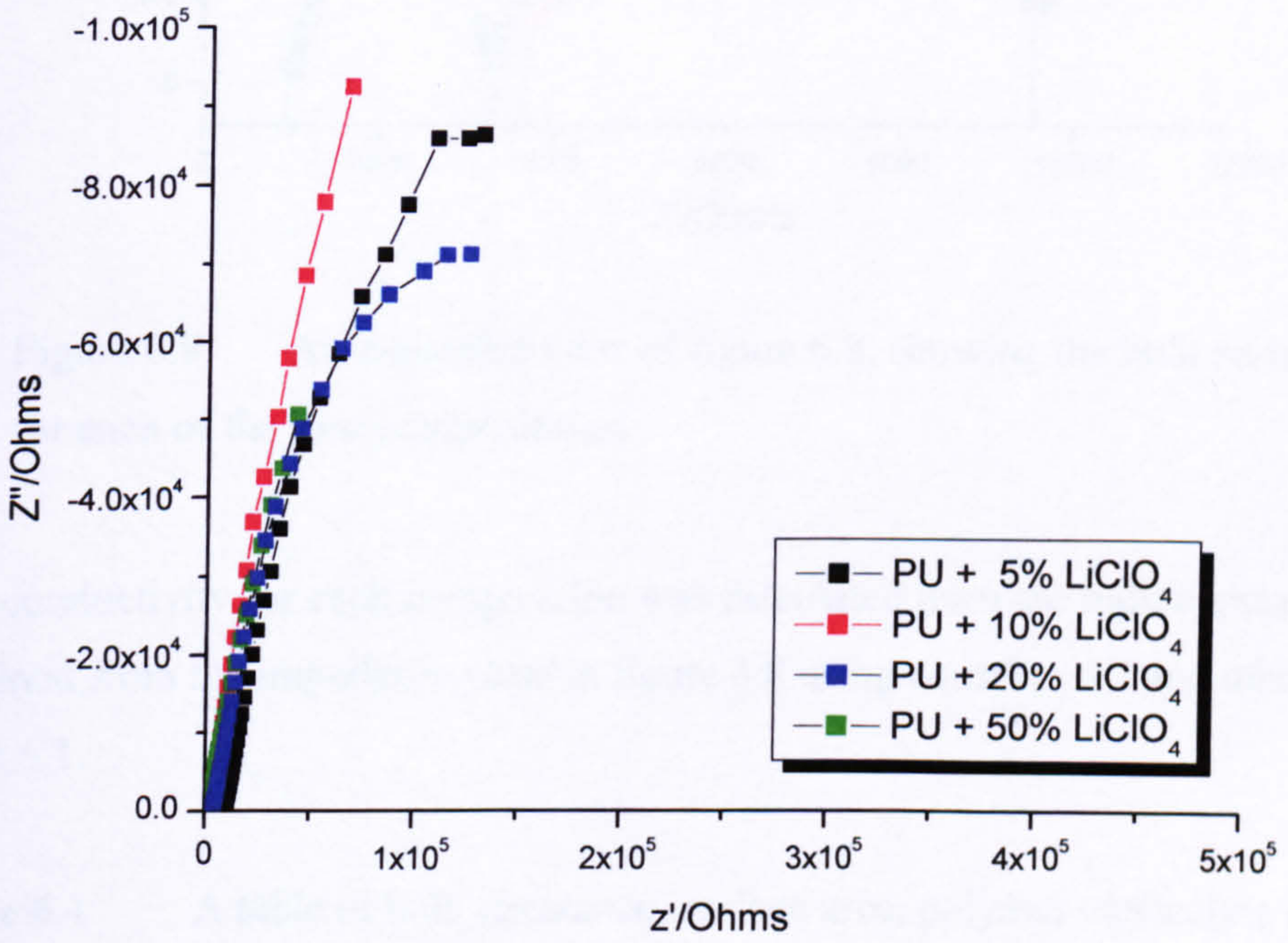

Figure 6.8 Complex plane impedance plot of four different concentrations of $LiClO_4$ in PU.

An initial inspection of the impedance results in figure 6.8 suggests that there is only a vertical spike in the complex plane, but expansion of the axis shows that there is the development of a semi-circle at high frequencies. This is limited by the upper working frequency of the Solatron 1260 FRA used in these experiments, which was 65kHz.

Figure 6.9 shows the complex plane plots of figure 6.8 with the real axis expanded.

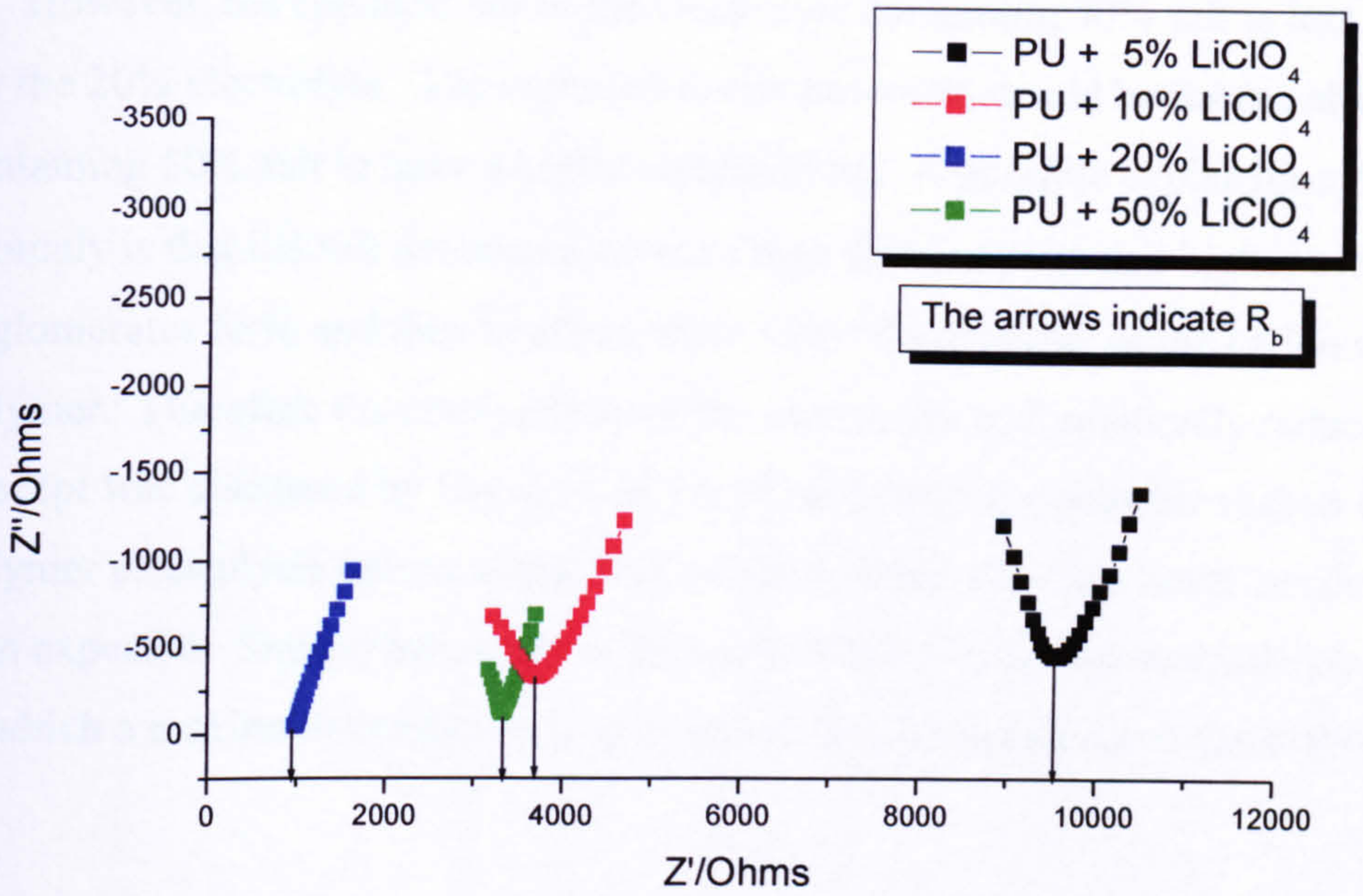

Figure 6.9 An expanded view of figure 6.8, showing the bulk resistance for each of the four compositions.

The conductivity for each composition was calculated from the bulk resistance obtained from the impedance plots in figure 6.8 using equation 6.2 and tabulated in table 6.1.

Table 6.1 A table of bulk resistance, surface area, polymer electrolyte thickness and calculated conductivity data for various compositions of salt in a PU electrolyte.

Composition of salt in PU/%	Bulk resistance R_b / Ω	Thickness l / cm	Surface area A / cm^2	Conductivity σ / S cm^{-1}
5	9600	0.046	1.25	$3.83x10^{-6}$
10	3300	0.045	1.25	$9.47x10^{-5}$
20	900	0.0343	1.25	$1.52x10^{-4}$
50	3400	0.0443	1.25	$1.04x10^{-5}$

The conductivity of the electrolyte increases with increasing salt content from 5 to 20 %. However, the conductivity of the electrolyte containing 50% salt is less than that for the 20% electrolyte. The expected result, however, would be for the electrolyte containing 50% salt to have a higher conductivity. A possible explanation for this anomaly is that the salt concentration is so high that ion pairs and higher order ion agglomerates form and thus in effect, slow down the mobility of the cation within the polymer. Therefore the conductivity of the electrolyte is dramatically reduced. This concept was discussed by Bruce *et. al.* [4, 5], and may be a possible reason for polymer electrolytes having higher salt concentrations showing lower conductivities than expected. Similar behaviour is shown by PEO-lithium salt polymer electrolytes in which a maximum conductivity is observed for compositions of about PEO_9: salt [6].

Since the final aim of this work was to incorporate a PU electrolyte in a practical supercapacitor device, an economic viewpoint needs to be considered, i.e., the cost of the salt versus the gain in conductivity. The conductivities of the 20 and 10% systems are of the same order. As there is a two-fold increase in salt content, it would then seem economically reasonable to take the system containing 10% salt and develop it further by the addition of low molecular weight plasticisers such as propylene carbonate, PC, and ethylene carbonate, EC. Chapter 6.3.4 describes the optimisation of the electrolyte plasticiser content.

6.3.4 Variation of the plasticiser concentration

This section describes the conductivity measurements of Polymer/gel electrolytes with varying concentrations of EC/PC plasticiser.

Five polymer/gel electrolyte compositions were prepared each containing PU+10% $LiClO_4$. The concentrations of plasticiser (a 1:1mixture of PC/EC) were 0%, 50%, 100%, 200% and 300% relative to the mass of PU.

Note: It was not possible to prepare a usable thin film polymer/gel electrolyte from the 300% added plasticiser. This was because too much plasticiser was present and hence the electrolyte had insufficient mechanical integrity to form a thin film. No conductivity data was obtained for this composition.

The conductivity measurements were taken as described above in chapter 6.3.2. A torque of 60 cN m (i.e. P=1600 kNm^{-2}) was also applied to the sample cell for continuity of results.

Figures 6.10 (a, b and c) show the complex plane plots of the five polymer/gel electrolytes with the varying plasticiser concentrations. As before it was necessary to expand the real axis to obtain the value of R_b.

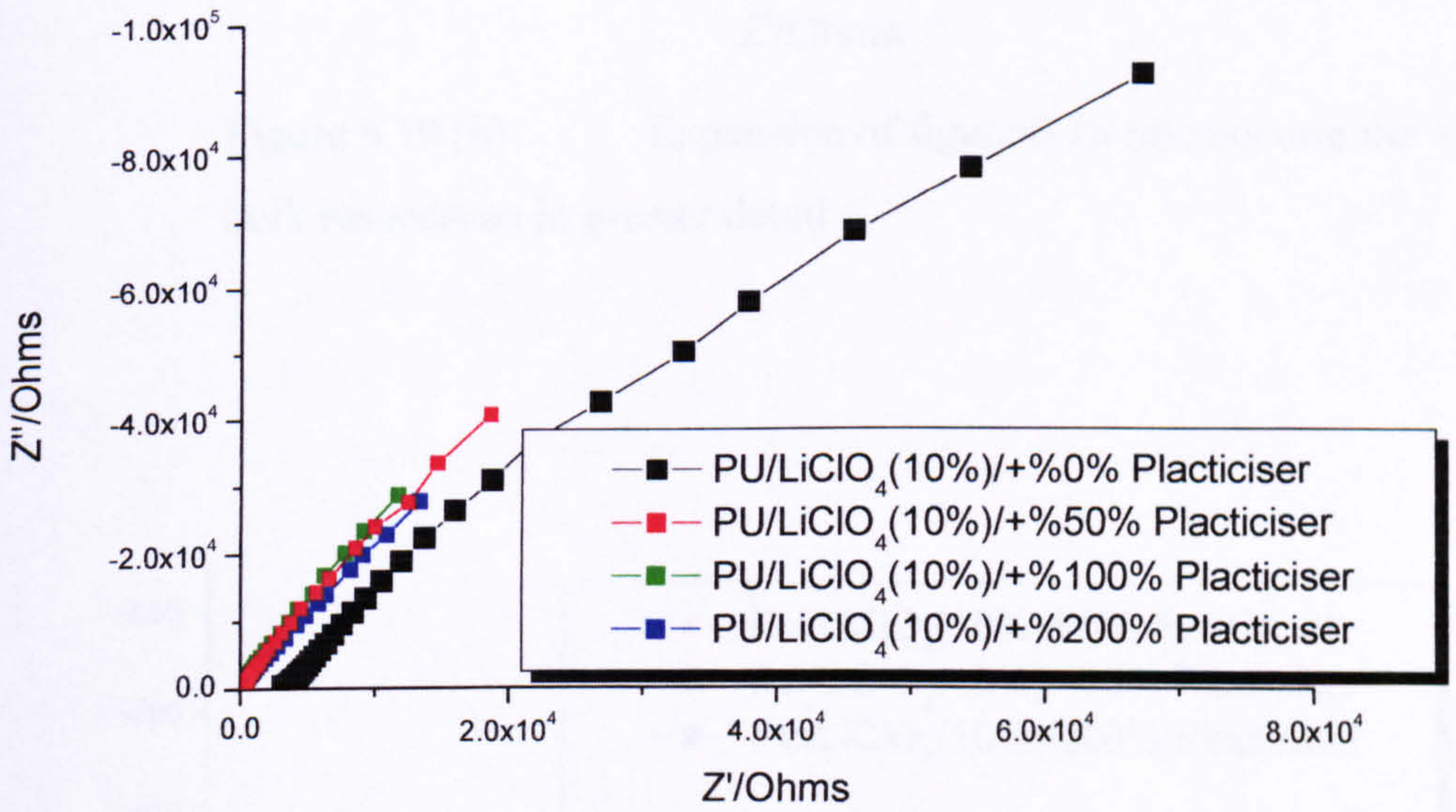

Figure 6.10 (a)Complex plane impedance plots of a PU electrolyte with 10% salt and varying amounts of plasticiser.

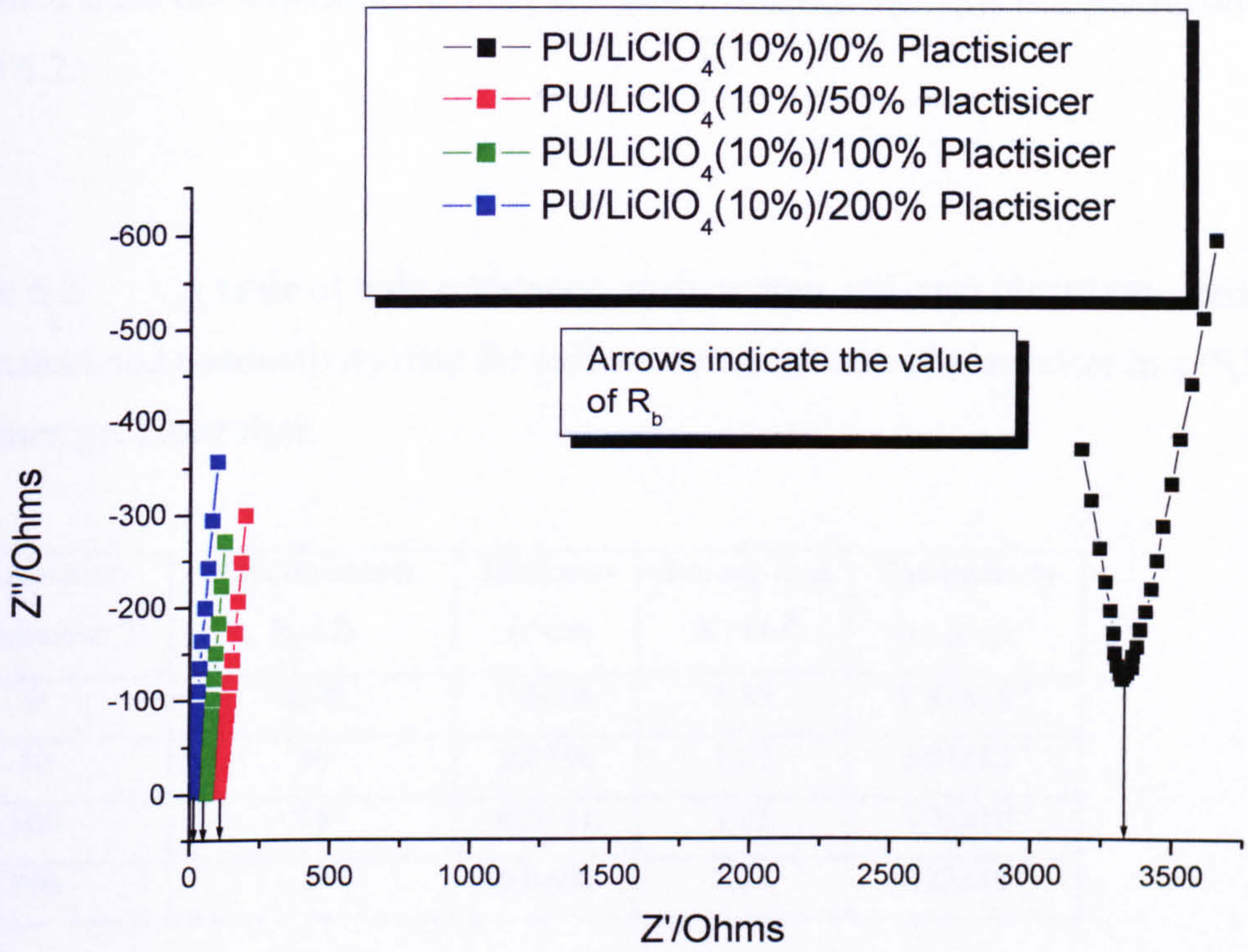

Figure 6.10 (b) Expansion of figure 6.10 (a) showing the bulk resistances in greater detail

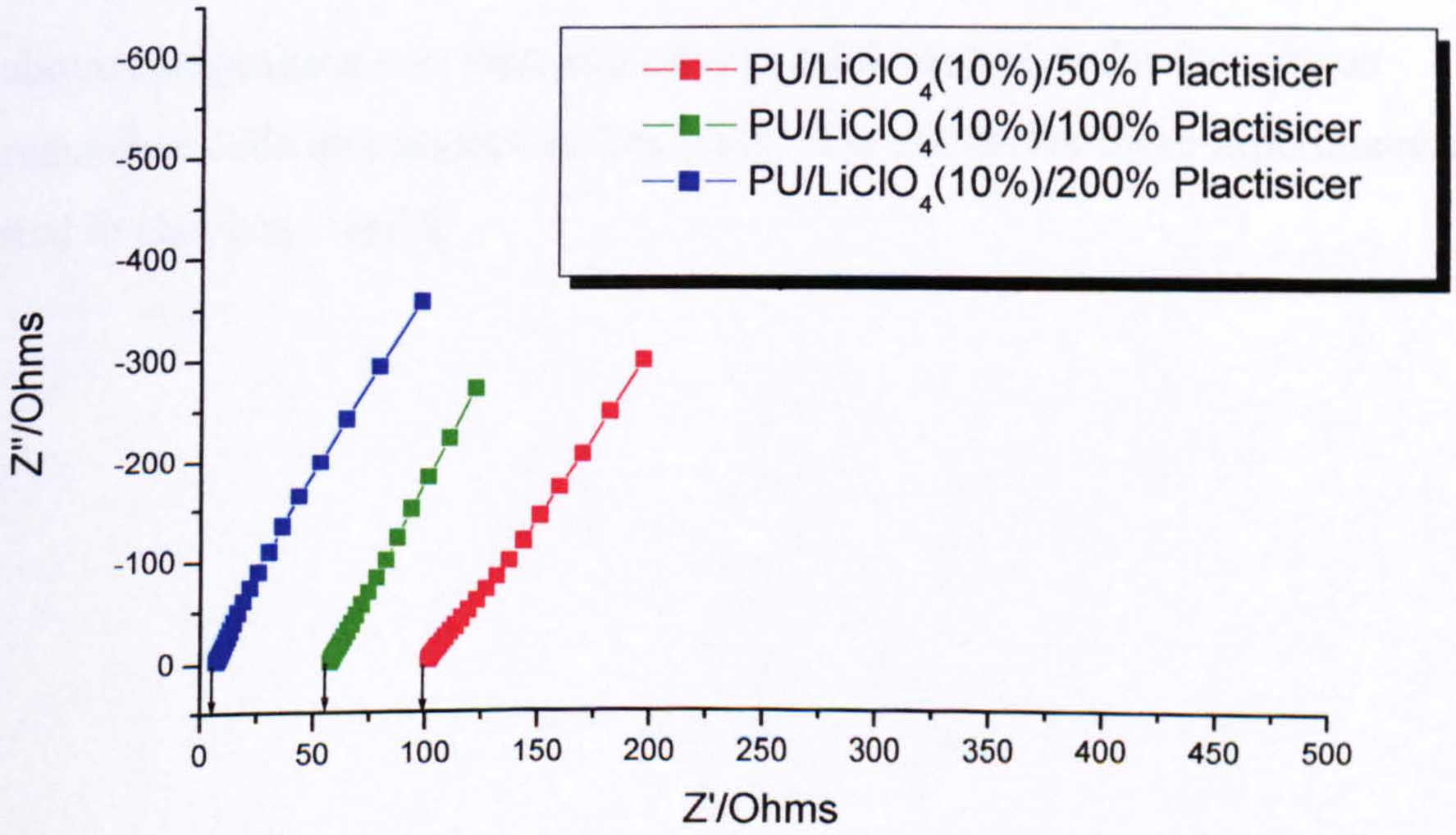

Figure 6.10 (c) Further expansion of 6.10 (a) showing R_b

The conductivity of each electrolyte was calculated using the bulk resistance obtained from the impedance results in figure 6.9 using equation 6.2 and recorded in table 6.2.

Table 6.2 A table of bulk resistance, surface area, polymer electrolyte thickness and calculated conductivity data for various compositions of plasticiser in a PU+10% polymer/gel electrolyte.

Composition of plasticiser/ %	Bulk resistance R_b / Ω	Thickness 1 / cm	Surface area A / cm^2	Conductivity σ / S cm^{-1}
0	3300	0.0456	1.25	$9.47x10^{-5}$
50	98	0.0436	1.25	$2.97x10^{-4}$
100	56	0.0427	1.25	$3.05x10^{-3}$
200	6	0.0466	1.25	$6.22x10^{-3}$

From the above data it can be seen that the system with PU+$LiClO_4$ (10%)+EC/PC (200%) is the blend which gave the highest conductivity, ($6.22x10^{-3}$ S cm^{-1}). This blend forms a mechanically stable, free-standing thin film gel electrolyte.

The above composition was therefore used as a gel electrolyte for the various supercapacitor cells investigated in this study. The results for these experiments are reported in chapters 7 and 8.

6.4 Differential scanning calorimetry

6.4.1 Introduction

Differential scanning calorimetry (DSC) is a technique used to determine thermal properties of a polymer. These properties include the glass transition temperature T_g, the melting temperature T_M, and temperatures at which point crystallisation and fusion occurs T_C and T_F, within the polymer system, as shown in figure 6.11.

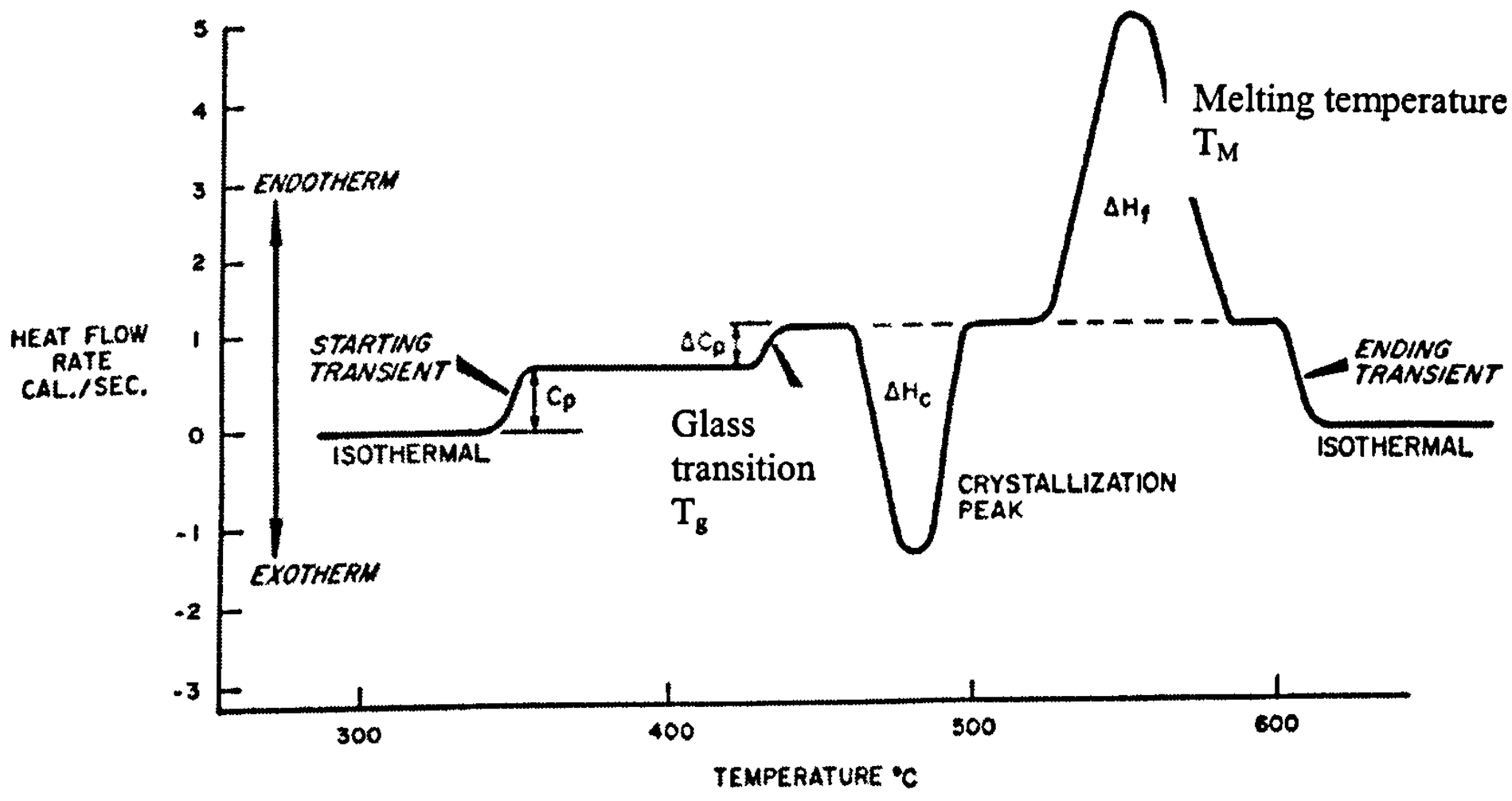

Figure 6.11 Schematic diagram of typical transitions in DSC [7].

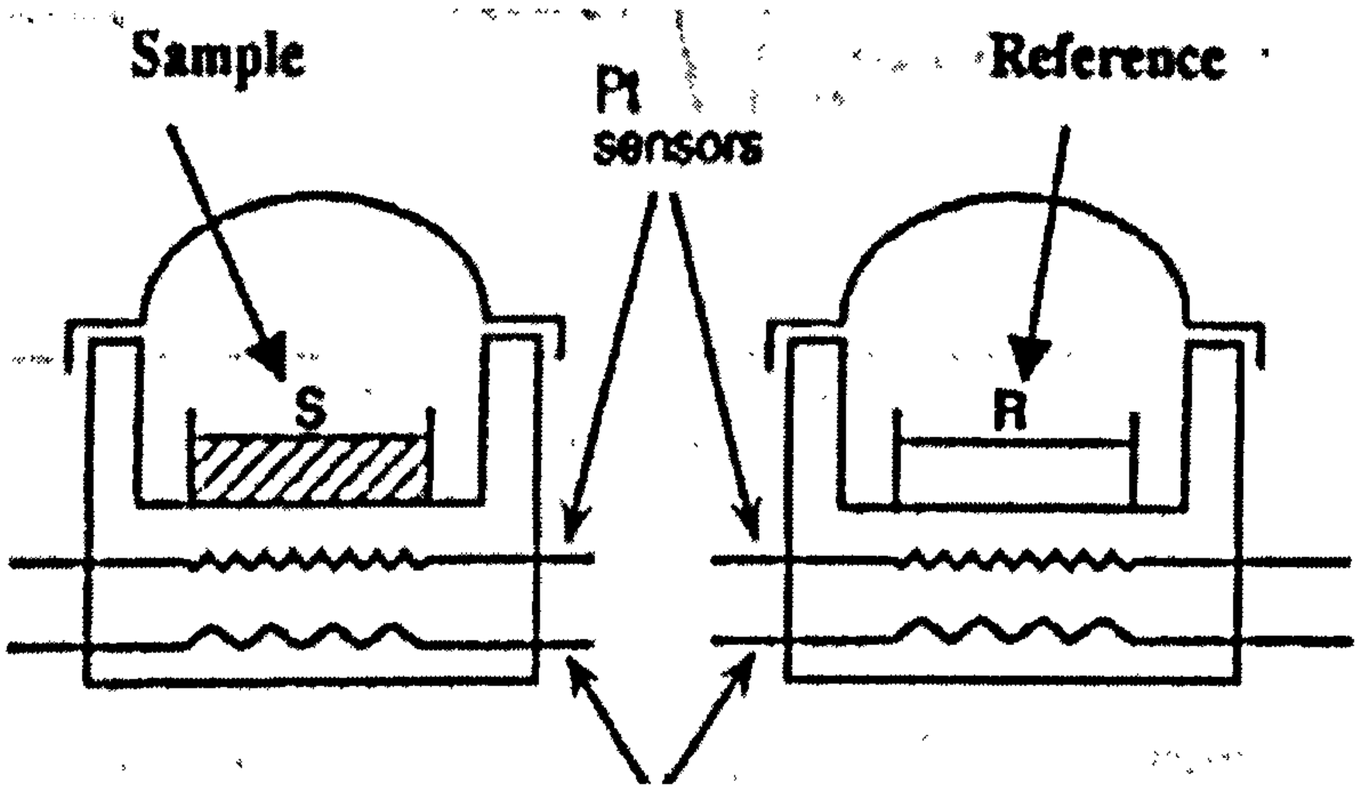

Figure 6.12 Schematic representation of the DSC-4 sample and reference pans [7].

The DSC investigations were carried out using the Perkin and Elmer DSC-4 instrument. The system-4 microcomputer controller was used to programme the DSC-4 from an initial temperature of -70^0C to a final temperature of 50^0C. Two stainless steel cups function as the sample holders on the DSC-4. By convention the left-hand cup contains the sample and the right hand cup holds the reference material. In this case the reference cup was left empty. These cups are mounted on a solid aluminium block, which holds the heater and the sensor. A schematic representation of the DSC-4 reference and sample pan configuration is shown in figure 6.12. As the system-4 programme controls changes (up or down) in temperature, transitions such as melting, boiling, dehydration or recrystallisation may occur in the sample material, resulting in an endo-or exothermic reaction. The amount of energy required to hold the sample cup at the same temperature as the reference cup during the transitions is recorded as a peak or trough on the DSC trace (figure 6.11). The values are read directly in millicalories per second, and this value is equivalent to the rate of energy adsorption or evolution of the sample.

General interpretation of DSC data

6.4.2 Interpretation of melting peaks

Most crystalline or semi-crystalline materials will undergo melting. Exceptions would occur if the material sublimed or decomposed prior to reaching the T_M. Melting is however the most commonly encountered thermal behaviour and is generally observed for low molecular weight substances as a rather sharp peak on a DSC trace. The area under the melting peak is a direct measure of the heat of fusion for the material. However, the sharpness of the peak is affected by factors such as purity and crystallite perfection, which tend to broaden the peak. For polymeric materials however, the peaks are far broader. This is a direct result of the molar mass distribution; i.e. polymers do not have a unique molar mass but a range, which melt at slightly different temperatures, resulting in a broadened melting peak. Melting is not always a simple one step behaviour. Frequently, multiple melting peaks are observed. These multiple peaks may arise due to a variety of reasons, some of which are briefly described below. The T_M is an isothermal transition and is said to be a first order transition. See chapter 6.4.8 for the Ehrenfest classification of phase transitions.

6.4.3 Thermal history

The crystallisation of a polymeric material, in particular, is extremely sensitive to the thermal history that it has been subjected to during processing. If the material was held at various temperatures, crystal growth may be encouraged in those regions. Consequently, on heating, a minimum will be observed at the annealing temperature, since those crystals formed on annealing will melt above the annealing temperature and those crystals formed on cooling from the annealing will melt below that temperature. All samples of the polyurethane electrolyte analysed for this study were manufactured at room temperature. The samples were dried at 25^0C as described in chapter 6.2. In the DSC experiments they were cooled to -70^0C at 10 degrees per minute and subsequently heated to 60^0C also at a rate of 10^0 / min. This ensured that the thermal history of each sample was as close to identical as practically possible,

thus reducing the possibility of any multiple melting and/or crystallisation peaks on the DSC trace.

6.4.4 Blends and mixtures

When two materials are physically mixed, they retain their individual thermal behaviour. This is true for a mixture of high and low-density polyethylene. Since branching will restrict crystal perfection, the low-density material melts at a lower temperature.

6.4.5 Copolymers

Copolymers are of two general classifications, random and block. A random copolymer is generally quite different from either of the homopolymers, while a block copolymer usually retains the characteristics of the homopolymers. The DSC of a block copolymer is somewhat like that of a physical blend.

The polyurethane electrolyte under investigation in this study contained hard and soft segments and to a certain extent will behave as either a physical mixture and/or a copolymer with respect to thermal analysis. This can lead to multiple melting peaks in the DSC trace. The system is also complicated because the electrolyte is essentially a blend of four different materials, namely, PU, EC, PC and the salt. In addition the PU can be considered as two phases i.e., the hard and soft segments. Thus there is a complex mixture of five components giving an array of melting peaks as shown below in figure 6.14 (a-n).

6.4.6 Scan Rate

The chosen scan rate is also an important factor in determining accurate transitions. This is equally important to other transitions such as T_g and crystallisation peaks as well as the T_M. If the scan rate is too high then the system detects a transition a number of degrees higher than what it should be. In effect the equipment leads the thermal behaviour of the polymer sample under investigation.
The scan rate used in this study was 10^0/min.

6.4.7 Interpretation of glass transition temperature (T_g)

The T_g is the temperature at which a polymer changes from hard and brittle to soft and pliable. A polymer has a greater heat capacity Cp above its T_g. (C_p is given by $q^*/\Delta T$. Where q^* is the heat supplied and ΔT is the corresponding change in temperature). Therefore the T_g is an endothermic transition and is said to be a second order transition. As shown in figure 6.11.

6.4.8 The Ehrenfest classification of phase transitions

There are many different types of phase transition, including the common examples of fusion and vaporisation. It is possible to use thermodynamic properties of substances to classify phase transitions into different types. The classification scheme was first proposed by Paul Ehrenfest, hence the name **Ehrenfest classification** [8]. Many phase transitions, like fusion and vaporisation, are accompanied by changes in enthalpy H, and volume V. These changes have implications for the slopes of the chemical potentials μ, of these phases at either side of the phase transition. Thus, at the transition from a phase α to another phase β,

$$\left(\frac{\delta\mu\beta}{\delta p}\right)_T - \left(\frac{\delta\mu\alpha}{\delta p}\right)_T = V_{\beta,m} - V_{\alpha,m} = \Delta_{trs}V \qquad \text{Equation 6.4}$$

$$\left(\frac{\delta\mu\beta}{\delta T}\right)_P - \left(\frac{\delta\mu\alpha}{\delta T}\right)_P = -S_{\beta,m} + S_{\alpha,m} = -\Delta_{trs}S = -\frac{\Delta_{trs}H}{T_{trs}} \qquad \text{Equation 6.5}$$

Where, S is the entropy of the system, $\Delta_{trs}H$ is the enthalpy change for the transition and T_{trs} is the temperature change for the transition.

Because $\Delta_{trs}V$ and $\Delta_{trs}H$ are non-zero for melting and vaporisation, it follows that for such transitions the slopes of the chemical potential plotted against either pressure or temperature are different on either side of the transition as shown in figure 6.13. Therefore, the first derivatives of the chemical potentials with respect to pressure and

temperature are discontinuous at the transition and are said to be first order transitions.

The constant pressure of a substance is the slope of a plot of the enthalpy with respect to temperature. At a first-order phase transition, the enthalpy changes by a finite amount for an infinitesimal change of temperature. Therefore, at the transition C_P is infinite. The physical reason is that heating drives the transition rather than raising the temperature, e.g. boiling water stays at the same temperature even though heat is being supplied.

A second order phase transition is one in which the first derivative of μ with respect to temperature is continuous but its second derivative is discontinuous. A continuous slope of μ (a curve with the same slope on either side of the transition) implies that the volume and entropy (and hence the enthalpy) do not change at the transition as shown in figure 6.13 (a) and (b). The heat capacity is discontinuous at the transition but does not become infinite there.

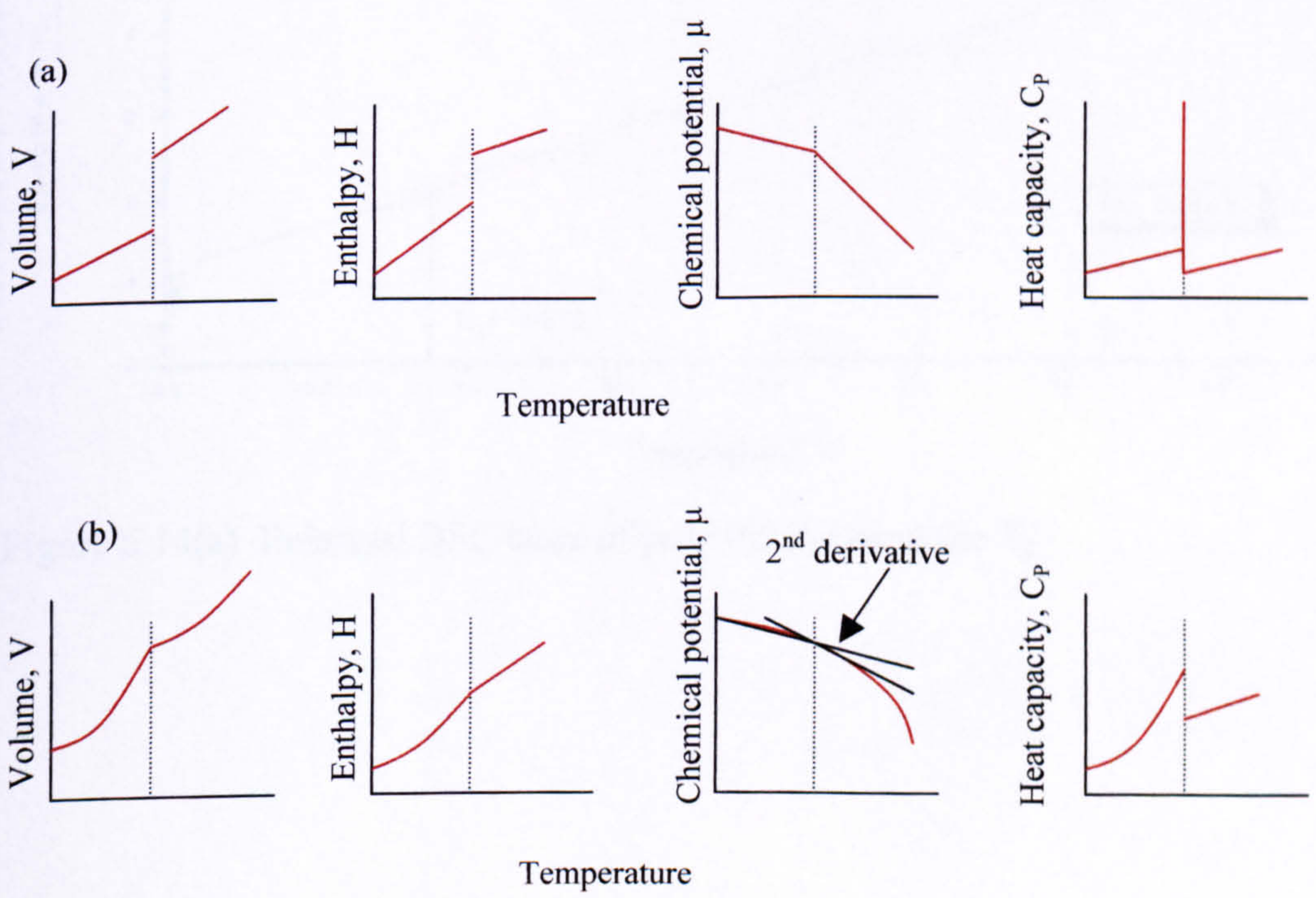

Figures 6.13 (a and b) The changes in thermodynamic properties accompanying (a) first-order and (b) second-order phase transitions

6.5 Polyurethane DSC results

DSC data were obtained for systems containing various compositions of plasticiser in order to understand the effect of plasticiser addition on the electrolyte system. Systems with added salt were also investigated and cross-referenced in order to determine the overall effect of adding the salt to the PU.

It was originally thought that there were two possibilities for ionic conductivity in the electrolyte. Firstly, the co-ordination of the cation to the polyether segments of the PU, and secondly the EC/PC plasticiser providing a liquid-type electrolyte within the PU matrix, i.e. forming a gel electrolyte. Figures 6.14(a-n) show the various DSC traces obtained.

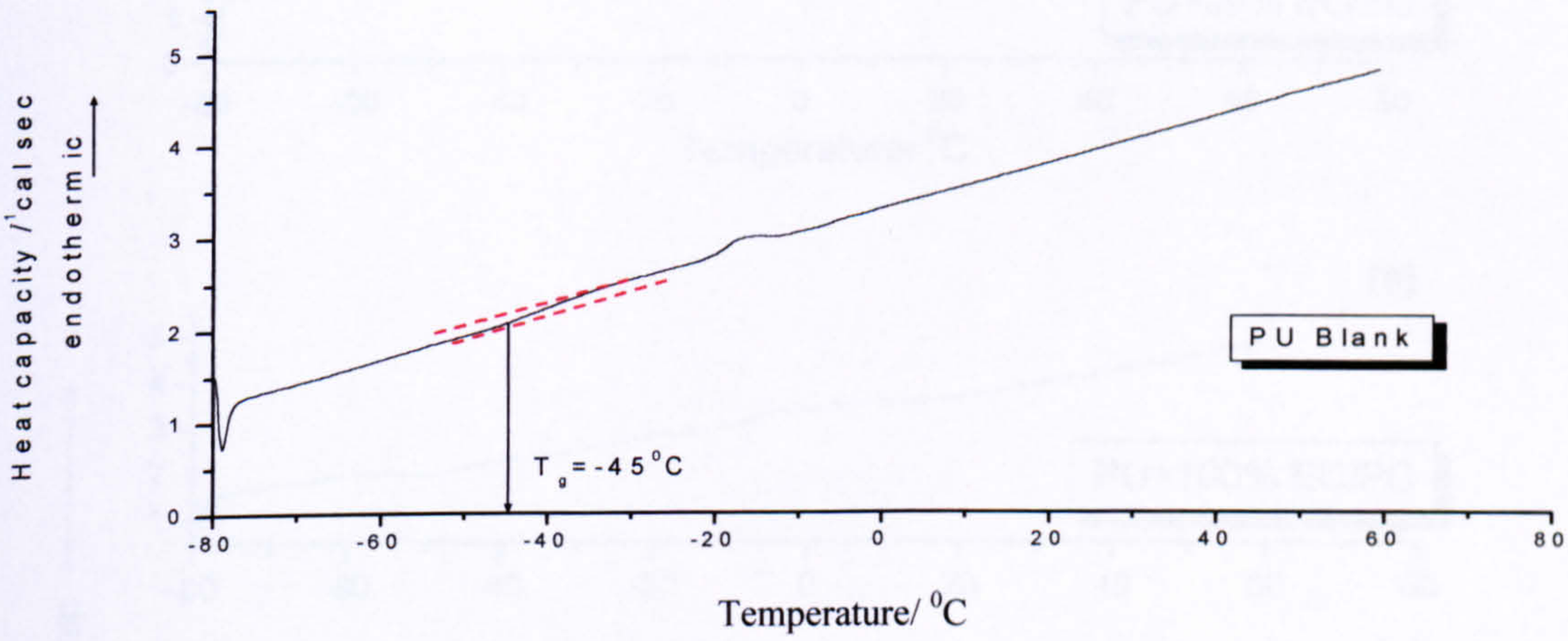

Figure 6.14(a) Enlarged DSC trace of pure PU showing the T_g

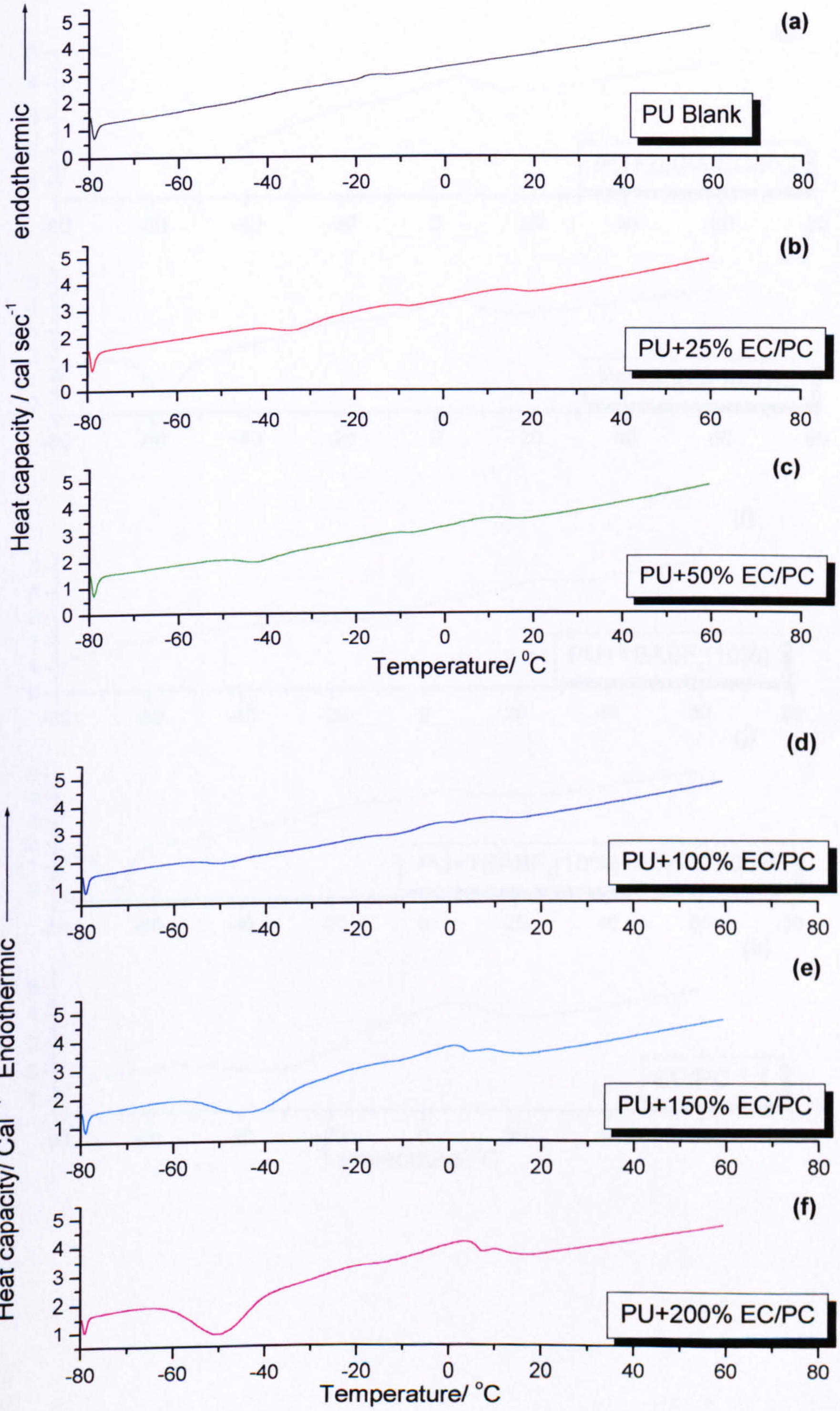
(a)
PU Blank
(b)
PU+25% EC/PC
(c)
PU+50% EC/PC
(d)
PU+100% EC/PC
(e)
PU+150% EC/PC
(f)
PU+200% EC/PC
Heat capacity / cal sec-1
Endothermic
Heat capacity/ Cal -1 Endothermic
Temperature/ °C
5
4
3
2
1
0
-80
-60
-40
-20
0
20
40
60
80

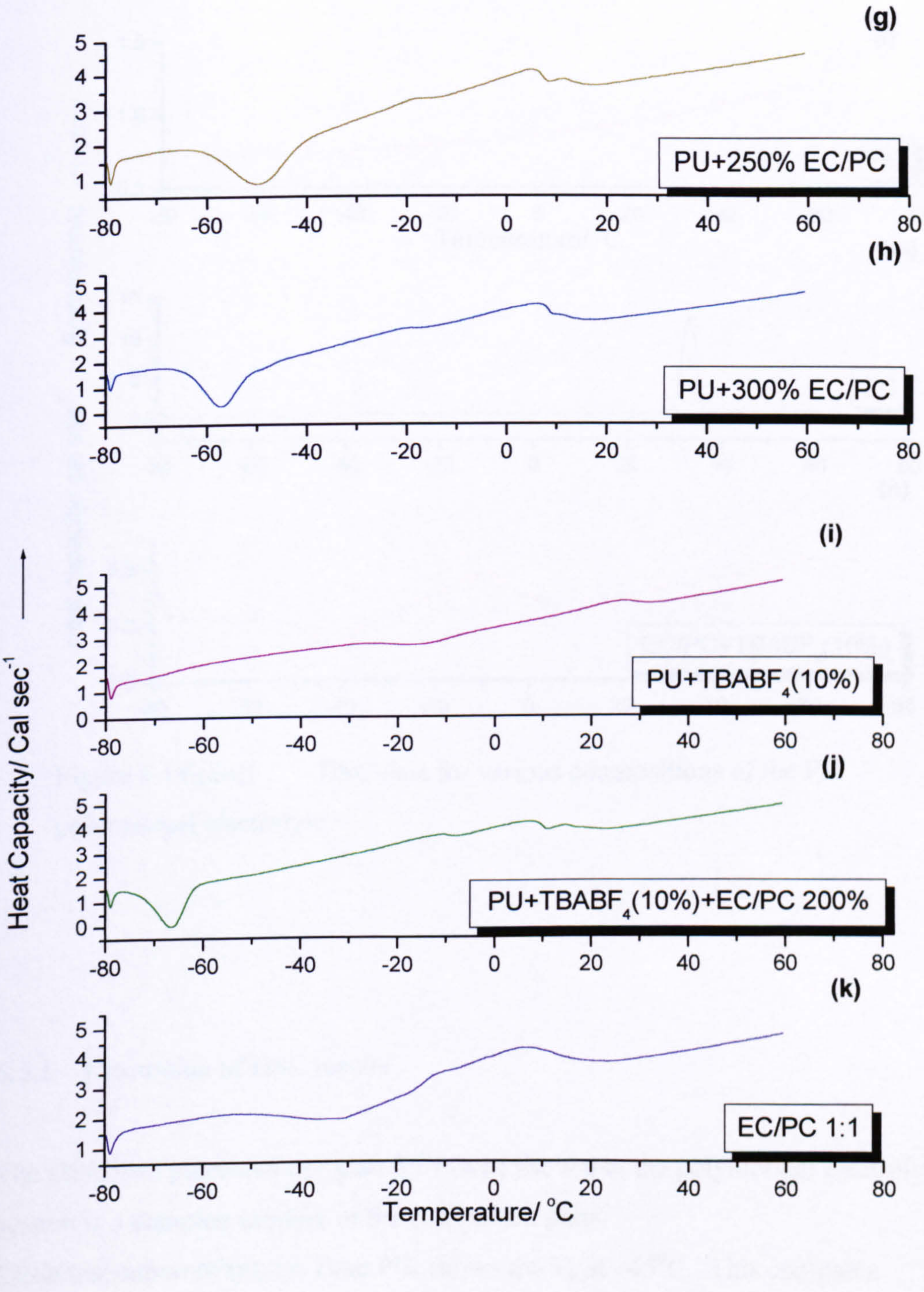
(g)
PU+250% EC/PC
(h)
PU+300% EC/PC
(i)
PU+TBABF4(10%)
(j)
PU+TBABF4(10%)+EC/PC 200%
(k)
EC/PC 1:1
Heat Capacity/ Cal sec-1
Temperature/ °C
-80
-60
-40
-20
0
20
40
60
80
1
2
3
4
5

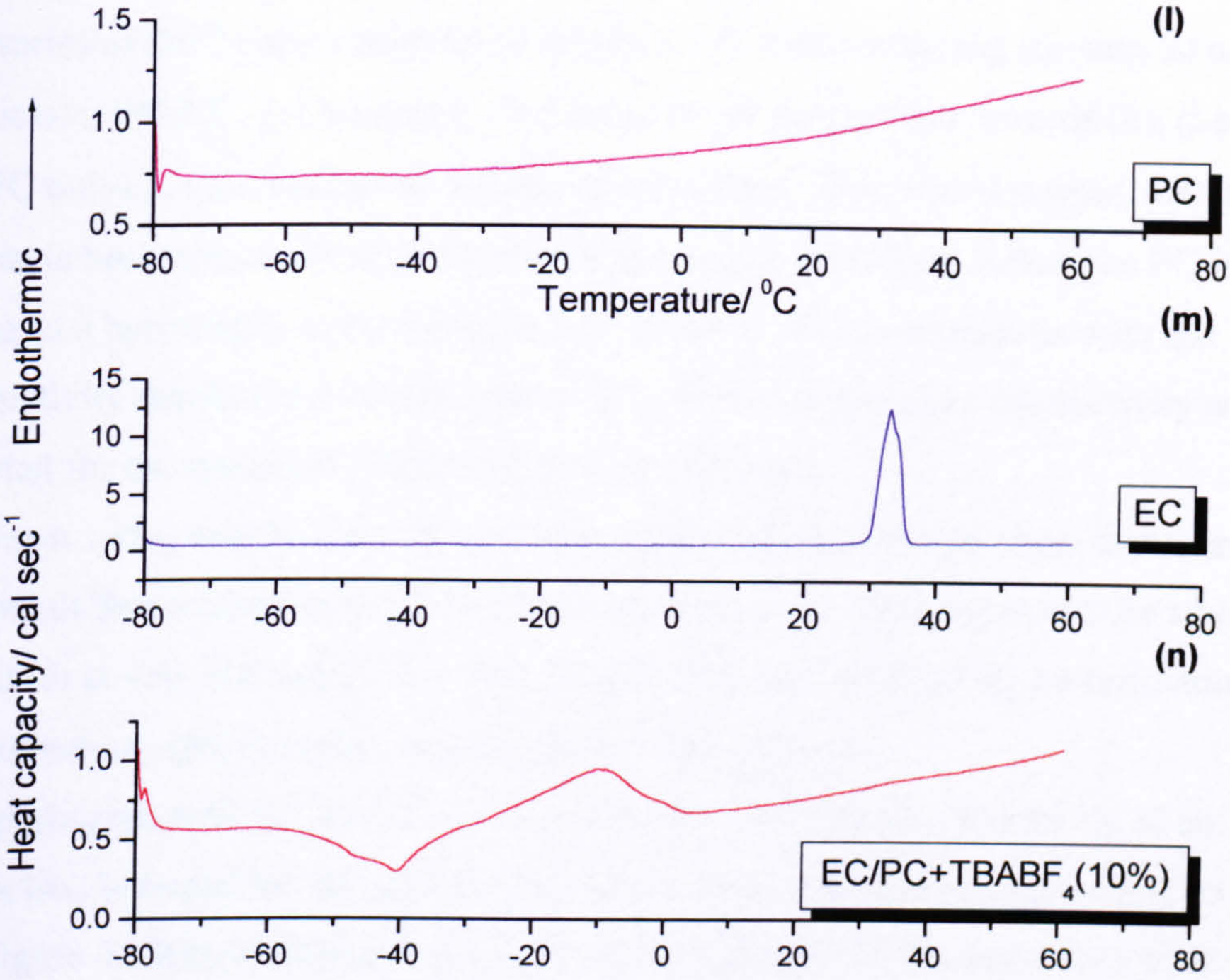

Figure 6.14 (a-n) DSC data for various compositions of the PU polymer/gel electrolyte

6.5.1 Discussion of DSC results

The DSC data presented in figure 6.14 (a-n) show that the polymer/gel electrolyte system is a complex mixture of the component parts.

Close inspection of (a), i.e. Pure PU, shows the T_g at -45^0C. This compares favourably with previous calorimetry results, (t_g of -45^0C) [9]. With some thermal event occurring at -15^0C.

Evidence from (l), (m) and (k), i.e., pure PC, pure EC and a 1:1 mixture of PC/EC, shows there is some interaction between the PC and EC components of the mixture, since the sharp melting peak of EC at 33^0C is not apparent in (k). The addition of PC

to EC may have the effect of lowering the melting point of EC and broadening of the melting peak, as shown in (k) between 0 and 10 ^{0}C.

The series of DSC curves from (a) to (h) show PU with increasing amounts of added plasticiser, (PC/EC, 1:1 mixture). The shape of the curves tend towards (k), (i.e., EC/PC only), on increasing the amount of plasticiser. This would suggest that the system is becoming more and more like a purely gel electrolyte, where the PU is acting as a host matrix to the liquid PC/EC mixture. This is consistent with the conductivity results described in chapter 6.3, where the optimum conductivity was reported for the system PU+200% plasticiser /10% salt.

Figures 6.14 (a) and (i), pure PU and PU+ added salt respectively show that there is a marked difference between the two thermogramms, e.g., there appears to be a broad transition at –30, -18 and 25 ^{0}C. This suggests the possibility of the co-ordination of the salt cation with the ether oxygens of the PU backbone.

Comparing (n) with (k), EC/PC + salt and EC/PC, suggests the possibility of an interaction between the salt and the plasticiser. The small transition at –15^{0}C on pure PU, figure 6.14(a), disappears on addition of salt, figure 6.14(i), possibly a shift in melting peak due to cationic co-ordination with the PU ether oxygens forming transient cross links which would increase the T_M of that particular phase.

Figures 6.14 (f) and (j), PU+200% EC/PC and PU+200% EC/PC + 10% $LiClO_4$ respectively, show a 15 ^{0} shift of an exotherm peak from –50^{0}C to –65^{0}C, again providing evidence of the possibility for salt-polymer and salt- plasticiser interactions.

6.5.2 Conclusions of DSC data

The PU electrolyte interacts with the $LiClO_4$ in a manner similar to that of Li^+ and the ether oxygens of PEO, i.e. a traditional polymer electrolyte system. On addition of a low molecular weight plasticiser, (EC/PC), the salt interacts to a greater degree with the plasticiser mixture. Until at approximately 200% added plasticiser a gel electrolyte was obtained. This is corroborated by conductivity measurements indicating that 200% added plasticiser was the optimum conductivity.

7 Supercapacitors with Carbon electrodes

7.1 Introduction

Activated carbon is a high surface area and conducting material. Supercapacitor electrodes must posses these two properties in order to produce high power-density capacitors as described in chapter 2.1. There have been numerous reports in the literature on activated carbon powders as supercapacitor and secondary battery electrodes [1-4]. This chapter describes the investigation of supercapacitor devices utilising a high surface area woven carbon fabric as supplied by Calgon Carbon corporation. Calgon are traditionally a company dealing in high surface area carbons for various filtration purposes.

Activated carbon cloth (ACC) is a family of activated carbons in the form of a cloth. These products are fundamentally unique, relative to traditional forms of activated carbon, and to other filtration media that incorporate small particles of activated carbon. Compared to other forms of activated carbon, ACC products are both similar and dramatically different. They are similar in that Calgon carbon's ACC products are 100% activated carbon. ACC is pure activated carbon, which has the same high capacity as does high quality granular or powdered activated carbon. ACC will perform the same function-purification, separation or concentration of liquids or gasses. The ability of this form of ACC to readily adsorb gasses and liquids is not necessarily an advantageous property in the field of supercapacitor electrodes. Since adsorbed atmospheric gasses and moisture will tend to block the active sites and hence reduce the effective surface area of the ACC, it is desirable to minimise the cloths exposure to the atmosphere. A further complication is that adsorbed substances may act as poisons and lead to unwanted Faradaic processes during operation of the supercapacitor. It was for this reason that the ACC was stored in a vacuum desiccator and was heated to 100^0C under vacuum before use.

The carbon fibre is approximately 50 μM in diameter.

Because of the continuous and graphitic nature of the threads, ACC is electrically conductive. The woven and knitted forms allow effective and rapid electrical regeneration. The electrical conductivity of this activated carbon combined with its thin and flexible form makes it useful in electrical devices such as supercapacitors.

The continuous threads within the cloth also result in a superior thermal conductivity compared to carbon felt or granular carbon systems. It follows that ignition and exotherm concerns are essentially eliminated.

7.2 Liquid electrolytes

The main purpose of this study was to characterise a PU polymer/gel electrolyte with various electrode systems. It was thought necessary, however, to use a low molecular weight (liquid) analogue for comparison with the solid polymer/gel electrolyte. This is often done in order to determine whether there are any interfacial or contact problems, which are associated with solid electrolytes.
The electrolyte solvent investigated as low molecular weight analogue was Propylene carbonate PC. Two different salts were used, namely lithium perchlorate ($LiClO_4$) and tetraethyltetrafluoroborate ($TEABF_4$).

7.2.1 Experimental

$LiClO_4$ and $TEABF_4$ (99.99%; supplied by Aldrich), with PC (analytical grade, supplied by Aldrich) were opened under an argon atmosphere inside a glove box to minimise exposure to atmospheric moisture. Li^+ and TEA^+ on exposure to water form hydroxides and become surrounded by hydrated sheaths, thus in effect increasing the size of the cation, reducing its mobility and hence reducing the ionic conductivity of the electrolyte.
Two supporting electrolyte solutions were prepared.

(i) $LiClO_4$/PC, 0.25M
(ii) $TEABF_4$/PC, 0.25M

Figure 7.1 below shows the liquid supercapacitor test cell.

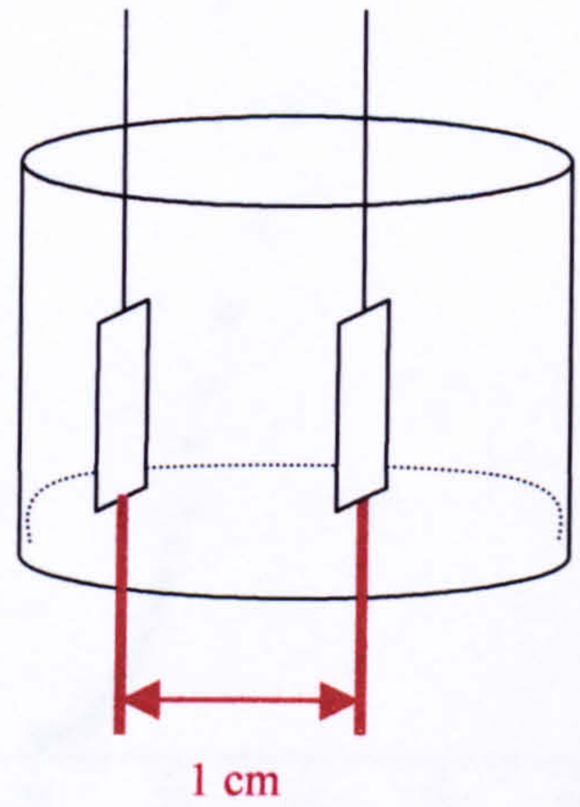

Figure 7.1 A schematic representation of the liquid supercapacitor test cell

The geometric surface area of each electrode was kept constant at 0.25 cm^2. The activated carbon cloth (ACC) was immobilised onto a piece of glass sheet using silver dag (Radio Spares). The graphite paper (GP) was mechanically strong enough to be free standing and was directly connected to the crocodile clips.

Figures 7.2 to 7.6 below show a.c. impedance spectra and cyclic voltammograms for the systems investigated.

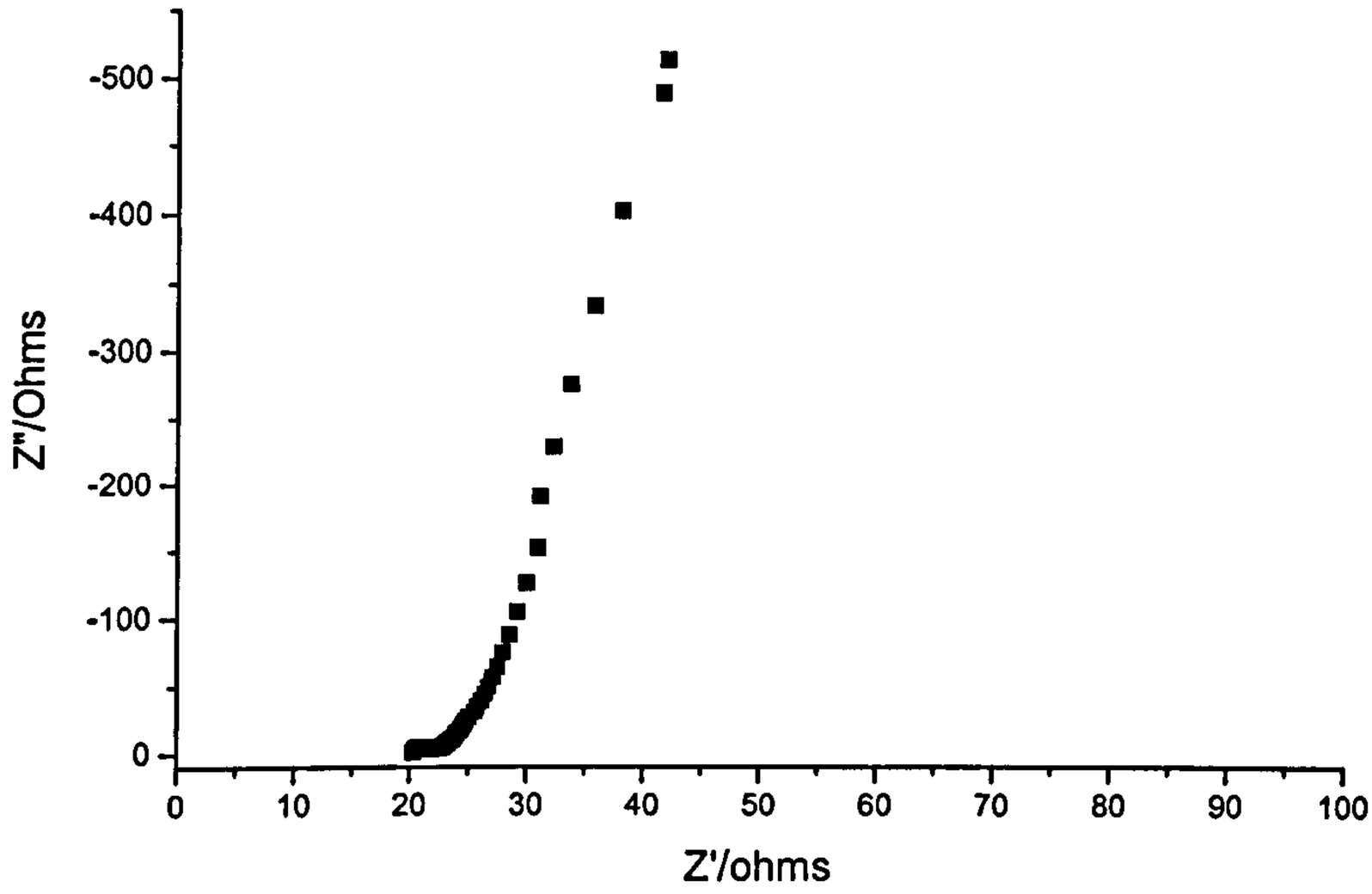

Figure 7.2 Complex plane impedance plot of ACC/PC/$LiClO_4$ (0.25M). Frequency range 65 kHz to 1 mHz.

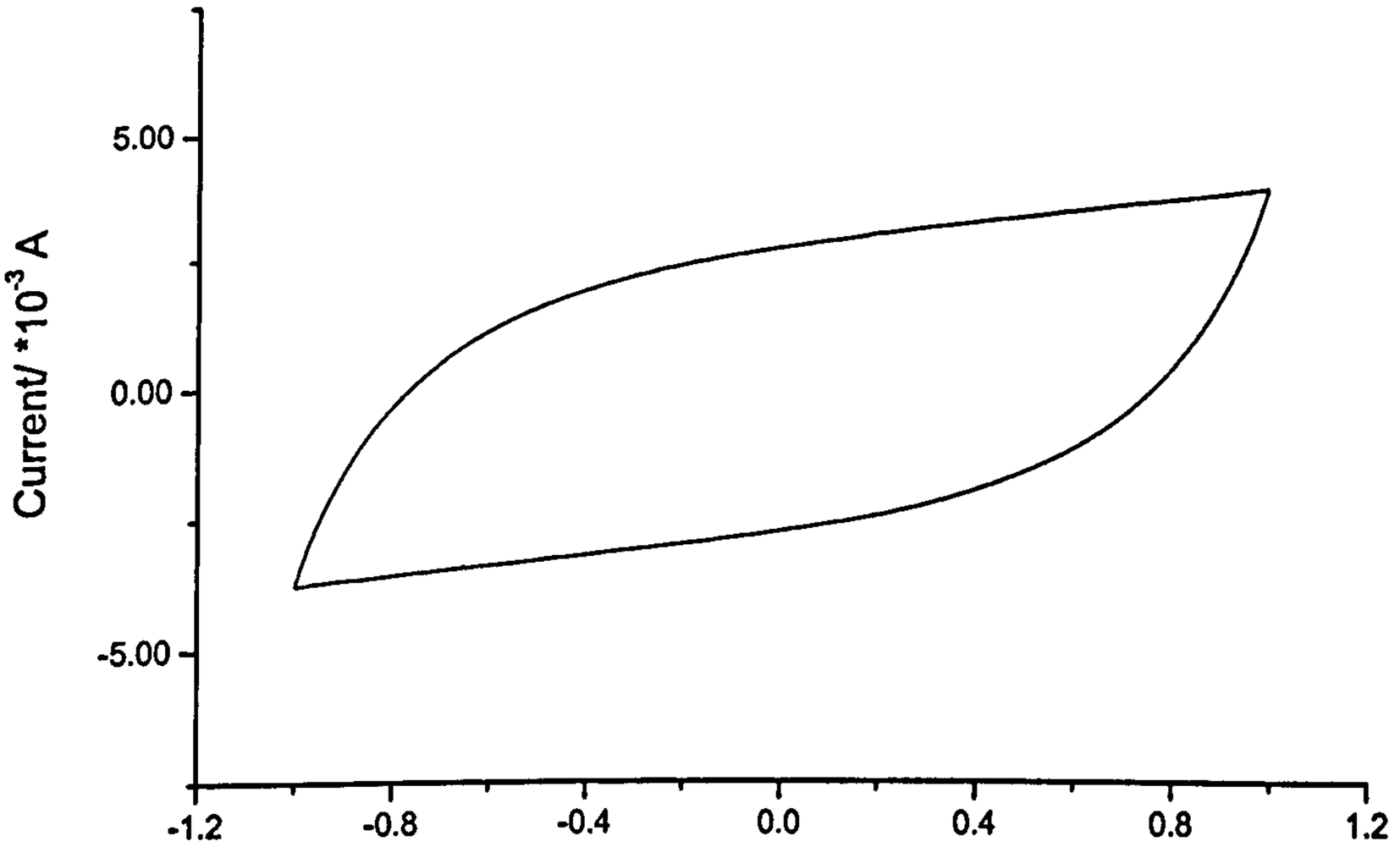

Figure 7.3 Cyclic voltammogram of ACC/PC/$LiClO_4$ (0.25M). Sweep rate 1 mV s^{-1}. ± 1V vs a floating potential.

From figures 7.2 and 7.3 the capacitance was calculated using equations 5.14 and 5.4 for impedance and CV respectively. A capacitance of 3.2 F cm^{-2} (from the impedance plot) and 3.0 F cm^{-2} (from the CV) were obtained. This related to a specific capacitance of 160 F g^{-1} and 150 F g^{-1} from impedance and CV data respectively.

Graphite paper, GP, (supplied by FMI composites) was used as an electrode material for comparison with the ACC to demonstrate the effect the high surface area of ACC has on the electrical parameters of a supercapacitor device.

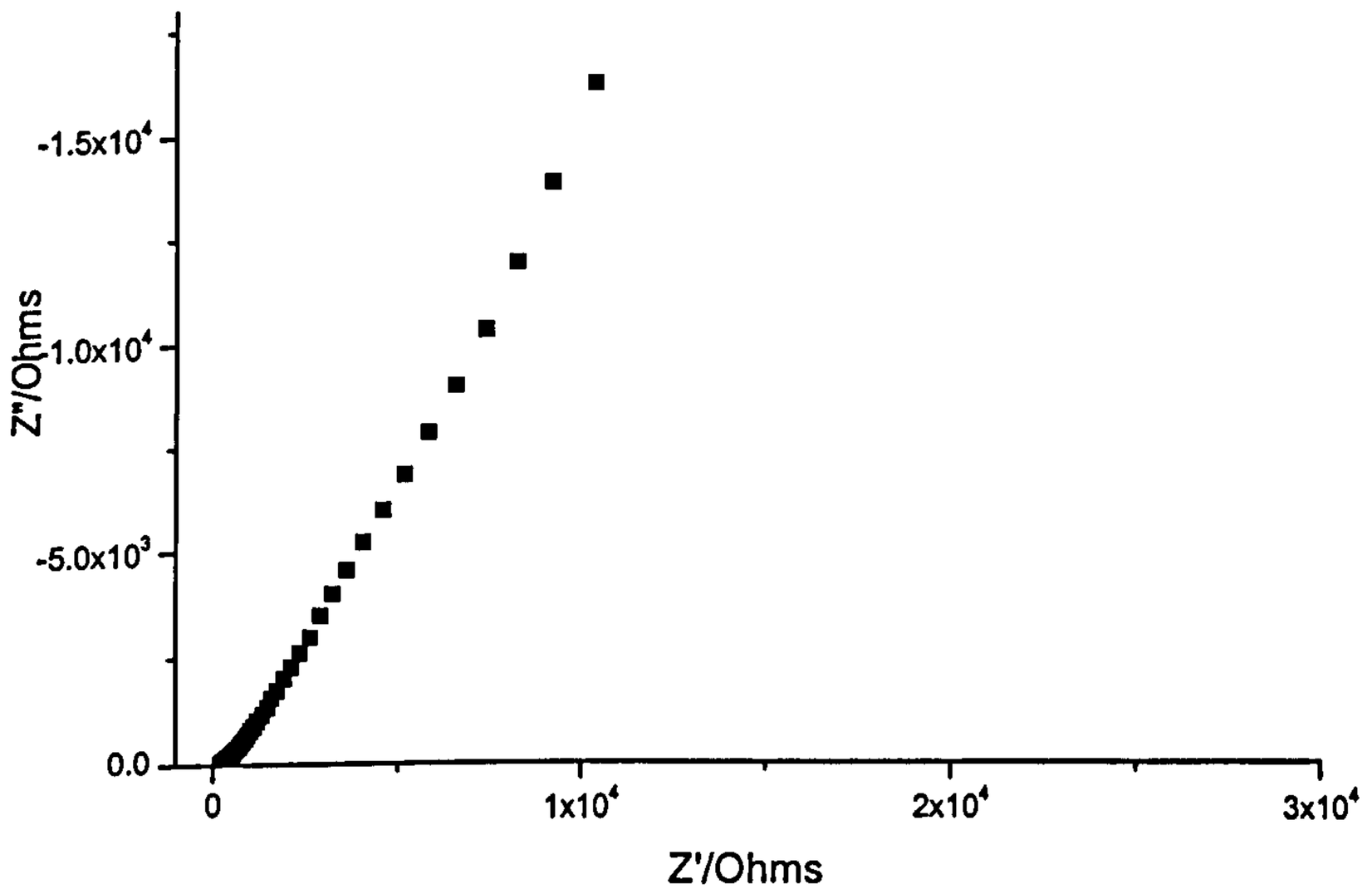

Figure 7.4 Complex plane impedance plot of GP/PC/$LiClO_4$ (0.25M). Frequency range 65 kHz to 1 mHz.

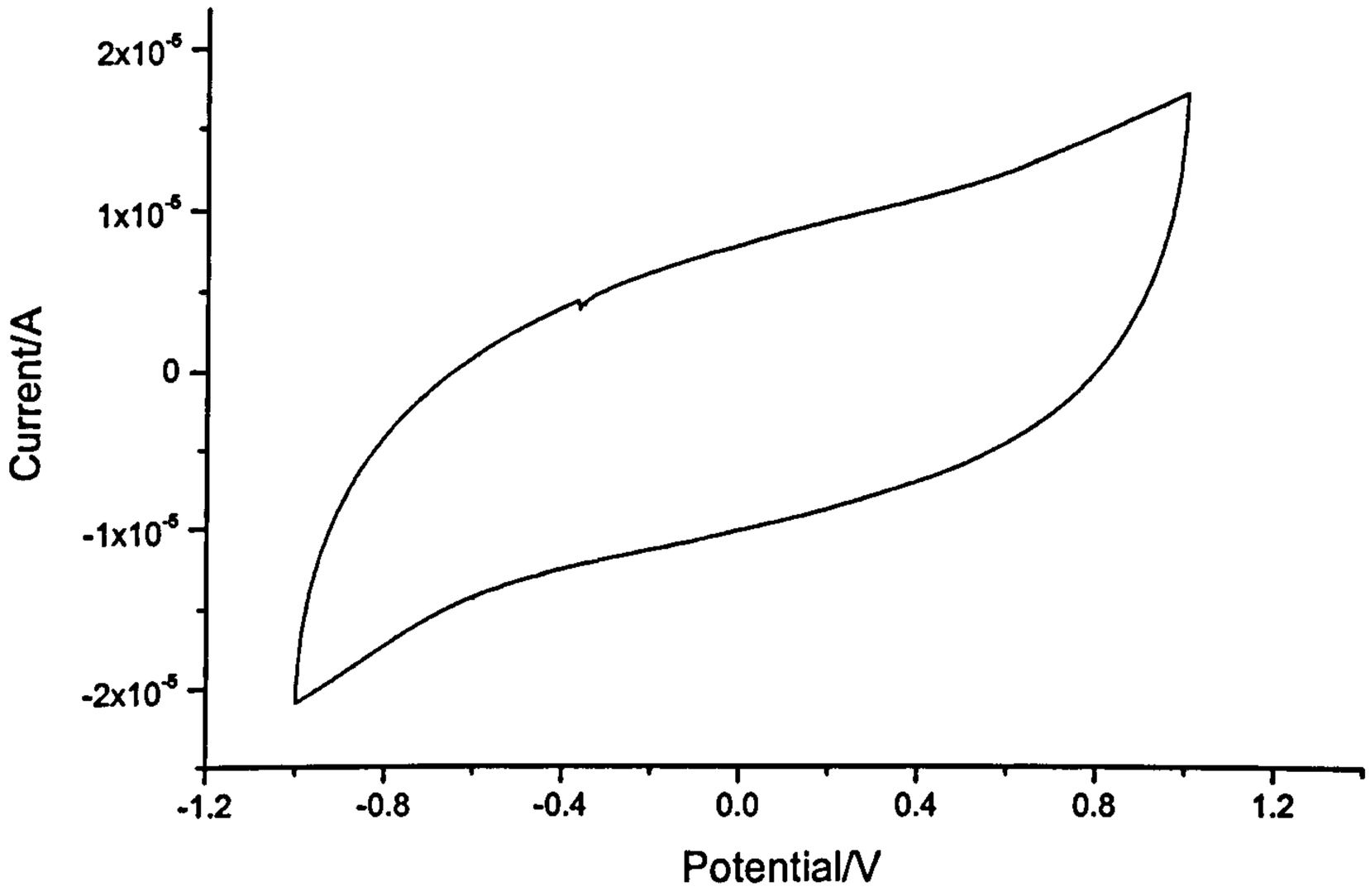

Figure 7.5 Cyclic voltammogram of GP/PC/$LiClO_4$ (0.25M). Sweep rate 1 mV s^{-1}. ± 1 V vs a floating potential.

From figures 7.4 and 7.5 capacitances of 8 and 5 mF cm^{-2} were calculated from the impedance and CV spectra respectively. The mass of the GP electrode was 0.026g, therefore a specific capacitance of 0.19 and 0.30 F g^{-1} was obtained. This is a difference of three orders of magnitude compared with the ACC electrode devices, clearly showing the effect of high surface area on the capacity of the device. Further evidence can be seen in figures 7.6 and 7.7 below which show the complex plane impedance plot and the cyclic voltammogram of GP/$TEABF_4$/PC (0.25M). This system gave capacitances of 0.05 F cm^{-2} and 0.08 F cm^{-2} calculated from impedance and CV data respectively. This related to specific capacitances of 1.92 F g^{-1} and 3.10 F g^{-1}.

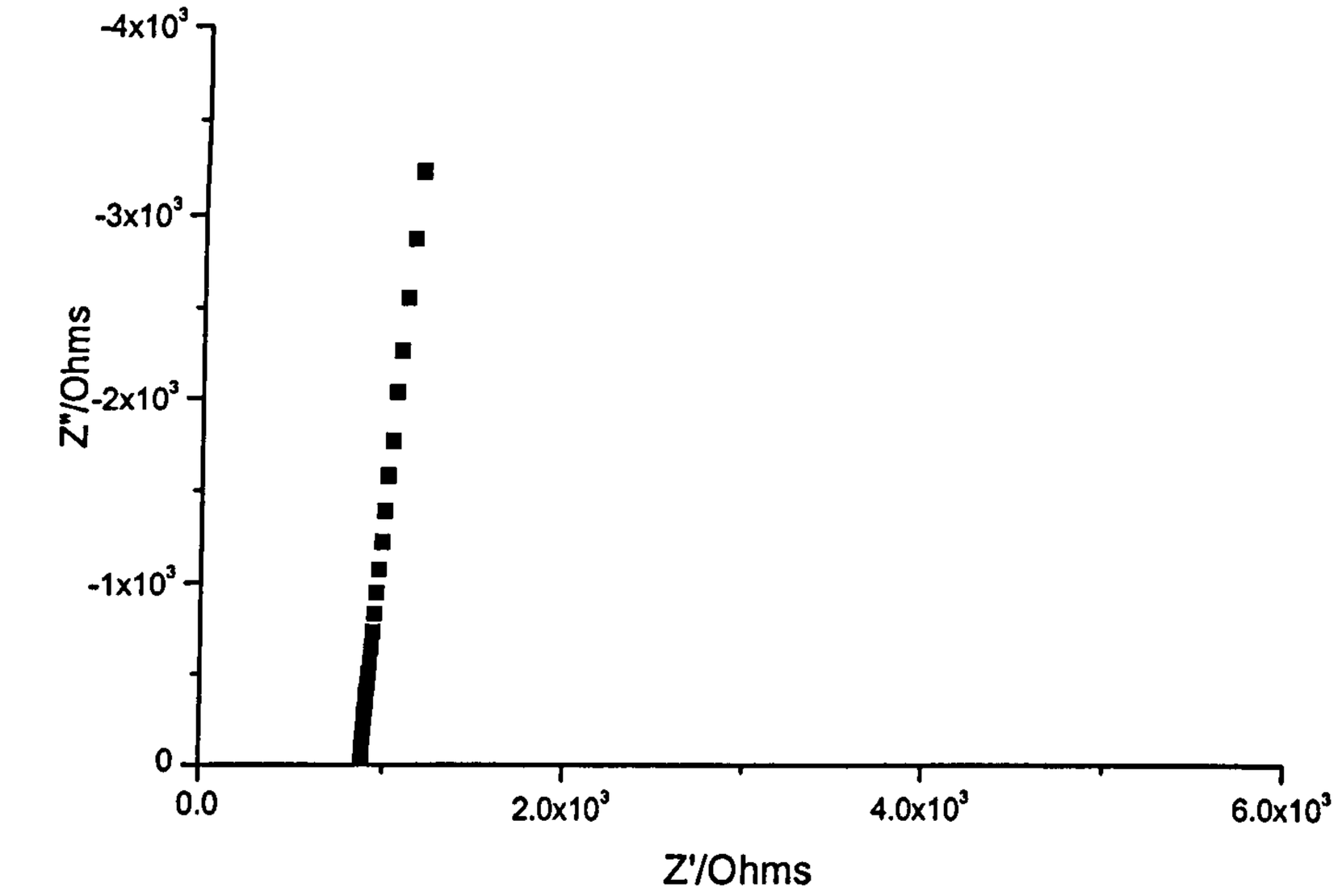

Figure 7.6 Complex plane impedance plot of GP/PC/$TEABF_4$ (0.25M). Frequency range 65 kHz to 1 mHz

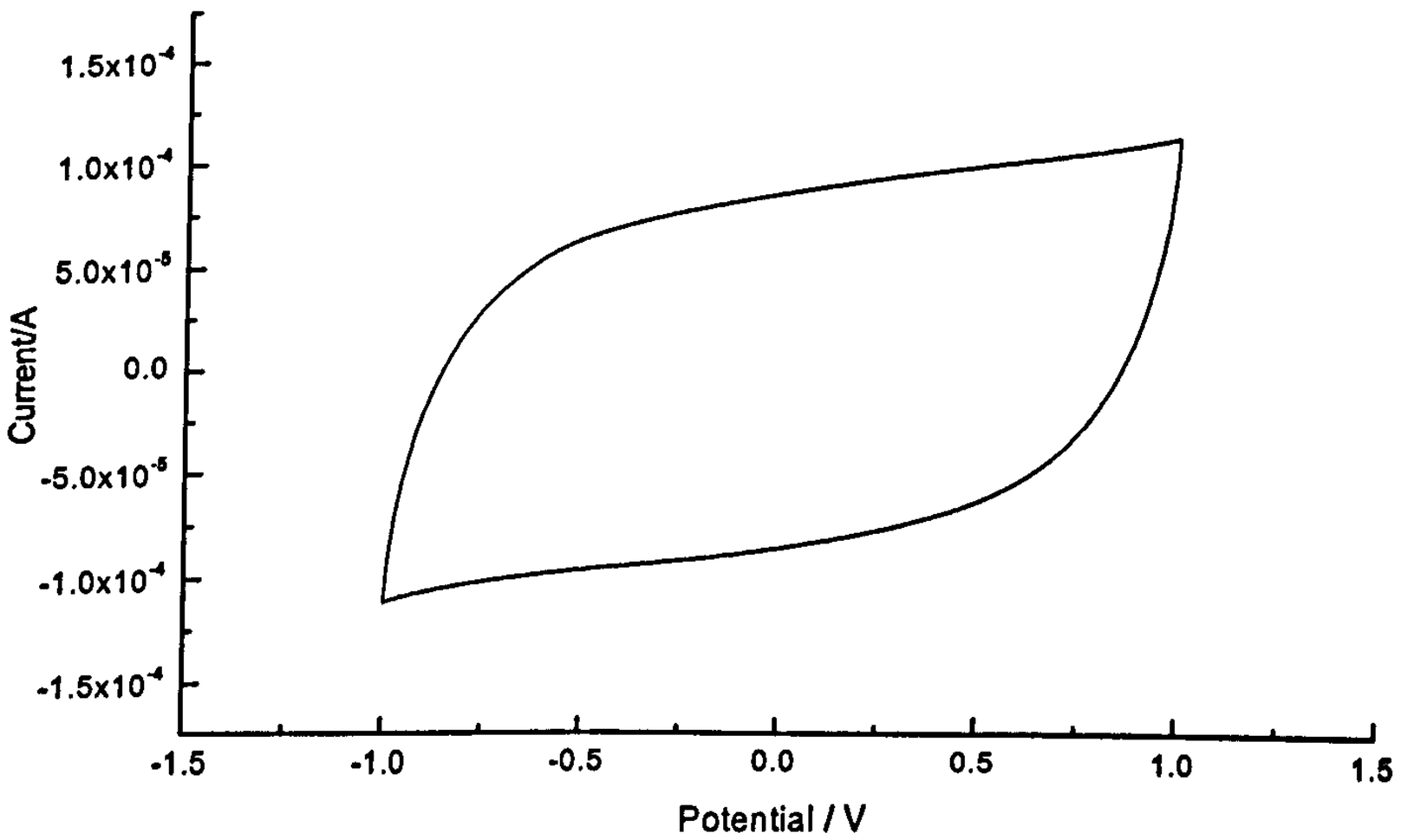

Figure 7.7 Cyclic voltammogram of GP/PC/$TEABF_4$ (0.25M). Sweep rate 1 mV s^{-1}. ± 1V vs a floating potential.

7.3 Solid / gel electrolytes

Supercapacitor cells were prepared using ACC electrodes with a PU gel electrolyte of composition PU/$LiClO_4$ (10%)/PC (200%)/EC (200%). The a.c. impedance characteristics and cyclic voltammetry were obtained using a Solatron 1260 FRA coupled with a 1286 electrochemical interface and a Windsor Scientific PGStat20 potentiostat respectively.

7.3.1 Experimental using the polyurethane gel electrolyte

For the solid state cells a two-electrode system was employed, hence the potential is versus a floating reference potential. It was first necessary to determine a stable potential window for CV analysis. The potential window was set between ± 1.5 V. It can be seen from figure 7.8 that a peak appears after +1 V, therefore the window was shortened to ± 1 V. Figure 7.8 below shows a CV demonstrating the stable working potential for this cell. Between –1 and +1 V the response is close to the ideal rectangular response for purely capacitive behaviour.

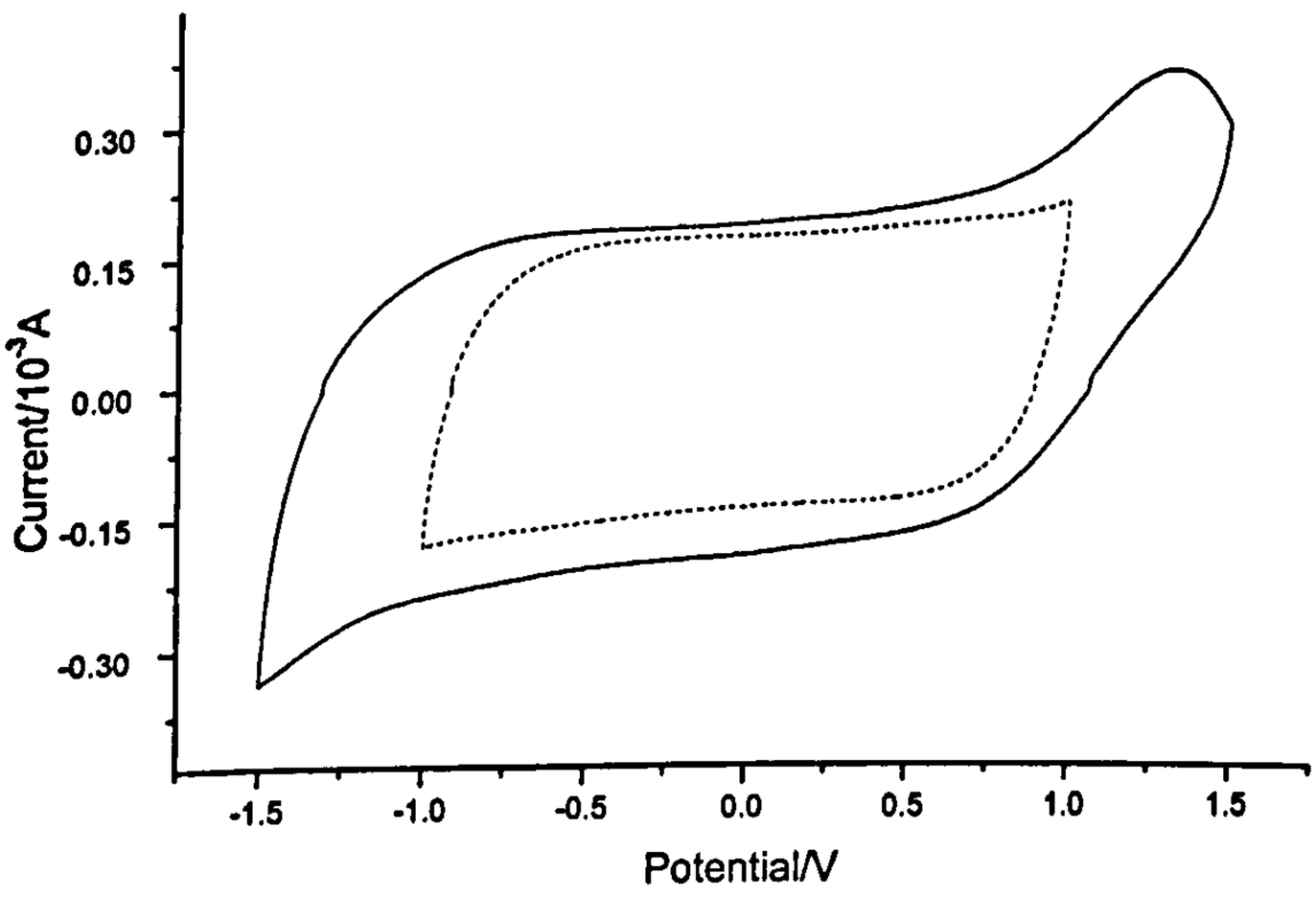

Figure 7.8 Cyclic voltammogram of the supercapacitor cell ACC/PU/$LiClO_4$/PC/EC, showing the stable potential window. Sweep rate 1 mV s^{-1}. ± 1.5 V vs a floating potential.

The complex plane impedance response and the cyclic voltammogram of this cell are shown below in figure 7.9 (a) and (b) below.

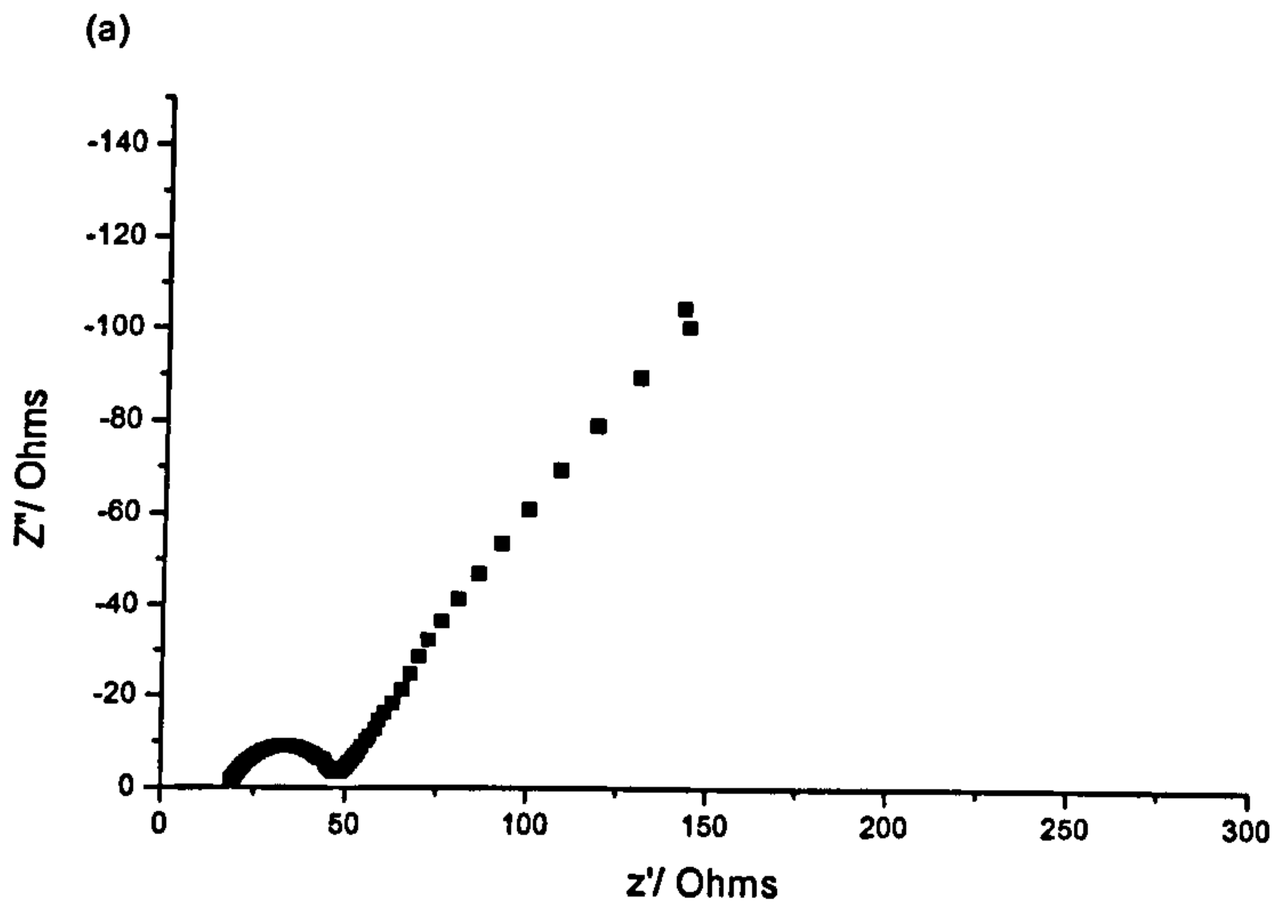

Figure 7.9 (a) and (b) Complex plane and CV of ACC/PU/$LiClO_4$/EC/PC supercapacitor. Frequency range of impedance trace was 65 kHz to 10 mHz, potential window of CV was ± 1V vs a floating potential.

The values for capacitance obtained for these two different experimental approaches compare favourably.

The capacitance calculated from the impedance spectrum using equation 5.14 is 0.15 F cm^{-2}, which translated to 3.75 F g^{-1} of electrolyte material and from the CV using equation 5.4 is 0.17 F cm^{-2} or 4.25 F g^{-1}.

7.3.1.1 Galvanostatic charge-discharge

As discussed earlier in chapter 5.3, the stability of a supercapacitor under constant current charging and discharging is an important parameter. The next section presents the results obtained from galvanostatic charge-discharge experiments performed on the supercapacitor cell of composition ACC/PU/$LiClO_4$/PC/EC.

The supercapacitor cell was cycled at a constant current of 4 mA for 1000 cycles [5]. A typical charge-discharge curve is shown in figure 7.10.

The stable potential window was found to be ± 1 V, using CV, hence the cell was cycled between 0.20 and 1 V. Note the cell was not completely discharged to 0 V since this may damage the cycling ability of the device. Figure 7.10 also shows that the cell is not stable above 1 V, where a discontinuity in dV/dt was observed.

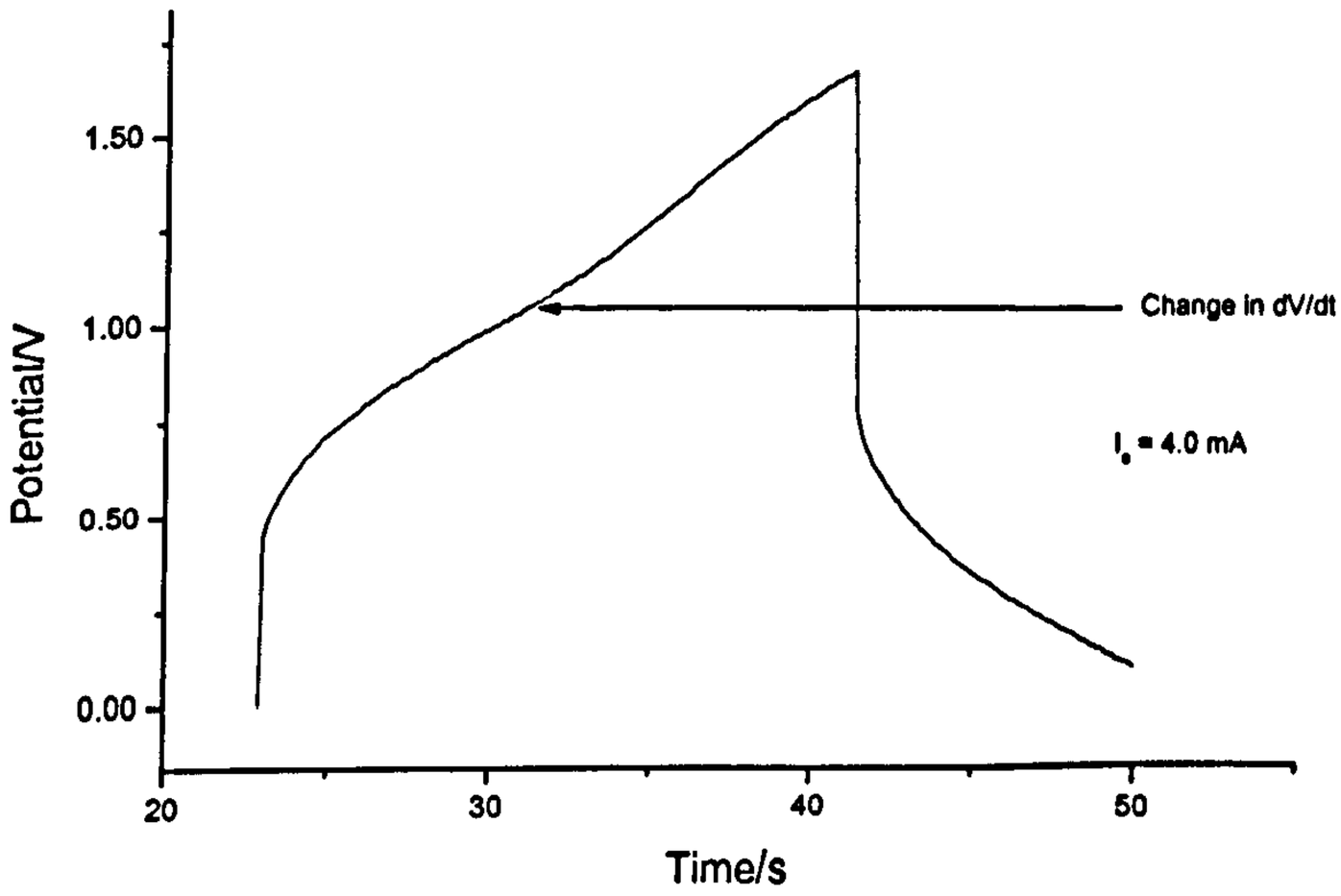

Figure 7.10 A typical charge-discharge curve, showing a discontinuity of dV/dt.

Figures 7.11 (a) to (e) show charge discharge curves for the 10 th, 50 th, 100 th, 500 th, and the 1000 th, cycle.

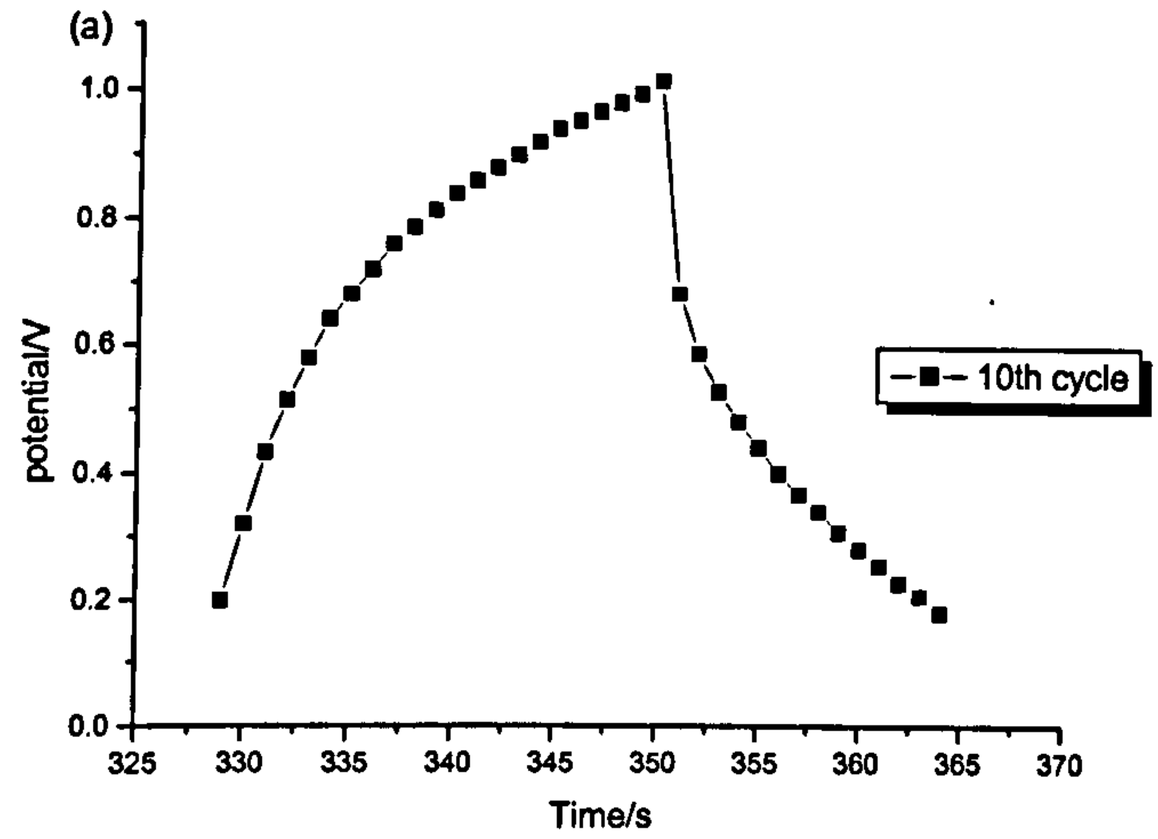

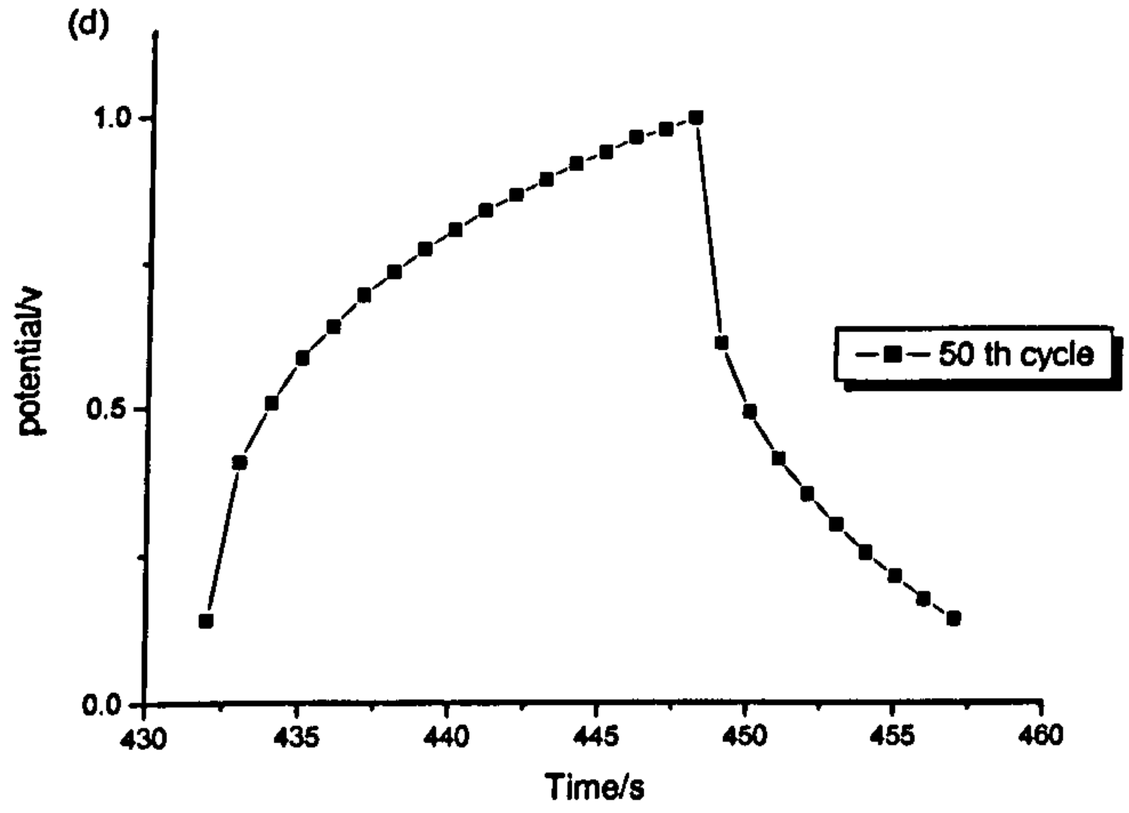

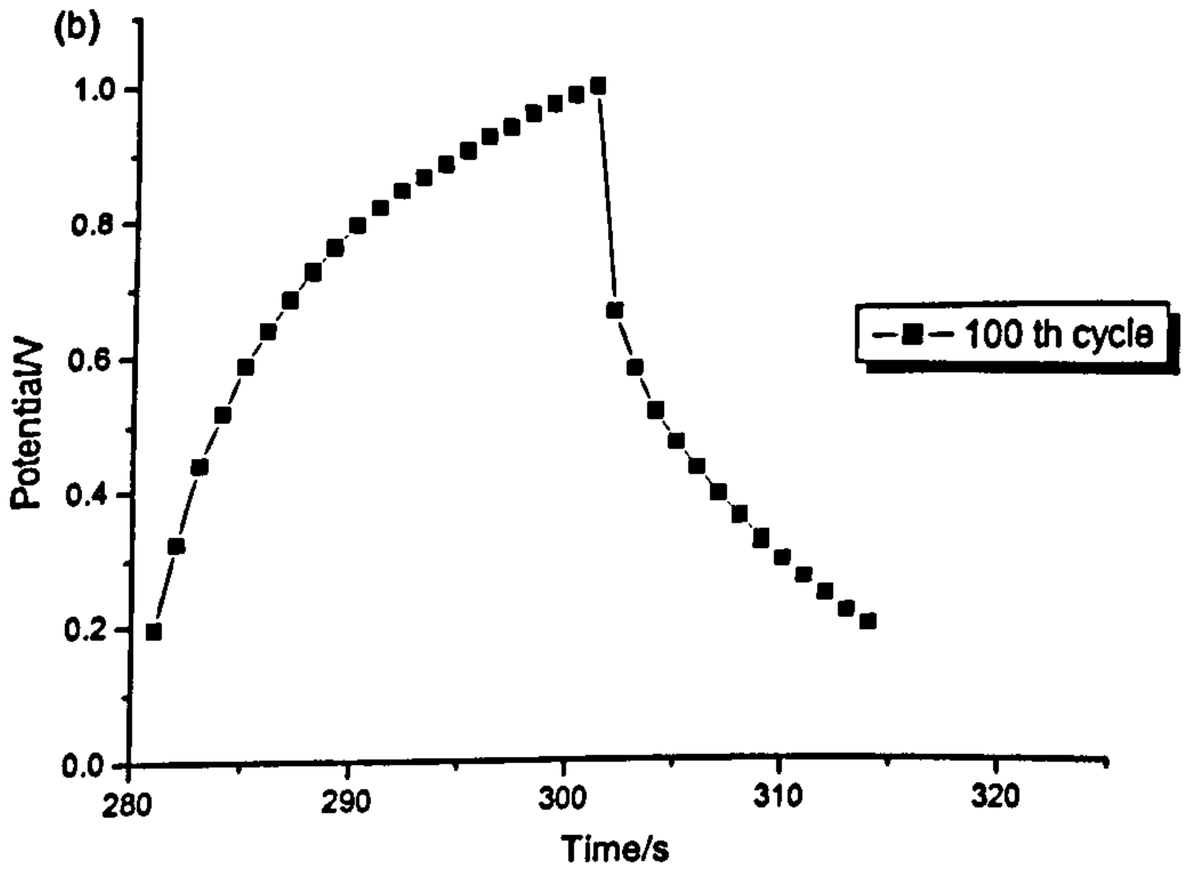

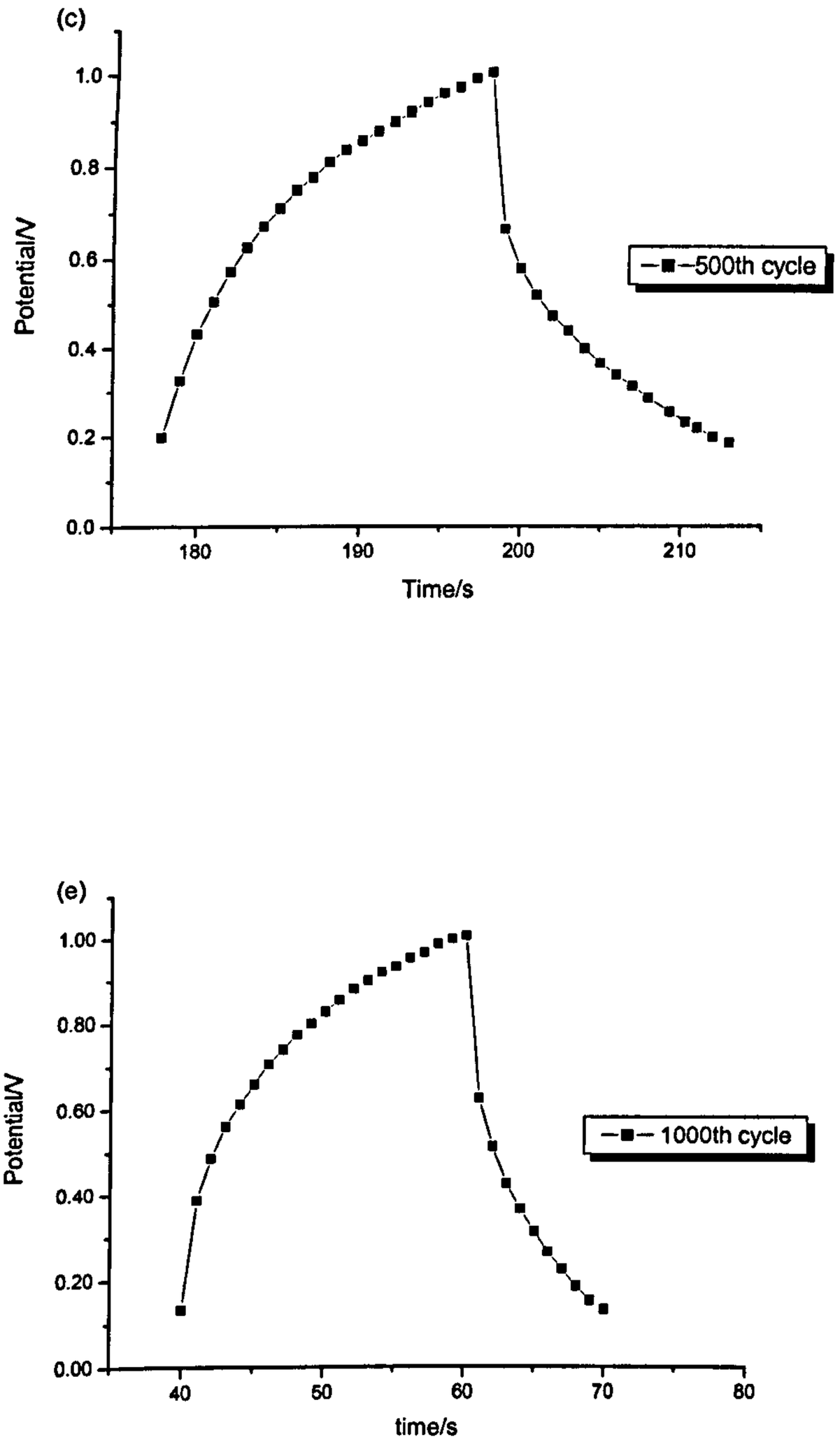

Figure 7.11 (a)-(e) Galvanostatic charge-discharge curves for the 10 th, 50 th, 100 th, 500 th, and the 1000 th, cycle. I=4 mA.

To monitor the capacitor characteristics over this number of charge-discharge cycles the complex plane impedance response and the CV of the cell were taken after completion of the 1000 cycles in order to determine any change in parameters such as R_b and capacitance. Figure 7.12 shows the changes in impedance plot.

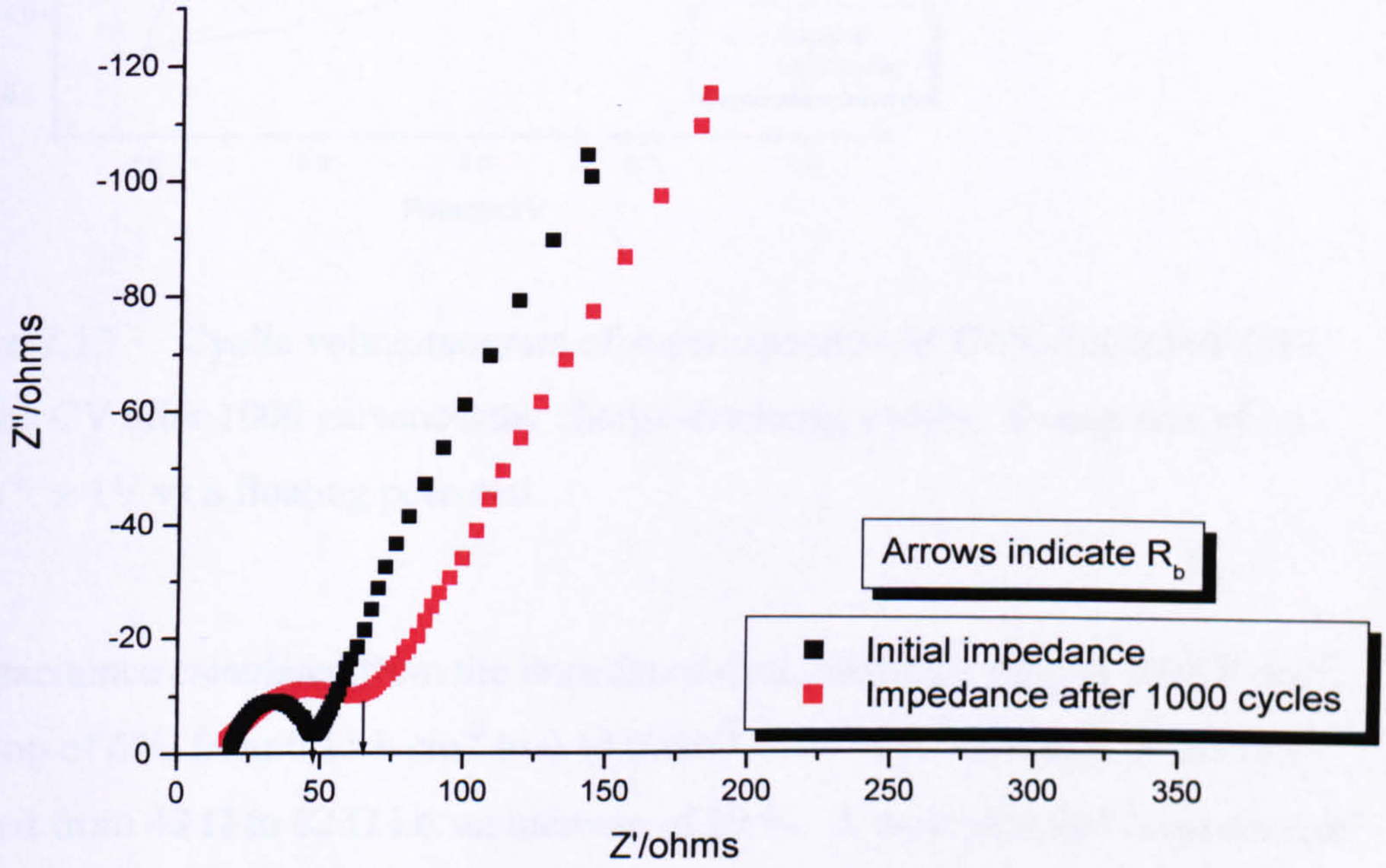

Figure 7.12 Complex plane of the initial impedance of supercapacitor ACC/PU/LiClO4/PC/EC and the impedance after 1000 galvanostatic charge-discharge cycles. Frequency range of 65 kHz to 10 mHz.

From figure 7.12 above, it can be seen that both the capacitance and the bulk resistance have indeed altered on cycling. Further evidence for loss of capacity on cycling was obtained from the cyclic voltammograms, shown below in figure 7.13. After 1000 cycles the response was much less ideal.

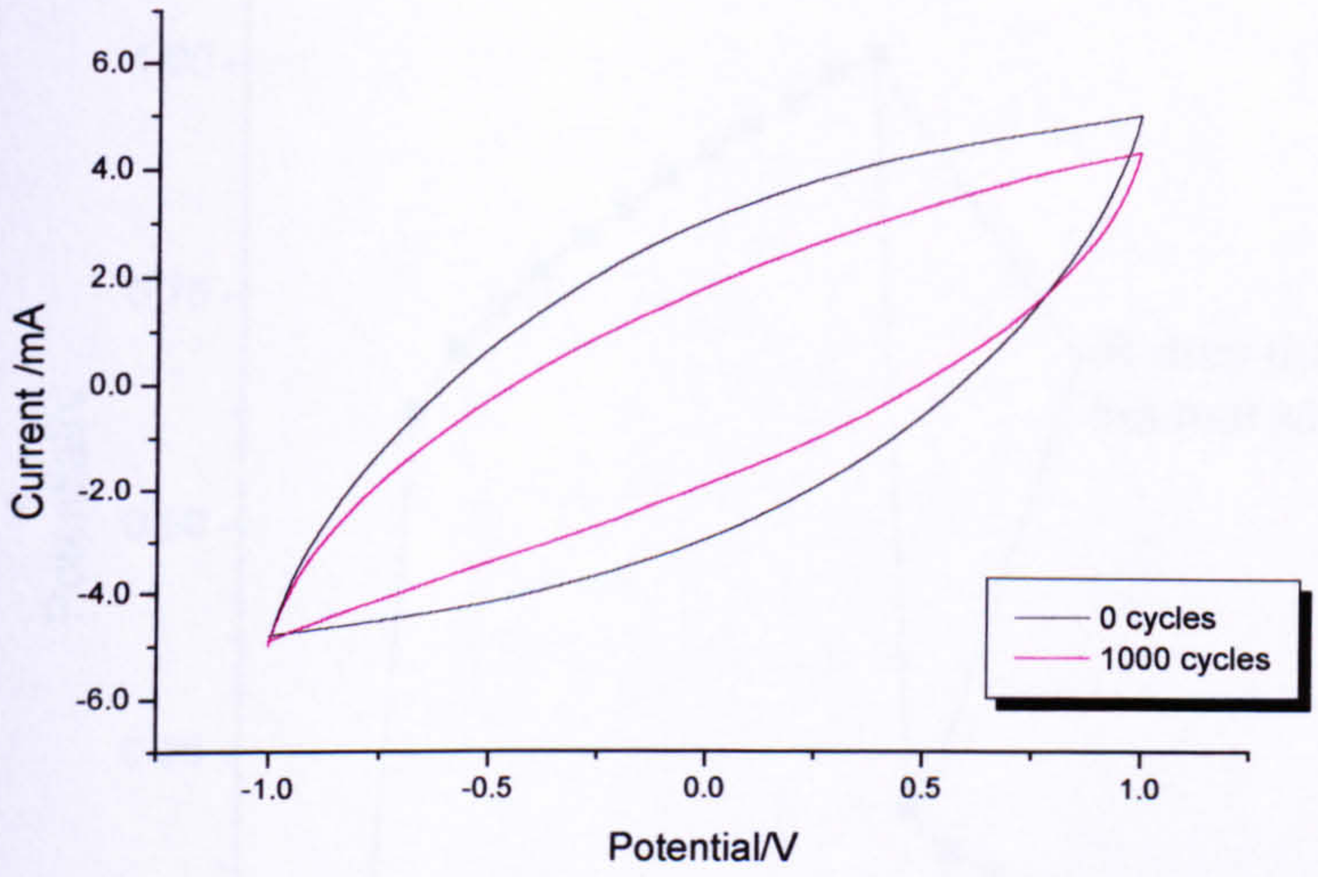

Figure 7.13 Cyclic voltammogram of supercapacitor ACC/PU/LiClO4/PC/EC and the CV after 1000 galvanostatic charge-discharge cycles. Sweep rate of 10 mV s^{-1}. ± 1V vs a floating potential.

The capacitance calculated from the impedance data, showed a drop of 0.01 F cm^{-2}, i.e. a drop of 6%, from 0.15 F cm^{-2} to 0.14 F cm^{-2}. The bulk resistance of the cell increased from 48 Ω to 62 Ω i.e. an increase of 29 %. A more detailed inspection of the charge-discharge curves was carried out in order to rationalise the observation. It can be seen in figure 7.14 below that the initial vertical drop on the discharge curve increases with increasing cycling. This was thought to be due to the iR drop across the cell increasing with increasing series resistance of the cell i.e. an increase in R_b. A standard 15000 μF electrolytic capacitor with various resistors connected in series was galvanostatically cycled. This clearly showed that on increasing the series resistance a corresponding increase in the iR drop was observed on the charge-discharge curve, as shown in figure 7.15 (a) to (f) below.

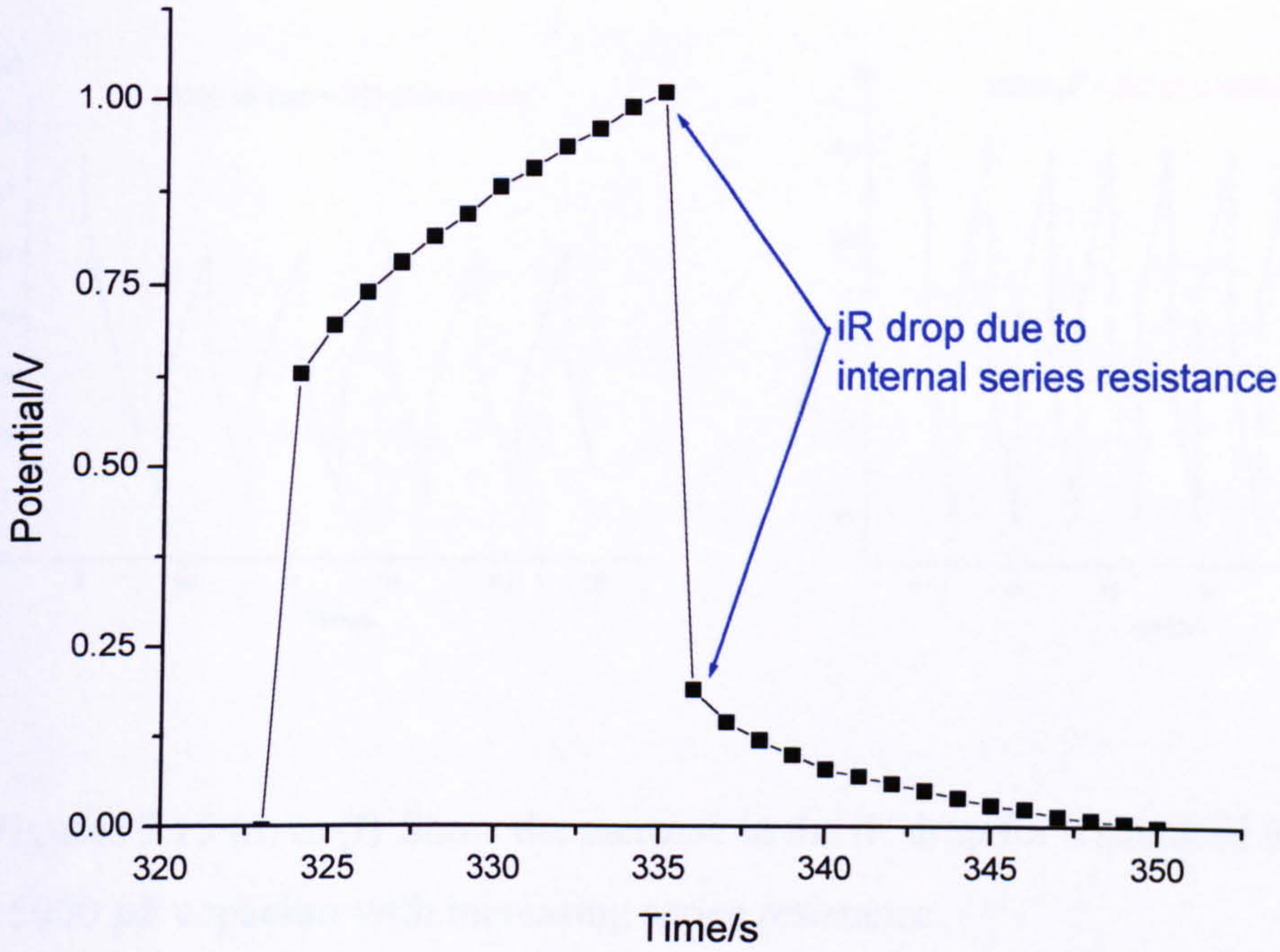

Figure 7.14 shows the iR drop due to the internal series resistance of the cell.

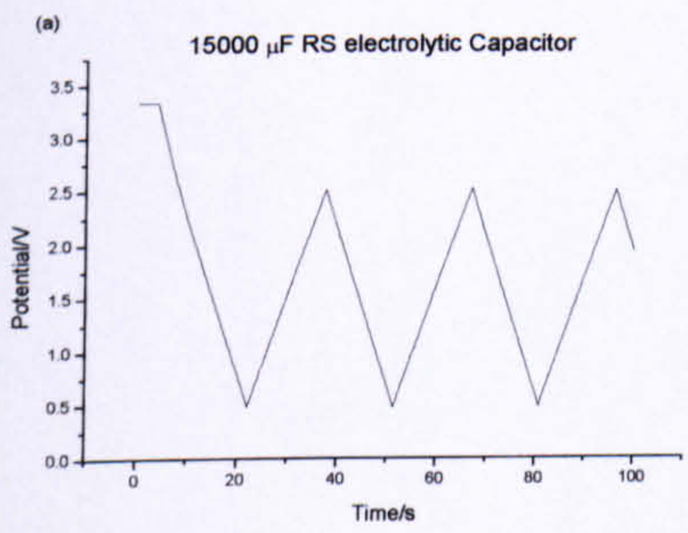

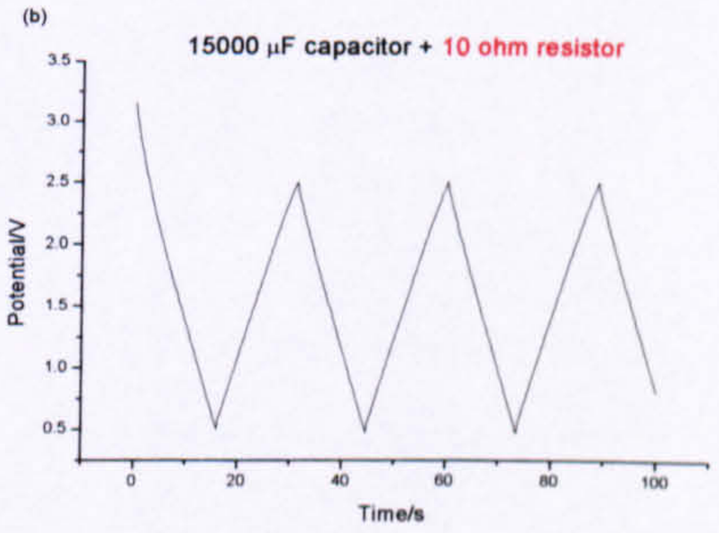

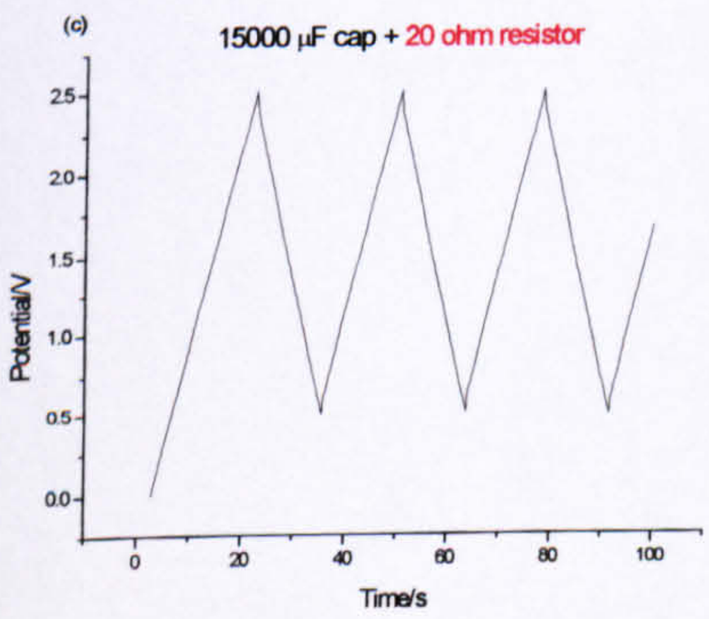

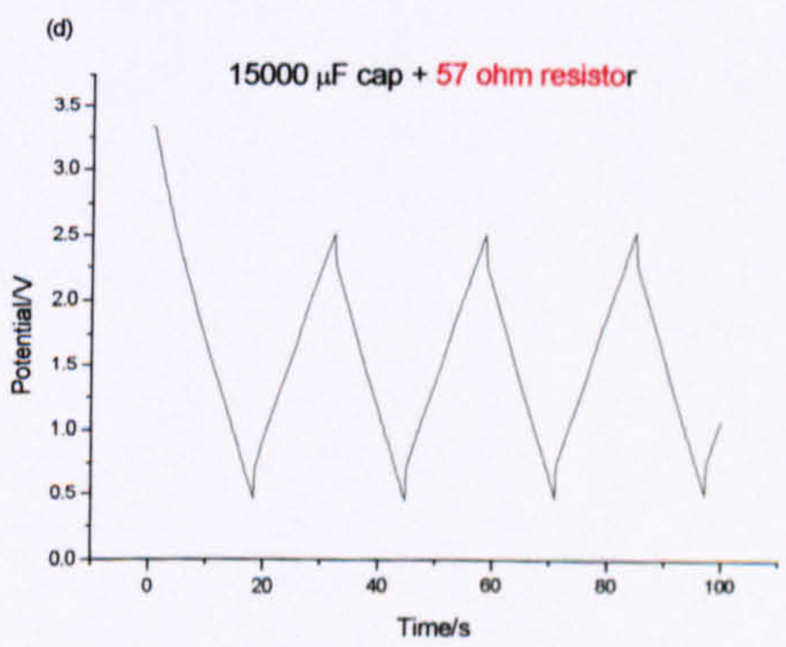

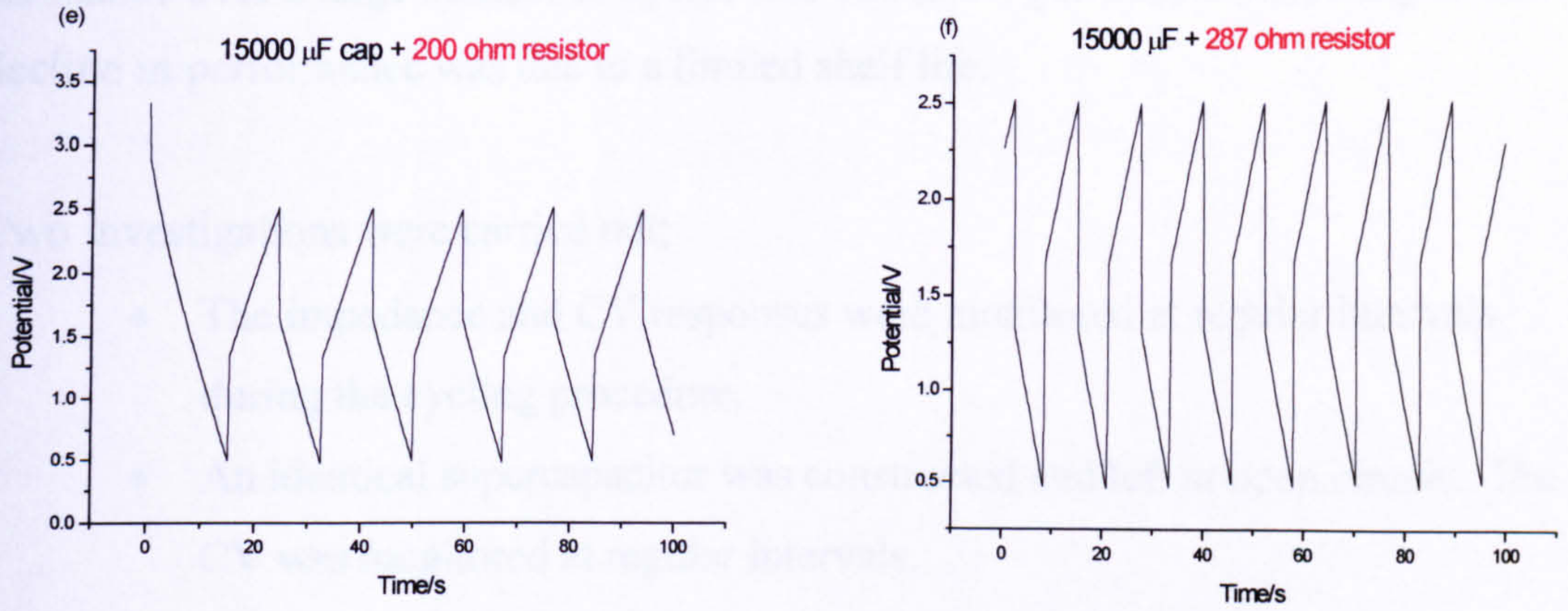

Figures 7.15 (a) to (f) Show the increase in the iR drop for a standard RS 15000 μF capacitor with increasing series resistance.

It was necessary to determine whether the observed change in capacitance and bulk resistance over a large number of cycles was due to the galvanostatic cycling or the decline in performance was due to a limited shelf life.

Two investigations were carried out;

- The impedance and CV responses were monitored at regular intervals during the cycling procedure.
- An identical supercapacitor was constructed and left at open circuit. The CV was monitored at regular intervals.

Figure 7.16 shows the complex plane impedance plots of a capacitor based on the lithium gel electrolytes and carbon cloth electrodes as a function of cycle number, in respect of the charge-discharge cycles.

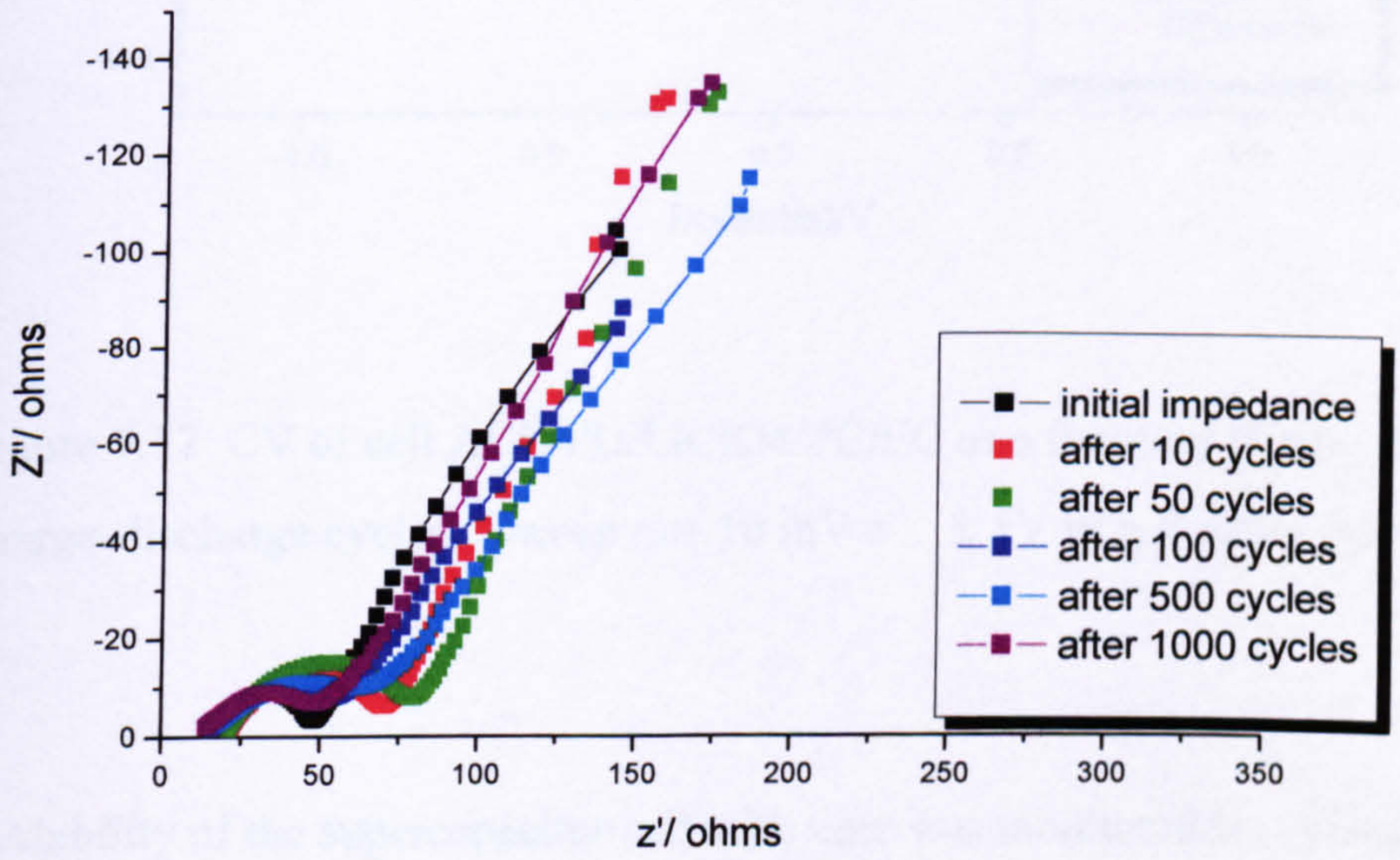

Figure 7.16 Complex plane impedance of cell ACC/PU/LiClO4/PC/EC as a function of galvanostatic charge-discharge cycles. Frequency range 65 kHz to 10 mHz.

Figure 7.17 shows cyclic voltammograms as a function of cycle number for the same sequence of charge-discharge cycles used for the impedance characteristics. As with the impedance results it can be seen that there are significant changes in the performance in the early cycles, i.e. there appears to be an "induction" process.

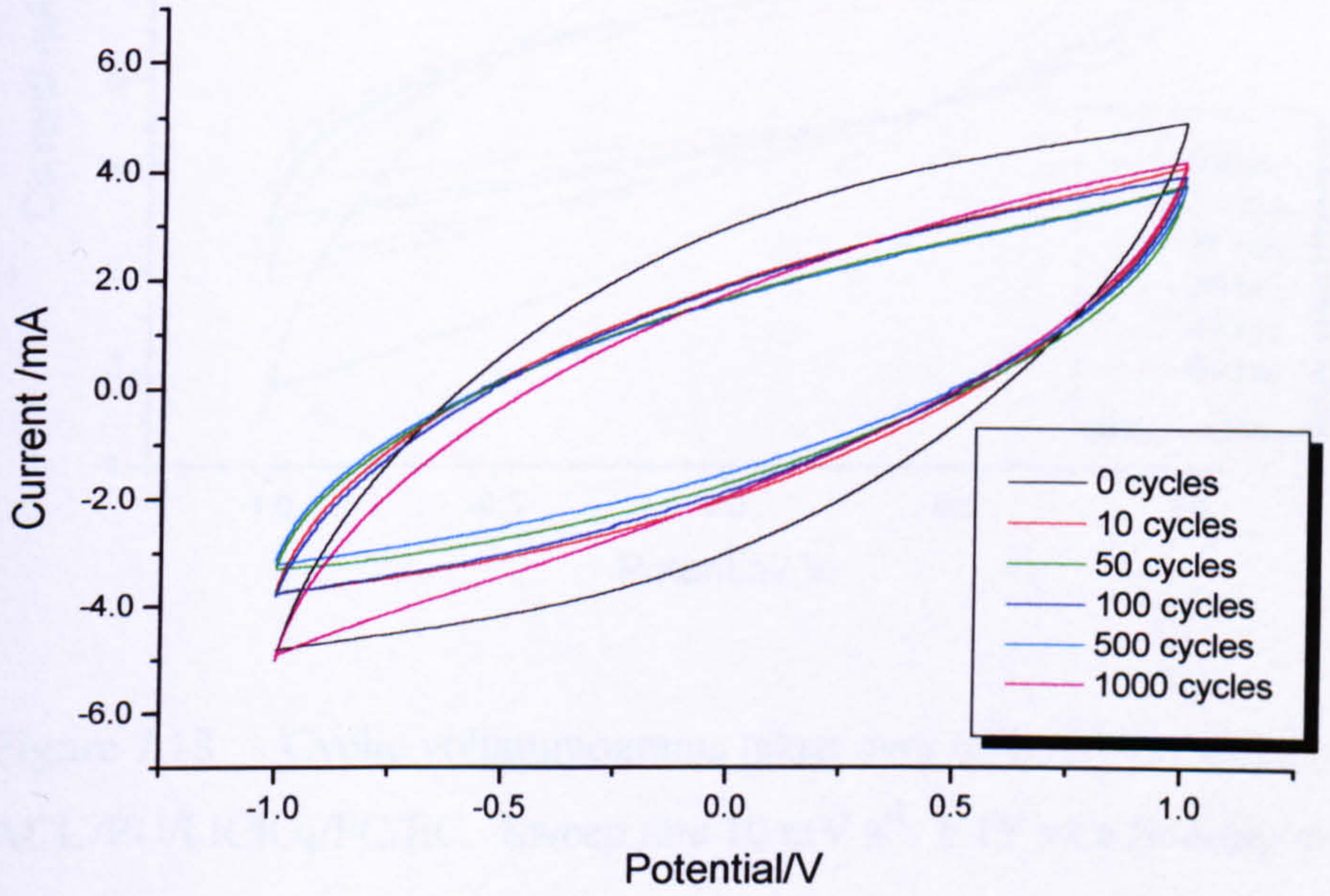

Figure 7.17 CV of cell ACC/PU/LiClO4/PC/EC as a function of galvanostatic charge-discharge cycles. Sweep rate 10 mV s^{-1}. ± 1V vs a floating potential.

The stability of the supercapacitor cell with time was monitored by cyclic voltammetry as shown in 7.18 below. In this experiment the cell was monitored at open circuit to evaluate on-the-shelf storage and the cyclic voltammetry was carried out at set times.

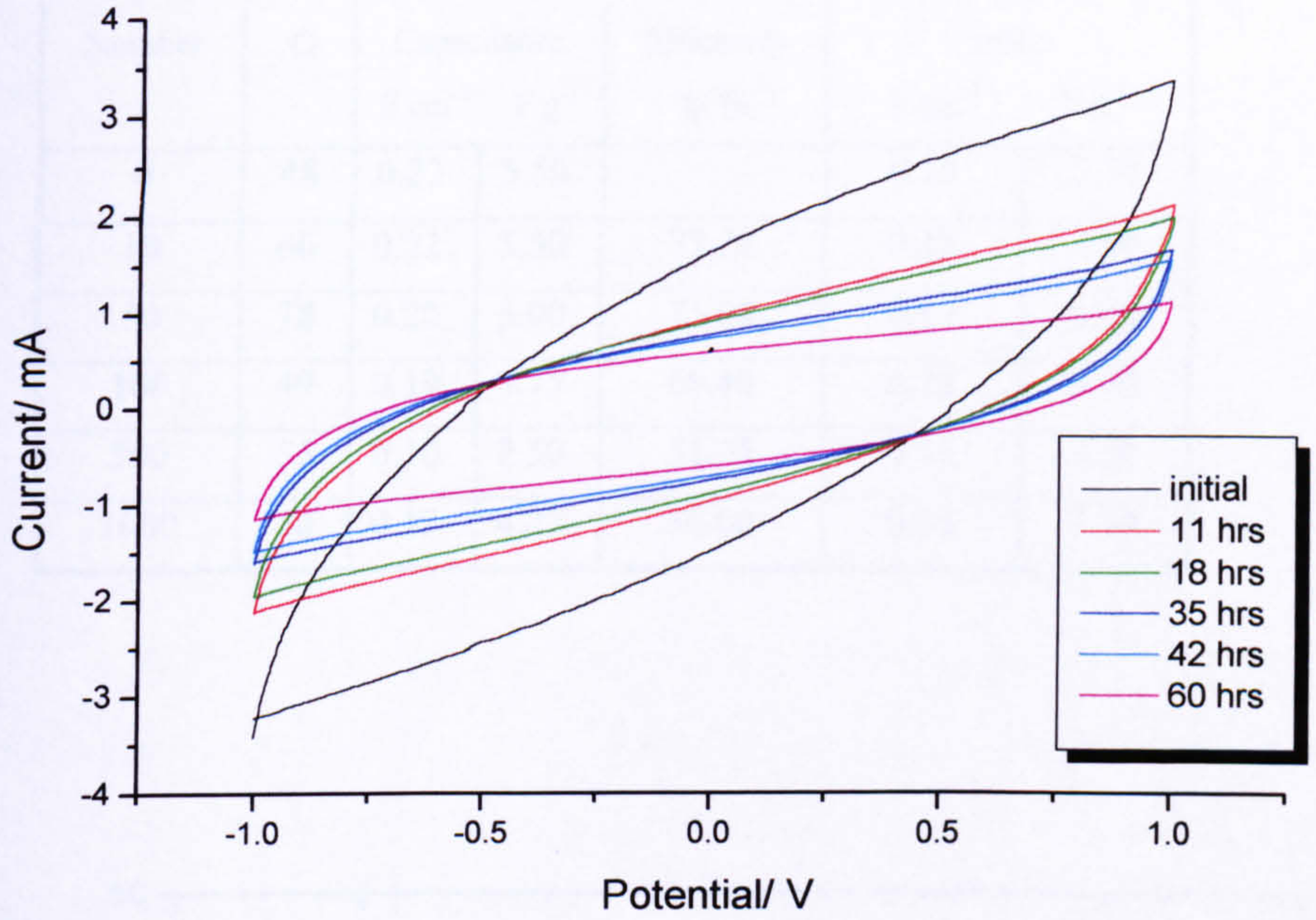

Figure 7.18 Cyclic voltammograms taken over 60 hours for a cell of ACC/PU/$LiClO_4$/PC/EC. Sweep rate 10 mV s^{-1}. ± 1V vs a floating potential.

The results for capacitances calculated from the impedance plots as a function of charge-discharge cycles using equation 5.14, the discharge capacitance calculated from the Charge-discharge curves using equation 5.15 and the coulombic efficiency calculated using equation 5.16 are shown in table 7.1.

Table 7.1. Electrical parameters of capacitor cell ACC/PU/$LiClO_4$/PC/EC

Cycle Number	R_b /Ω	Discharge Capacitance		Coulombic Efficiency	Capacitance @ 10 mHz	
		F cm^{-2}	F g^{-1}	η/ %	F cm^{-2}	F g^{-1}
0	48	0.22	5.50		0.15	3.75
10	66	0.22	5.50	77.28	0.12	3.00
50	78	0.20	5.00	75.00	0.12	3.00
100	49	0.19	4.75	68.40	0.12	3.00
500	55	0.10	2.50	51.25	0.18	4.50
1000	50	0.17	4.25	50.00	0.14	3.50

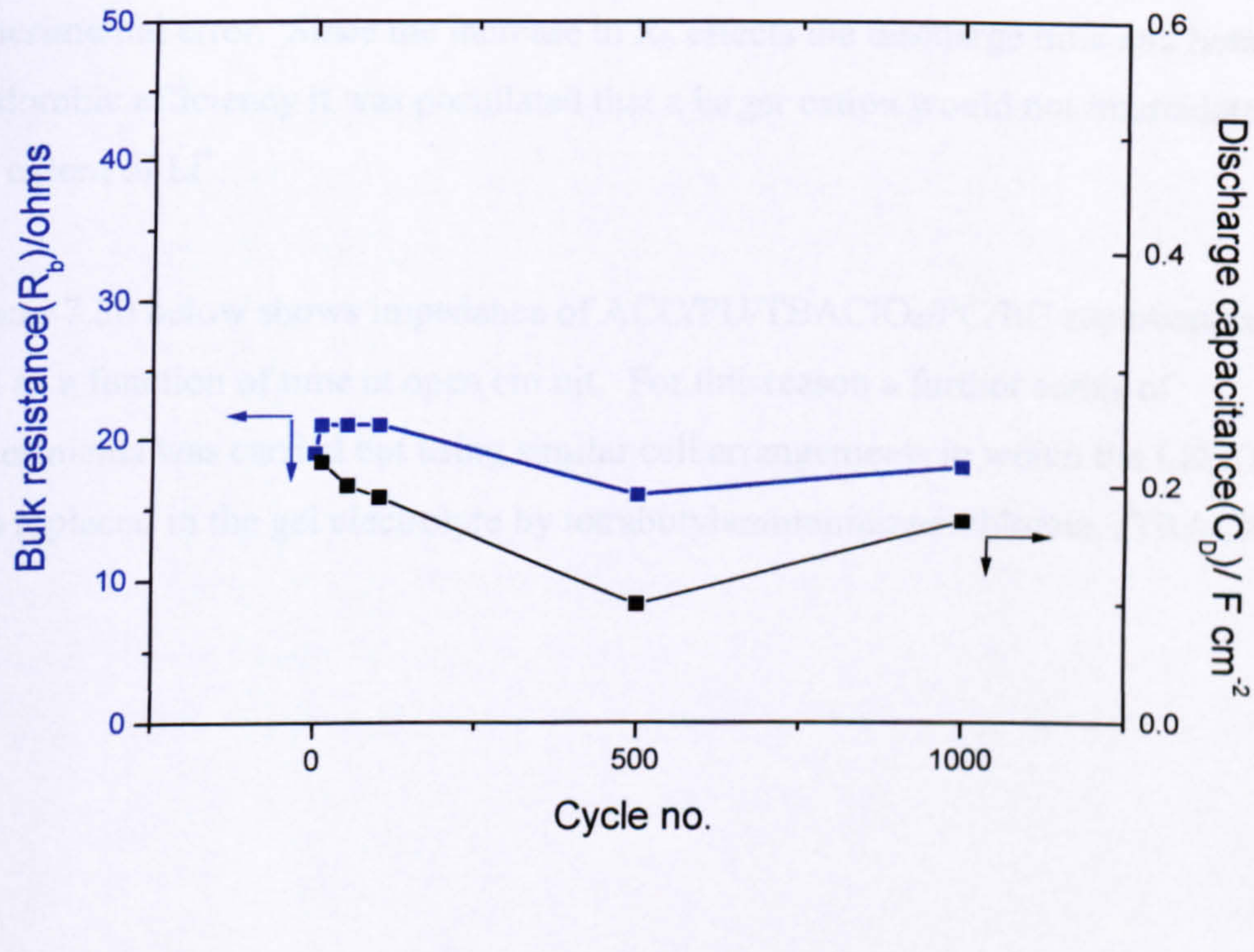

Figure 7.19 A plot of discharge capacitance and bulk resistance versus cycle number for the supercapacitor cell ACC/PU/$LiClO_4$/PC/EC

7.3.2 Discussion for $LiClO_4$ based electrolyte

The bulk resistance increases by 30 Ω from the initial value on cycling to approximately 50 cycles, as shown in figure 7.16. A decrease to near the original value of 48 Ω was then observed when cycled to 1000 cycles, although preliminary data from figure 7.12 showed a significant difference remained. This suggests the growth of an interfacial boundary, which breaks down on further cycling, or the possibility of intercalation of Li^+ ions into the electrode pores [5]. This intercalation may only be partially reversible until an equilibrium condition is reached, this could also explain the conditioning effect or induction period in the observed impedance and CV data. A similar trend is observed for the capacitance of the cell, where the capacitance decreases and reverts to near the original value. It must be noted, however, that the difference in capacitance is relatively small and could fall within experimental error. Since the increase in R_b effects the discharge time and hence the coulombic efficiency it was postulated that a larger cation would not intercalate to the extent of Li^+.

Figure 7.20 below shows impedance of ACC/PU/$TBAClO_4$/PC/EC supercapacitor cell as a function of time at open circuit. For this reason a further series of experiments was carried out using similar cell arrangements in which the $LiClO_4$ salt was replaced in the gel electrolyte by tetrabutylammoniumperchlorate, ($TBAClO_4$).

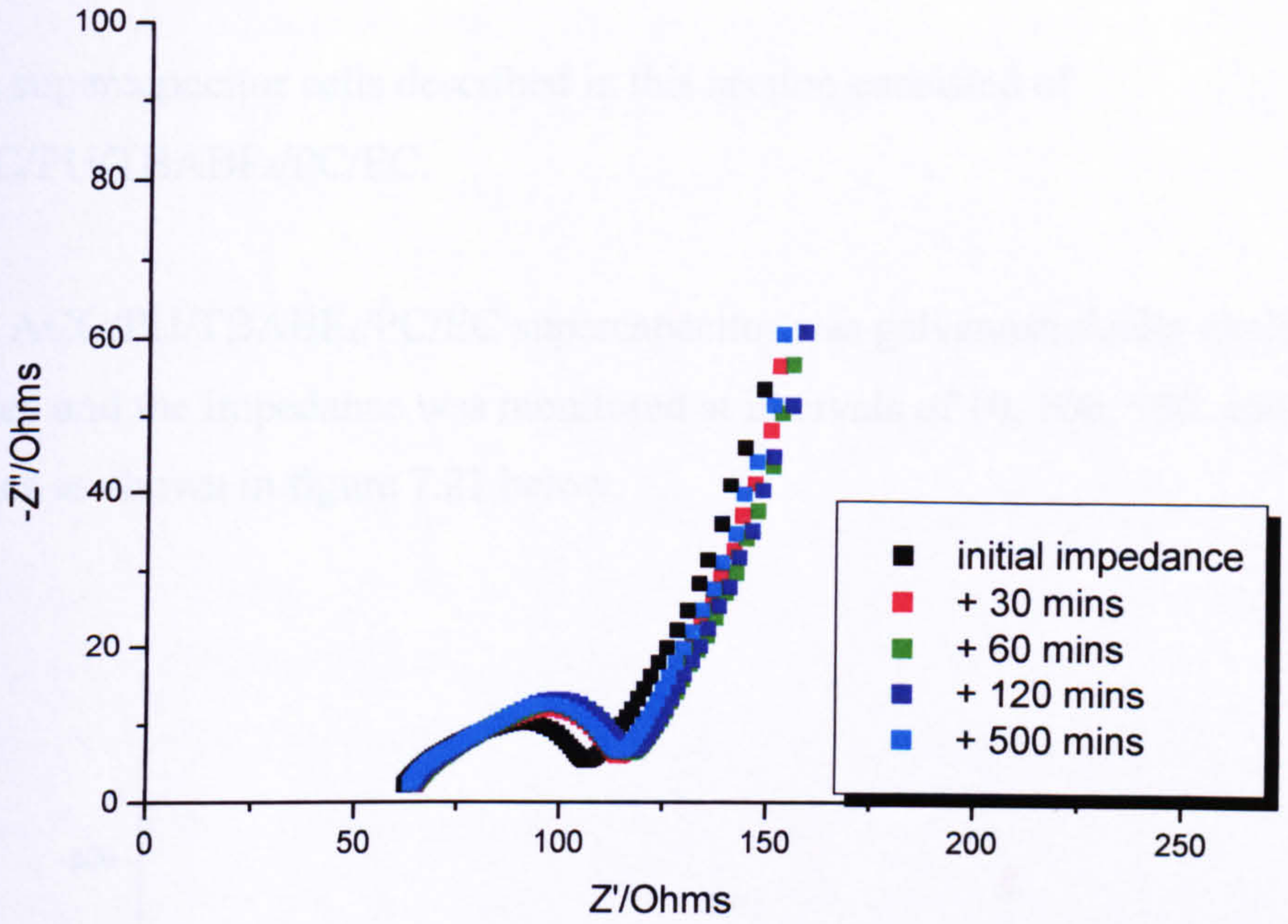

Figure 7.20 Complex plane impedance plots of the supercapacitor cell ACC/PU/TBAClO_4/PC/EC as a function of time at open circuit. Frequency range 65 kHz to 10 mHz.

Using TBAClO_4 as the electrolyte salt in place of the Lithium analogue increases the value of the bulk resistance by an average of 20 Ω.

The next section describes the study performed using TBABF_4 as the electrolyte salt.

7.3.3 *Experimental using $TBABF_4$ as electrolyte salt*

The supercapacitor cells described in this section consisted of ACC/PU/$TBABF_4$/PC/EC.

The ACC/PU/$TBABF_4$/PC/EC supercapacitor was galvanostatically cycled to 1000 cycles and the impedance was monitored at intervals of 10, 100, 500, and 1000 cycles as shown in figure 7.21 below.

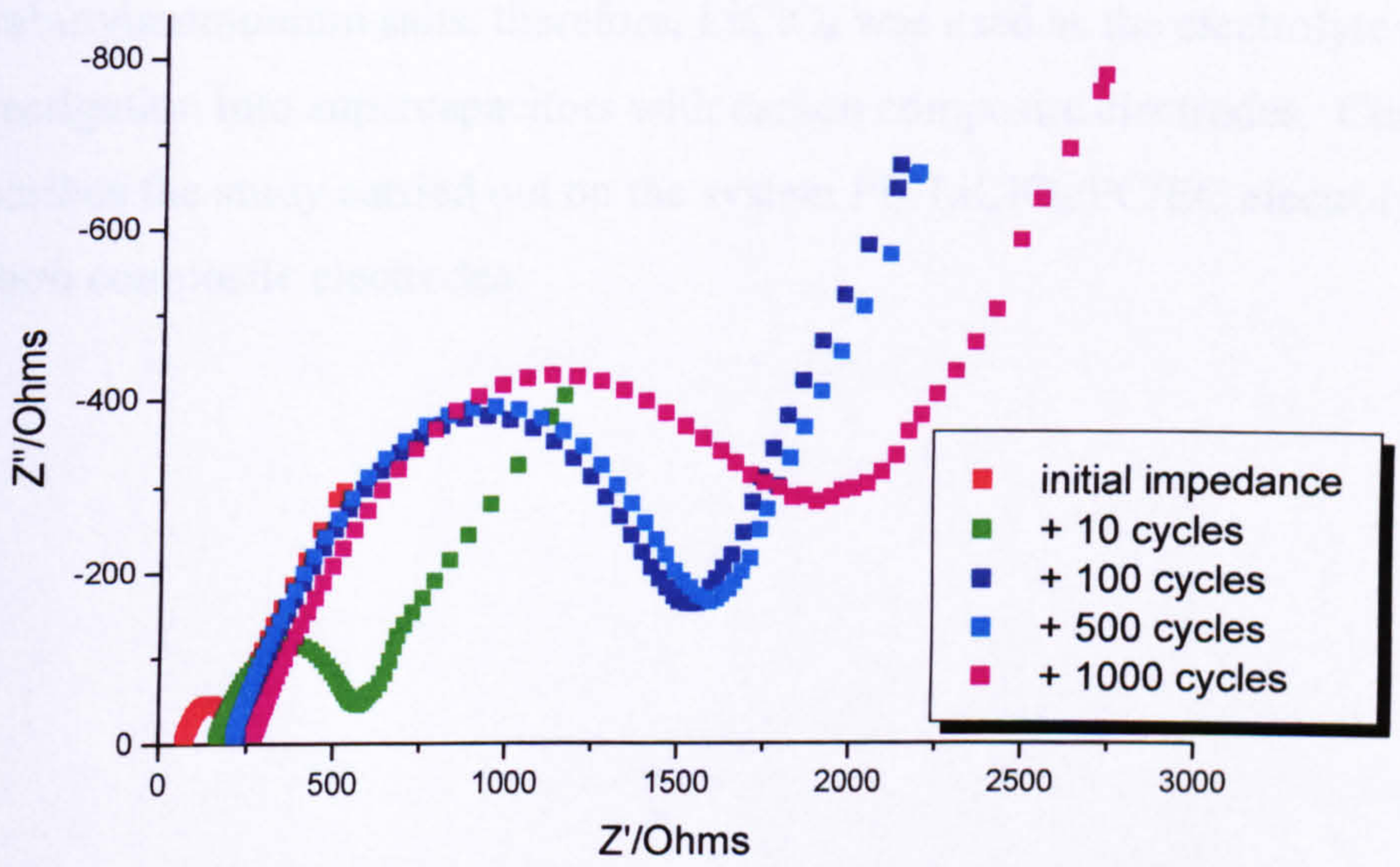

Figure 7.21 Complex plane impedance plots of the supercapacitor cell ACC/PU/$TBABF_4$/PC/EC as a function of time at open circuit.

It was clearly seen from figure 7.21 that the cell ACC/PU/$TBABF_4$/PC/EC shows poor capacitive characteristics on galvanostatic cycling. The value of the bulk resistance increases dramatically from 200 Ω to 1600 Ω. The capacitance decreases from 0.06 F cm^{-2} to 0.02 F cm^{-2}. Also, the complex plane plots show that the cell does not show good capacitor characteristics, i.e. the spike is not close to vertical and the semi-circle is large suggesting a high resistance in parallel with the geometric

capacitance of the cell. This was thought to be due to poor contact between the electrode and electrolyte leading to a large interfacial resistance and the prevention of diffusion of ions towards the electrode thus impeding the set-up of the double layer along the high surface area of the ACC.

In order to obtain a greater intimate contact between the electrode and electrolyte materials a carbon composite electrode, CC, was prepared and analysed as a supercapacitor cell using a PU gel electrolyte. Osaka and co-workers [4] successfully utilised $TBABF_4$ as a support electrolyte salt for carbon composite based supercapacitors with a PVdF gel and composite electrodes.
In this study $LiClO_4$ showed better capacitive characteristics than the tetrabutylammonium salts, therefore, $LiClO_4$ was used as the electrolyte salt for the investigation into supercapacitors with carbon composite electrodes. Chapter 7.4 describes the study carried out on the system PU/$LiClO_4$/PC/EC electrolyte with carbon composite electrodes.

7.4 Carbon composite electrodes

Composite electrodes are those in which the electrolyte is mixed with an electronically conducting medium, e.g. carbon powder, CP, and pressed into an electrode. The carbon powder used was Pearl Black 2000, Cabot carbon, which is already in use as an electrode material for composite secondary battery electrodes.

The gel electrolyte blend used for this study was PU/$LiClO_4$/PC/EC, and was prepared as described in chapter 3.

The first requirement was to optimise the composition of the electrode. The three governing parameters were conductivity, mechanical integrity and whether the electrodes showed supercapacitor characteristics in conjunction with the gel electrolyte discussed above.

7.4.1 Optimisation of the composition of the electrode

Preparation of Composite Electrodes

Pearl Black 2000 Carbon powder was added to the above electrolyte solution, in a 1:2 ratio ensuring good homogenisation, (the electrolyte was dissolved in THF-i.e. in the pre-cast state). This provided the base composition of all the different electrode systems analysed. Added to this mixture were various amounts of the plasticiser/salt solution. The plasticiser/salt solution was prepared by adding EC/PC and $LiClO_4$ in the ratio of EC/PC and $LiClO_4$ of 10:1.

The percentage plasticiser/salt was measured with respect to the mass of the electrolyte component in the composite electrode. The different compositions of added plasticiser/salt were as follows:-

- 100% added plasticiser/salt
- 150%
- 200%
- 400%
- 500%

0.003g of the mixture was pressed onto a stainless-steel button (surface area of 1 cm^2).
A sandwich-type supercapacitor cell was then constructed using the above gel electrolyte. The complex plane impedance of each cell was obtained.
A torque of 60cNm was applied to each cell.

Electrochemical analysis of the composite electrodes

Mechanical integrity, the bulk resistance and the capacitive characteristics of the cells were the governing factors for optimisation of the electrode systems.
The impedance responses from the five supercapacitor cells described by the compositions above are shown below in figures 7.22 to 7.26.

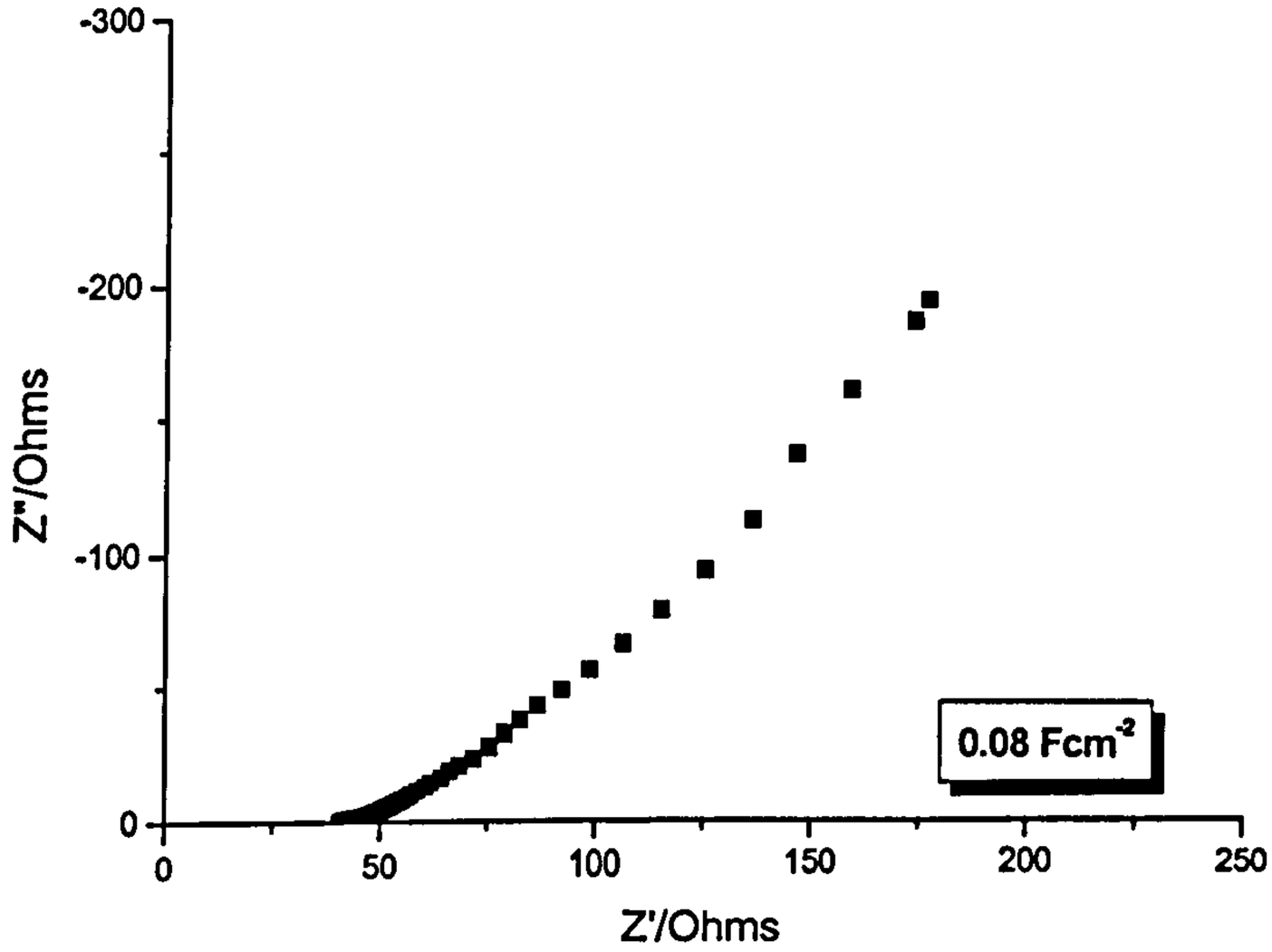

Figure 7.22 Complex plane impedance plot of a supercapacitor cell with 100% added plasticiser/salt solution. Frequency range 65 kHz to 10 mHz.

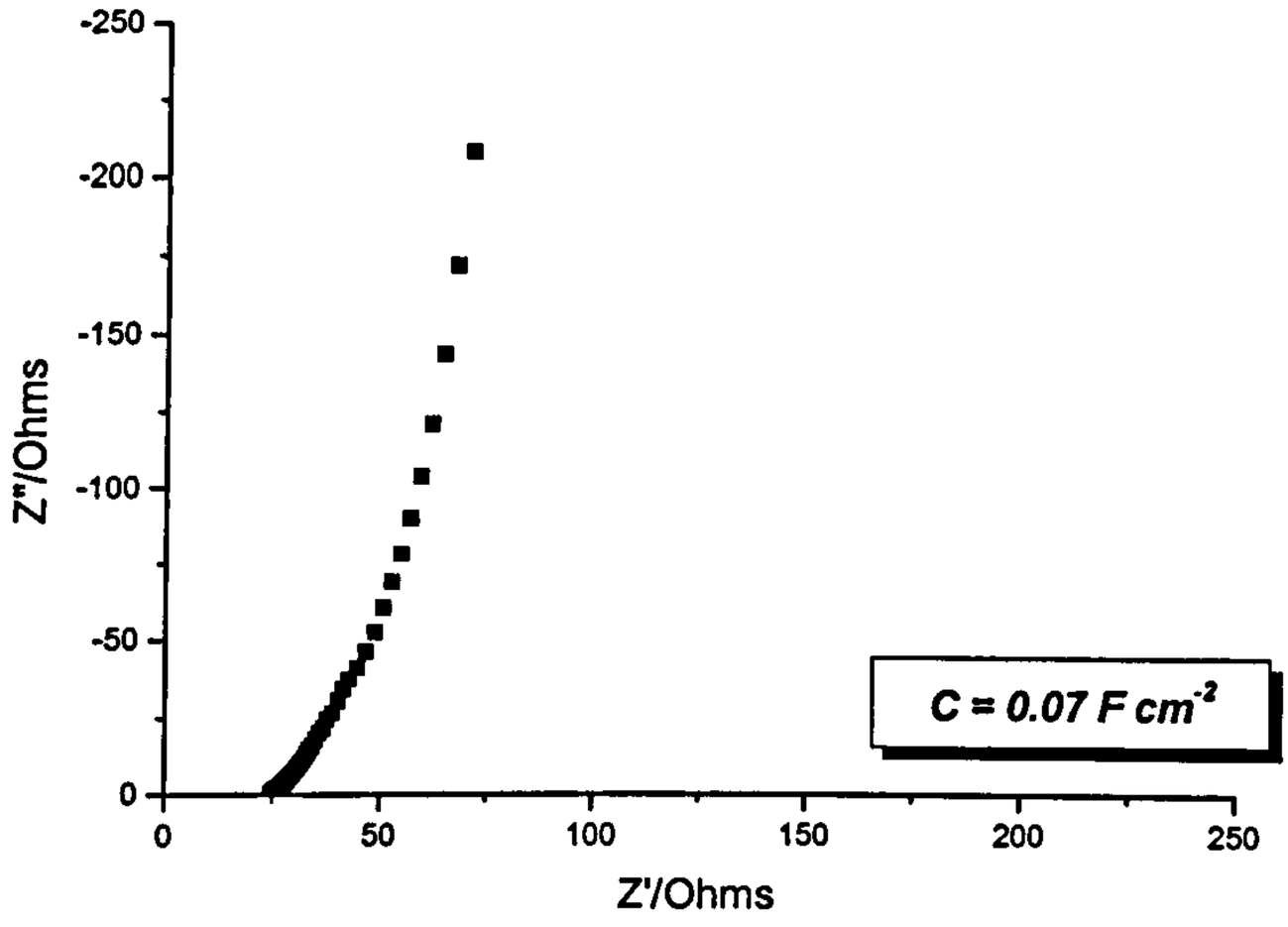

Figure 7.23 Complex plane impedance plot of a supercapacitor cell with 150% added plasticiser/salt solution. Frequency range 65 kHz to 10 mHz.

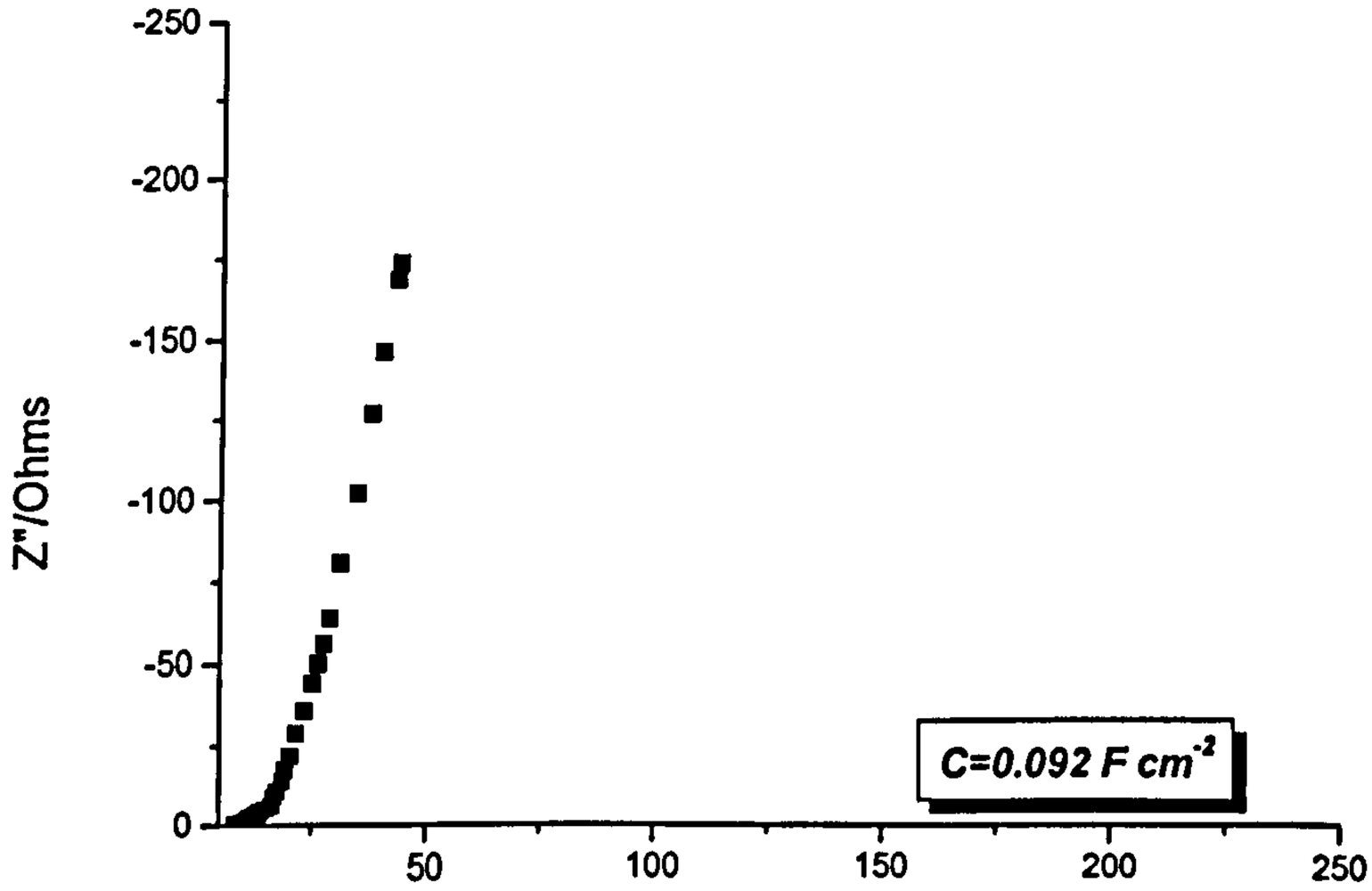

Figure 7.24 Complex plane impedance plot of a supercapacitor cell with 200% added plasticiser/salt solution. Frequency range 65 kHz to 10 mHz.

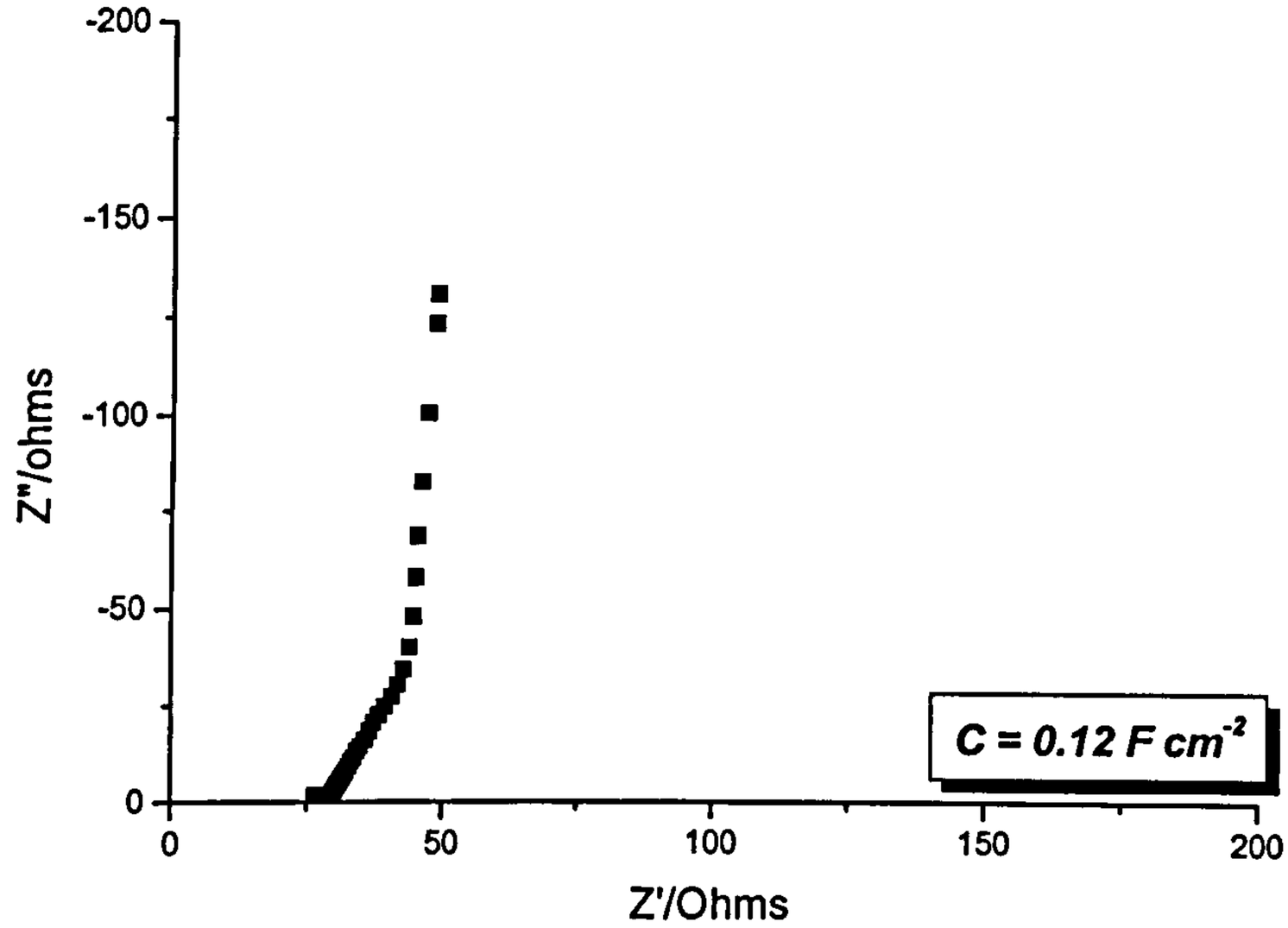

Figure 7.25 Complex plane impedance plot of a supercapacitor cell with 400% added plasticiser/salt solution. Frequency range 65 kHz to 10 mHz.

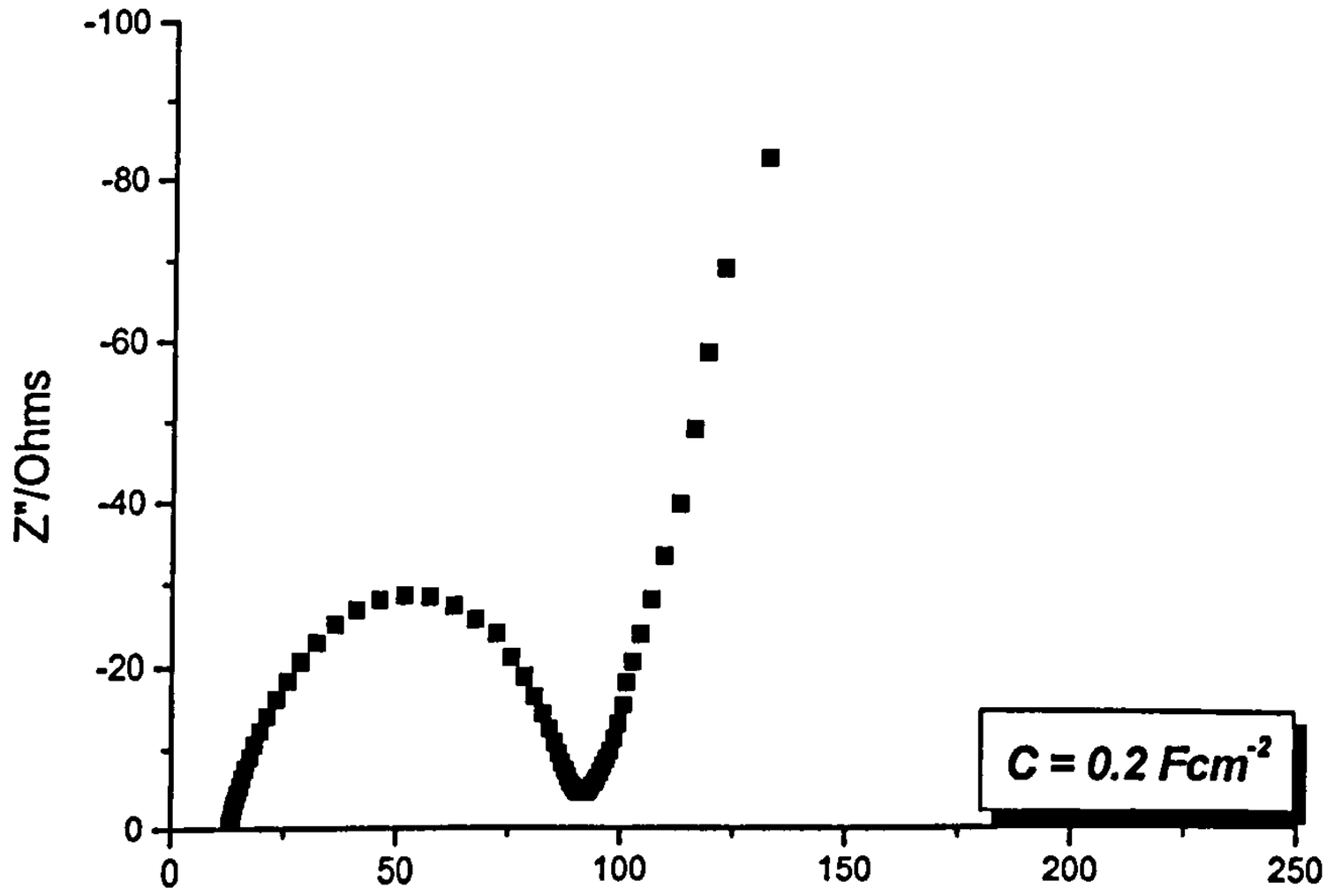

Figure 7.26 Complex plane impedance plot of a supercapacitor cell with 500% added plasticiser/salt solution. Frequency range 65 kHz to 10 mHz.

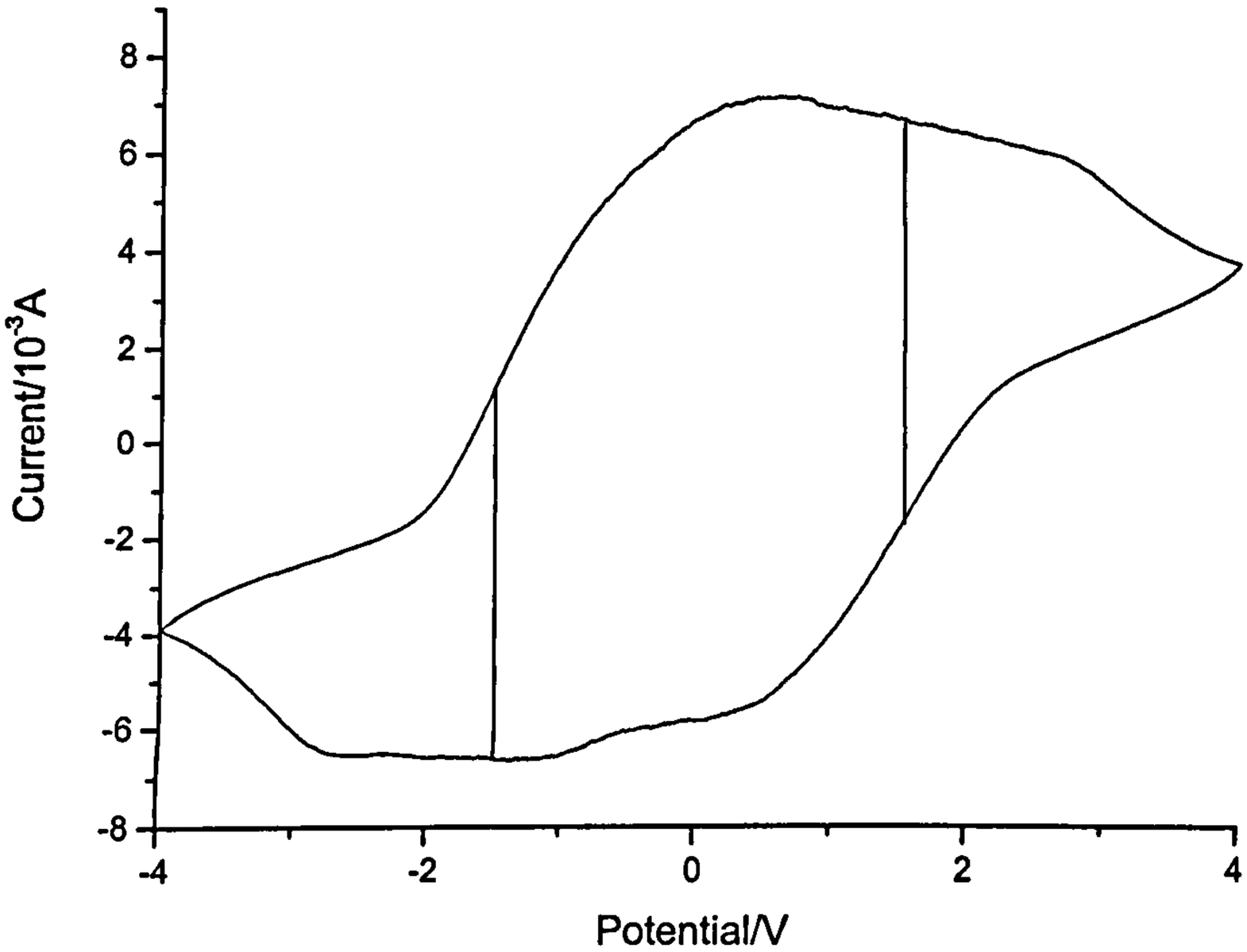

Figure 7.27 Cyclic voltammogram of the supercapacitor cell with 200% added plasticiser/salt solution. Sweep rate 10 mV s^{-1}. Showing a stable potential window between +1.5 and – 1.5 V vs a floating potential.

The impedance plots in figures 7.22 to 7.26 showed that the two best compositions were 200% (R_b = 9 Ω and C = 0.092 F cm^{-2}), and 400% (R_b = 26 Ω and C = 0.12 F cm^{-2}). Note that the composition of electrode with 500% added plasticiser had the highest capacitance value, but had a bulk resistance of 96 Ω which was too large. The composite electrode with 200% added plasticiser was chosen as the optimum composition since it had a lower value of bulk resistance and showed good capacitor characteristics. The increase in capacitance from 200% to 400% added plasticiser was not regarded as economically sound, (i.e., the cost of doubling the amount of plasticiser did not double the capacitance value), considering the relatively small increase. Therefore the electrodes containing 200% added plasticiser were taken as the optimum composition.

7.4.2 Stability of the supercapacitor with composite electrodes

The supercapacitor cell comprising of the composite electrodes (100% Pearl Black CP/200% electrolyte+200% added plasticiser/salt) and the gel electrolyte (PU/ $LiClO_4$/PC/EC) was left at open circuit and the impedance was taken at regular intervals. Figure 7.28 below shows the complex plane impedance plots as a function of time at open circuit.

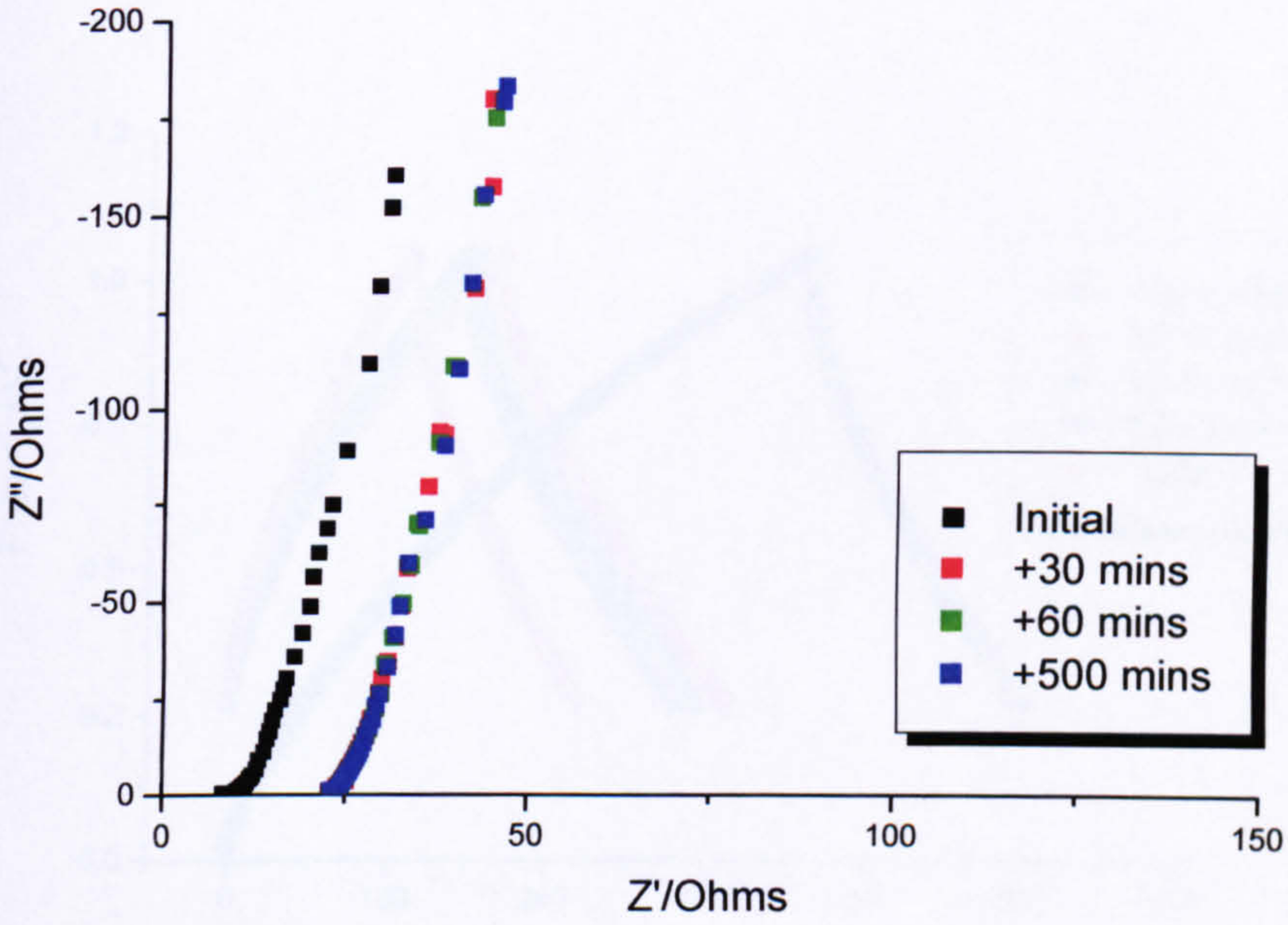

Figure 7.28 Complex plane impedance plots as a function of time at open circuit for supercapacitor cell Composite carbon CC electrodes /PU/ $LiClO_4$/PC/EC//with added 200% PC/EC/ $LiClO_4$. Frequency range 65 kHz to 10 mHz.

As with earlier experiments on the charge-discharge cycling there is clearly an induction process, probably of an interfacial nature, which is manifested in an increase in the value of bulk resistance after the initial assembly.

7.4.3 Galvanostatic charge-discharge experiments

The supercapacitor cell described in chapter 7.4.2 above was galvanostatically charged and discharged at 0.5 mA between 0.20 and 1 V for 1000 cycles. Figure 7.29 below shows the charge-discharge curves at 1, 10, 100, 500, 1000 cycles. The impedance of the same cell was obtained at intervals of 1, 10, 100, 500, 1000 cycles and the curves shown in figure 7.30 below.

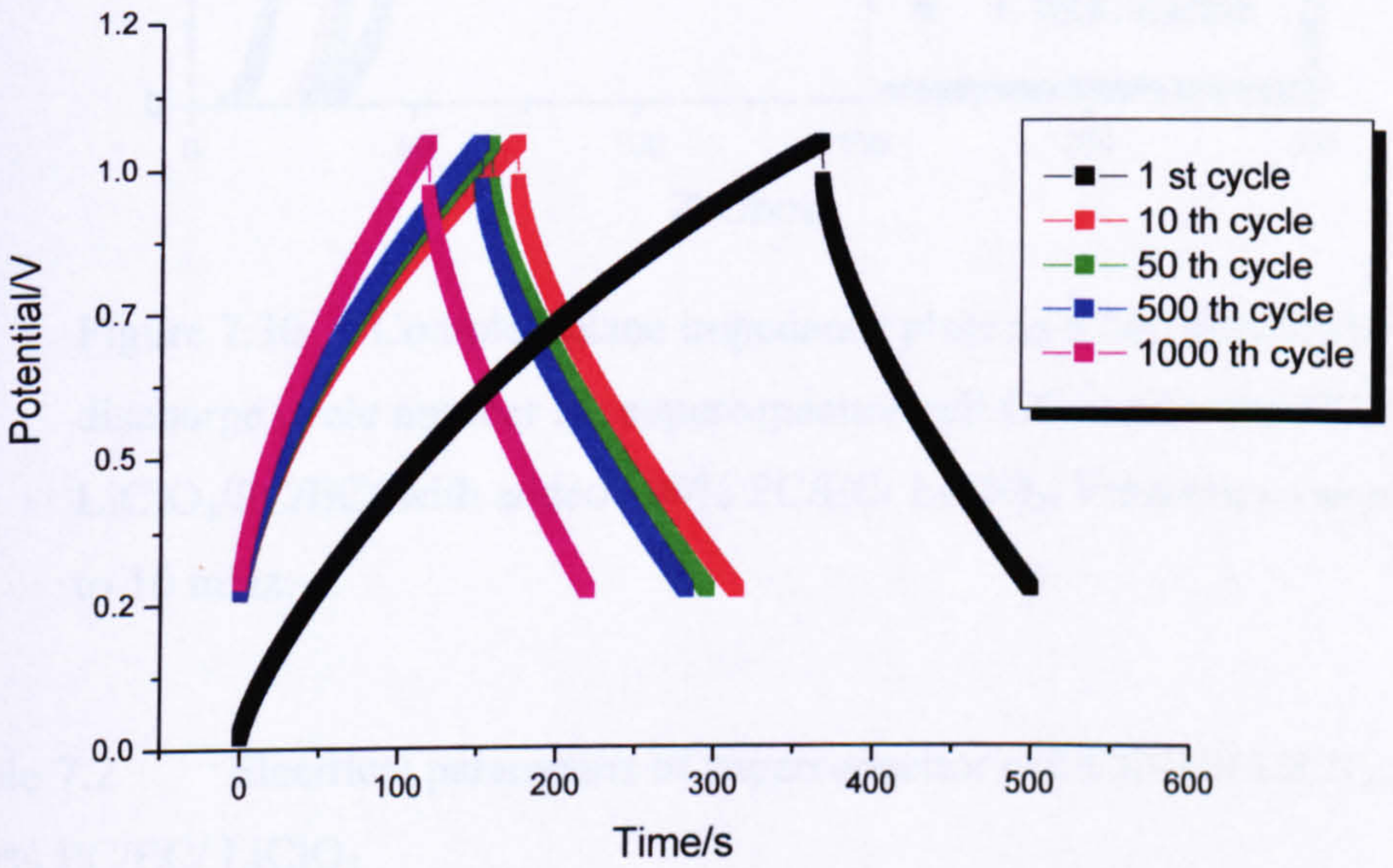

Figure 7.29 Charge-discharge curves for the supercapacitor cell CC/PU/ $LiClO_4$/PC/EC/ + 200% PC/EC/ $LiClO_4$. i=0.5 mA. v = 0.20 to 1 V.

Both the charge-discharge curves and the impedance results show evidence of the induction process observed when the impedance was measured as a function of time for an open circuit cell.

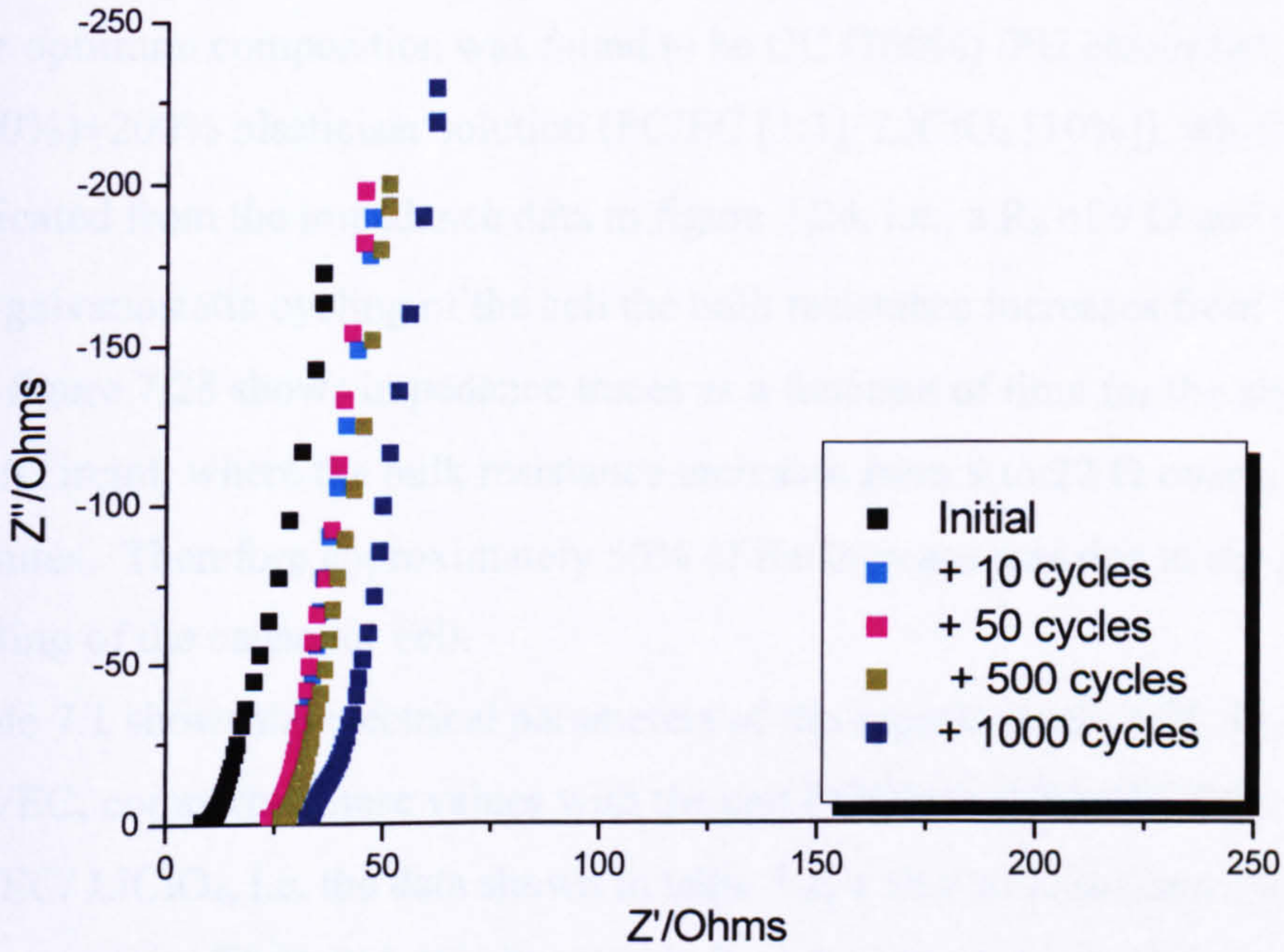

Figure 7.30 Complex plane impedance plots as a function of charge-discharge cycle number for supercapacitor cell CC electrodes /PU/ $LiClO_4$/PC/EC//with added 200% PC/EC/ $LiClO_4$. Frequency range 65 kHz to 10 mHz.

Table 7.2 Electrical parameters of supercapacitor cell CC/PU/ $LiClO_4$/PC/EC/ + 200% PC/EC/ $LiClO_4$.

Cycle Number	R_b /Ω	Discharge Capacitance		Coulombic Efficiency	Capacitance @ 10 mHz	
		F cm^{-2}	F g^{-1}	η/ %	F cm^{-2}	F g^{-1}
0	10	0.091	30.00		0.092	30.67
10	30	0.091	30.00	86	0.086	28.67
50	29	0.087	29.00	88	0.080	26.67
500	34	0.079	26.33	83	0.079	26.33
1000	40	0.071	23.67	80	0.069	23.07

7.4.4 Summary of composite electrodes

The optimum composition was found to be CC (100%) /PU electrolyte (200%)+200% plasticiser solution (PC/EC [1:1]/ $LiClO_4$ [10%]), which was indicated from the impedance data in figure 7.24, i.e., a R_b of 9 Ω and 0.092Fcm^{-2}. On galvanostatic cycling of the cell the bulk resistance increases from 10 to 40 Ω, but figure 7.28 shows impedance traces as a function of time for the above cell at open circuit, where the bulk resistance increases from 9 to 22 Ω over a period of 500 minutes. Therefore approximately 50% of the increase was due to the galvanostatic cycling of the capacitor cell.

Table 7.1 shows the electrical parameters of the capacitor cell ACC/PU/$LiClO_4$ /PC/EC, comparing these values with the cell CC/PU/ $LiClO_4$/PC/EC/ + 200% PC/EC/ $LiClO_4$, i.e. the data shown in table 7.2, a similar capacitance is obtained for both systems. The trend of increasing bulk resistance and decreasing capacitance on cycling is observed for both systems. Also an initial induction or conditioning period is apparent for the devices using carbon cloth and carbon composite electrodes.

Table 7.2 shows a marked improvement in coulombic efficiency from the devices utilising the composite electrodes. This may be due to a greater intimate contact between the electrode and electrolyte and hence a greater reversibility of ions to and from the electrode surfaces.

8. Supercapacitors with porous silicon electrodes

8.1 Introduction

As described earlier in chapter 4.2 PSi is a high surface area material which is particularly interesting as an electrode material in capacitor devices. For example, Lehmann and co-workers have produced a parallel plate capacitor using an oxide-nitride-oxide dielectric sandwich and PSi electrodes [1] utilising the high surface area of PSi.

This chapter reports the preliminary studies carried out utilising the high surface area properties of PSi as electrode materials for supercapacitor devices with polymer gel electrolytes.

8.2 Preparation of porous silicon

There are two general methods of producing PSi, namely anodic and chemical (or stain) etching, the basic mechanisms of which are described in chapter 4.2.

PSi prepared by both anodically etched and the stain etched methods was used in this investigation. In this section of the study anodically etched PSi was used.
PSi prepared by the stain etched method is reported in section 8.3.6

The PSi was prepared by electrochemical anodisation of a p-type crystalline silicon substrate in a 15% HF/ethanol/H_2O or D_2O solution at a current density of 25 mA cm^{-2} for 10 minutes.
The anodisation cell was constructed of two halves of PTFE and the silicon substrate sandwiched in between, as shown in figure 8.1. The polished side of the wafer was electrically connected via the etch solution to the positive terminal of a d.c. power supply hence making it the anode. The reverse side of the wafer was pre-treated by vacuum deposition of aluminium and annealed at 550 ^{0}C under nitrogen for 30 minutes. This provided an ohmic contact to the wafer, which is needed, for both etching and current collection in the capacitor device.

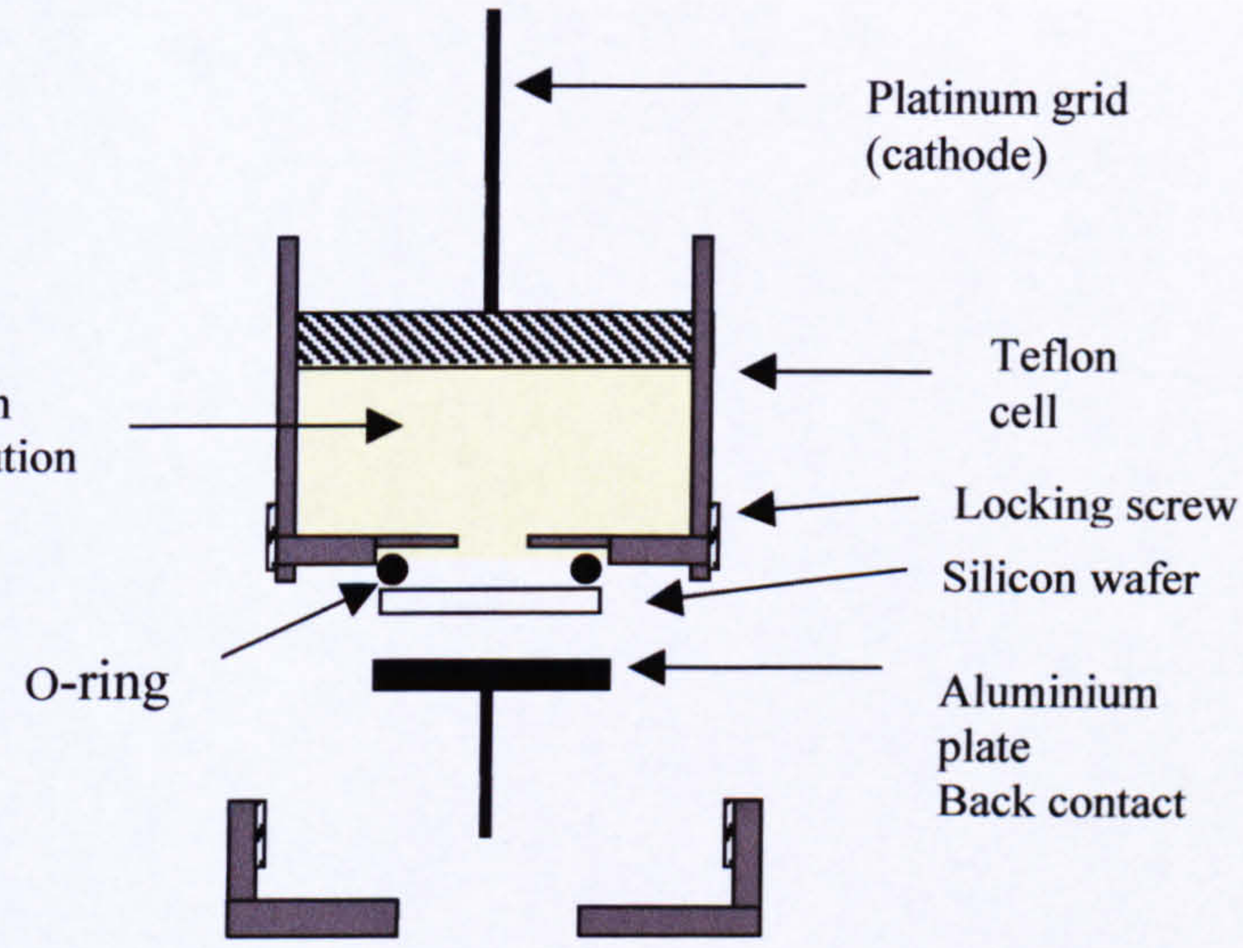

Figure 8.1 Schematic representation of an anodisation cell for the electrochemical etching of crystalline silicon.

The type of silicon substrate used was p-type (resistivity 0.02 Ωcm^{-1}), with a crystallographic orientation of 111. P-doped silicon was used for ease of manufacture of the PSi. The crystallographic orientation selected was 111 because of the ease of manipulation of the PSi pieces, i.e. the PSi pieces fractured along all axes with relative ease. An orientation of 001 fractured in one direction, but not consistently in the other two, proving difficult to obtain the required 1 cm^2 piece used for the cell designed for device evaluation.

Typical scanning electron micrographs of anodically etched PSi are shown in figure 8.2 (a) and (b).

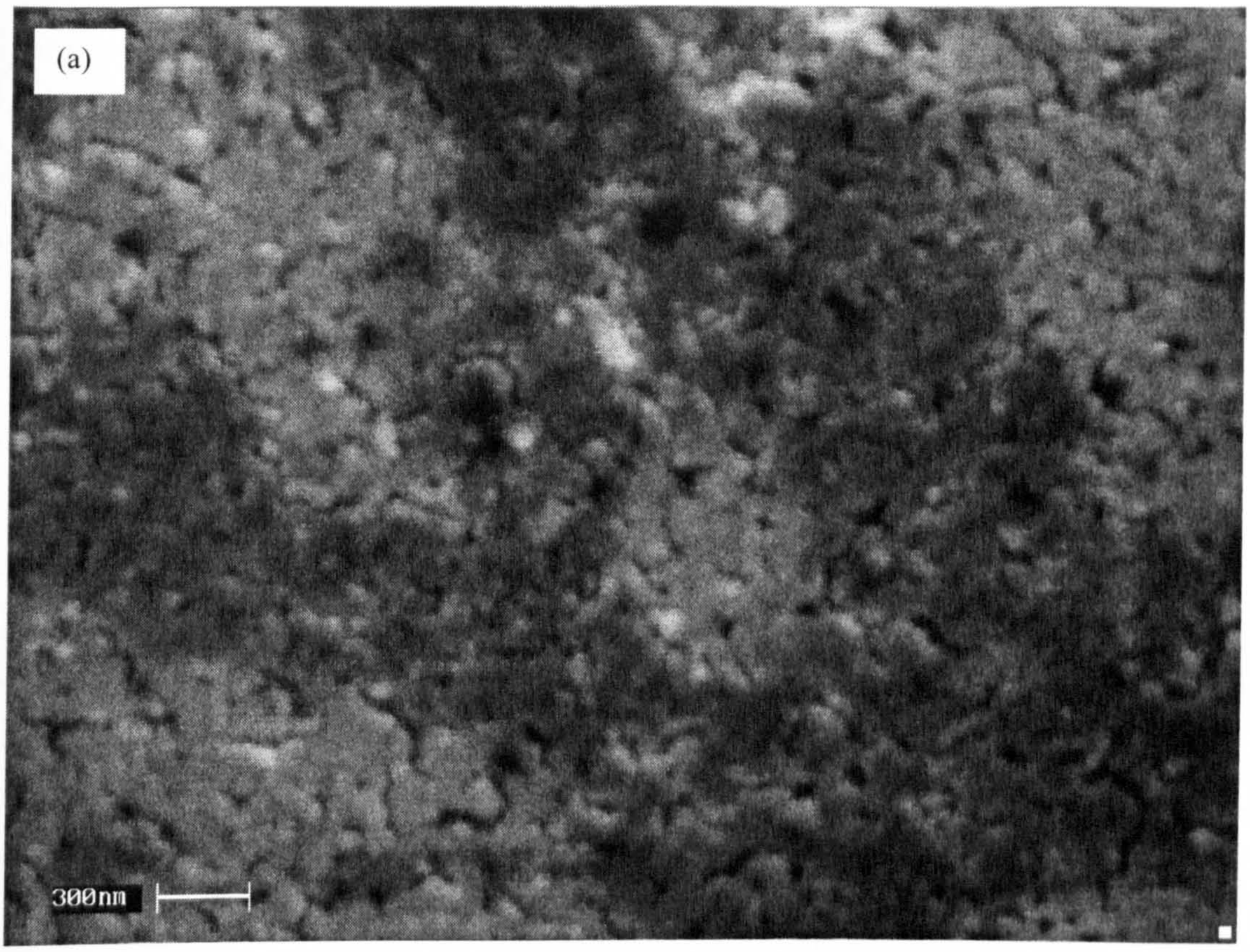

Figure 8.2 (a) and (b) SEM micrographs of nano-porous silicon. P-type, 111, 0.02 Ω cm^{-1}, etched for 10 minutes at 25 $mAcm^{-2}$ in a 15% ethanolic HF solution. Both micrographs show cracking of the PSi layer, with figure 8.2 (b) magnified further.

Typically on drying PSi the surface cracks. Water stabilises the porous structure, but on drying of the PSi capillary induced tensile stresses occur, thus the surface of the porous silicon cracks. These cracks can be minimised by washing the fresh PSi in a low surface tension liquid such as pentane. This reduces the tensile stresses within the pores on drying and hence the PSi shows less surface cracking.

Since PSi is a very reactive substance, it readily oxidises in air and thus increases its resistance. This is undesirable for the application being investigated in this study since a low resistance is desired for supercapacitor devices. This can be avoided by storing the fresh PSi under pentane to reduce the oxidation of the PSi surface.

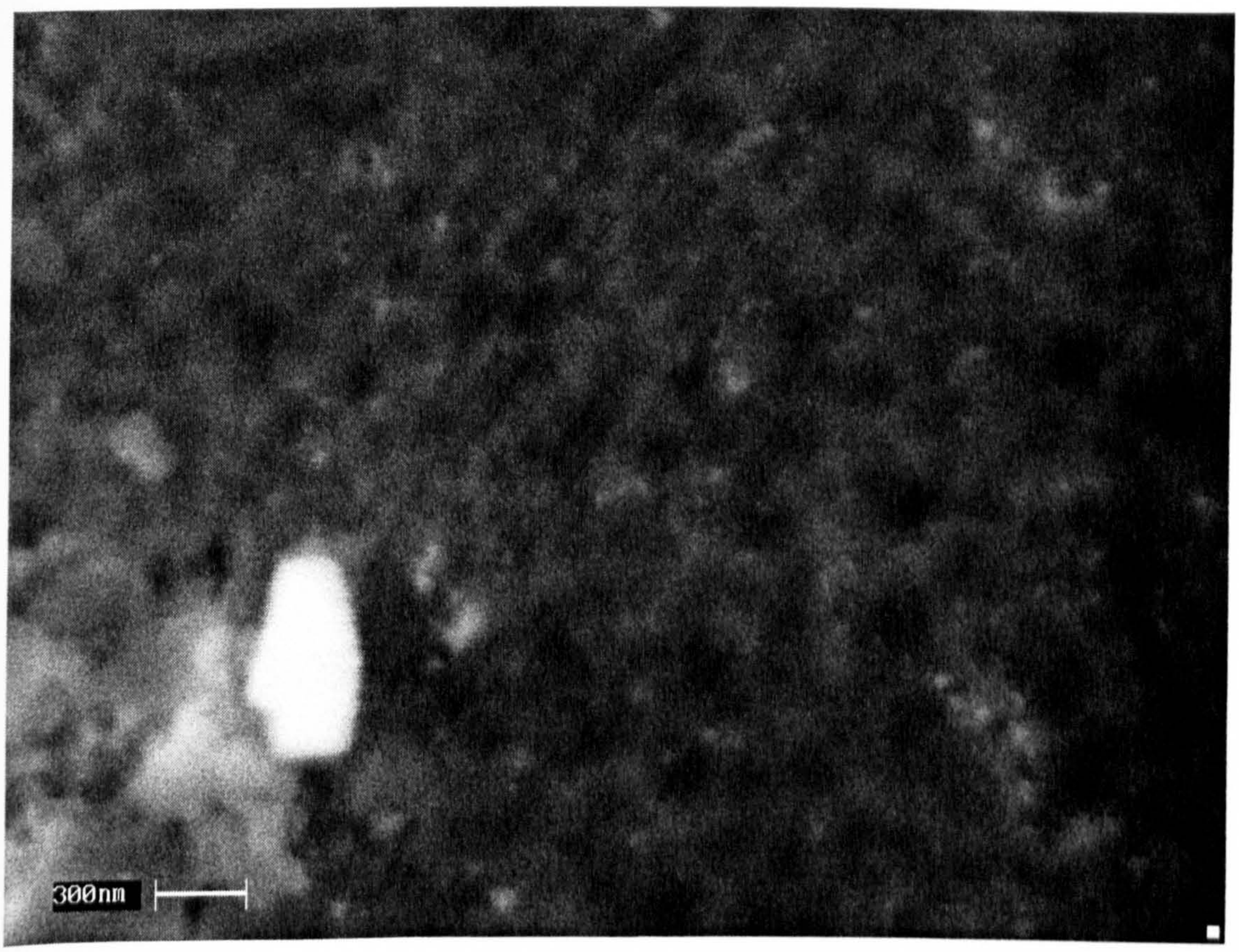

Figure 8.3 SEM micrograph of nano-porous silicon, washed in pentane. P-type, 111, 0.02 Ω cm^{-1}, etched for 10 minutes at 25 mA cm^{-2} in a 15% ethanolic HF solution. Washed in pentane and dried under a nitrogen atmosphere.

As with the carbon based supercapacitor devices described in chapter 7, the aim of the investigation was to establish the capacitive response, if any, of PSi electrodes with the PU electrolyte described in chapter 6. Again for initial experiments a low molecular weight analogue electrolyte was investigated for comparison. The electrolyte used was a 0.25 M $TEABF_4$/PC solution. (Both reagents were supplied by Aldrich and were 99.99% pure).

As the use of PSi as an electrode material is a novel application in supercapacitor devices it was thought prudent to investigate initially a liquid supercapacitor cell using Si as the electrode material. The Si used was the same type as that used for producing the PSi, i.e. 0.02 Ω cm^{-1}, 111 orientated p-type crystalline Si. The reverse side of the wafer was coated in aluminium and annealed under nitrogen for 30 minutes at 550 °C.

The test cell used was identical to the one used for carbon electrodes shown in figure 7.1.

8.3 Results

8.3.1 Silicon electrodes with a liquid electrolyte

A supercapacitor cell of Si/TEABF$_4$/PC (0.25M) was constructed in the manner described above. The complex plane impedance response and CV are shown in figures 8.4(a and b) and 8.5. Figure 8.4(b) shows the region of high frequency response of the cell. The a.c. impedance of the cell was measured using a Windsor scientific potentiostat coupled with the impedance module. The data is presented in an engineering format, i.e. as though the complex plane was in the 1st quadrant and not in the 3rd quadrant as is normally quoted in electrochemical reports. For the following complex plane responses it should be read that the imaginary part of the impedance is negative although the axis is quoted as positive.

Figure 8.4(b) shows that the bulk resistance of the cell from the high frequency intercept was 38 Ω. This value is comparable with the values obtained with a carbon-based supercapacitor, but the CV shown in figure 8.5 does not show ideal capacitive behaviour within the specified potential limits. The capacitance calculated using equation 5.14, from the complex plane impedance data at 10 mHz, is 0.16 mF cm^{-2}, relating to a specific capacitance of 2.71 mF g^{-1}, since the mass of one electrode was 0.059g.

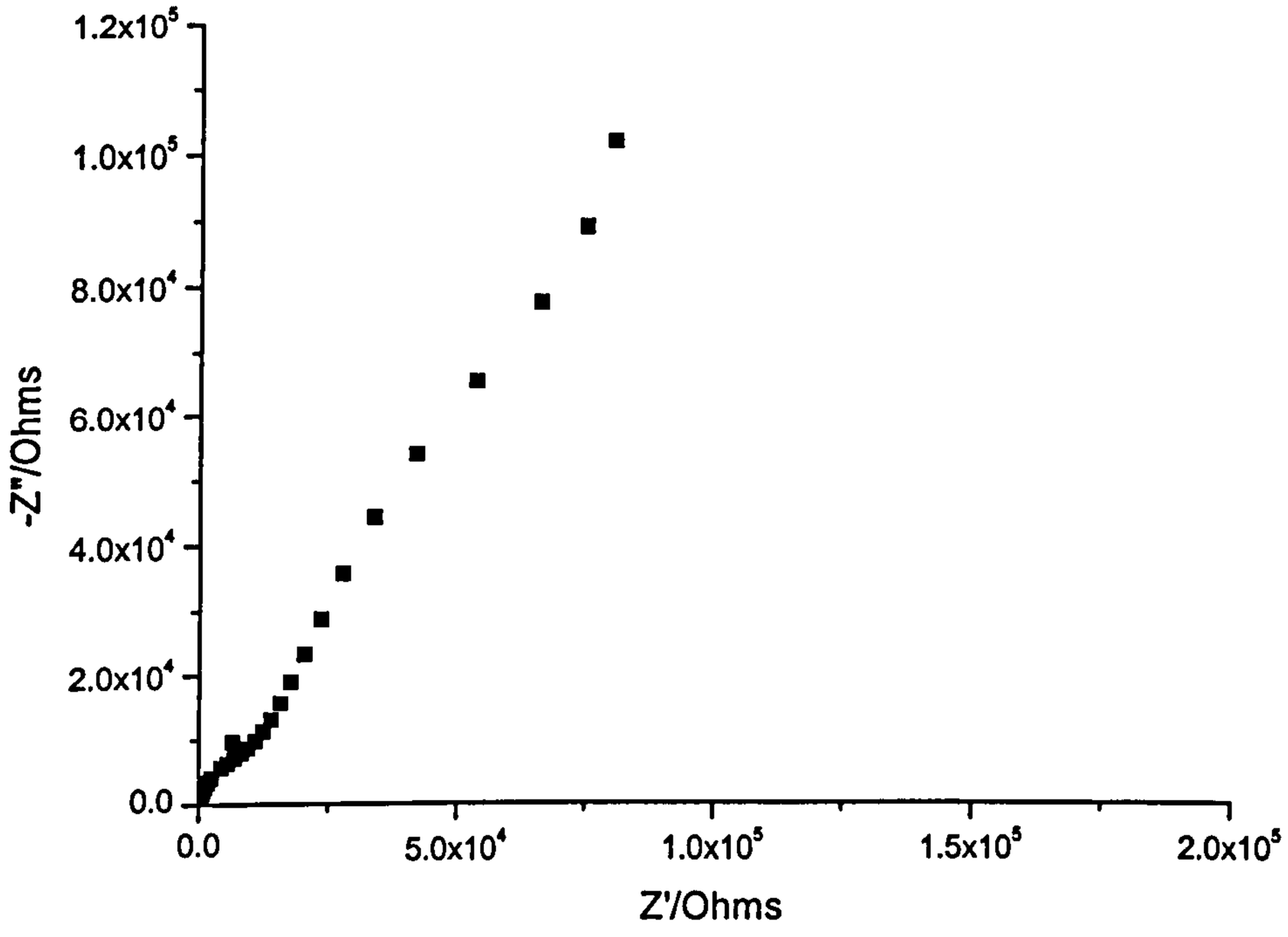

Figure 8.4(a) Complex plane impedance plot of the liquid cell Si/TEABF$_4$/PC (0.25M). Frequency range 65 kHz to 10 mHz.

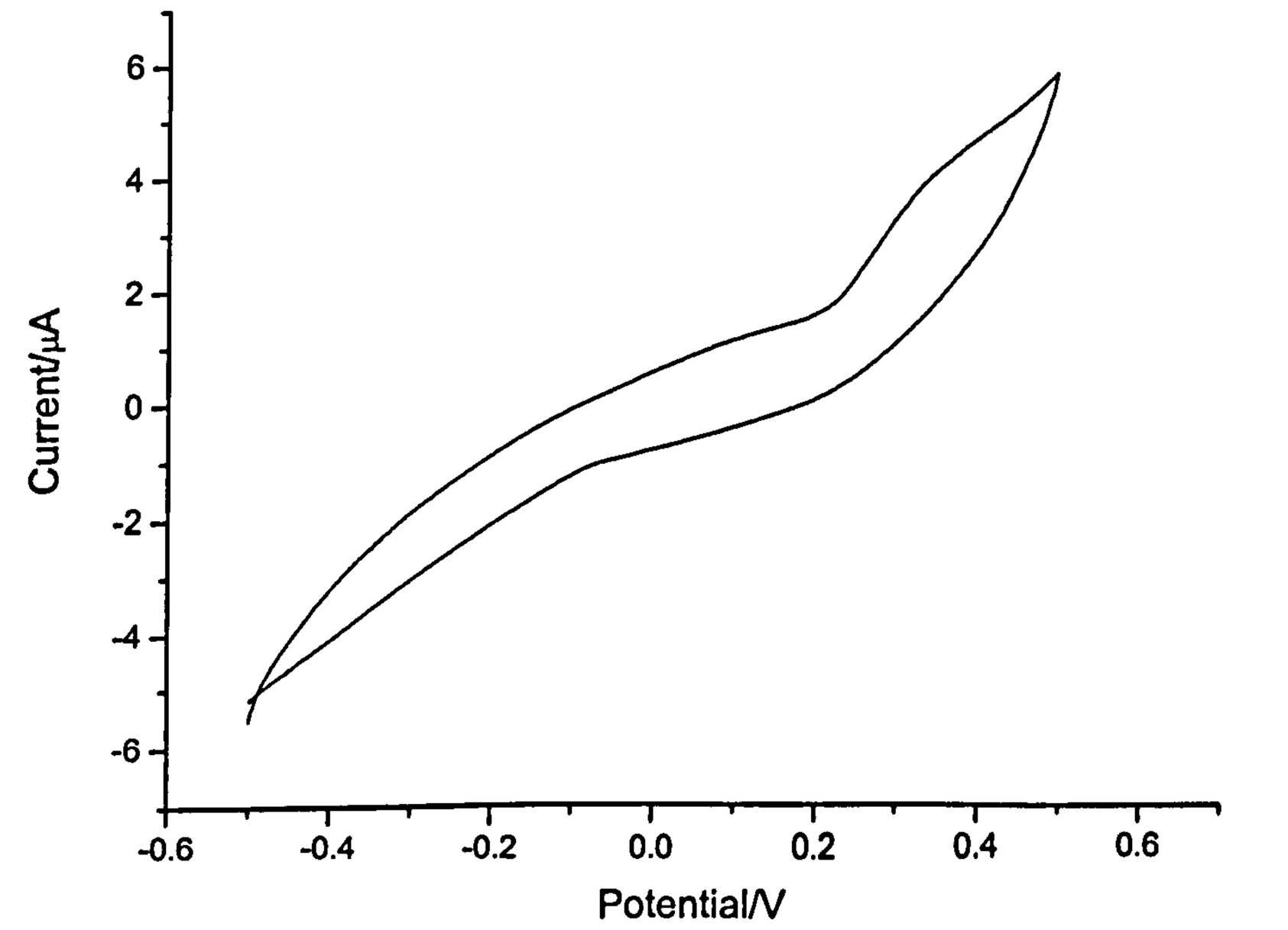

Figure 8.5 CV of the liquid cell Si/TEABF$_4$/PC (0.25M). Sweep rate 10mVs^{-1}, vs a floating potential.

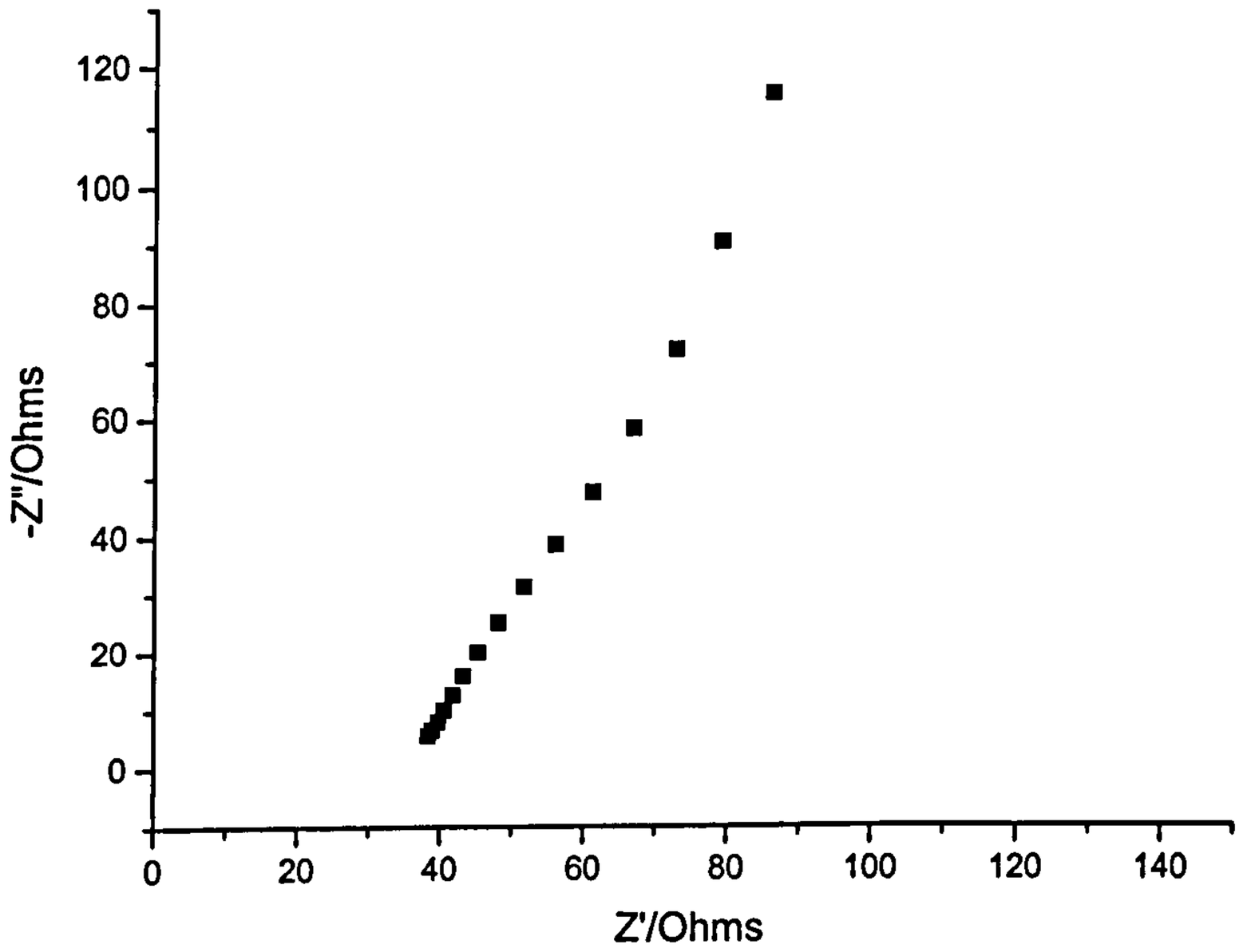

Figure 8.4(b) Enlarged view of the high frequency region of the complex plane plot of the cell Si/$TEABF_4$/PC (0.25M).

8.3.2 Anodically etched PSi electrodes with $TEABF_4$/PC electrolyte

PSi/$TEABF_4$/PC (0.25 M), supercapacitor cells were constructed and characterised using a.c. impedance spectroscopy and CV.

Figures 8.6 and 8.7 show the CV and complex plane impedance response of the cell PSi/$TEABF_4$/PC.

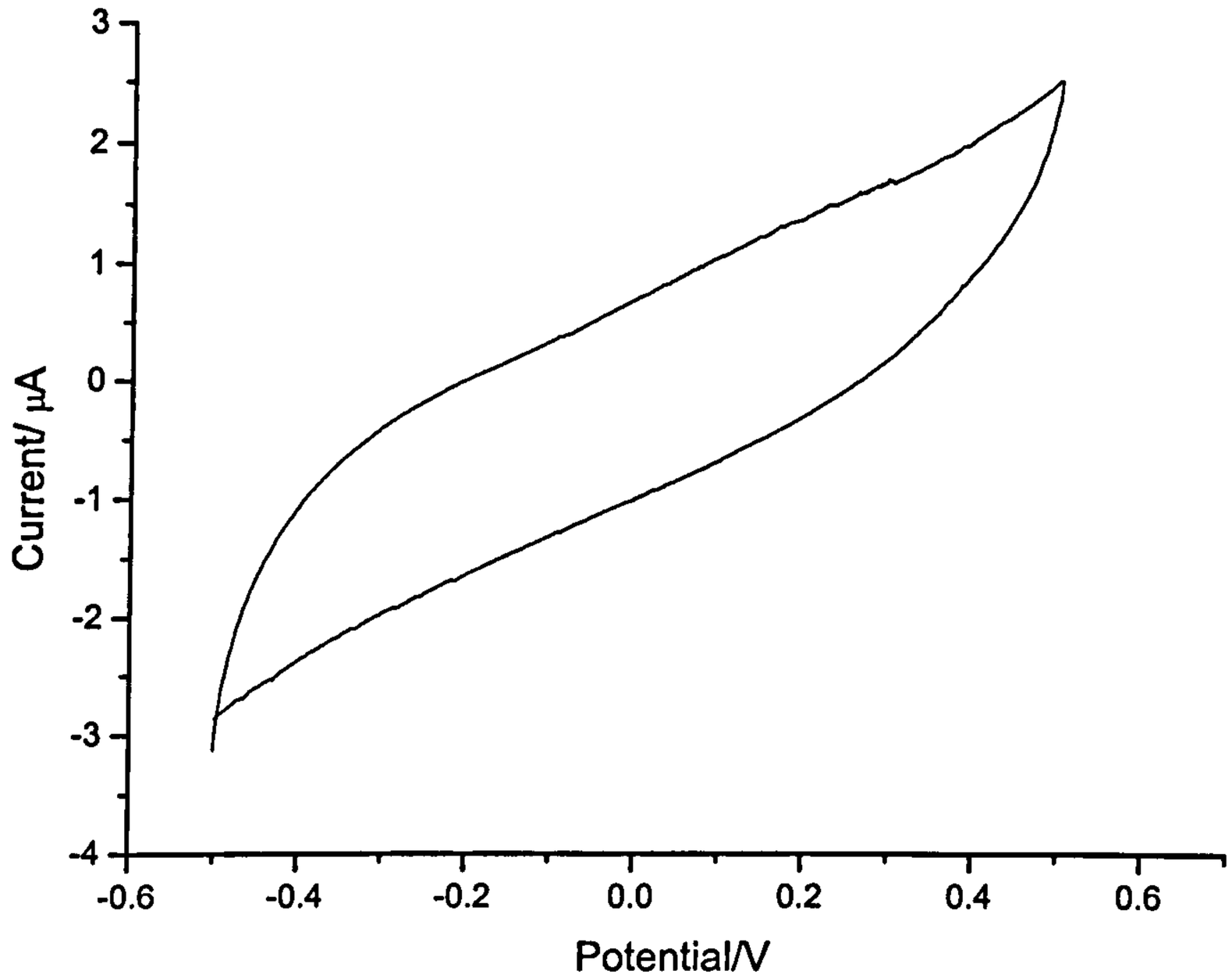

Figure 8.6 CV of cell PSi/$TEABF_4$/PC (0.25 M). Sweep rate 10 mVs^{-1}.

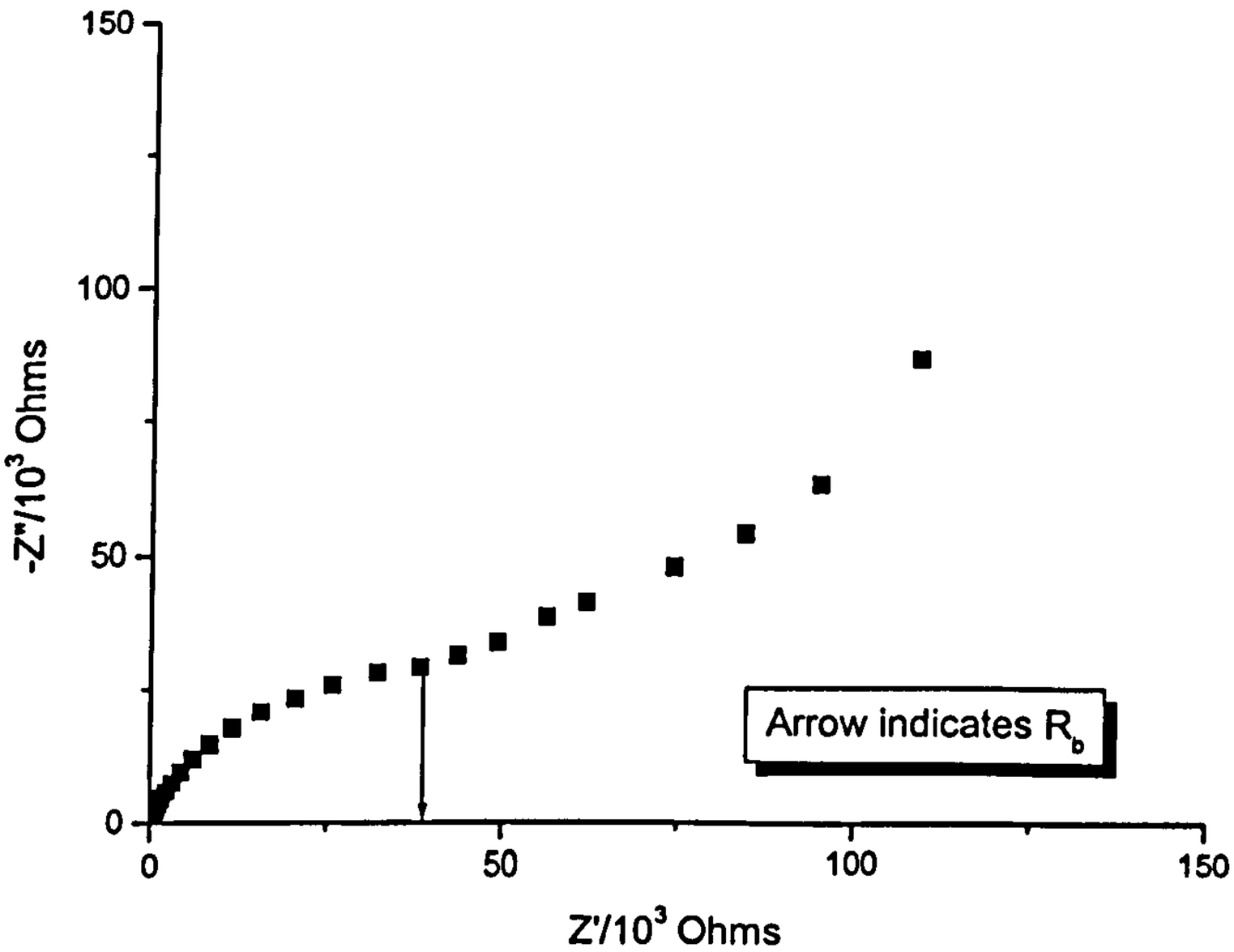

Figure 8.7 Complex plane impedance response of the cell PSi/$TEABF_4$/PC (0.25 M). Frequency range of 65 kHz to 1 mHz.

PSi/$TEABF_4$/PC (0.25 M) configuration shows poor capacitive characteristics. At the low frequency region the complex plane impedance plot, figure 8.7, shows erratic behaviour. Also the bulk resistance of the device is in the order of 40 kΩ, since the bulk resistance is taken at the midpoint between the intersection of the vertical spike and the extrapolation of the semi-circle onto the real axis of the complex plane, as shown in figure 8.7.

Both the CV and impedance data for the PSi cell deviate somewhat from ideality. The CV curves are not as smooth as those are for carbon, as reported in chapter 7. They are less rectangular, slightly tilted and show self-discharge characteristics at the extremes of the potential window.

These phenomena may be explained by considering the active surface of the porous layer. The surface oxide is not a uniform one and the porous layer may be looked upon as series of defects in the crystal lattice. Further dislocations occur within the porous layer when the etch solution it removed (the water stabilises the porous structure, as described in chapter 8.2). These defects, oxide islands and dislocations give rise to circulating electrochemical currents across the porous layer [2]. Thus fluctuations in the measured current are observed in the CV data and what appears to be random impedance data at low frequency regions are observed in the a.c. impedance analysis (figure 8.8). The self-discharge does not seem to be due to normal overpotential induced discharge since it also occurs at lower potential sweeps. This discharge route could be due to faradic charge transfer associated with surface impurities and oxide islands.

A possible method for reducing the oxide growth on the PSi surface was to coat the surface with a thin layer of gold. The technique used to coat the PSi with gold was an a.c. sputtering technique, identical to that used to sputter gold onto electronegative surfaces when obtaining SEM images.

8.3.2.1 Gold sputtering technique

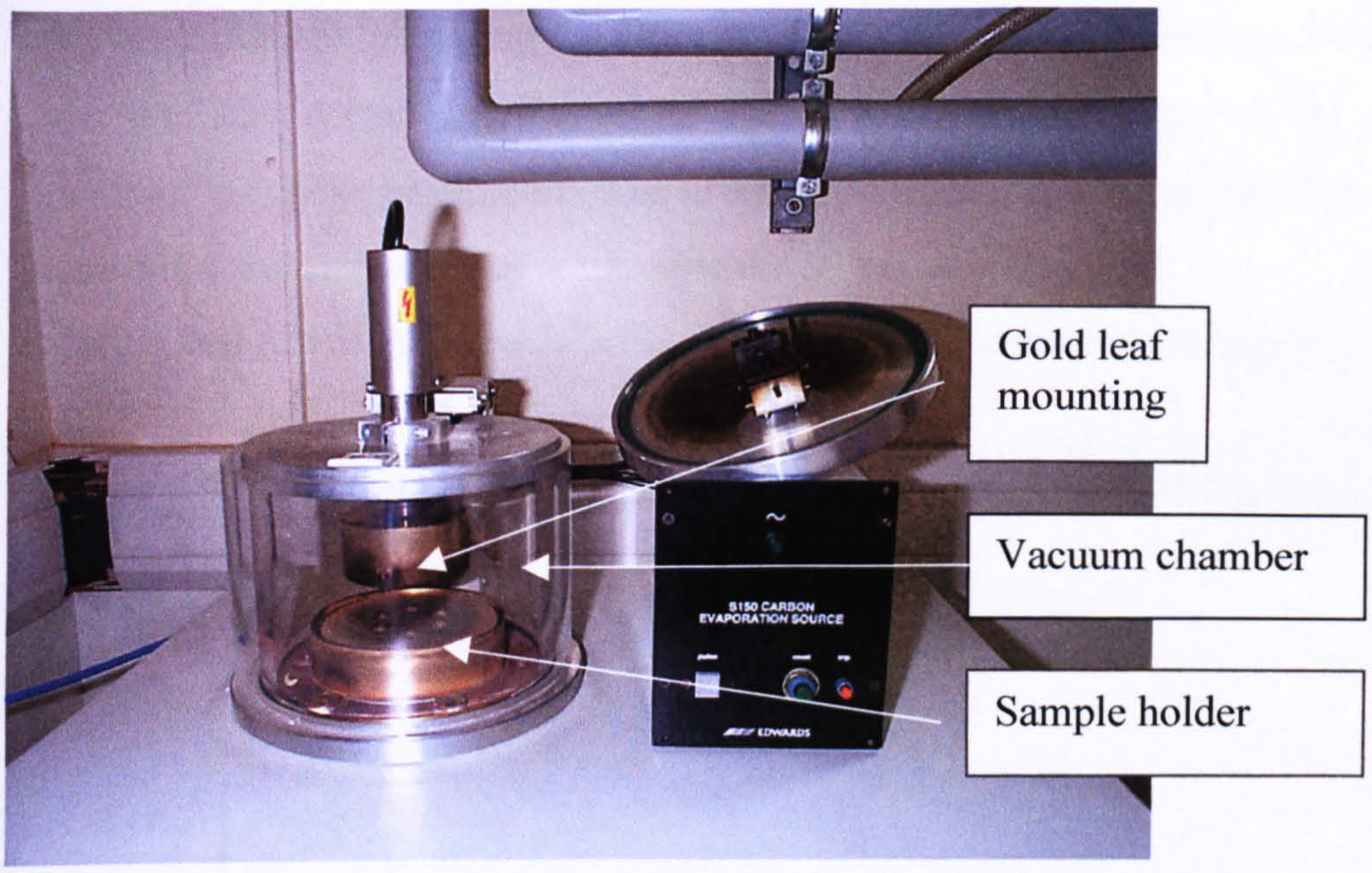

Figure 8.8 Photograph of the gold sputtering chamber used to coat the PSi with a 300Å layer of gold.

The samples were loaded onto the holder and the chamber was pumped down to a pressure of 0.1 mbar.
Argon was introduced into the chamber until a pressure of 2 to 4 mbar was attained.
An a.c. current was passed across the argon filled chamber, which created a plasma.
The Argon plasma bombards the gold leaf and the sample is coated with a layer of gold.
In these experiments gold was deposited onto the sample at a rate of 15 nm/min.

8.3.3 Anodically etched PSi/Au electrodes with $TEABF_4$/PC electrolyte

A 300 Å layer of gold was sputtered onto 1 cm^2 pieces of freshly prepared PSi. The etch conditions for preparing the PSi were a 15% ethanolic HF solution, with an etch current of 25 mA cm^{-2} for 10 minutes. The PSi was prepared using 0.02 Ω cm^{-1}, 111 orientated p-type crystalline Si. The reverse side of the wafer was coated in aluminium and annealed under nitrogen for 30 minutes at 550 °C.
A liquid cell of PSi/AU/$TEABF_4$/PC was prepared as described in chapter 7.1.

Figures 8.9 (a), (b) and 8.10 show the a.c. impedance response and the CV of the cell PSi/AU/$TEABF_4$/PC.

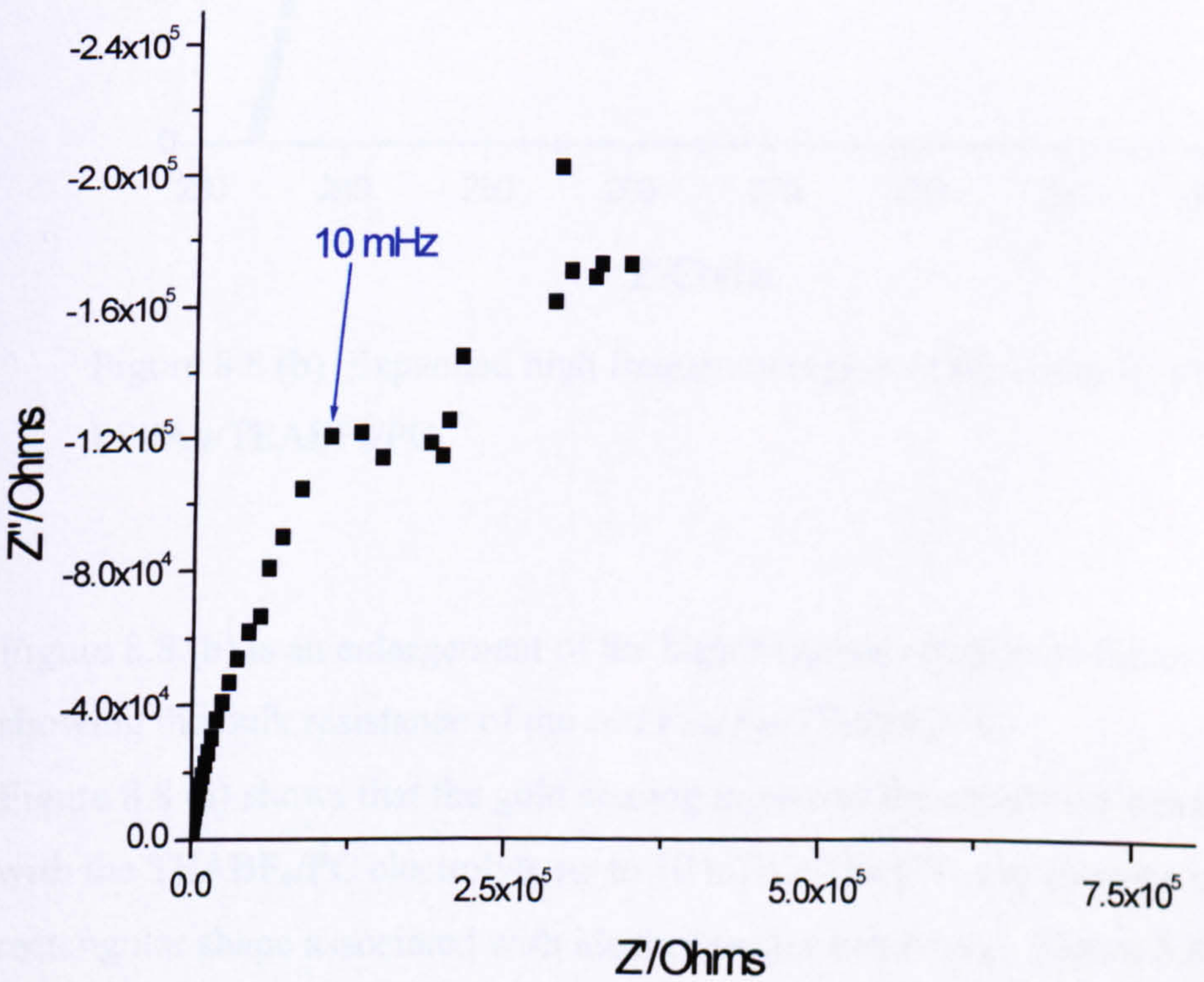

Figure 8.8 (a) Complex plane impedance plot of cell PSi/Au/$TEABF_4$/PC. Frequency range 65 kHz to 1 mHz.

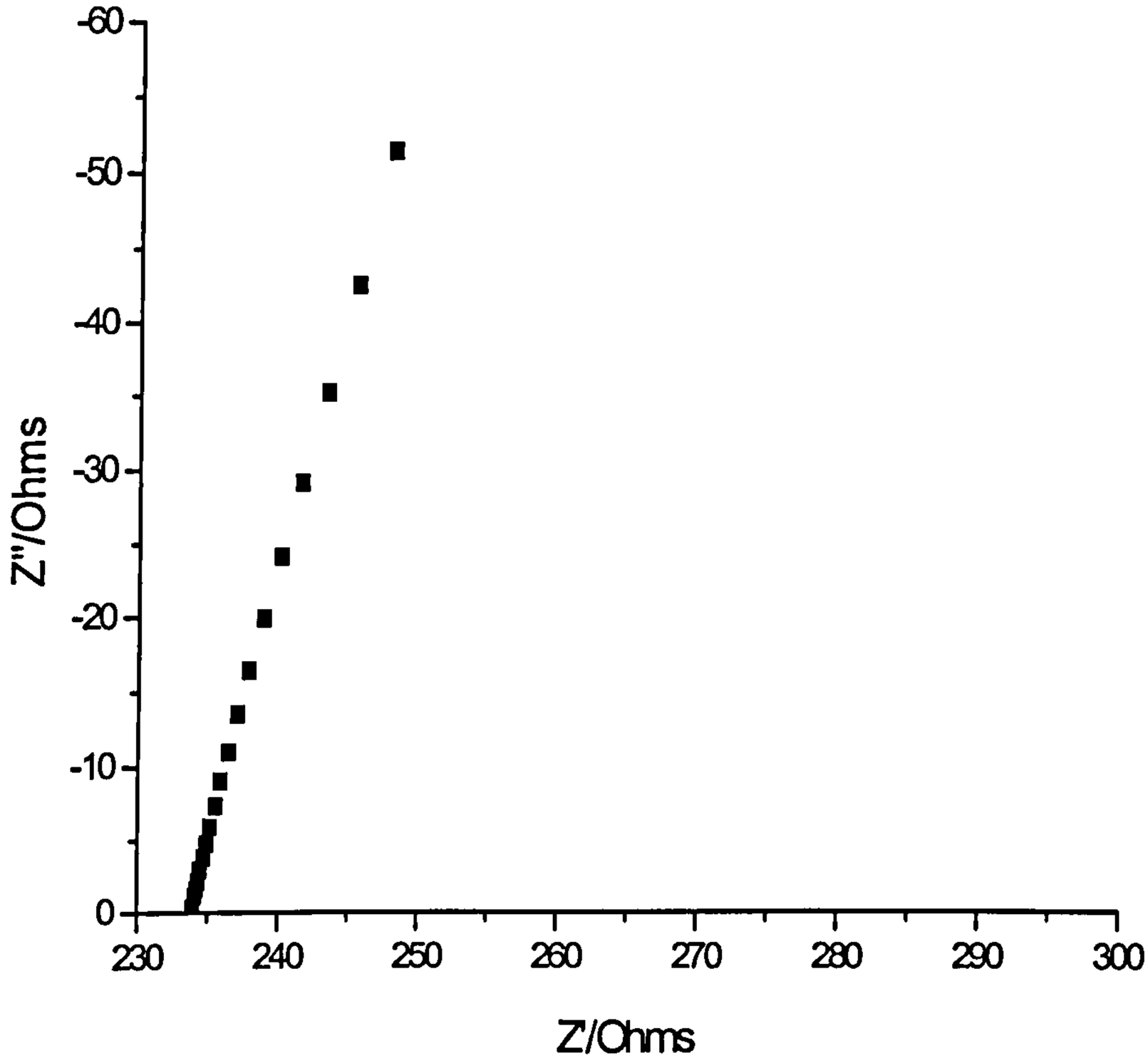

Figure 8.8 (b) Expanded high frequency region of the complex plane of cell PSi/Au/TEABF$_4$/PC.

Figure 8.8 (b) is an enlargement of the high frequency region of figure 8.8 (a) showing the bulk resistance of the cell PSi/Au/TEABF$_4$/PC.

Figure 8.8 (a) shows that the gold coating improves the capacitive behaviour of PSi with the TEABF$_4$/PC electrolyte up to 10 mHz. The CV also shows a more the rectangular shape associated with ideal capacitor behaviour. Figure 8.8 (b) shows that the bulk resistance has decreased from approximately 40 kΩ to 234 Ω, which is a marked improvement.

The capacitance calculated from the a.c. impedance at 10 mHz using equation 5.14, was 0.13 mF cm^{-2} relating to a specific capacity of 2.21 mF g^{-1}. The capacitance calculated from the CV at zero potential using equation 5.4, was 0.12 mF cm^{-2}, relating to a specific capacitance of 2.04 mF g^{-1}.

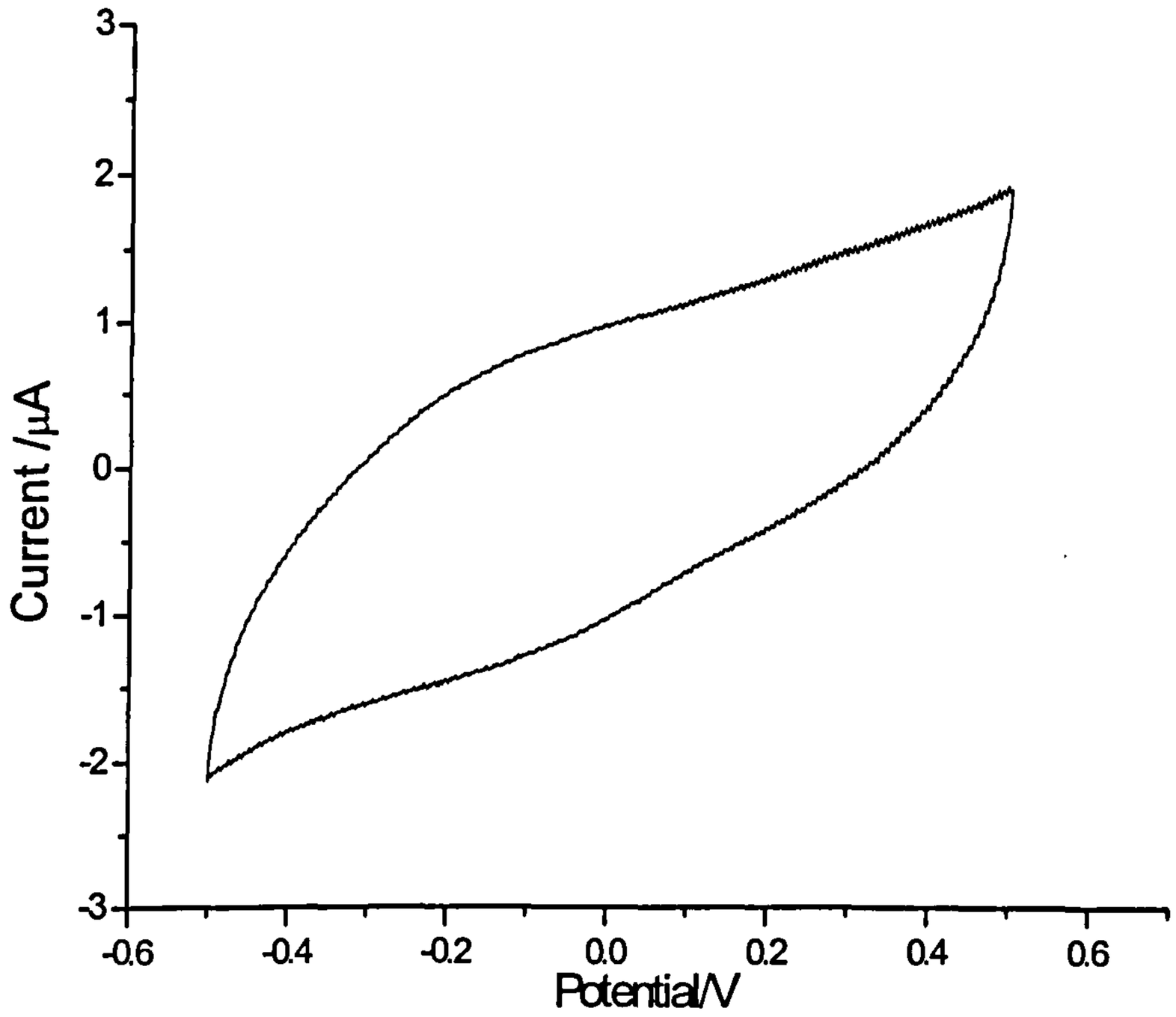

Figure 8.9 CV of cell PSi/Au/$TEABF_4$/PC. Sweep rate 10 mV s^{-1}.

8.3.4 Anodically etched PSi electrodes with PU electrolyte

PSi/PU (PU electrolyte composition as was described in chapter 6), supercapacitor cells were constructed and analysed using a.c. impedance spectroscopy and CV. The etch conditions were a 15% ethanolic HF solution, with an etch current of 25 mA cm^{-2} for 10 minutes. The PSi was prepared using 0.02 Ω cm^{-1}, 111 orientated p-type crystalline Si. The reverse side of the wafer was coated in aluminium and annealed under nitrogen for 30 minutes at 550 °C.

Figures 8.10 and 8.11 show the complex plane impedance response and CV of the PSi/PU cell.

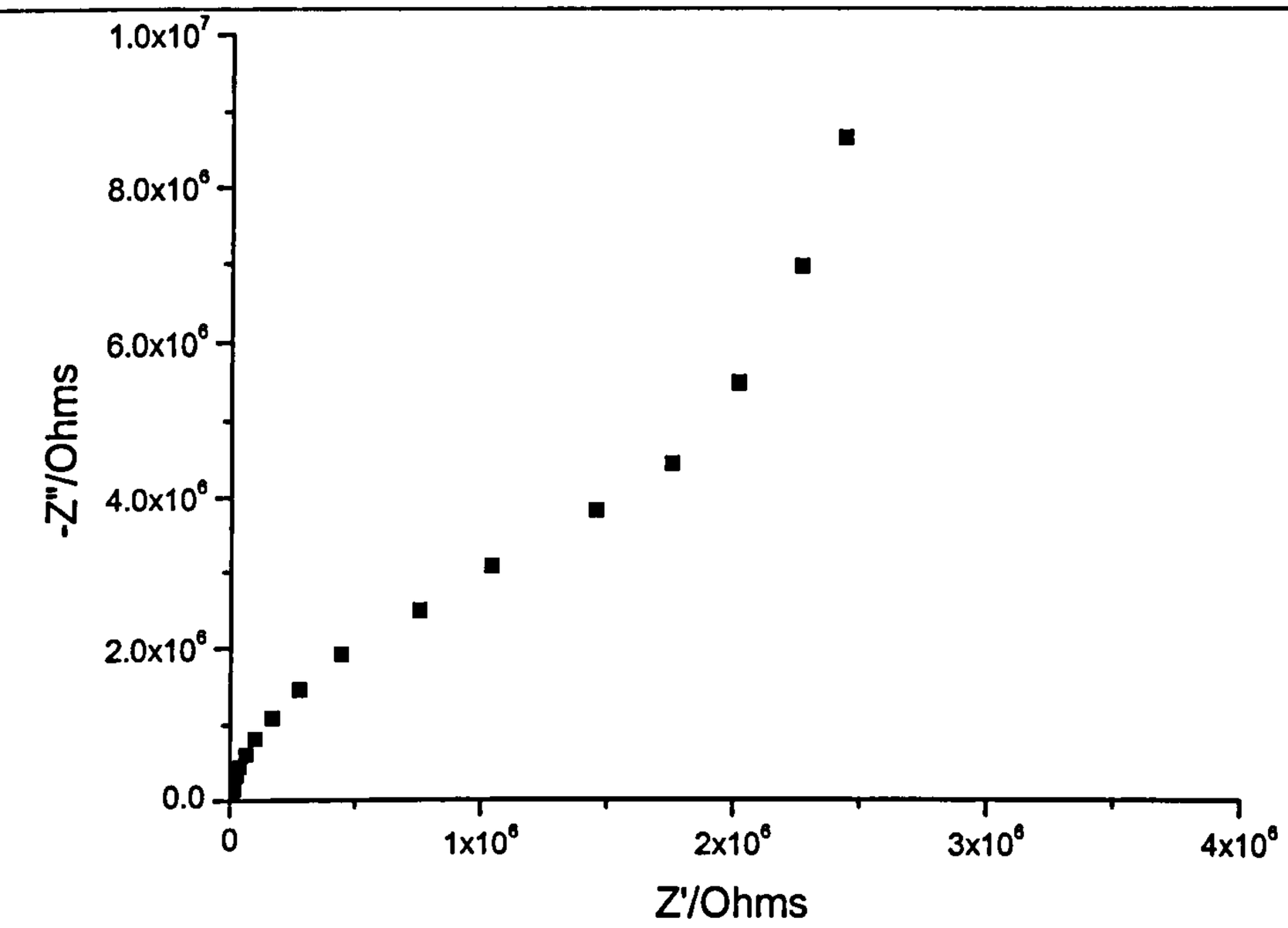

Figure 8.10 Complex plane impedance of PSi/PU cell.
Frequency range 65 kHz to 10 mHz.

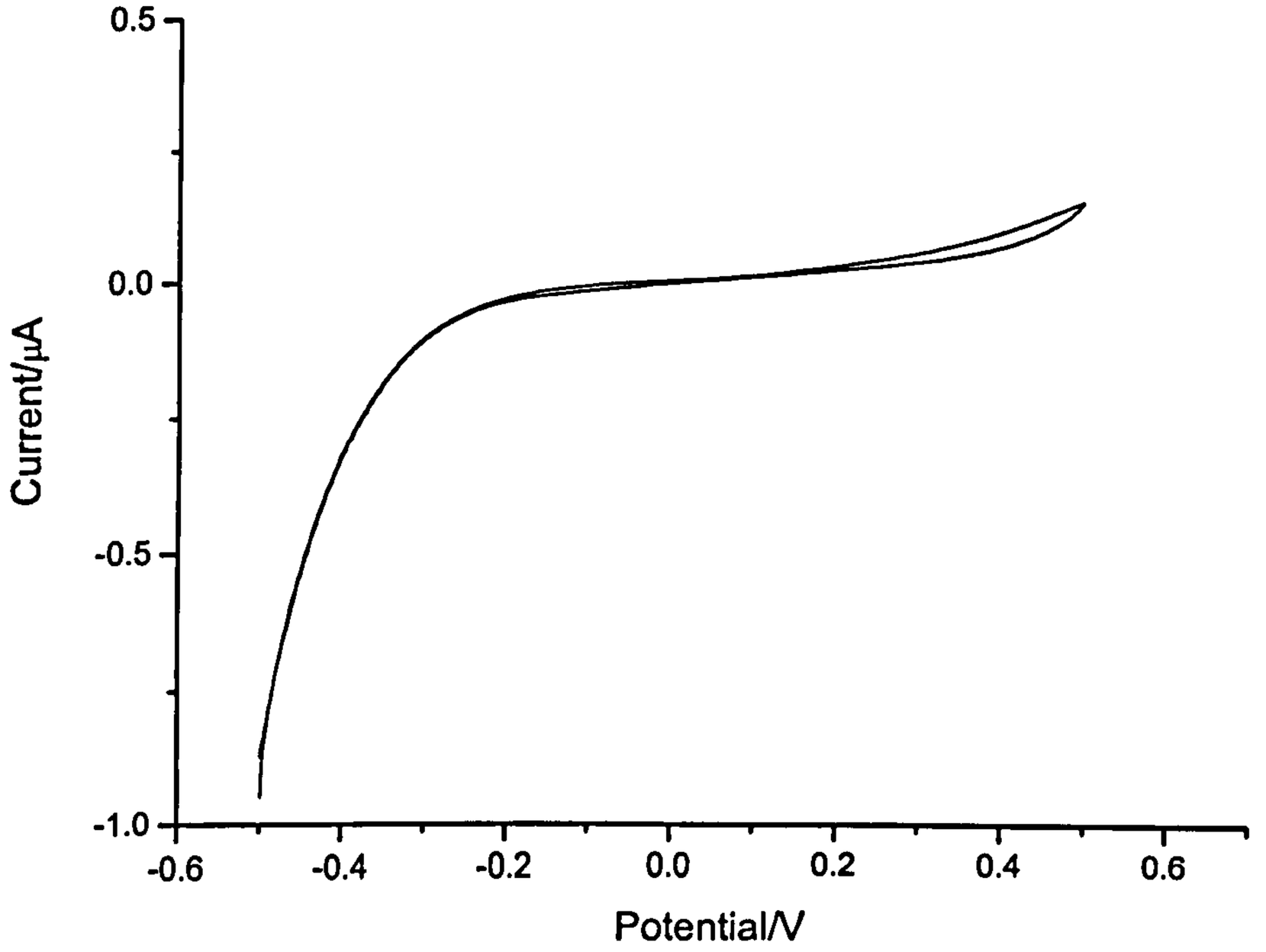

Figure 8.11 CV of cell PSi/PU. Sweep rate of 10 mV s^{-1}, vs a floating potential.

Figure 8.11 illustrates that there are virtually no capacitive characteristics for the PSi electrodes with the PU gel electrolyte. The common problem with supercapacitors using polymer or gel electrolytes is the poor contact between electrode and electrolyte. This problem is accentuated with PSi since the porous structure is nano-scale, i.e. much smaller than the micro-porous structure of common woven carbon fabrics, described in chapter 7 and the polymer electrolyte is apparently unable to penetrate the pores and maximise the effect of the surface area.

The capacitance calculated at 10 mHz using equation 5.14 was 1.7 $\mu F\ cm^{-2}$. This value was less than the values commonly attained for a liquid electrolyte with a planar electrode [3].

8.3.5 Anodically etched PSi/Au electrodes with PU electrolyte

A 300 Å layer of gold was sputtered onto a piece of anodically etched PSi. The etch conditions were as described in chapter 8.3.4.

The electrodes were analysed using a.c. impedance spectroscopy and CV. Figures 8.12 (a) and 8.13 show the complex plane and CV response for the cell PSi/Au/PU.

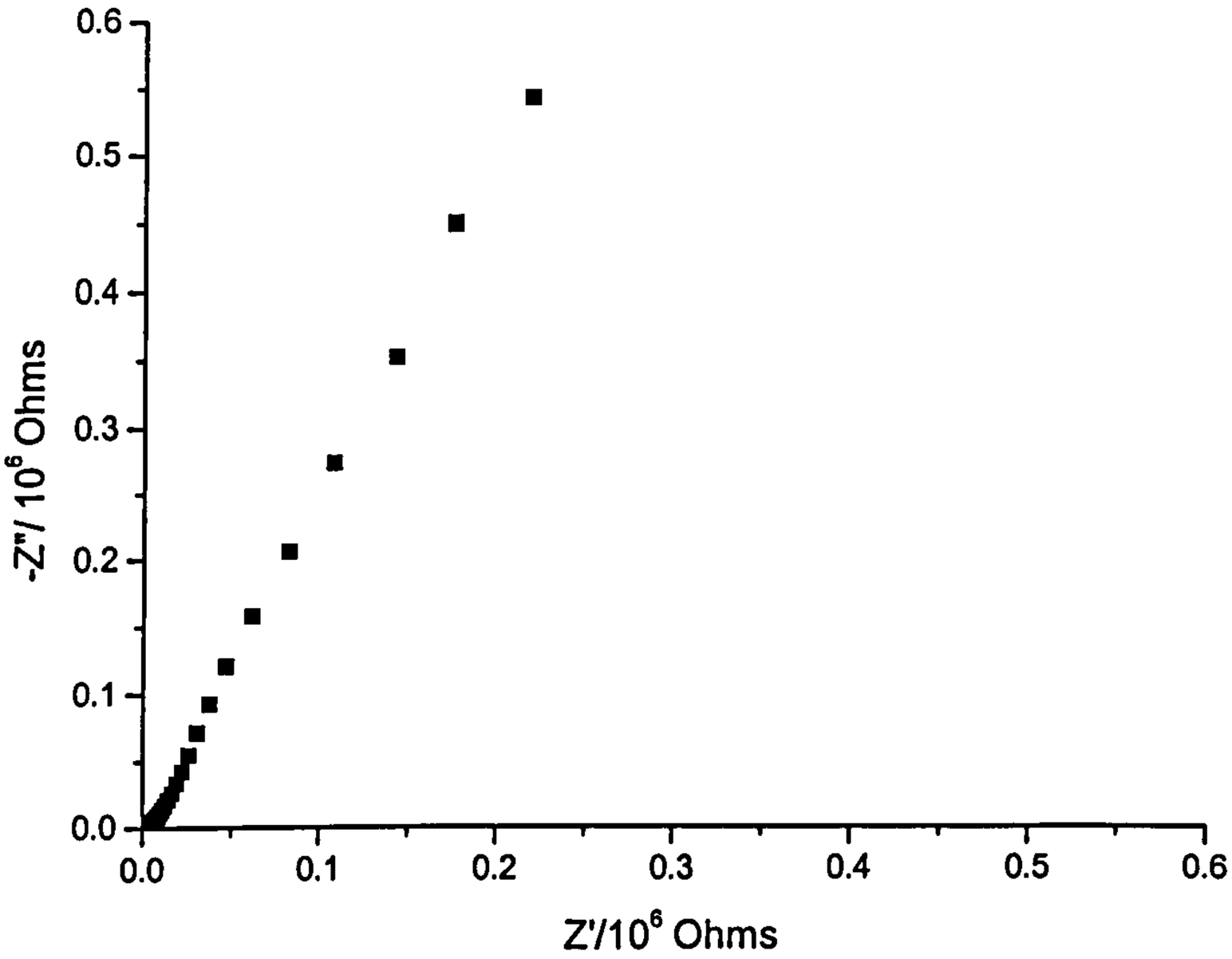

Figure 8.12 (a) Complex plane impedance of cell PSi/Au/PU. Frequency range 65 kHz to 10 mHz.

Figure 8.12 (b) is the high frequency region indicating the bulk resistance.

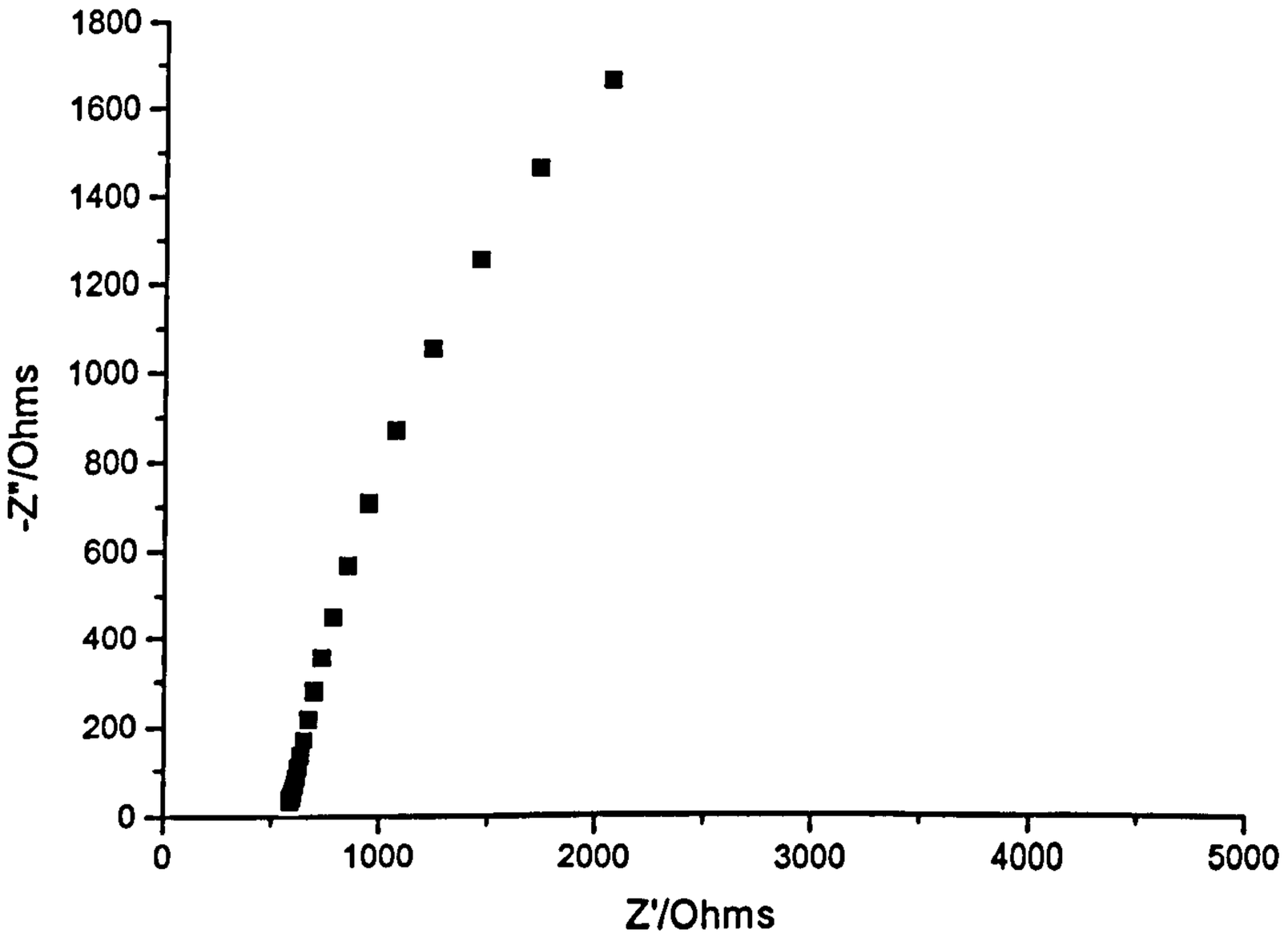

Figure 8.12 (b) Expanded high frequency region of the complex plane plot of cell PSi/Au/PU

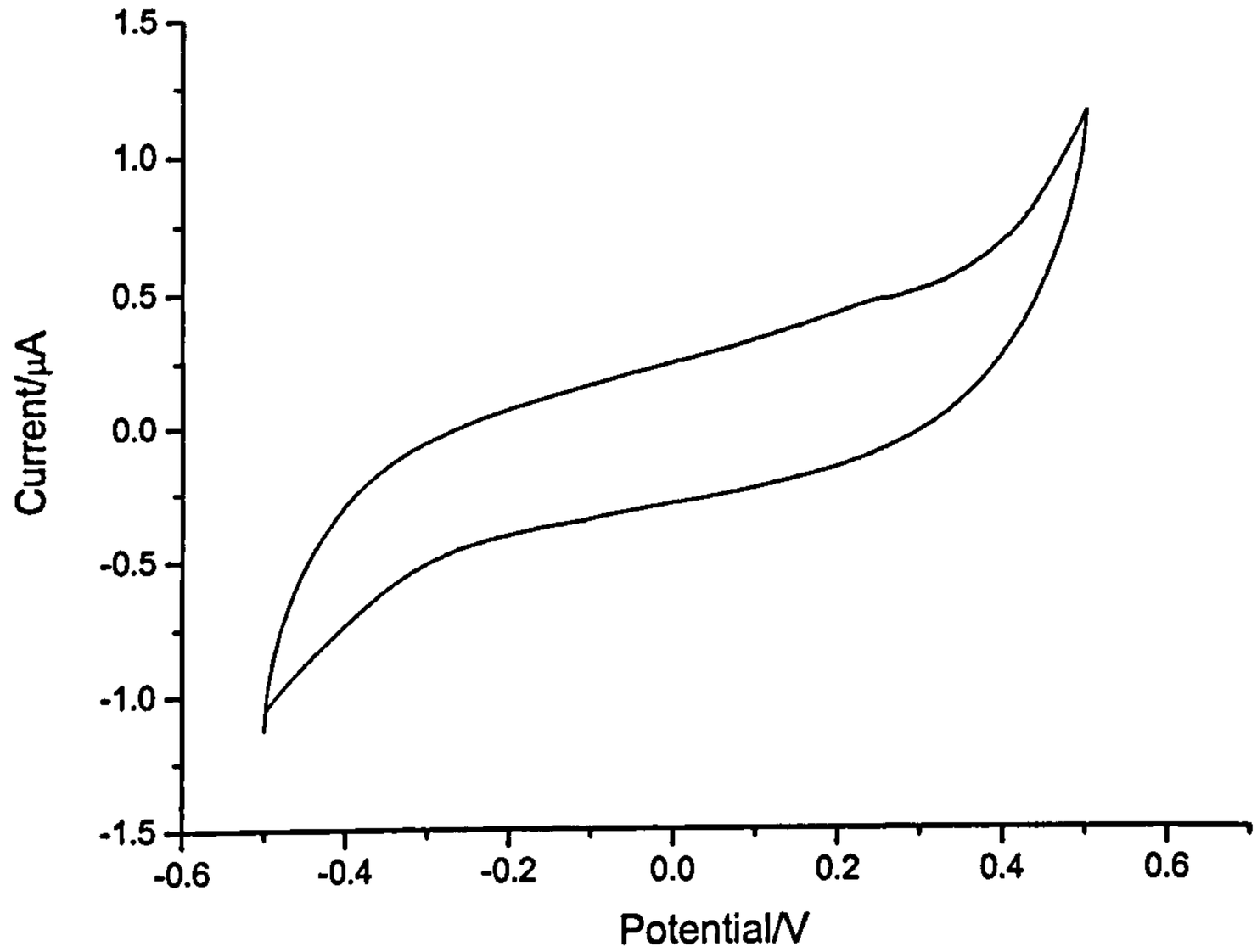

Figure 8.13 CV plot of cell PSi/Au/PU. Sweep rate 10 mV s^{-1} vs floating potential.

Coating the PSi with a 300-Å layer of gold has increased the capacitive characteristics of the cell. The steeper vertical spike in figure 8.12 (a) demonstrates this. The CV trace in figure 8.13 also showed a more rectangular shape associated with that of an ideal capacitor.

Some self-discharge characteristics at the extremes of the potential window are still evident. However, a marked improvement is observed when a layer of gold is deposited. This was also the case for the system for the corresponding liquid electrolyte cell PSi/Au/$TBABF_4$/PC described in section 8.3.3. Figure 8.12 (b) showed the bulk resistance of the cell has improved dramatically with a decrease from tens of kΩ to 600 Ω. This is a marked improvement but still too high to be considered a good candidate for supercapacitor devices.

The capacitance calculated at 10 mHz using equation 5.14 was 29.5 μF cm^{-2}, relating to a specific capacitance of 0.50 mF g^{-1}. The capacitance calculated from CV data using equation 5.4 was 27μF cm^{-2}, relating to a specific capacitance of 0.46 mF g^{-1}.

8.3.6 Stain etched PSi/Au with $TEABF_4$/PC electrolyte

The stain or chemical etch solution was HF/HNO_3/EtOH, in a 1:5:3 ratio respectively. Absolute ethanol was used in place of water due to its superior surface wetting ability.

An identical Si wafer to those described in sections 8.3.1 to 8.3.5 was used. A well was formed on the wafer surface using adhesive PTFE tape. The etch solution was poured into the well and left for 2 minutes. The resulting PSi was washed in pentane and dried under nitrogen.

Two capacitor cell configurations were prepared and analysed using a.c. impedance spectroscopy and CV. The two cells were,

i. Stain etched PSi/Au/$TEABF_4$/PC (0.25M)
ii. Stain etched PSi/Au/PU gel electrolyte

For the stain etched systems only those coated with gold were analysed since anodically etched PSi electrodes alone did not show capacitive characteristics. The gold was a 300 Å layer deposited in the same manner as described in section 8.3.2.1.

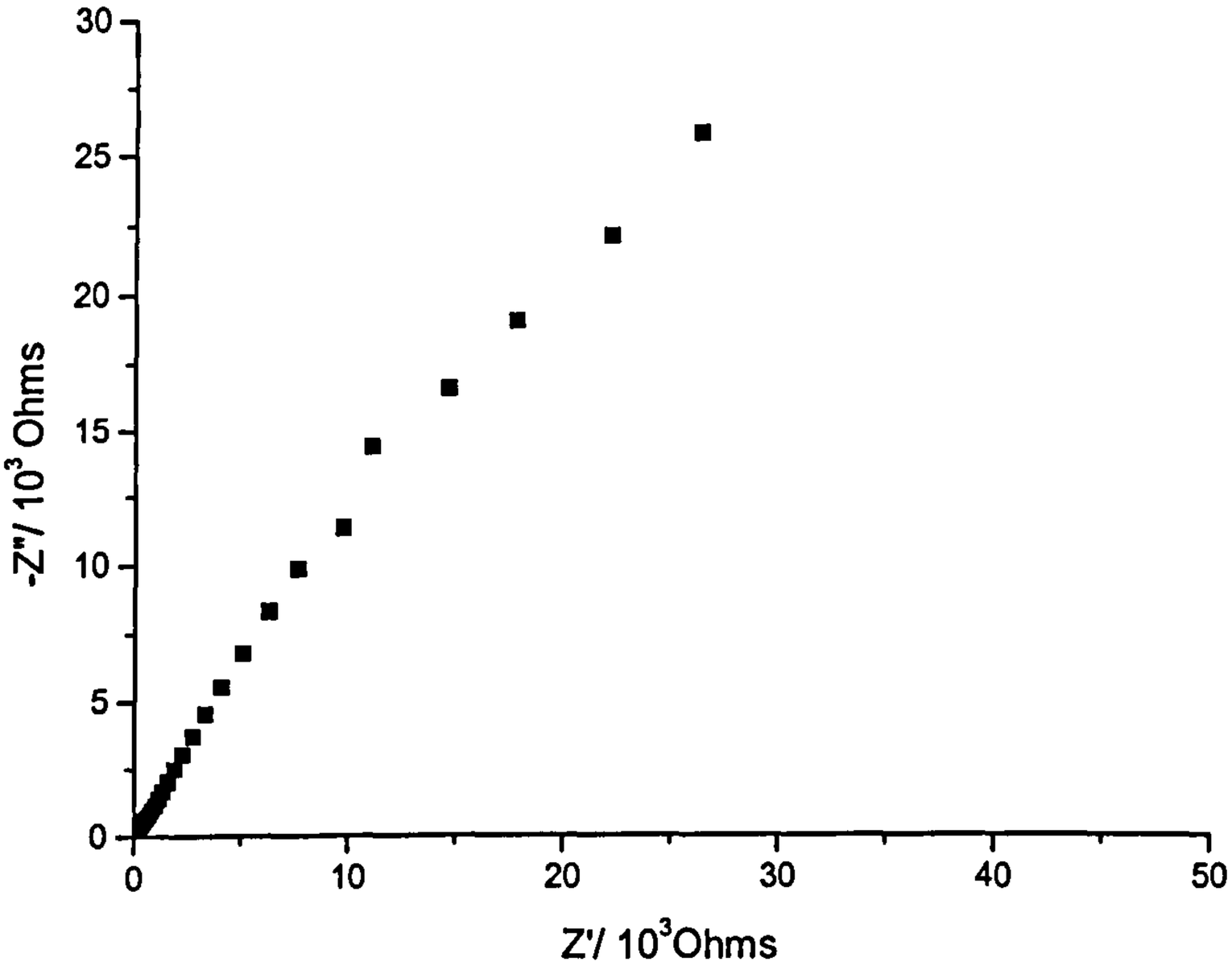

Figure 8.14 (a) Complex plane impedance of the stain etched PSi/Au/TEABF$_4$/PC cell.

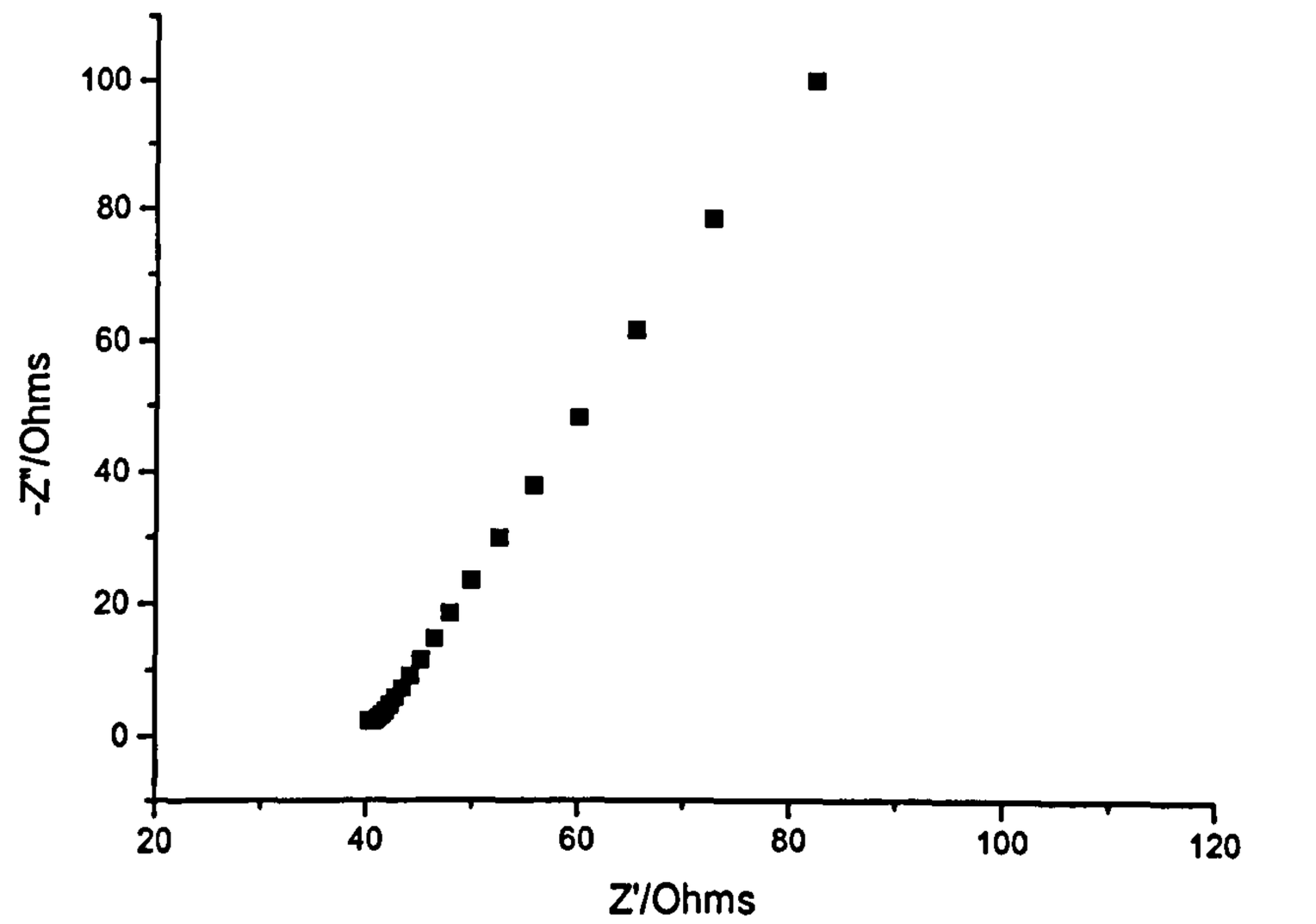

Figure 8.14 (b) Expanded high frequency region of the complex plane impedance of the stain etched PSi/Au/TEABF$_4$/PC cell.

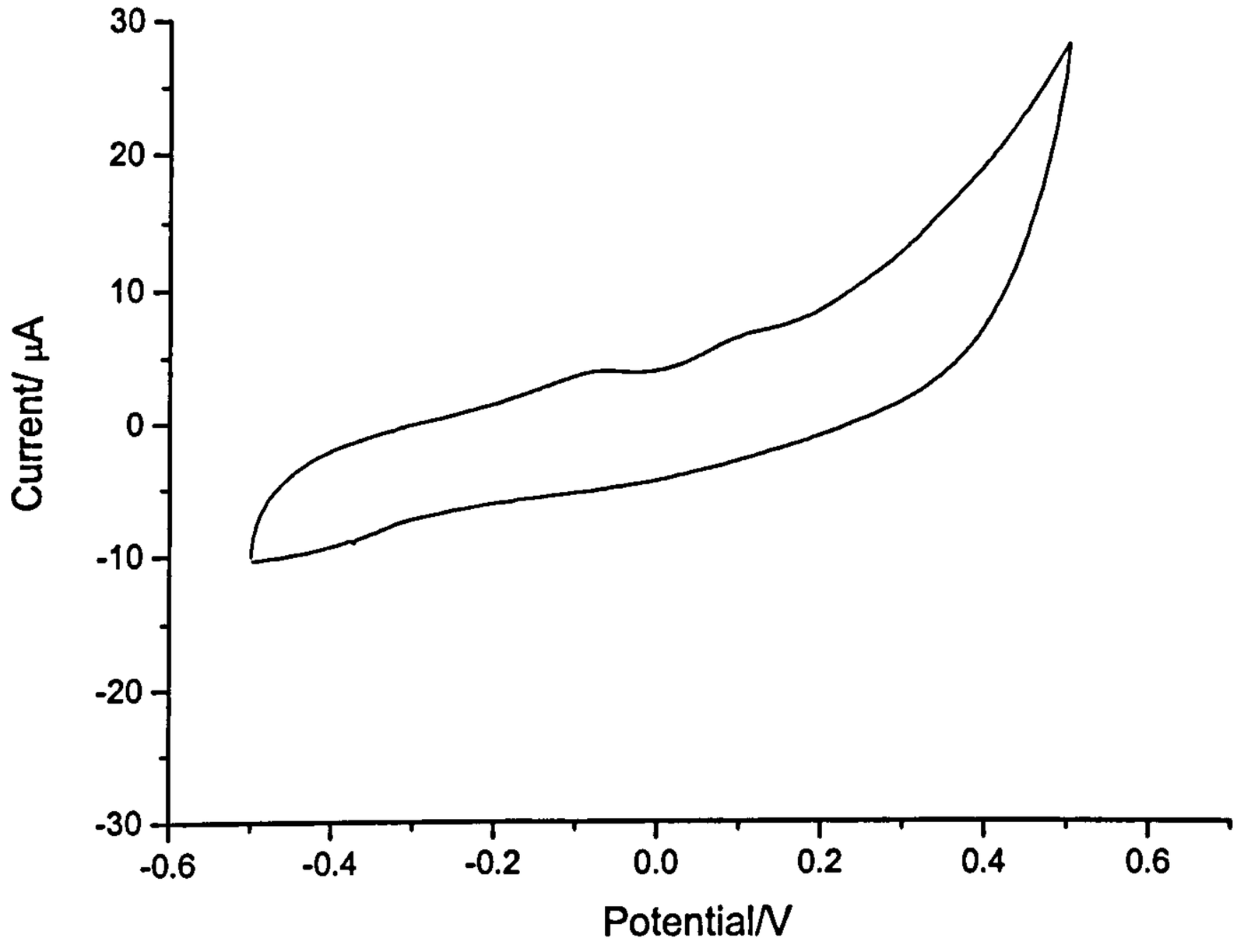

Figure 8.15 CV plot of the stain etched PSi/Au/TEABF$_4$/PC (0.25M) cell. Sweep rate 10 mV s^{-1}. Vs a floating potential.

The capacitance calculated at 10 mHz from equation 5.14 was 0.6 mF cm^{-2} and from the CV data using equation 5.4, 0.5 mF cm^{-2}.

Comparing the capacity calculated from the anodically etched PSi/Au/TEABF$_4$/PC cell with the capacitance calculated for the stain etched PSi/Au/TEABF$_4$/PC cell, a factor of ten difference was obtained. Also the bulk resistance was a factor of ten less for the stain etched PSi.

The difference in bulk resistance was due to the anodically etched PSi having a multi-layered structure, whereas multi-layering occurs to a much less extent in stain etched PSi. Therefore the stain etched PSi shows a lower resistance.

Anodically etched PSi has a much higher surface area and one would expect therefore a higher capacitance. Due to the multi-layer structure, however, a large percentage of the PSi surface area is not accessible to the electrolyte and therefore explains the relatively low capacitance values obtained for the cell.

8.3.7 Stain etched PSi/Au with PU electrolyte

The gold coated PSi electrodes were prepared as described in section 8.3.6. Capacitor cells were prepared using the PU gel electrolyte as described in chapter 6 and analysed with a.c. impedance spectroscopy and CV.

Figures 8.16 and 8.17 show the complex plane and CV of the cell PSi/Au/PU.

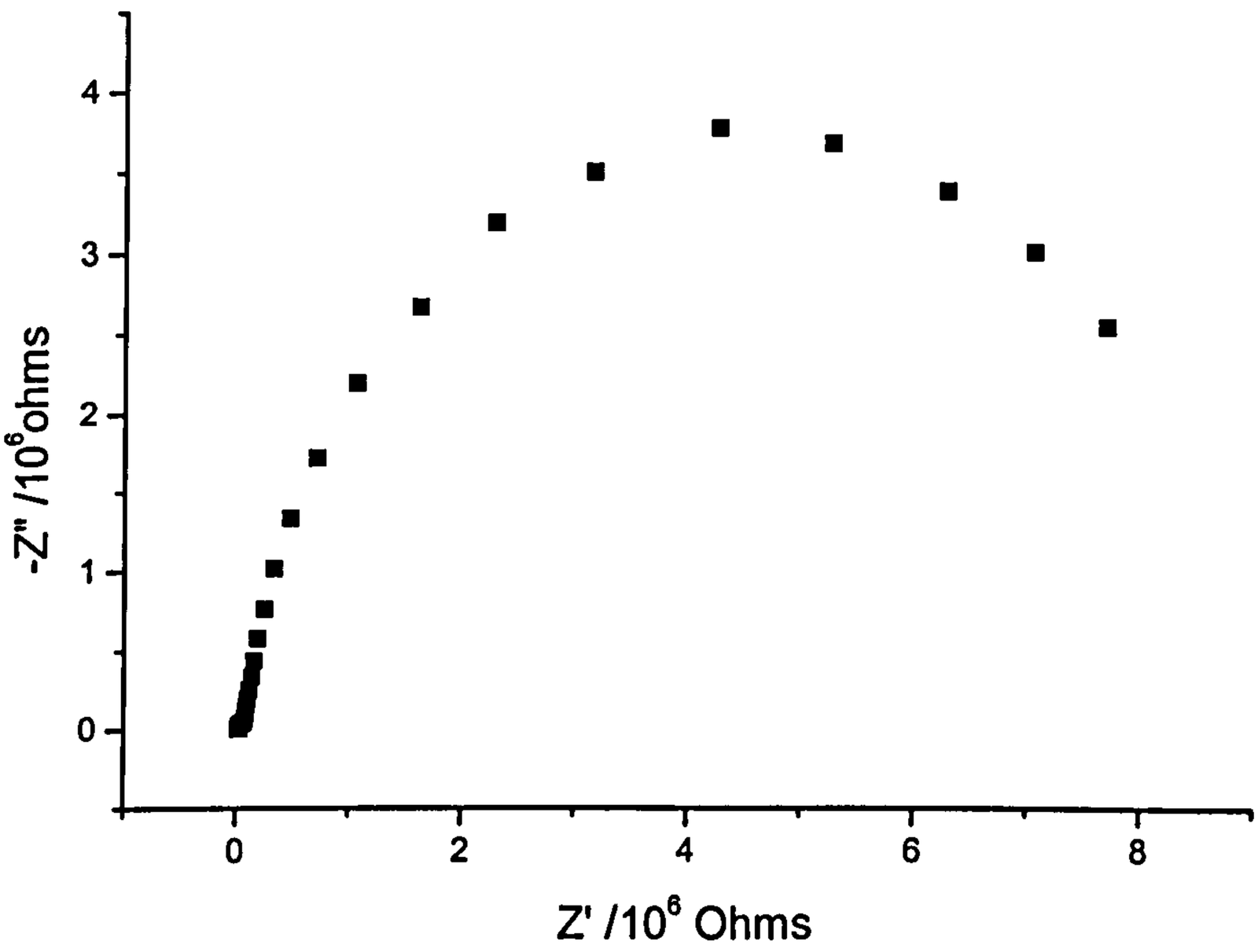

Figure 8.16 Complex plane of the cell stain etched PSi/Au/PU. Frequency range 65 kHz to 10 mHz.

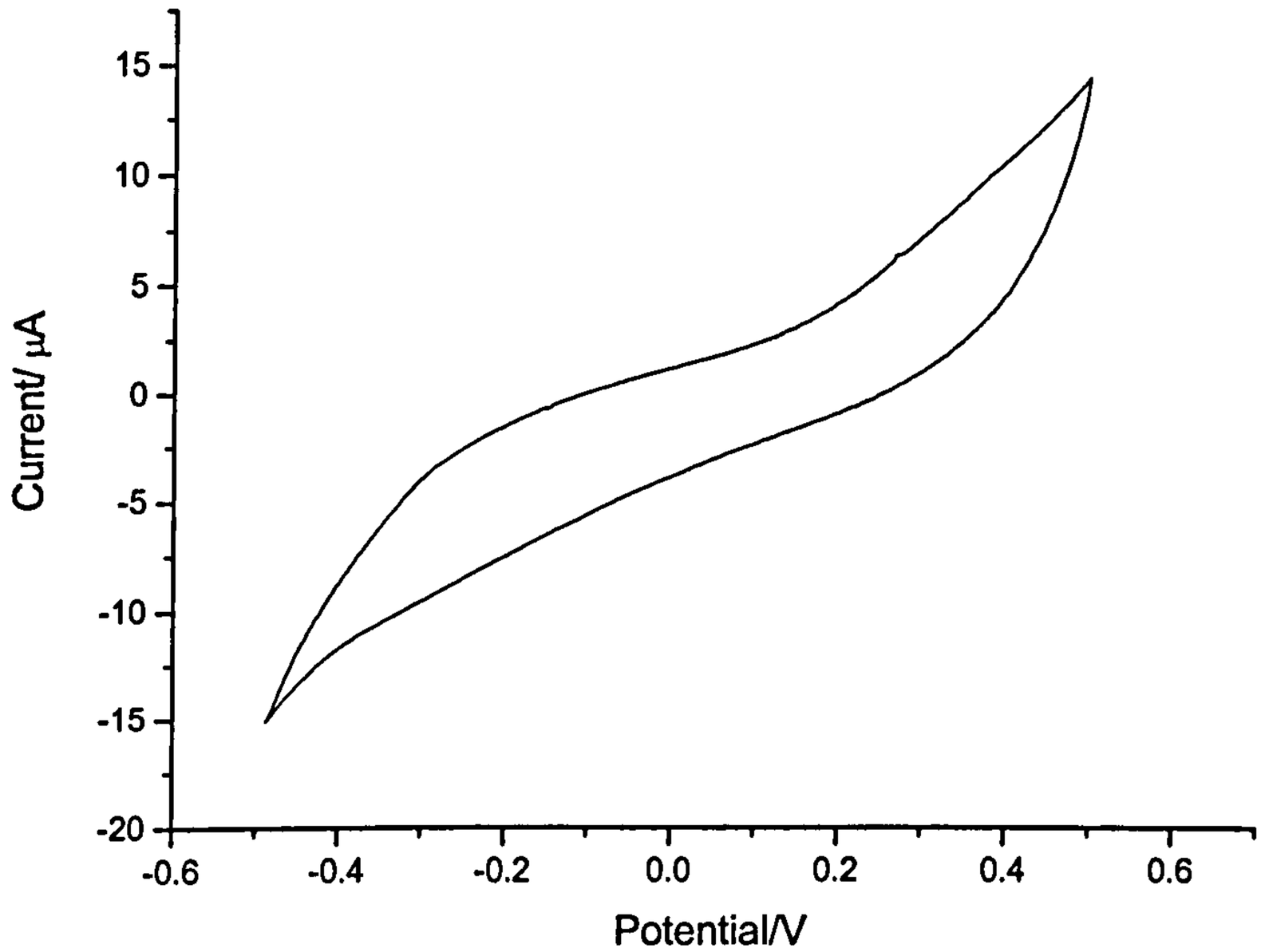

Figure 8.17 CV plot of the stain etched PSi/Au/PU cell. Sweep rate 10 mV s^{-1}. Vs a floating potential.

Figure 8.16 shows a large semi-circle in the complex plane, suggesting a large interfacial resistance between the electrode and gel electrolyte. Therefore intimate contact between the electrode and electrolyte was not occurring.

Figure 8.8, 8.9, 8.12 and 8.13 demonstrate that the production of an EDLC is possible using gold coated PSi. It is, however important to have a lower bulk resistance than the hundreds of Ohms associated with the cells comprised of PSi/Au/PU. A possible method for the lowering of the bulk resistance was to vacuum deposit a thin layer of Si onto a mechanically stable substrate. Advantages were also anticipated in that the specific capacitance values would be enhanced because a smaller quantity of active electrode material would be involved. Chapter 8.4 describes the deposition method and the results obtained.

It was thought that the poor capacitive characteristics shown for cell PSi/PU was due to the inability of the electrolyte to penetrate the porous structure of the PSi. This certainly contributes to the problem but cannot be the sole reason. When the PSi electrodes were coated with gold a marked improvement in capacitive characteristics was observed, the layer of gold would reduce the pore size further but still a larger capacitance value is obtained for the cell PSi/Au/PU.

8.4 Thin layer Silicon

A thin layer of silicon was vacuum deposited onto a glass microscope slide using a CVC sputter unit coupled with a UFC-1210 mass flow controller/ URS-100-5 readout supply (unit instruments, inc.) and an MDX power supply.

The major handicap with this work was the lack of adhesion of the Si to various conductive substrates such as aluminium or chromium. Early attempts at depositing silicon onto deposited aluminium and chromium failed since the silicon peeled off the substrate. The reason for this was postulated to be due to the exposure of the substrate to an unclean atmosphere before being introduced into the CVC sputter unit. The CVC d.c. sputtering equipment was able to sputter silicon and indium tin oxide, therefore indium tin oxide was deposited onto glass followed by silicon. In this case adhesion was not a major problem since the sample was kept inside the sputter chamber throughout the procedure.
The indium tin oxide was sputtered using a tin target coated with indium while oxygen was introduced into the chamber via the URS/mass flow controller.
A photograph of the equipment used is shown in figure 8.18.

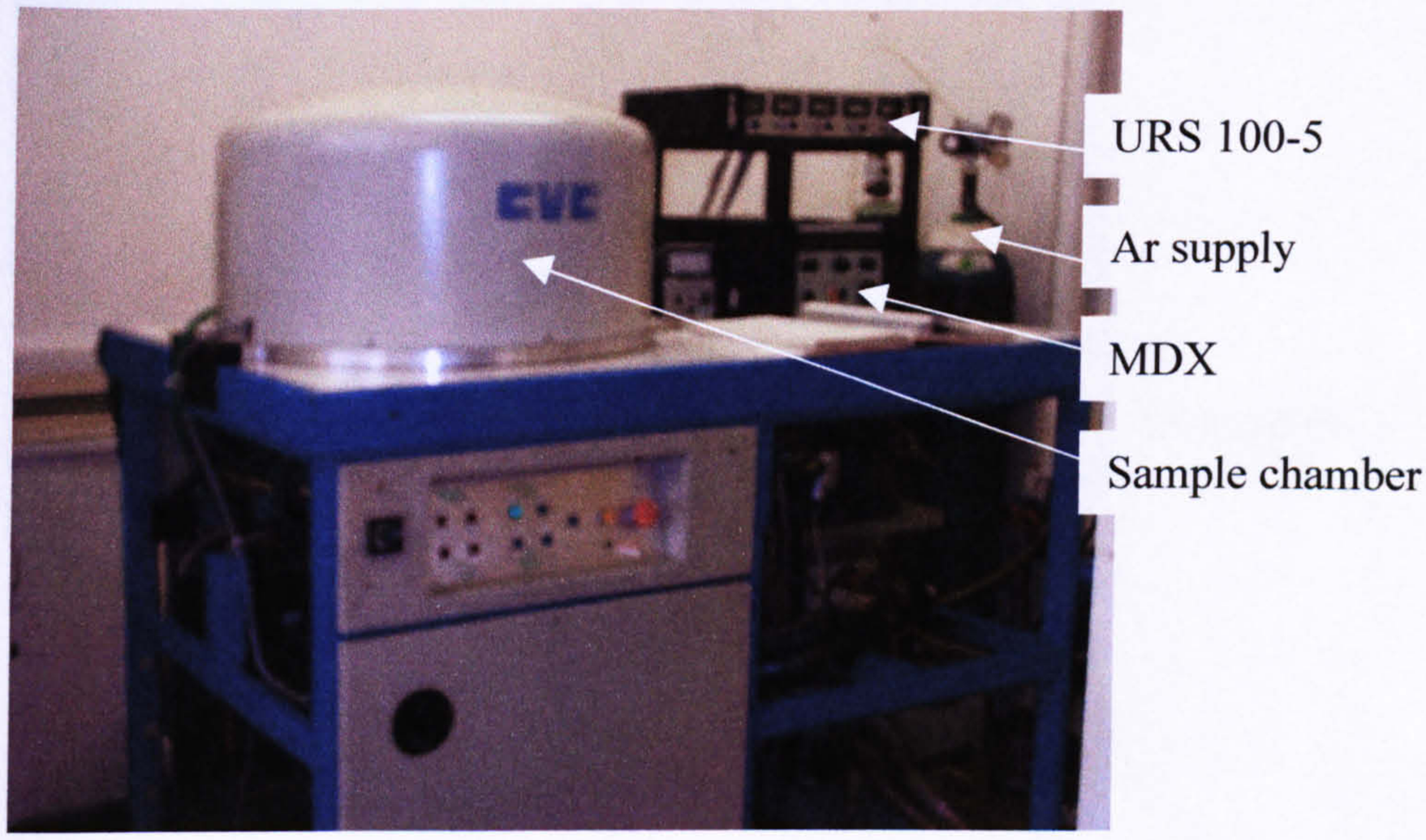

Figure 8.18 Photograph of the CVC d.c. sputter equipment.

8.4.1 Sputtering procedure

The glass microscope slides were cleaned in an ethanolic solution of HF/H_2O_2. This procedure also roughened the surface of the glass, which improved the adhesion of the indium tin oxide to the glass. The slides were washed in pure water (millipore quality) and dried by blowing a jet of nitrogen over the glass surface.

The slides were introduced into the chamber face down, since the targets lie beneath the sample mounting. Figure 8.19 shows the slide-mounting table within the chamber.

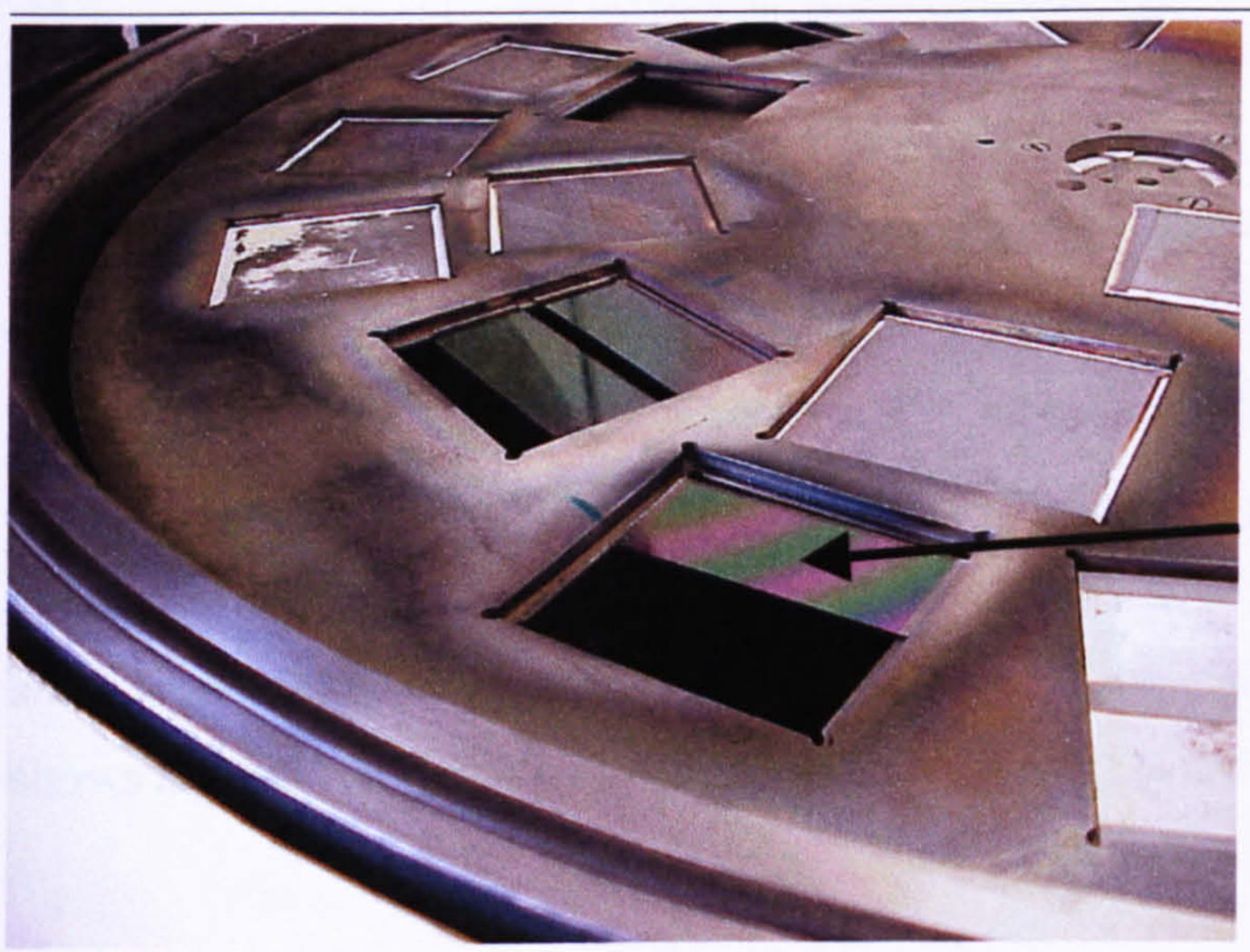

Figure 8.19 Photograph of the slide mounting plate inside the sample chamber

The system had a two-stage pumping procedure. A rotary pump brought the pressure of the system to down $1x10^{-3}$ mbar. A cryopump was then used to pump the sample chamber from $1x10^{-3}$ mbar down to the required $1x10^{-7}$ mbar.

Once the desired vacuum level was reached and the power unit supply was connected to the tin/indium target, argon was introduced into the chamber and the MDX set at a power output of 100 W, (this value had previously been established as optimal for the equipment). Once the MDX was switched on, an argon plasma was created within the chamber.

Oxygen is introduced via the mass flow/URS unit.

Under the conditions within the chamber the tin/indium react with the oxygen thus depositing a layer of indium tin oxide onto the glass.

It was found that a time of 25 minutes gave a thickness of approximately 500 nm of indium tin oxide on the glass slide.

After 25 minutes the oxygen supply was switched off, the plasma was left on to ensure all the oxygen was burnt.

The MDX and the power supply were switched off while the target supply was manually switched over to the silicon target. A similar procedure was followed for

sputtering silicon onto the indium tin oxide/glass without the oxygen supply and the MDX set at 110 W.

A sputter time of 40 minutes gave a silicon thickness of 600 to 1000 nm.

A problem with this technique was that pinholes were apparent in the Si layer, which allowed the etch solution to penetrate the surface and attack the indium tin oxide/ silicon interface. Therefore a minimum thickness of approximately 600 to 1000 nm was required. If too thick a layer was deposited, surface tension effects caused silicon/ indium tin oxide to crack and peel away from the glass slide. Figure 8.20 shows a photograph of a slide with deposited silicon/ indium tin oxide.

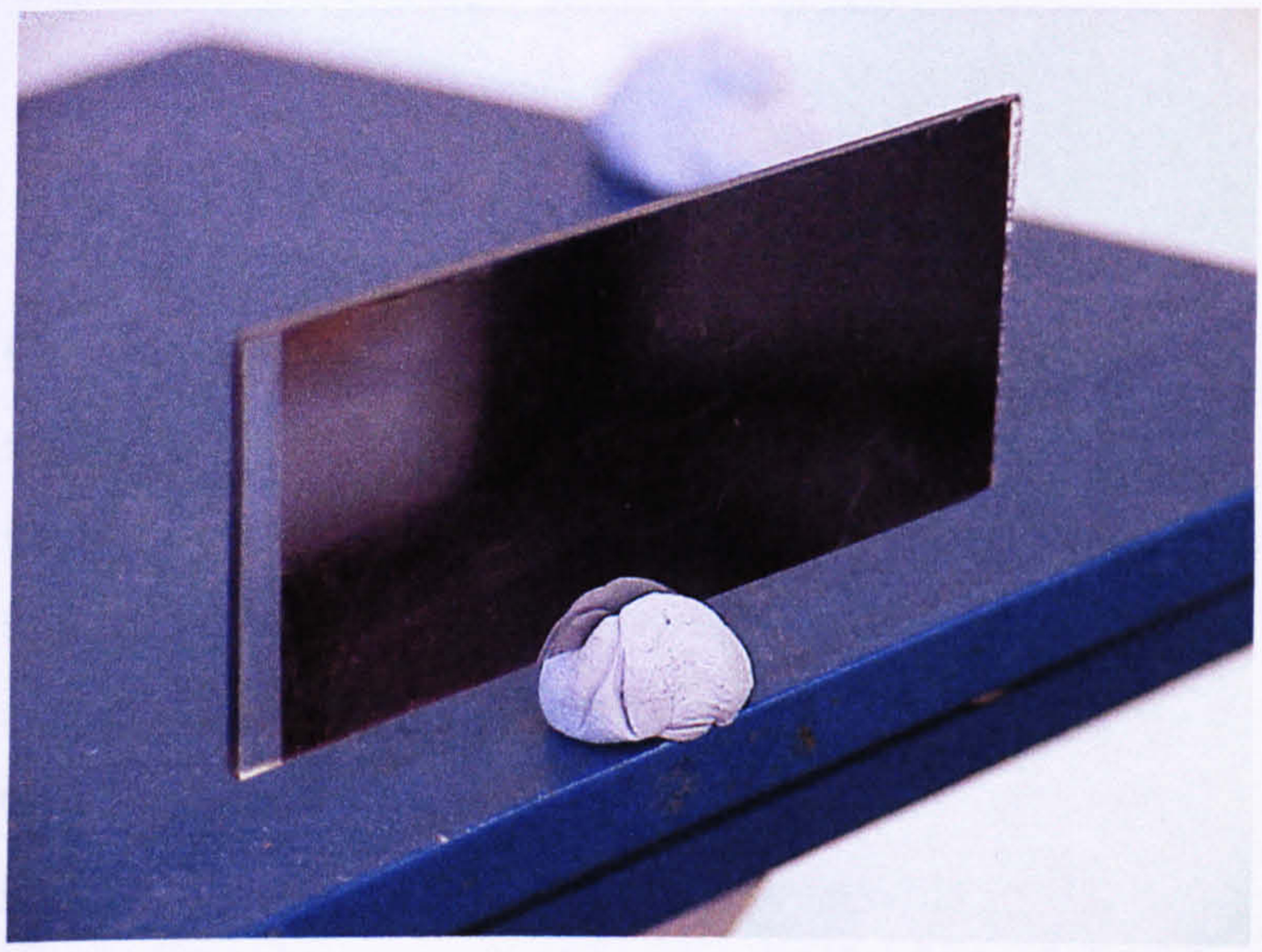

Figure 8.20 Photograph of a glass slide with silicon deposited on indium tin oxide.

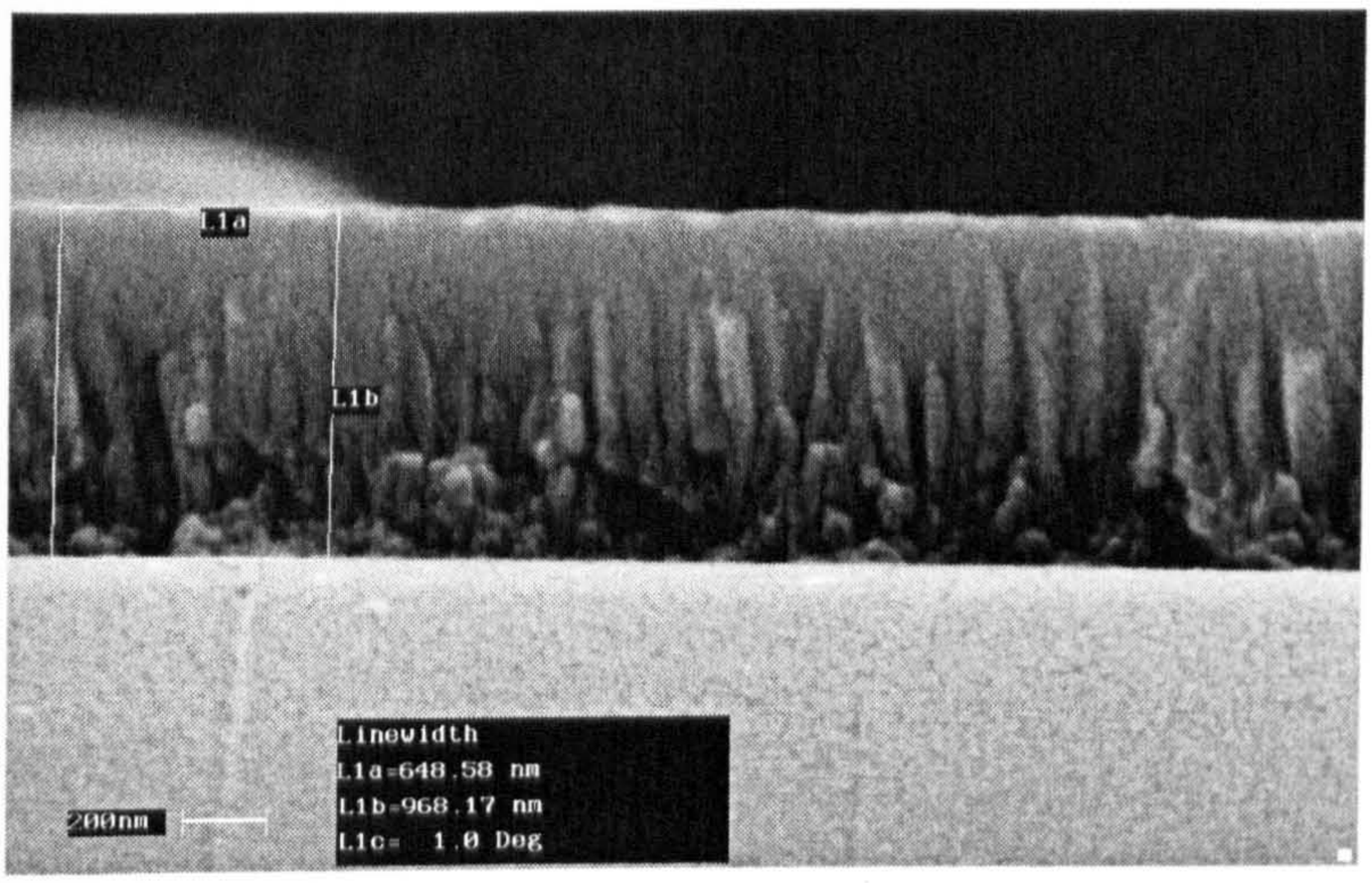

Figure 8.21 SEM micrograph of a section through a glass slide with silicon deposited. Silicon layer is 968.17 nm thick.

Once the silicon slides were produced a further problem was encountered. Since the slides had to be kept in the chamber between depositing the indium tin oxide and the silicon a part of the slide could not be masked from silicon deposition. This meant that a direct electrical contact could not be made to the indium tin oxide. An attempt was made at etching the silicon away leaving the indium tin oxide beneath, but each time the indium tin oxide film was destroyed. It was for this reason that the thin layered silicon could not be anodically etched and the following results are for chemically etched PSi.

8.4.2 Results of the thin layer silicon with $TEABF_4$/PC electrolyte

1 cm^2 pieces of deposited silicon/indium tin oxide /glass were cut and a liquid cell was prepared as described in chapter 7.

The a.c. impedance and CV of the cell were investigated. Figures 8.22 (a) shows the complex plane impedance, figure 8.22 (b) an expanded view of the high frequency region and of the cell Si/ITO /glass /$TEABF_4$/PC.

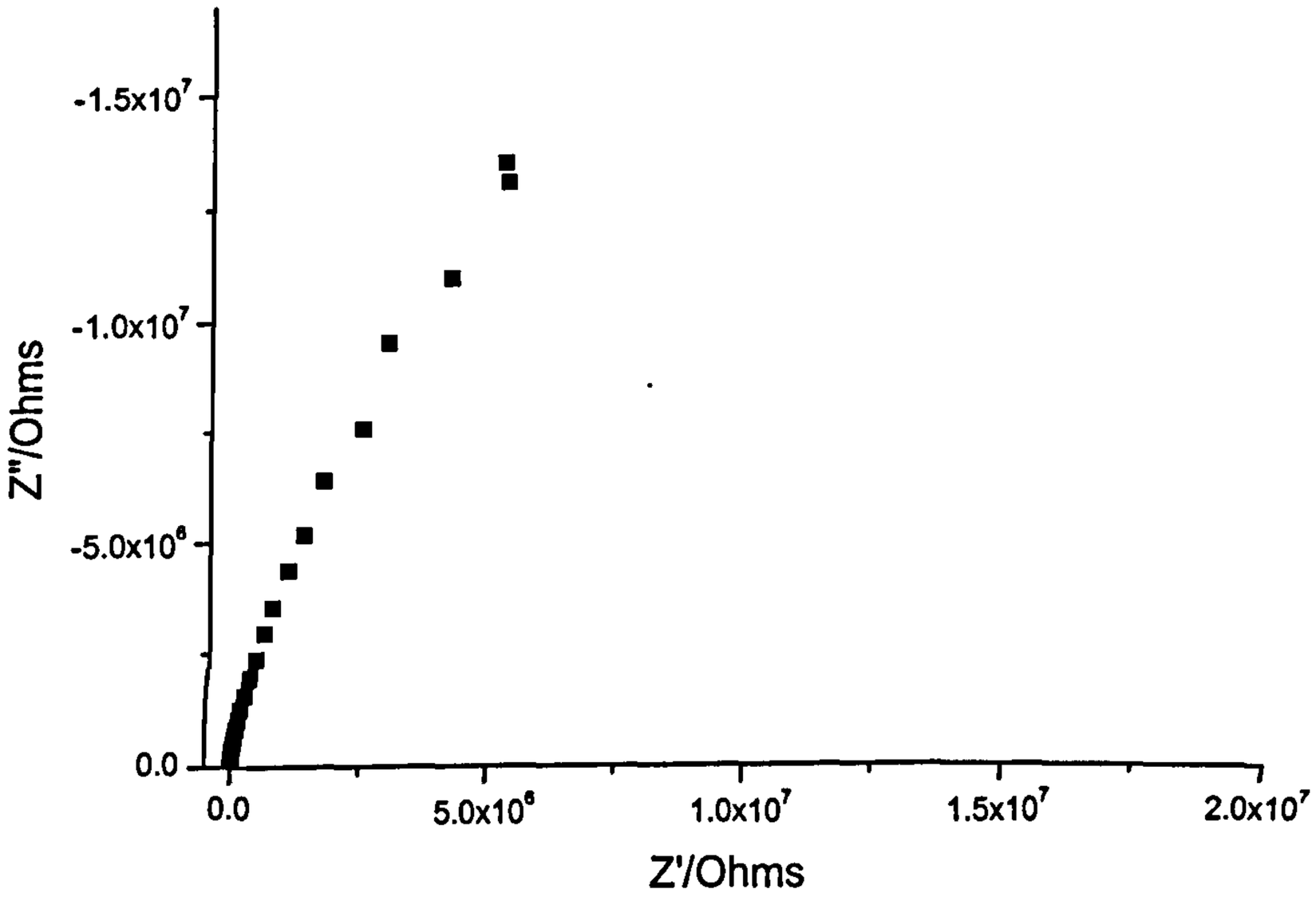

Figure 8.22(a) Complex plane impedance plot of cell Si/ITO/Glass/TEABF$_4$/PC. Frequency range 65 kHz to 10 mHz.

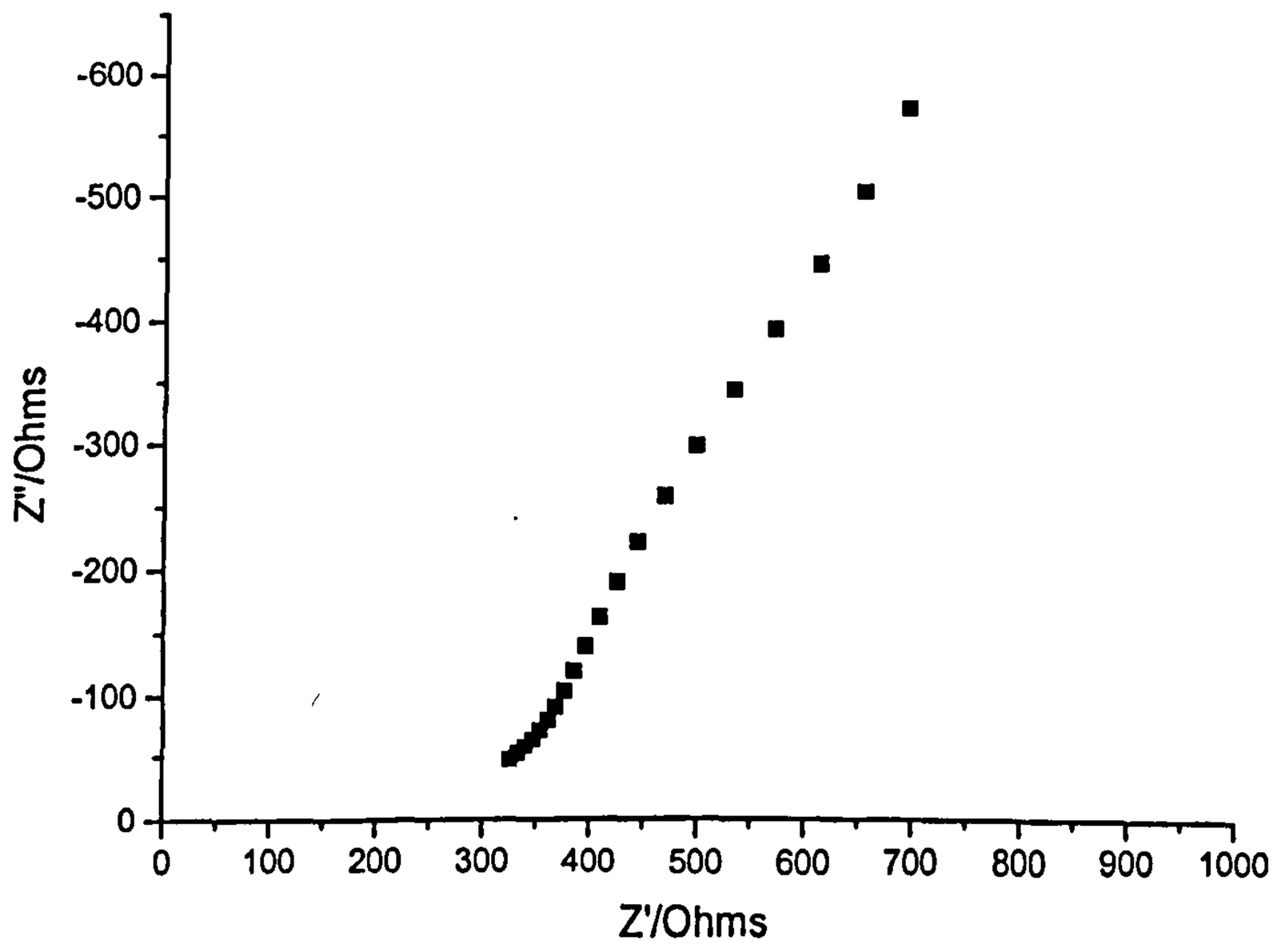

Figure 8.22(b) Expanded high frequency region of the complex plane impedance of the cell Si/ITO/Glass/TEABF$_4$/PC (0.25M).

8.4.3 Stain etched thin layer porous silicon with $TEABF_4$/PC electrolyte

A 1-cm^2 piece of vacuum deposited Si/ITO /glass was stain etched as described in chapter 8.4.1. A liquid cell was constructed as described in chapter 7.
The complex plane impedance plot of the cell is shown in figure 8.23(a) and the expanded high frequency region of the cell is shown in figure 8.23(b).

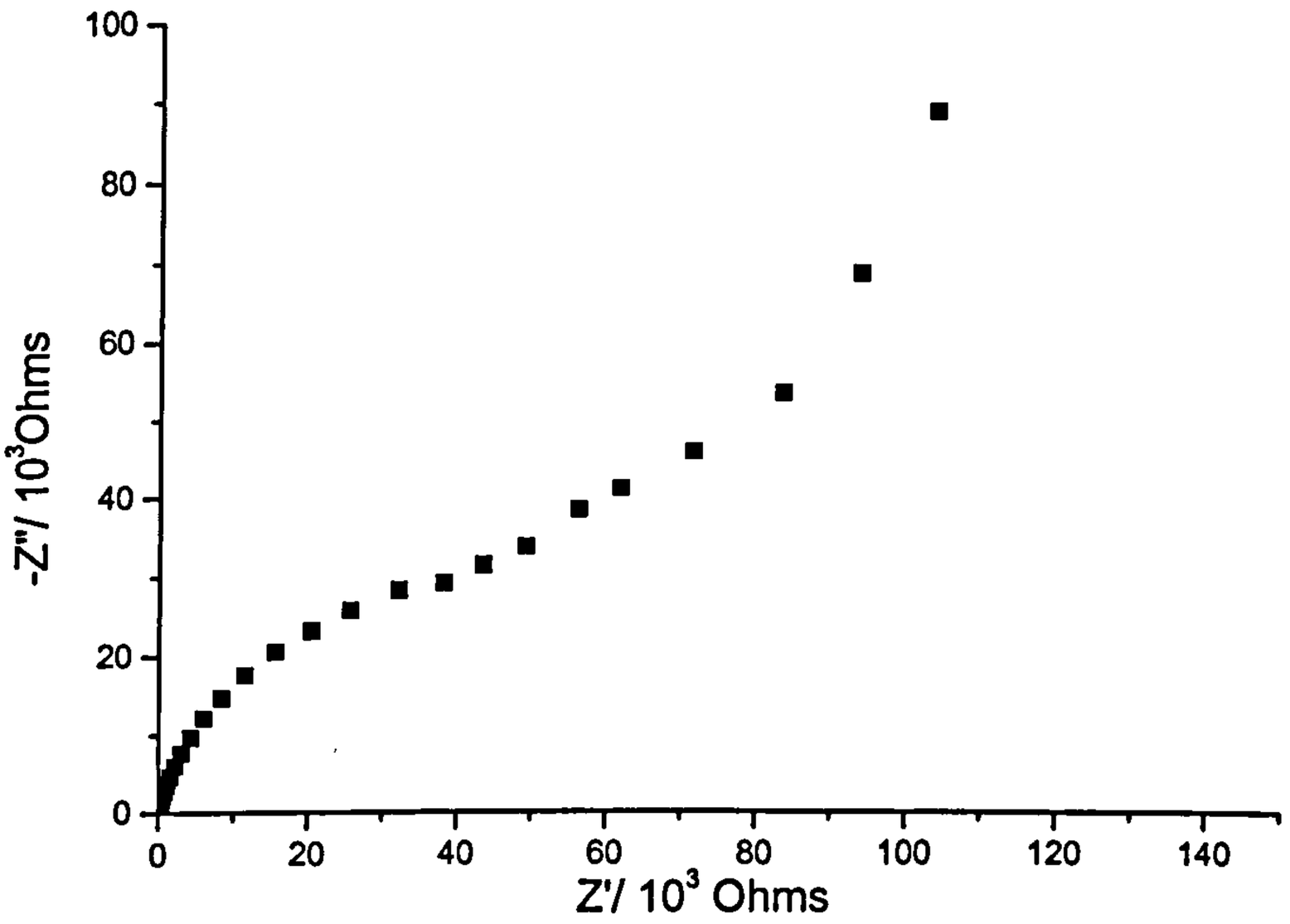

Figure 8.23 (a) Complex plane impedance plot of cell PSi/ITO/Glass/$TEABF_4$/PC. Frequency range 65 kHz to 10 mHz.

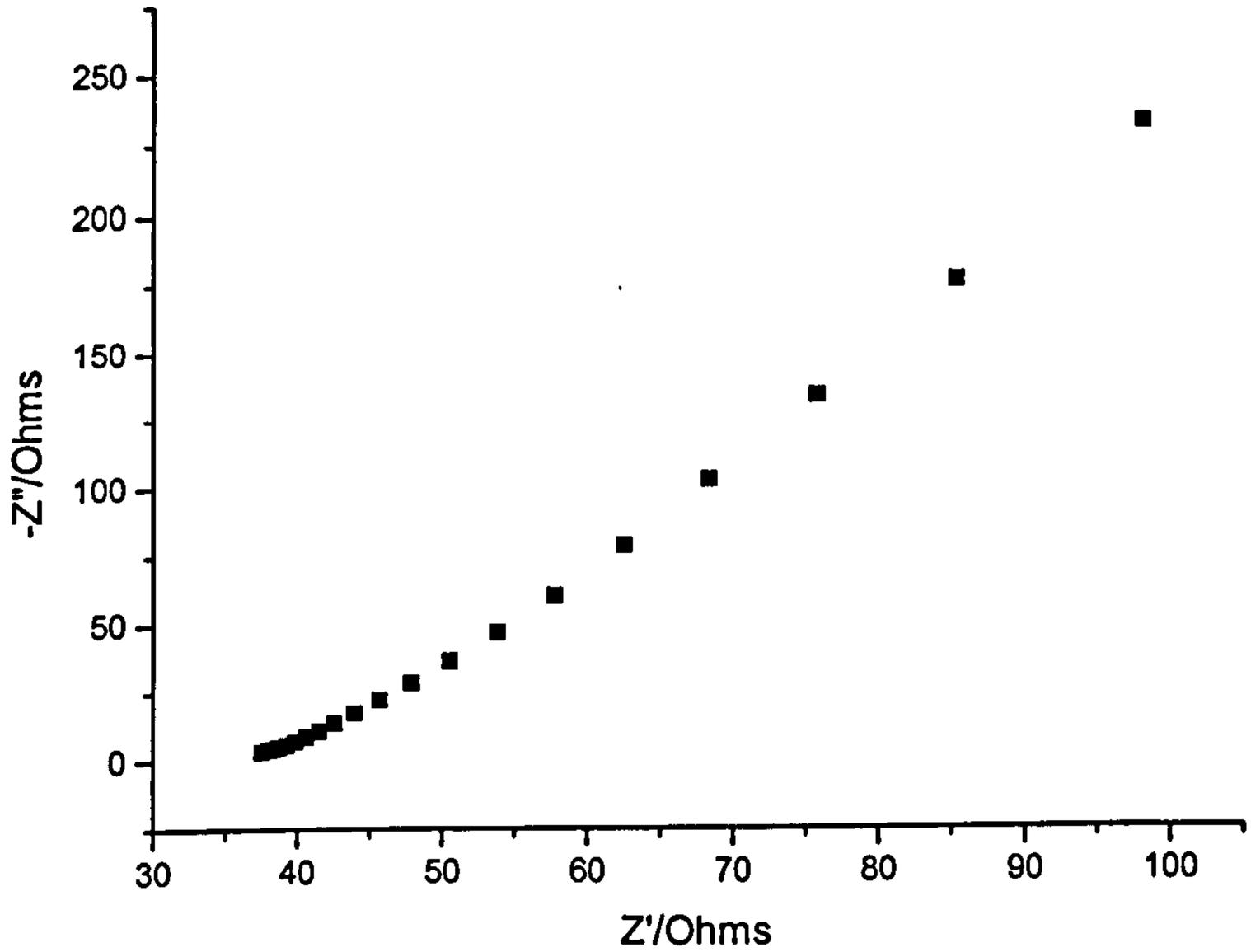

Figure 8.23 (b) Expanded high frequency region of the complex plane impedance of the cell PSi/ITO/Glass/TEABF$_4$/PC (0.25M).

8.4.4 Stain etched, thin layer porous silicon/gold with TBABF$_4$/PC electrolyte

Identical pieces of stain etched thin layer silicon to those used in chapter 8.4.3 were coated with a 300 Å layer of gold as described in chapter 8.3.2.1. Figures 8.24 (a) and (b) show the complex plane, and figure 8.25 shows the CV of cell thin layer PSi/Au/TEABF$_4$/PC.

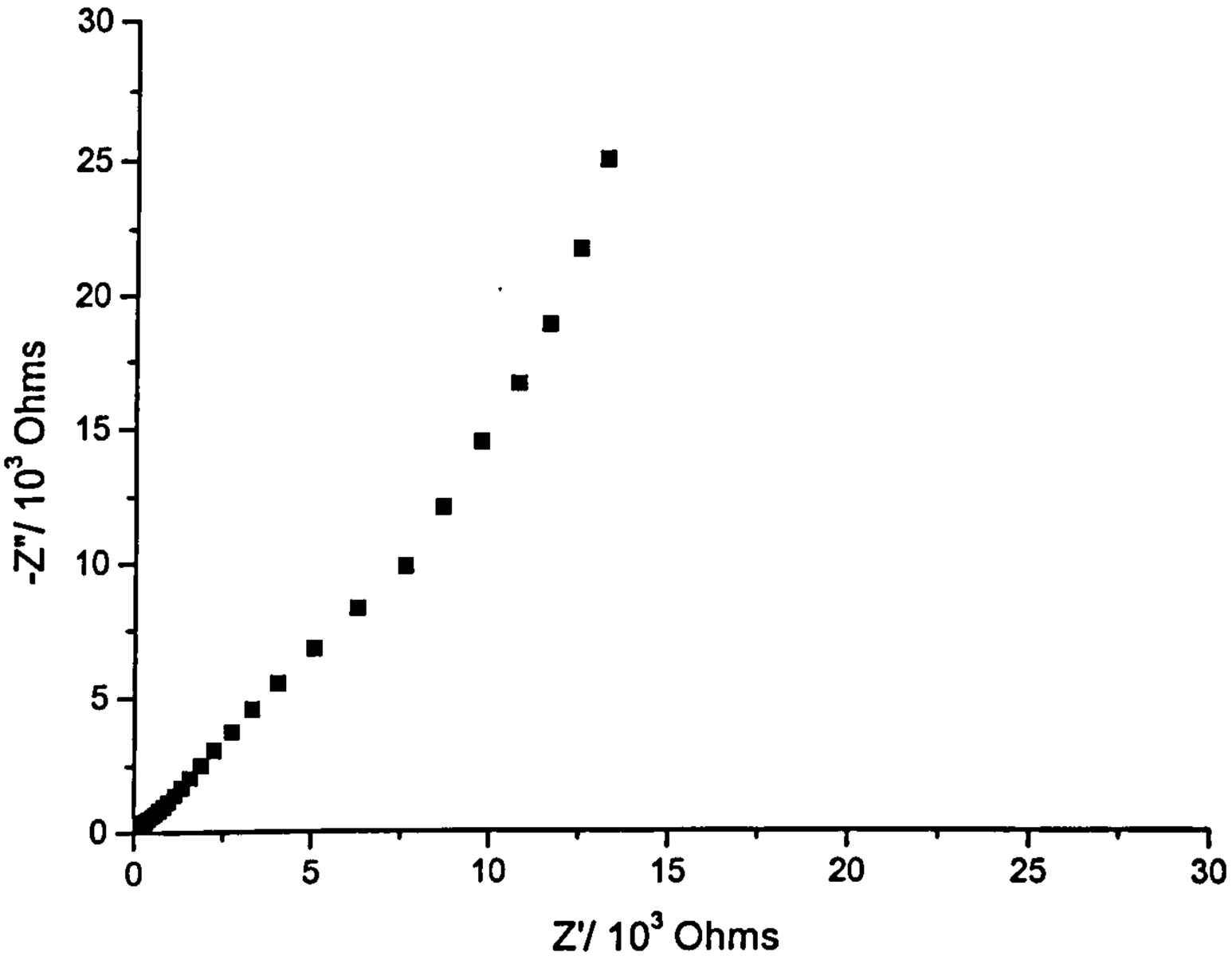

Figure 8.24 (a) Complex plane impedance plot of cell PSi/Au/ITO/Glass/TEABF$_4$/PC. Frequency range 65 kHz to 10 mHz.

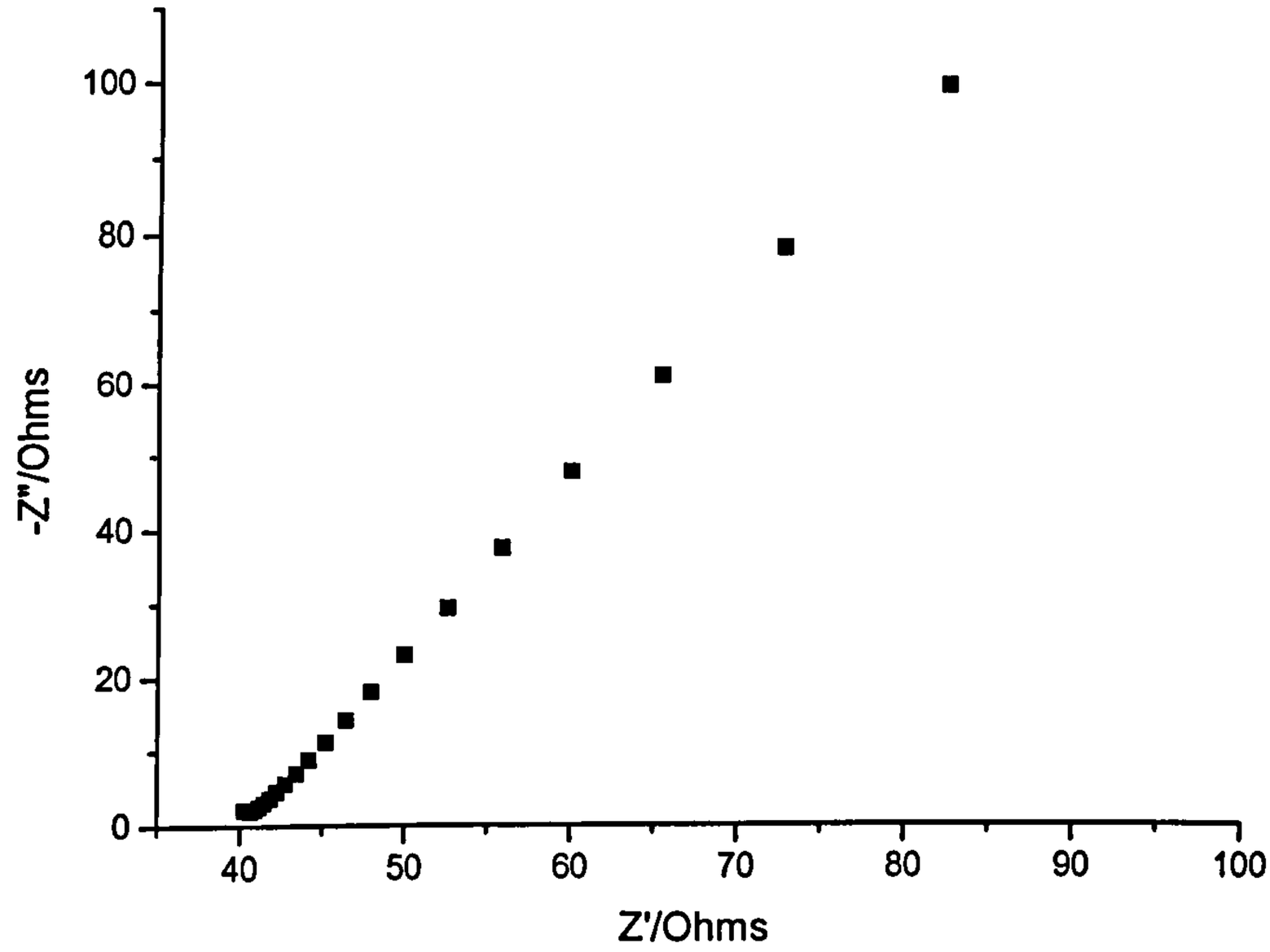

Figure 8.24 (b) Expanded high frequency region of the complex plane impedance of the cell PSi/Au/ITO/Glass/TEABF$_4$/PC (0.25M).

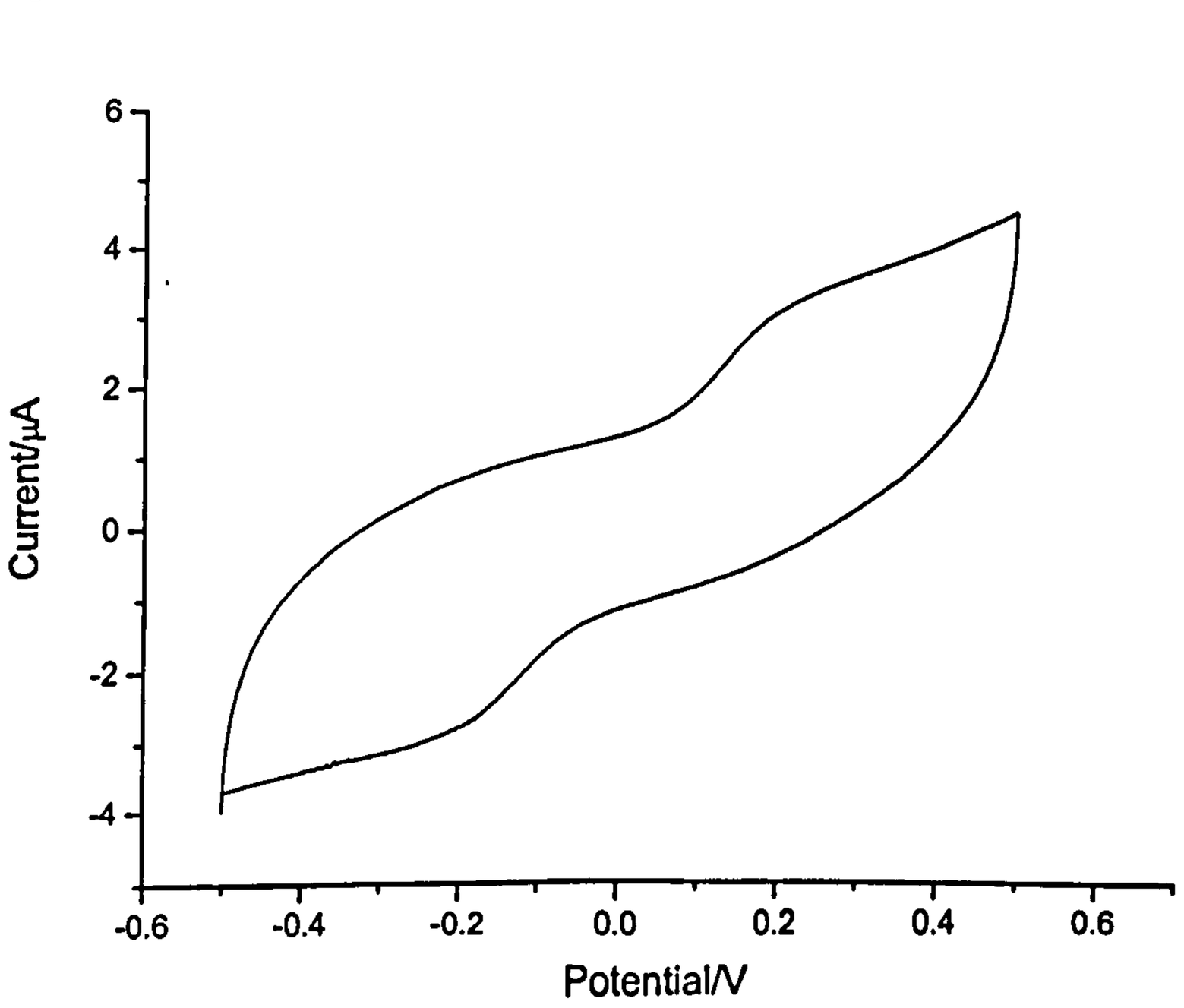

Figure 8.25 CV plot of cell PSi/Au/ITO/Glass/TEABF$_4$/PC. Sweep rate 10 mV s^{-1}. Vs a floating potential.

The bulk resistance of the cell was reduced to 35 Ω, close to that of the carbon based cells. Capacitance values of 0.64 mF cm^{-2}, relating to a specific capacitance of 2.82 F g^{-1} were obtained for the cell PSi (stain)/Au/$TEABF_4$/PC (0.25M).

8.4.5 Stain etched, thin layer porous silicon/gold with PU electrolyte

Figure 8.26(a) shows the complex plane impedance plot of a cell prepared from stain etched thin layer silicon with a 300 Å layer of gold electrodes, sandwiching a PU gel electrolyte prepared as described in chapter 6. Figure 8.27 shows the CV of cell PSi/Au/ITO/glass/PU.

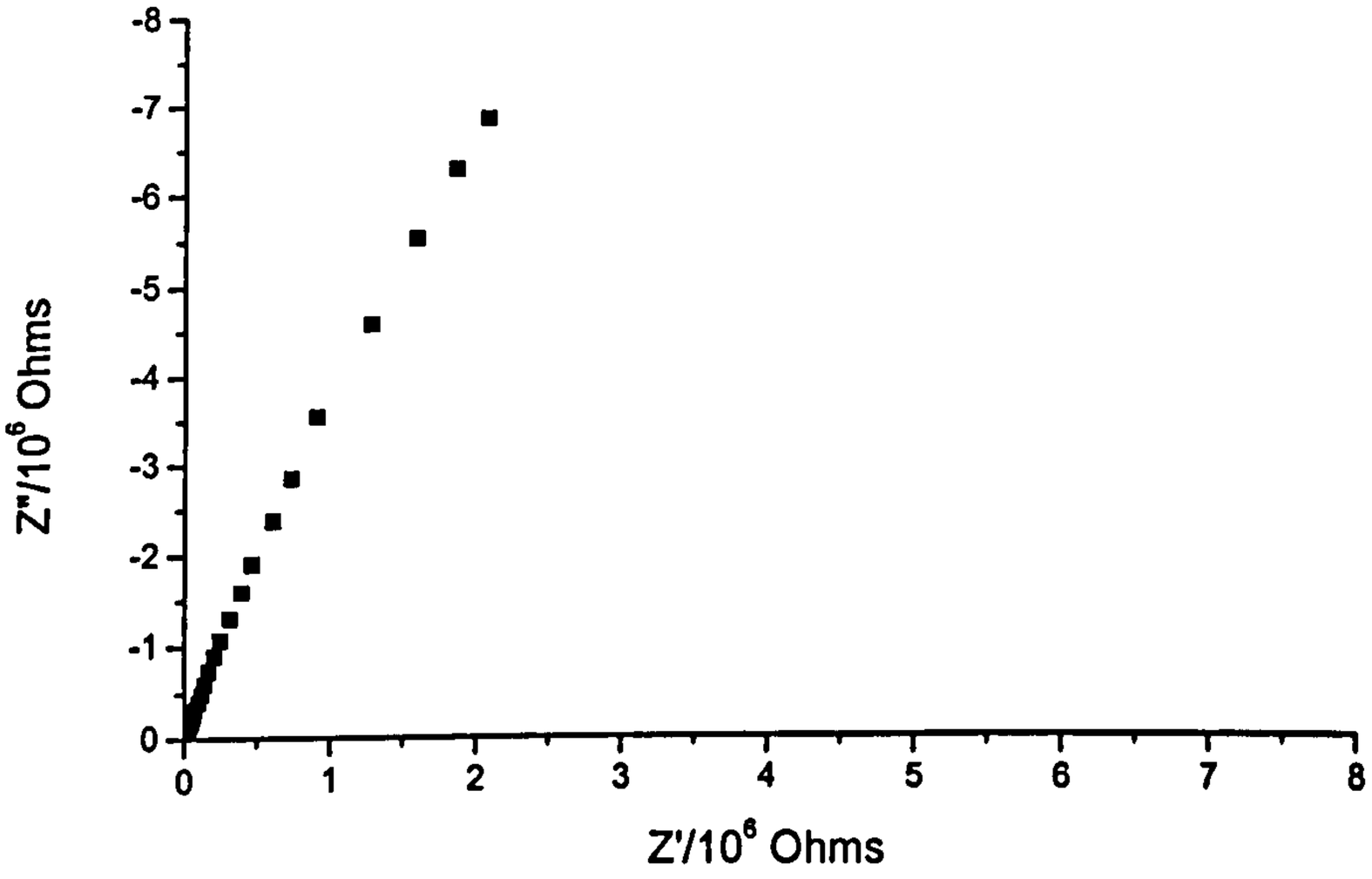

Figure 8.26(a) Complex plane impedance plot of cell PSi/Au/ITO/Glass/PU. Frequency range 65 kHz to 10 mHz.

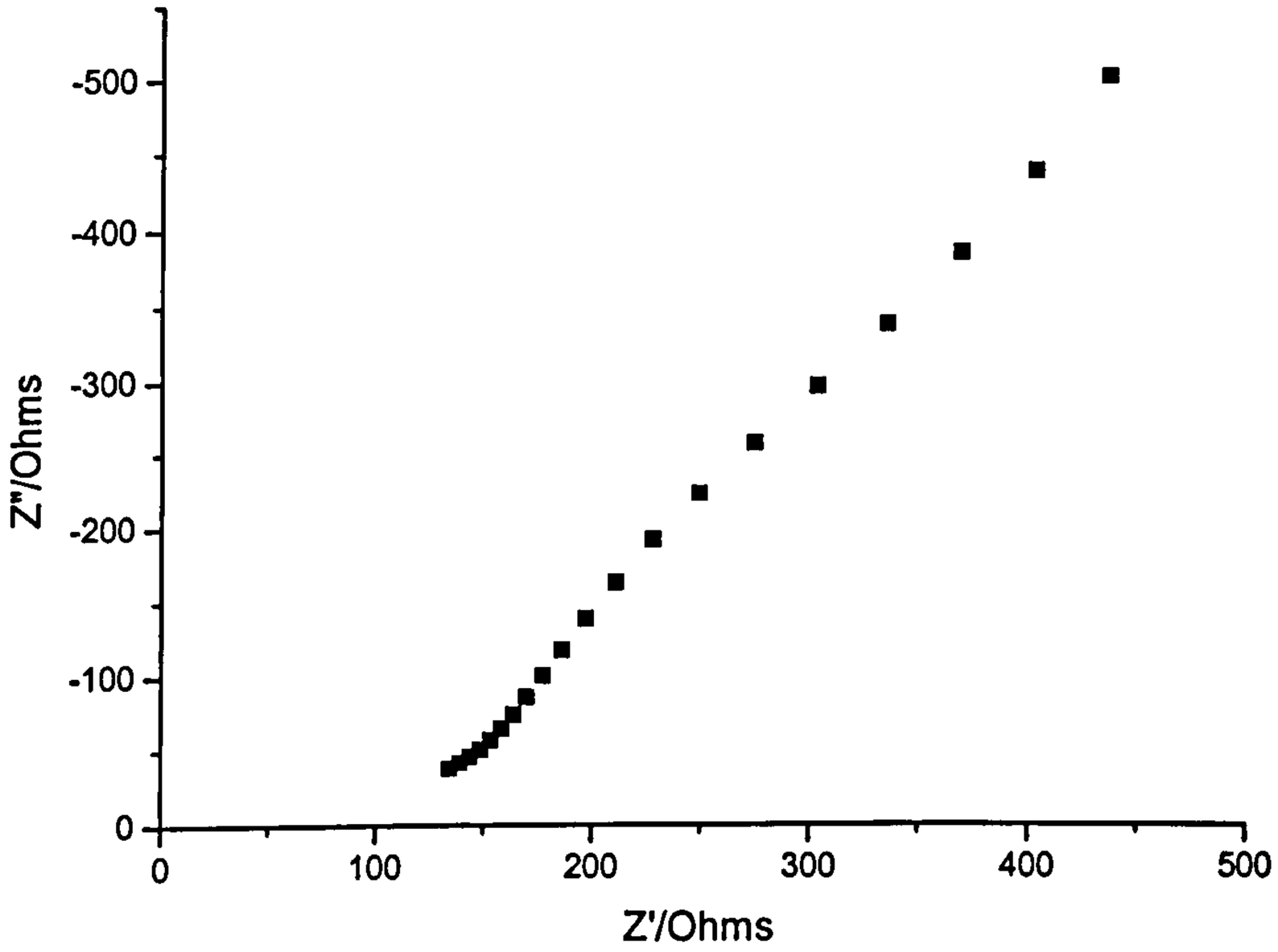

Figure 8.26 (b) Expanded high frequency region of the complex plane impedance of the cell PSi/Au/ITO/Glass/PU.

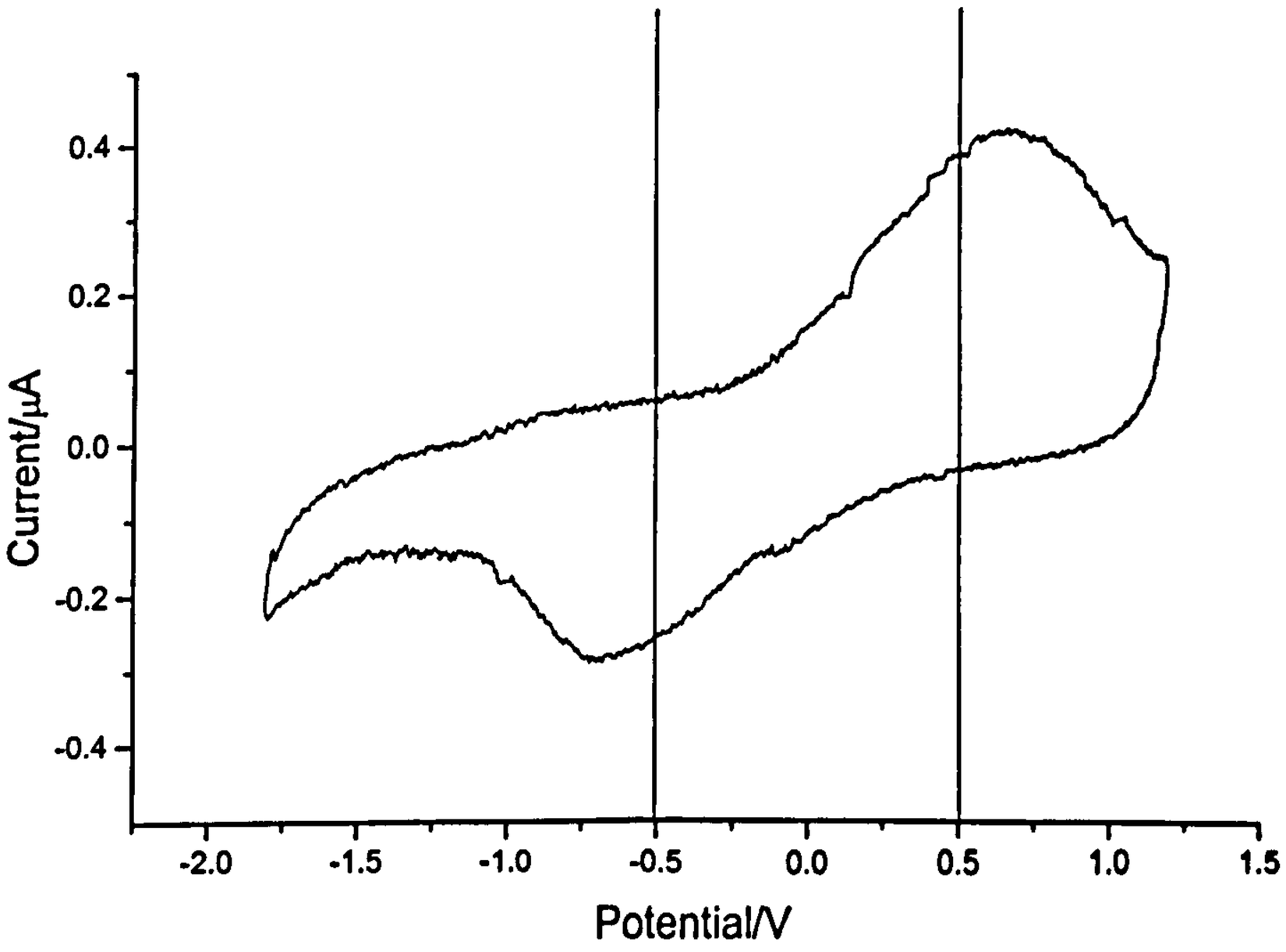

Figure 8.27 CV plot of cell PSi/Au/ITO/Glass/PU.
Sweep rate 10 mV s^{-1}. Vs a floating potential.

Figure 8.26(a) shows that the electrodes produced from stain etched, thin layer PSi, coated with gold were the best silicon candidates for solid state supercapacitors with the PU gel electrolyte. Although the capacitance was low, 2.7 $\mu F\ cm^{-2}$, calculated at 10 mHz using equation 5.14, the specific capacitance was high because of the thin layer cell construction

The mass of an electrode can be calculated using the density of Silicon and gold, which is 2.33 and 19.3 g cm^{-3} respectively. The volume of silicon per electrode was 1cm by 1cm by $9.68x10^{-5}$ cm i.e. a volume of $9.68x10^{-5}$ cm^3, therefore the mass of silicon per electrode is $2.26x10^{-4}$ g. The volume of gold used was 1 cm by 1cm by $300x10^{-8}$ cm, i.e. a volume of $300x10^{-8}$ cm^3. Therefore, the mass of gold was $5.79x10^{-5}$ g. Hence, the total mass of an electrode was $2.84x10^{-4}$ g.

The specific capacitance was therefore $\underline{9.51\ mF\ g^{-1}}$.

Figure 8.26 (b) shows the bulk resistance of the cell to be 135 Ω.

Figure 8.27 demonstrates that the cell exhibits capacitive behaviour between the potential limits of $\pm$ 0.5 V.

Since the cell PSi/Au/ITO/Glass/PU was the best candidate for a Si/solid state device, it was galvanostatically cycled to 1000 cycles and the impedance monitored at regular intervals. Figure 2.28 shows the cycles at 1, 50, 100, 500 and 1000. Figure 8.29 shows the impedance taken at intervals of 1, 50, 100, 500 and 1000.

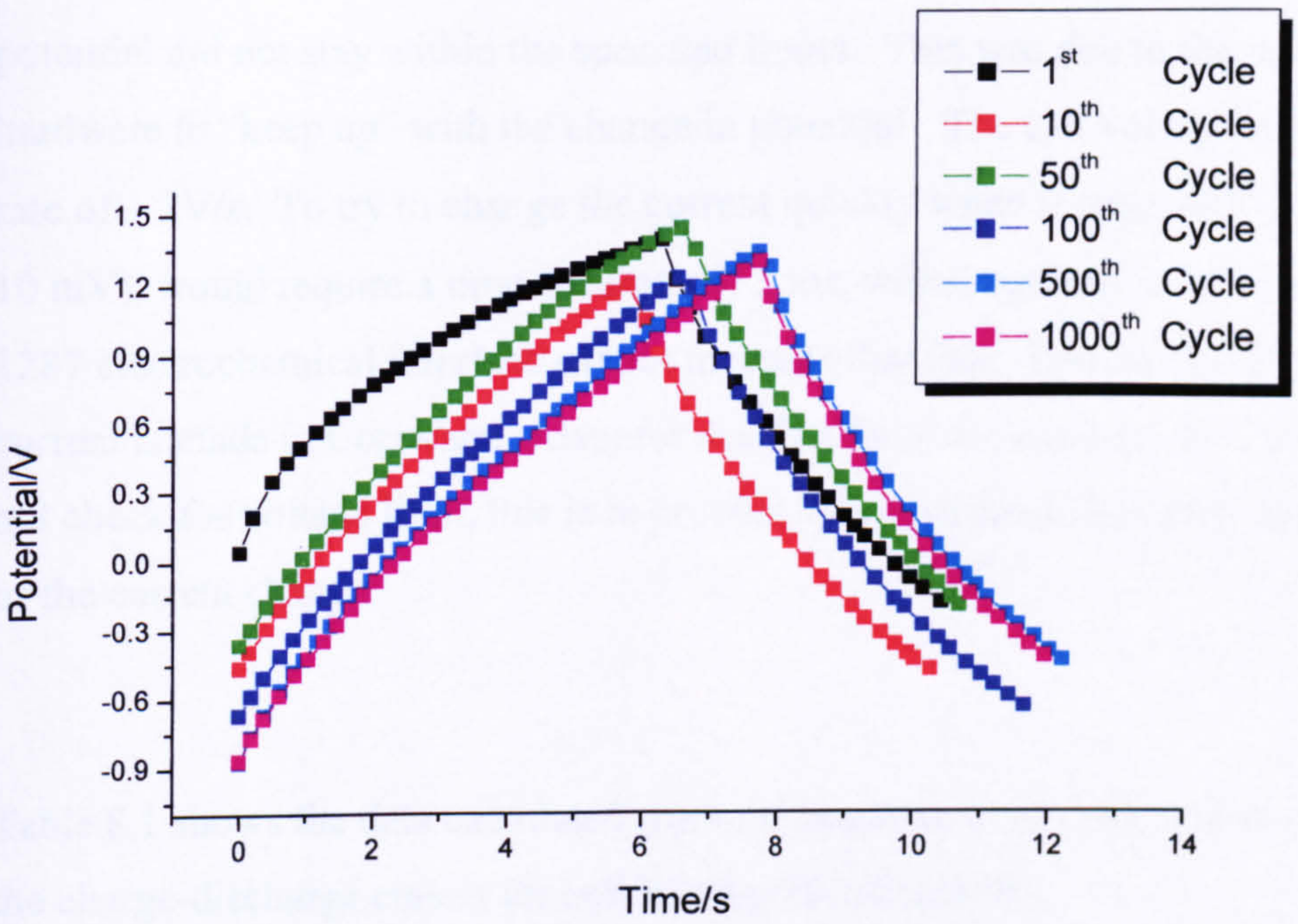

Figure 8.28 Plot of the 1st, 50th, 100th, 500 th and 1000 th, galvanostatic charge discharge curves for the cell PSi/Au/ITO/Glass/PU.

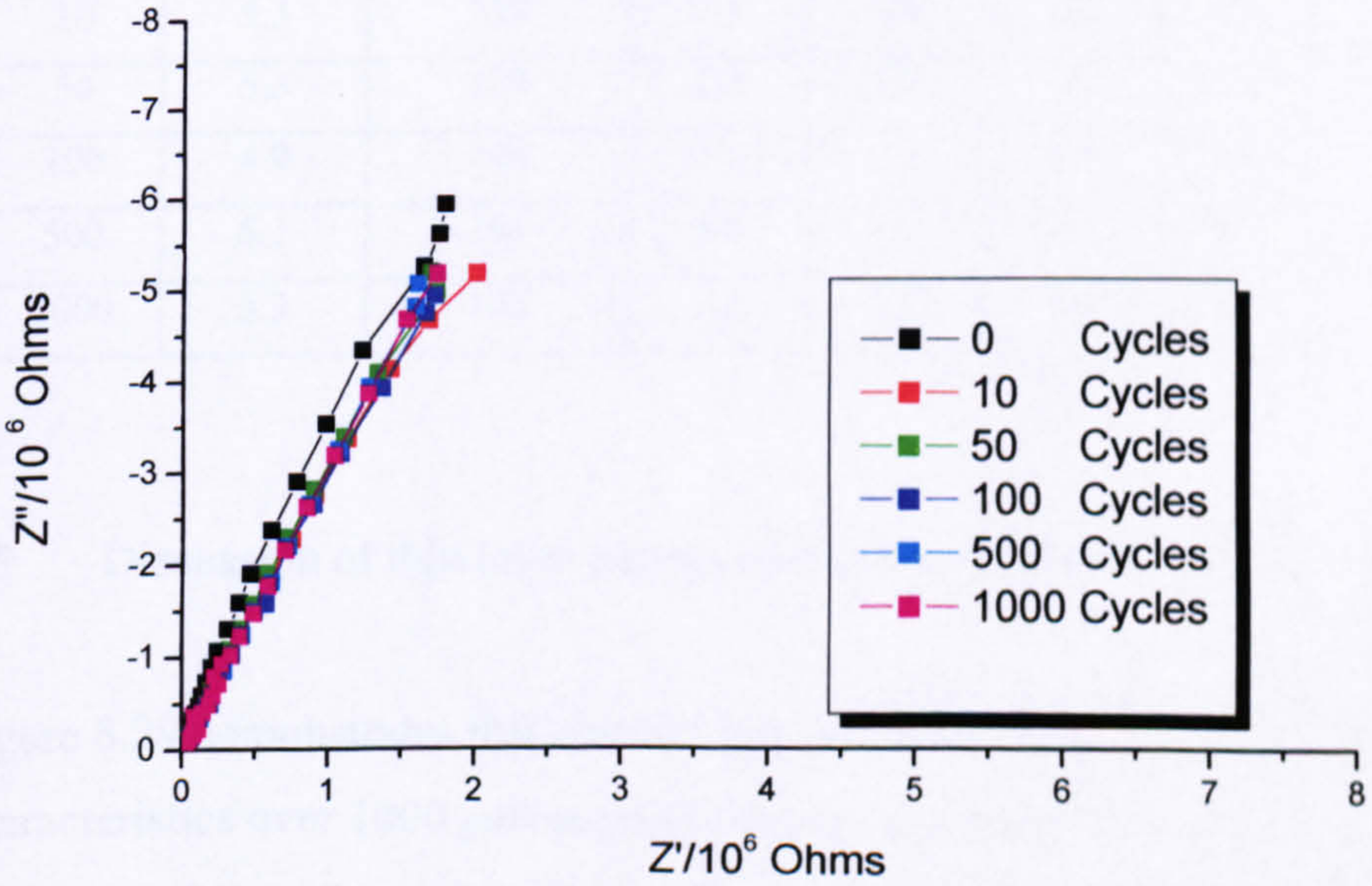

Figure 8.29 Complex plane impedance plots of cell PSi/Au/ITO/Glass/PU as a function of galvanostatic charge-discharge cycles. Frequency range 65 kHz to 10 mHz.

The cell was galvanostatically charged and discharged at 1μA cm^{-2}. Note the potential did not stay within the specified limits. This was due to the inability of the hardware to "keep up" with the change in potential. The cell voltage is changing at a rate of ~ 2V/s. To try to change the current quickly when it reaches 1V (say within 10 mV), would require a time accuracy of 5 ms, which equates to 200 points /s. The 1287 electrochemical interface cannot measure that fast. The decision to change the current is made in Corrware. Also, for the first 5s of the experiment Corrware does not check for voltage limit, this is to prevent spikes in the data during the triggering of the current change.

Table 8.1 shows the data calculated from the impedance vs cycle number and from the charge-discharge curves for cell PSi/Au/ITO/Glass/PU.

Cycle number	-Z" @ 10 mHz/ 10^6 Ω	Bulk resistance R_B/ Ω	Discharge capacitance μF cm^{-2}	mF g^{-1}	Capacitance @ 10 mHz μF cm^{-2}	mF g^{-1}	Coulombic efficiency/%
1	6.5	135	2.5	9.0	2.7	10	68
10	5.3	139	2.5	9.0	3.0	11	76
50	5.3	139	2.8	10	3.0	11	63
100	4.9	140	4.5	16	3.3	12	82
500	5.1	141	4.6	16	3.1	11	58
1000	5.3	142	3.2	11	3.0	11	54

8.5 Discussion of thin layer porous silicon electrodes with PU electrolyte.

Figure 8.29 demonstrates that the cell PSi/Au/PU shows very good capacitive characteristics over 1000 galvanostatic charge-discharge cycles. Giving capacitance values of between 8 and 16 mF g^{-1}. The use of thin layer PSi is completely novel in its application for supercapacitor systems and it may be possible to integrate this power storage system into chip technology where currents of micro-amps are required.

8.6 Polypyrrole/PSi electrodes

Previous studies on supercapacitor devices comprised of polypyrrole electrodes (grown galvanostatically on ITO), with PU/$LiClO_4$ electrolyte has been carried out by C. Owen, [4]. Capacitance values of approximately 7 Fg^{-1} were reported.
This chapter reports the results obtained from supercapacitor devices prepared from galvanostatically grown polypyrrole on PSi electrodes with PU/$LiClO_4$ electrolyte, (i.e., ppyr/PSi/PU/PC/EC {200%}/ $LiClO_4$ {10%}, system).
The polypyrrole was grown on the PSi substrate to achieve a higher surface area polypyrrole electrode than those reported to date.
Thin layer porous silicon was prepared as described in chapter 8.4.

The pyrrole monomer solution was prepared taking into account the parameters for optimum conductivity and mechanical integrity of the film as discussed in chapter 3.

- The solvent must minimise nucleophilic reactions and aprotic solvents appear to be the best for polypyrrole growth. Acetonitrile is the most common choice.
- A large cation improves mechanical strength and conductivity of the film.
- Electrolyte concentrations of up to 1M have seen improvements in conductivity and tensile strength of the as grown polypyrrole film.

Considering these points, 1M $TBABF_4$/ACN was used as the support electrolyte.
The concentration of the pyrrole monomer in the support electrolyte was 0.01M.
The pyrrole was distilled before use, b.p. of pyrrole was 131^{0}C.
The final monomer solution was $TBABF_4$/ACN (1M)/Pyrrole (0.01M).

A three-electrode cell was arranged and the polypyrrole was grown galvanostatically at 20 mA cm^{-2} for 20 seconds on the porous silicon working electrode, versus a Ag/AgCl reference electrode. A platinum mesh counter electrode was used.

The appearance of the as grown polypyrrole was black and showed poor adhesion to the PSi substrate. The compliance potential of the potentiostat increased to over 10 V in order to hold the current at 20 mA. Since the oxidation potential of pyrrole is 0.78V versus Ag/AgCl, applying a potential of an order of magnitude higher would certainly adversely affect the as grown polymer film.

Otero and DeLarreta [5], proposed that using constant potential and constant current techniques lead to poor adhesion between the polypyrrole film and the substrate.

The above procedure was repeated for another piece of PSi, the two ppyr/PSi electrodes were then used as a supercapacitor cell with a PU gel electrolyte. The cell configuration was ppyr/PSi/PU/EC/PC{200%}/ $LiClO_4${10%}.
The cell was galvanostatically charged and discharged at 1 $\mu A\ cm^{-2}$

Figure 8.30 shows the complex plain impedance plot of the above capacitor cell.

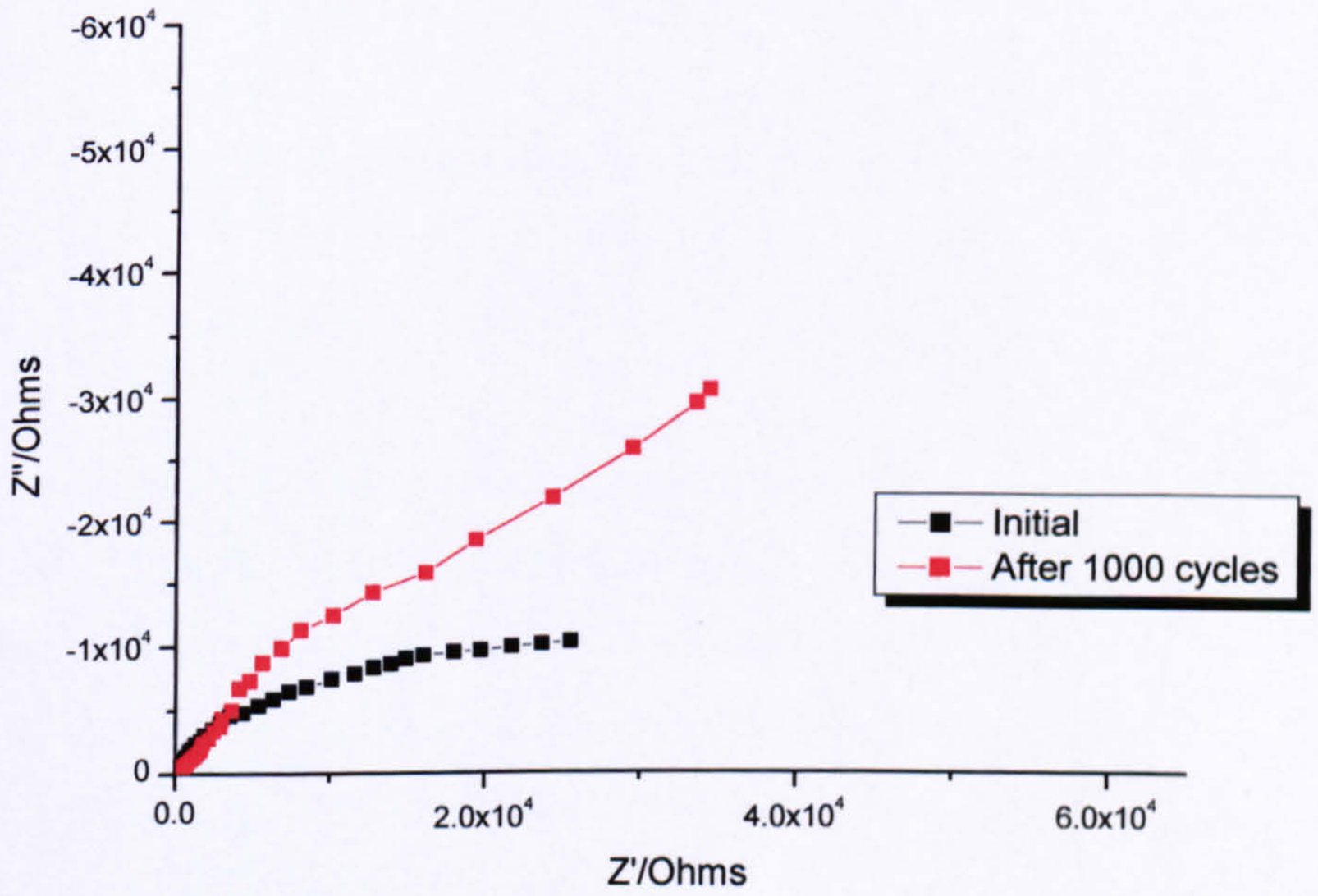

Figure 8.30 Complex plane impedance plots of cell ppyr/PSi/PU/EC/PC/$LiClO_4$ as a function of galvanostatic charge-discharge cycles. Frequency range 65 kHz to 10 mHz.

Clearly figure 8.30 demonstrates that the cell ppyr/PSi/PU/EC/PC/ $LiClO_4$ does not show ideal capacitive behaviour. A large semi-circle suggests a large resistance in parallel with the pseudocapacitance associated with the polypyrrole. This may be due to a large interfacial resistance between the PSi and the polypyrrole film. The

bulk resistance of the cell is also large (~500Ω). This may be due to the poor adhesion and poor conductivity of the film, which is a result of the compliance voltage rising to over 10 V during the galvanostatic growth of the polypyrrole film. The possibility of producing capacitance values higher than those reported for polypyrrole systems alone, by using the high surface area of PSi remains an attractive prospect, but clearly a further investigation into the growth of polypyrrole on PSi is required.

9. General Discussion and Conclusions

The aim of this project was to investigate the possible use of a polyurethane electrolyte with various electrode materials in supercapacitor devices. The study initially focused on optimising the conductive properties of the polymer/gel electrolyte whilst maintaining mechanical integrity. The conductivity was analysed using a.c. impedance spectroscopy and cyclic voltammetry. The thermal properties of the polymer/gel electrolyte were analysed using differential scanning calorimetry so that the extent of salt-polymer and salt-plasticiser interaction could be established. The conclusions of this part of the study are presented in chapter 9.1.
The polyurethane gel electrolyte was then used in solid state supercapacitor devices with carbon and porous silicon electrodes. The conclusions of this part of the study are presented in chapter 9.2 and 9.3 respectively.

9.1 Polyurethane electrolyte.

9.1.1. Conductivity of electrolyte

The initial study was to establish the optimum salt concentration ($LiClO_4$) in the PU film, which would give the best conductivity and mechanical strength in a thin film form.
The conductivity of the electrolyte increases with increasing salt content from 5 to 20 %, giving conductivities of 3.83×10^{-6} S cm^{-1} (5% salt), 9.47×10^{-6} S cm^{-1} (10% salt), 1.52×10^{-4} (20% salt) and 1.04×10^{-5} S cm^{-1} for (50% salt).
The conductivity of the electrolyte containing 50% salt was less than that for the 20% electrolyte. The optimum conductivity was therefore 20% added salt. A possible explanation for the decrease in conductivity may be due to the formation of ion pairs and higher order ion agglomerates in the 50% salt concentration. This would have the effect of slowing down the mobility of the cation within the polymer and thus reducing the conductivity of the polymer electrolyte. Similar effects have been reported for polymer electrolytes with high salt concentrations [1]. Also, similar behaviour is shown by PEO-lithium salt polymer electrolytes in which a maximum conductivity is observed for compositions of about PEO_9: salt [1].

The increase in conductivity from 10% to 20% was not high enough to merit the doubling of the cost of the salt therefore 10% added salt was taken as the optimum concentration of salt.

The optimum conductivity of the polymer electrolyte described above was in the order of 10^{-5} S cm^{-1}. However, the conductivity of a polymer electrolyte is known to increase on addition of a low molecular weight plasticiser [2]. Therefore to improve the conductivity propylene carbonate and ethylene carbonate were used as a plasticiser.

The amount of plasticiser added to the PU/ $LiClO_4$ (10%) polymer electrolyte was optimised for conductivity and mechanical integrity in thin films.

Table 6.2 shows that the system with PU+$LiClO_4$ (10%)+EC/PC (200%) is the blend which gave the highest conductivity, (6.22×10^{-3} S cm^{-1}). This blend forms a mechanically stable, free-standing thin film gel electrolyte. Note it was not possible to form a stable thin film gel electrolyte on adding 300% plasticiser to the PU/salt. The above composition was therefore used as a gel electrolyte for the various supercapacitor cells investigated in this study.

9.1.2 Differential Scanning Calorimetry

Chapter 3.2 briefly discusses some of the mechanisms of ionic conductivity in polymer/gel electrolytes. The PU gel electrolyte was investigated using DSC in order to establish the extent of the co-ordination of the cation to both the polymer and the plasticiser. Figures 6.14(a-n) show the DSC traces obtained and indicate that the polymer/gel electrolyte system is a complex mixture of the component parts. Close inspection of 6.14(a), i.e. Pure PU, shows the T_g at -45^0C. This compares favourably with previous calorimetry results, (T_g of -45^0C), [3]. DSC traces for pure PU and PU plus added $LiClO_4$ respectively, show that there is an interaction between the PU and the $LiClO_4$. As expected for a polymer electrolyte this is due to the co-ordination of the lithium cation with the ether oxygens of the PU backbone. Examination of the traces for pure PC, pure EC and a 1:1 mixture of PC/EC, shows there is some interaction between the PC and EC components of the mixture, since the sharp melting peak of EC at 33^0C is not apparent in the DSC trace for the mixture. The addition of PC to EC may have the effect of lowering the melting point

of EC and broadening of the melting peak, as shown in figure 6.14 (k) between 0 and 10 ^{0}C.

On adding more plasticiser to pure PU the DSC trace tends towards the trace obtained for the PC/EC mixture. This would suggest that the system is becoming more and more like a purely gel electrolyte, where the PU is acting as a host matrix to the liquid PC/EC mixture. This is consistent with the conductivity results concluded in chapter 9.1 above, where the optimum conductivity was reported for the system PU+200% plasticiser /10% $LiClO_4$ of $6.22x10^{-3}$ S cm^{-1}.

Also DSC traces for EC/PC plus $LiClO_4$ and EC/PC show an interaction between the salt and the plasticiser occurred.

Figures 6.14 (f) and (j), PU+200% EC/PC and PU+200% EC/PC + 10% $LiClO_4$ respectively, show a 15 ^{0} shift of an exotherm peak from –50^{0}C to –65^{0}C, again providing evidence for salt-polymer and salt- plasticiser interactions. This may be due the crystallisation of PC.

The PU electrolyte interacts with the salt in a manner similar to that of Li^+ and the ether oxygens of PEO, i.e. a traditional polymer electrolyte system. On addition of a low molecular weight plasticiser, (EC/PC), the salt interacts to a greater degree with the plasticiser mixture. In conclusion, the conductivity of the gel electrolyte had contributions from the co-ordination of the cation to the ether oxygens on the PU backbone and from a liquid-like conductivity mechanism in the plasticiser regions.

9.2 Supercapacitors with Carbon Electrodes

9.2.1 Carbon electrodes with liquid electrolytes.

The aim of this section was to evaluate carbon based supercapacitor devices with the PU electrolyte described in chapter 6. A low molecular weight analogue was initially investigated as a comparison.

Two electrolyte solutions were prepared, ($LiClO_4$/PC, 0.25M and $TEABF_4$/PC, 0.25M). Figures 7.2 to 7.6, CV and a.c. impedance data, indicate that the above electrolytes show close to ideal capacitive characteristics with activated carbon fabric and graphite paper electrodes. In the complex plane a semi-circle followed by an

almost vertical spike is apparent and the CV shows a rectangular shape associated with ideal capacitive behaviour.

Capacitance values of 3.2 F cm^{-2} (from the impedance plot) and 3.0 F cm^{-2} (from the CV) were obtained for the liquid cell ACC/PC/$LiClO_4$ (0.25M). This related to a specific capacitance of 160 F g^{-1} and 150 F g^{-1} from impedance and CV data respectively.

Graphite paper was used as an electrode material for comparison with the ACC to demonstrate the effect the high surface area of ACC has on the electrical parameters of a supercapacitor device. A capacitance value of 8 mF cm^{-2} was calculated from a.c. impedance data. The mass of the GP electrode was 0.026g, therefore a specific capacitance of 0.30 F g^{-1} was obtained. This is a difference of three orders of magnitude compared with the ACC electrode devices, clearly showing the effect of high surface area on the capacity of the device. The cell GP/$TEABF_4$/PC (0.25M) gave capacitances of 0.05 F cm^{-2} calculated from impedance data. This related to specific capacitances of 3.10 F g^{-1}, again three orders of magnitude less than the capacitance value achieved for supercapacitor devices using ACC electrodes.

9.2.2 Carbon electrodes with a PU electrolyte.

Supercapacitor devices using ACC electrodes with the PU gel electrolyte were constructed and evaluated using a.c. impedance spectroscopy and cyclic voltammetry. Both techniques showed that the ACC/PU/EC/PC/$LiClO_4$ cell had excellent capacitive characteristics, i.e., a semi-circle followed by an almost vertical spike was obtained in the complex plane impedance plot and a rectangular shaped CV between the stable potential limits of ± 1V versus a floating potential was obtained. A capacitance of 0.15 F cm^{-2}, which translated to 3.75 F g^{-1} was obtained for this cell, using equation 5.14 at a frequency of 10 mHz.

The cell ACC/PU/EC/PC/$LiClO_4$ was galvanostatically cycled at a current density of 4 mA cm^{-2} between 0.20 and 1 V.

The complex plane impedance response of the cell after 1000 cycles differed from the initial response. The bulk resistance increased from 48 Ω to 62 Ω i.e. an increase of 12 % and the capacitance decreased by 0.01 F cm^{-2}, from 0.15 F cm^{-2} to 0.14 F cm^{-2}. A more detailed inspection of the charge-discharge curves was carried out in

order to rationalise this observation. Impedance data was collected at regular intervals during the galvanostatic charging and discharging of the cell. Also the capacitance was evaluated at regular intervals of a cell ACC/PU/EC/PC/$LiClO_4$ at open circuit. Both these experiments gave results which show an initial drop in capacitance and an increase in bulk resistance, after which a steadier value of capacitance and reduced bulk resistance was obtained. A decrease from 50 Ω to near the original value of 48 Ω was then observed when cycled to 1000 cycles. This suggests the growth of an interfacial boundary, which breaks down on further cycling, or the possibility of intercalation of Li^+ ions into the electrode pores [4]. This intercalation may only be only be partially reversible until an equilibrium condition is reached. A similar trend is observed for the capacitance of the cell, where the capacitance decreases and reverts to near the original value. Since the increase in R_b effects the discharge time and hence the coulombic efficiency it was postulated that a larger cation would not intercalate to the extent of Li^+.
$TBAClO_4$ and $TBABF_4$ were used as an electrolyte salt since it was thought that the larger cation would not intercalate into the electrode porous structure to the extent of lithium. Using $TBAClO_4$ gave a large semi-circle in the complex plane impedance response and on average a bulk resistance of 20 Ω higher than the lithium analogue. Devices based on $TBABF_4$ showed poor capacitive characteristics and a large bulk resistance of 200 to 1600 Ω when galvanostatically charged and discharged to 1000 cycles.

A greater intimate contact between electrode and electrolyte was thought to be achievable by using carbon composite electrodes, [5], formed by addition of a known amount of a PU/plasticiser/salt mixture to carbon powder.

$LiClO_4$ was used as the electrolyte salt and the composition of composite electrodes were optimised for their mechanical stability and capacitive characteristics with a PU gel electrolyte PU/ $LiClO_4$/PC/EC.
The optimum composition was found to be the electrodes containing 200% added plasticiser. The increase in capacitance from 200% to 400% added plasticiser was not regarded as economically sound considering the relatively small increase in capacitance.

As with earlier experiments on the charge-discharge cycling there is clearly an induction process, probably of an interfacial nature, which is manifested in an increase in the value of bulk resistance after the initial assembly.

Both the charge-discharge curves and the impedance results show evidence of the induction process observed when the impedance was measured as a function of time for an open circuit cell.

The bulk resistance increases from 10 to 40 Ω on cycling 1000 times, the bulk resistance also increases from 9 to 22 Ω over a period of 500 minutes at open circuit. Comparing the system with carbon cloth electrodes with the carbon composite electrode analogue, a similar capacitance is obtained for both systems, i.e., a capacitance of between 3 and 4.5 F g^{-1} for the $LiClO_4$/ACC system and between 23 and 30 F g^{-1} for the $LiClO_4$/CC analogue. The trend of increasing bulk resistance and decreasing capacitance on cycling is observed for both systems. Also an initial induction or conditioning period is apparent for the devices using carbon cloth and carbon composite electrodes. A marked improvement in coulombic efficiency from the devices utilising the composite electrodes was observed as was summarised in table 7.2. This may be due to a greater intimate contact between the electrode and electrolyte and hence a greater reversibility of ions to and from the electrode surfaces.

9.3 Supercapacitors with porous silicon electrodes

Porous silicon was produced anodically and by chemical etching. It was found that washing the fresh porous silicon in pentane and drying under a nitrogen atmosphere reduced the capillary induced tensile stresses within the porous structure and thus reduced the surface cracking associated with porous silicon production.

As with the carbon electrodes a low molecular weight liquid electrolyte was used with PSi electrodes.

Supercapacitor cells of Si/$TEABF_4$/PC (0.25M) configuration were constructed for comparison with cells constructed with PSi. There is a large difference in bulk

resistance between the silicon and PSi electrodes. The multylayered porous structure has a high electrical impedance, with a bulk resistance of tens of kΩ.

Both the CV and impedance data for the PSi cell deviate somewhat from ideality. They are less rectangular, slightly tilted and show high self-discharge characteristics at the extremes of the potential window.

These phenomena may be explained by considering the active surface of the porous layer. The surface oxide is not a uniform one and the porous layer may be looked upon as series of defects in the crystal lattice. Further dislocations occur within the porous layer when the etch solution it removed. These defects, oxide islands and dislocations give rise to circulating electrochemical currents across the porous layer [6]. Thus fluctuations in the measured current are observed in the CV data and what appears to be random impedance data at low frequency regions are observed in the a.c. impedance analysis. The self-discharge does not seem to be due to normal overpotential induced discharge since it also occurs at lower potential sweeps. This discharge route could be due to faradic charge transfer associated with surface impurities and oxide islands.

A possible method for reducing the oxide growth on the PSi surface was to coat the surface with a thin layer of gold.

A 300Å layer of gold was sputtered onto the PSi surface. The resulting cell, PSi/Au/$TEABF_4$/PC (0.25M), showed much improved capacitive characteristics up to 10 mHz , as shown in figures 8.8 (*a and b*). The CV also shows a more the rectangular shape associated with ideal capacitor behaviour. Figure 8.8 (b) shows that the bulk resistance has decreased from approximately 40 kΩ to 234 Ω, which is a marked improvement.

The capacitance calculated from the impedance data was 0.13 mF cm^{-2} relating to a specific capacity of 2.21 mF g^{-1}. The capacitance calculated from the CV was 0.12 mF cm^{-2}, relating to a specific capacitance of 2.04 mF g^{-1}.

Cell configurations of PSi with the PU gel electrolyte showed poor capacitive characteristics for both impedance data and CV.

Coating the PSi with a 300-Å layer of gold increased the capacitive characteristics of the cell. The steeper vertical spike in figure 8.12 (a) demonstrates this. The CV trace in figure 8.13 also showed a more rectangular shape associated with that of an ideal capacitor. Some self-discharge characteristics at the extremes of the potential window are still evident. However, a marked improvement is observed when a layer of gold is deposited. This was also the case for the system for the corresponding liquid electrolyte cell PSi/Au/$TEABF_4$/PC. The bulk resistance of the cell has improved dramatically with a decrease from tens of kΩ to 600 Ω. This is a marked improvement but still too high to be considered a good candidate for supercapacitor devices.

The capacitance calculated at 10 mHz using equation 5.14 was 29.5 μF cm^{-2}, relating to a specific capacitance of 0.50 mF g^{-1}. The capacitance calculated from CV data using equation 5.4 was 27μF cm^{-2}, relating to a specific capacitance of 0.46 mF g^{-1}.

PSi was also produced by the chemical etching technique. The capacitance calculated at 10 mHz from equation 5.14 was 0.6 mF cm^{-2} and from the CV data using equation 5.4, 0.5 mF cm^{-2}.

An increase in the capacity of a factor of ten was achieved from the anodically etched PSi/Au/$TEABF_4$/PC to that calculated for the stain etched PSi cell PSi(stain)/Au/$TEABF_4$/PC cell. Also the bulk resistance was a factor of ten less for the cell using stain etched PSi electrodes.

As discussed in chapter 8, the difference in bulk resistance was due to the anodically etched PSi having a multi-layered structure, whereas multi-layering occurs to a much less extent in stain etched PSi. Therefore the stain etched PSi shows a lower resistance.

Anodically etched PSi has a much higher surface area and one would expect therefore a higher capacitance. Due to the multi-layer structure, however, a large percentage of the PSi surface area is not accessible to the electrolyte and therefore explains the relatively low capacitance values obtained for the cell.

Thin layered silicon electrodes were produced and investigated with the idea that the bulk resistance could be reduced using this method.

Liquid cells were initially investigated as a comparison with the PU gel electrolyte configuration. Again poor capacitive characteristics were apparent as indicated from

the complex plane impedance plot and the CV. Capacitive characteristics closer to the ideal were obtained for gold coated stain etched PSi with $TEABF_4$/PC electrolyte. The bulk resistance of the cell was reduced to 35 Ω, close to that of the carbon based cells. Capacitance values of 0.64 mF cm^{-2}, relating to a specific capacitance of 2.82 F g^{-1} were obtained for the cell PSi(stain)/Au/$TEABF_4$/PC (0.25M).

Figure 8.26(a) shows that the electrodes produced from stain etched, thin layer PSi, coated with gold were the best silicon candidates for solid state supercapacitors with the PU gel electrolyte. Although the capacitance was low, 2.7 μF cm^{-2}, the specific capacitance was high because of the thin layer cell construction. The specific capacitance was 10 mF g^{-1}.

Figure 8.29 demonstrates that the cell PSi/Au/PU shows very good capacitive characteristics over 1000 galvanostatic charge-discharge cycles. Giving capacitance values of between 8 and 16 mF g^{-1}. The use of thin layer PSi is completely novel in its application for supercapacitor systems and it may be possible to integrate this power storage system into chip technology where currents of micro-amps are required.

The main concern with the use of PSi is the lack of high reproducibility in its production. As described earlier it is very difficult to eliminate surface cracking and oxide formation.

Polypyrrole was galvanostatically grown on PSi in order to obtain a high surface area polypyrrole electrode. Clearly figure 8.30 demonstrates that the cell ppyr/PSi/PU/EC/PC/ $LiClO_4$ does not show ideal capacitive behaviour. A large semi-circle suggests a large resistance in parallel with the pseudocapacitance associated with the polypyrrole. This may be due to a large interfacial resistance between the PSi and the polypyrrole film. The bulk resistance of the cell is also large (~500Ω). This may be due to the poor adhesion and poor conductivity of the film, which is a result of the compliance voltage rising to over 10 V during the galvanostatic growth of the polypyrrole film.

The possibility of producing capacitance values higher than those reported for polypyrrole systems alone, by using the high surface area of PSi remains an attractive prospect, but clearly a further investigation into the growth of polypyrrole

on PSi is required. Suggestions for a series of experiments to improve the capacitive characteristics of the ppyr/PSi/PU cell are shown in chapter 10.

10. Future work

- The nature of the interfacial boundary build-up between the ACC and CC electrodes with the PU electrolyte needs to be investigated further so that the bulk resistance of the supercapacitor cell can be reduced and hence the coulombic efficiency of the cell can be improved and kept constant throughout the lifetime of the device.
- Devices with thin layer PSi were novel but further improvements in capacitive performance are necessary if the system is to be utilised commercially. Lowering the bulk resistance of the device would be possible by doping the silicon with elements such as boron (for p-doping) and phosphorous (for n-doping). Equipment for carrying out these procedures are already operational in the Faculty of Applied Sciences at De Montfort University.
- Doping the PSi surface would also be beneficial for conducting polymer growth, since a major factor in obtaining a poor quality polypyrrole film was the fact that PSi has a high electrical impedance which drove the compliance voltage of the potentiostat to over 10 V in order to maintain a 20 mA cm^{-2} current density.
- Different polymer growth techniques may be employed to obtain a better quality film.
- S.E.M. and AFM techniques may be used to characterise the quality of the polymer film.
- Supercapacitor electrodes utilising both the pseudocapacitance associated with electronically conducing polymers and the high surface area obtained from doped thin layer PSi can be constructed with the PU gel electrolyte described in this study may be characterised using a.c. impedance spectroscopy, cyclic voltammetry and galvanostatic charge-discharge cycling experiments.

List of Publications and Presentations

1. Publications

R.J. Latham, S.E. Rowlands, W.S. Schlindwein, "Supercapacitors using Polymer Electrolytes based on Polyurethane", Solid State Ionics, **147,** (2002), 243-248.

R.J. Latham, S.E. Rowlands, W.S. Schlindwein, "Supercapacitor Devices using Porous Silicon Electrodes", Ionics, **5,** (1999), 144-149.

2. Conference Presentations

R.J. Latham, S.E. Rowlands, W.S. Schlindwein, "Supercapacitors using Polymer Electrolytes", Polymer Electrolytes 2001, Noordwijkerhout, The Netherlands, May 2001.

R.J. Latham, S.E. Rowlands, W.S. Schlindwein, "Porous Silicon as an Electrode Material in Supercapacitors", *Polar solids/Solid State Chemistry Discussion Group Royal Society of Chemistry,* Oxford University, March 2001.

R.J. Latham, S.E. Rowlands, W.S. Schlindwein, "Supercapacitors using Polymer Electrolytes", *Electrochemistry 2000*, Dublin University, September 2000.

R.J. Latham, S.E. Rowlands, W.S. Schlindwein, "Porous Silicon as an Electrode Material in Supercapacitor devices", 6th *Euroconference on Solid State Ionics,* Calabria, Italy, September 1999.

T. Bardrick, S. Bayliss, R.J. Latham, S.E. Rowlands, W.S. Schlindwein, "Characterisation and Applications of Electrochemically Produced Porous Silicon", *Electrochemistry 99*, University of Portsmouth, September 1999.

R.J. Latham, S.E. Rowlands, W.S. Schlindwein, "Porous Silicon as an Electrode Material in Supercapacitor Devices", *MEG, 99*, Warwick University, May 1999.

References

Chapter 1

1. R. Kotz, M. Carlen, Electrochim. Acta, **45** (2000) 2483.
2. F.M. Delnick, D. Ingersoll, X. Andrieu, K. Naoi, Electrochemical Capacitors II, Electrochem. Soc. Proc. Ser. A, Pennington, NJ, (1997).
3. K. Sanada, M. Hosokawa, "Electrical Double Layer Capacitor, "Supercapacitor"", NEC Res. & Develop., **55** (1979) 2.
4. B.E. Conway, V. Birss, J. Wojtowicz, J. Power Sources, **66** (1997) 1.
5. B.E. Conway, J. Electrochem. Soc., **138** (1991) 1539.
6. A. Rudge, S. Gottesfeld, J. of Power sources, **47** (1994) 89.
7. A.Rudge, J. Davey, S. Gottesfeld, J.P. Ferarris, Proc. Electrochem. Soc., **74** (1993) 93.
8. X. Lui, T. Momma, T. Osaka, Chem. Lett., 625 (1996).
9. X. Lui, T. Momma, T. Osaka, J. Electrochem. Soc., **143** (1996) 3982.
10. X. Lui, T. Momma, T. Osaka, J. Electrochem. Soc., **144** (1997) 3066.
11. S.A. Hashmi, R.J. Latham, R.G. Linford, W.S. Schlindwein, J. Chem. Soc., Faraday Trans., **93** (1997) 4177.
12. S.A. Hashmi, R.J. Latham, R.G. Linford, W.S. Schlindwein, Polym. Int., **47** (1998) 28.
13. V. Lehmann, J. Electrochem. Soc., **140** (1993) 283.
14. A. Halimaoui, Porous Silicon Data Rev., (1997) 12.
15 L. T. Canham, Porous Silicon Data Rev., (1997) 83.
16 T. Tada, Appl. Phys. Let., **70** (1997) 2538.
17 R. E. Hummel, S. S. Chang, Appl. Phys. Let., **61** (1997) 1965.
18 T. D. Shen, I. Shmagin, C.C. Koch, R. M. Kolbas, M. X. Quan, Phys. Rev. B, **55** (1997) 7615.
19 R. A. Bley, S. M. Kavclarich, J. Am. Chem. Soc., **118** (1996) 12461.
20 F. P. Romstad, Phys. Rev. B, **55** (1997) 5220.
21 R. L. Smith, S. D. Collins, J. App. Phys., **71** (1992) R1-R22.
22 S. R. Morrison, "Electrochemistry at Semiconductor and Metal Oxide Interfaces", Plenum Press, London and New York, 1980.

23 R. Hermo, Porous Silicon Data Rev., (1997) 66.

Chapter 2

1. K. Sanada and M. Hosokawa, "Electrical Double Layer Capacitor, "Supercapacitor"", NEC Res. & Develop., **55** (1979) 2.
2. I. Tanahashi, A. Yoshida, A.Mishino, J. Electrochem. Soc., **137** (1990) 3052.
3. B.E. Conway, V. Birss, J. Wojtowicz, J. Power Sources, **66** (1997) 1.
4. B.E. Conway, J.Electrochem. Soc., **138** (1991) 1539.
5. F.M. Delnick, D. Ingersoll, X. Andrieu, K. Naoi, Electrochemical Capacitors II, Electrochem. Soc. Proc. Ser. A, Pennington, NJ, (1997).
6. A. Nishimo, J. Power Sources, **60** (1996) 137.
7. C. Arbizzani, M. Mastragosino, L. Mengello, R. Paraventi, Adv. Mater., **8** (1996) 331.
8. R.A. Huggins, Philos. Trans. R. Soc., Ser. A, **345** (1996) 1555.
9. D.C. Grahame, Chem. Rev., **47** (1947) 441.
10. A. Von Helmoltz, Weid. Ann., **7** (1897) 337.
11. G. Gouy, Ann. Phys., (Paris), **7** (1917) 183.
12. O. Stern, Z. Elektrochem., **30** (1924) 508.
13. The Southampton Electrochemistry Group, "Instrumental Methods in Electrochemistry", Ellis Horwood limited, Chichester, (1985).
14. S.A. Hashmi, R.J. Latham, R.G. Linford, W.S. Schlindwein, Polym. Int., **47** (1998) 28.
15. R. Kotz, M. Carlen, Electrochim. Acta, **45** (2000) 2483.
16. E. Koppitz, J. W. Schultze, Electrochim. Acta, **21** (1976) 327.
17. A. Burk, J. Power Sources, **91** (2000) 37.
18. B. W. Ricketts, C. Ton-That, J. Power Sources, **89** (2000) 64.
19. B.E. Conway, W. G. Pell, T-C. Liu, J. Power Sources, **65** (1997) 53.
20. B.E. Conway, W. G. Pell, W. A. Adams, J. de Olivera, J. Power Sources, **80** (1999) 134.

Chapter 3

1. C.K. Chaing, A. J. Heeger, H. Shirikawa, E. J. Louis, A. G. MacDiarmid, j. Chem. Soc., J. Chem. Commun., (1977) 578.
2. C.K. Chaing, C. R. Fincher, Jr., Y. W. Park, A. J. Heeger, H. Shirikawa, E. J. Louis, S. C. Gau, A. G. MacDiarmid, Phys. Rev. Lett., **39** (1977) 1098.
3. C.K. Chaing, Y. W. Park, A. J. Heeger, H. Shirikawa, E. J. Louis, S. C. Gau, A. G. MacDiarmid, J. Am. Chem. Soc., **100** (1978) 1013.
4. A.J. Bard, L.R.Faulkner, "Electrochemical Methods Fundamentals and Applications", John Harwood and Sons, Chichester, 1980.
5. H. S. Nalwa, "Handbook of Conductive Molecules and Polymers, **Vol. 2**, John Wiley and sons, Chichester, 1997.
6. A. Angeli, Gazz. Chim. Ital., **46** (1916) 279.
7. A. Angeli, L. Alissandri, Gazz. Chim. Ital., **46** (1916) 283.
8. A. Dall'Ollio, Y. Dascola, V. Varraca, V. Bocchi, Comptes Rendus **C267** (1968) 433.
9. G. Bidan, A. F. Diaz, E. M. Genies, J. Electroannal. Chem., **149** (1983) 101.
10. A. F. Diaz, B. L. Funt, Organic Electrochemistry: An Introduction and a Guide, Marcel Dekker, New York (1991) 1337.
11. G. B. Street, in Handbook of Conducting Polymers, 1st edition, ed. T J. Skotheim, Marcel Dekker, New York, (1986) 188.
12. N. Brodie, G. Sabouraud, S. Sadki, P. Schottland, Chem. Soc. Rev., **29** (2000) 283.
13. J. D. Kim, K. J. Kim, H. S. Song, Bull. Korean Chem. Soc.,9 (1998) 248, in Chem. Soc. Rev., **29** (2000) 283.
14. Q. Pei, R. Qian, Synth. Met., **45** (1991) 35.
15. S. Asavapiriyanont, G. K. Chandler, G. A. Gunawardena, D. Pletcher, J. Electroanal. Chem., **177** (1984) 229.
16. K. Imanishi, M. Satoh, K. Yoshino, J. Electroanal. Chem., **317** (1991) 139.
17. M. Takakubo, J. Electroanal. Chem., **258** (1989) 303.
18. Y. J. Qui, J. R. Reynolds, J. Polym. Sci., Part A: Polym. Chem., **30** (1992) 1315.

19. A. F. Diaz, A. Martinez, K. K. Kanazawa, M. Salmon, J. Electroanal. Chem., **130** (1980) 181, in Chem. Soc. Rev., **29** (2000) 283.
20. A. Kaynak, Mater. Res. Bull., 32 (1997) 271, in Chem. Soc. Rev., **29** (2000) 283.
21. R. G. Compton, Q. Hong, T. Silk, J. Tamm, Synth. Met., **93** (1998) 59.
22. M. j. Miles, W. T. Smith, J. S. Shapiro, Polymer, **41** (2000) 3349.
23. J. I. Castillo, A. J. Diaz, W. Y. J. Lee, J. A. Logan, J. Electroanal. Chem.,**129** (1981) 115.
24. J. R. Reynolds, P. Schottland, C. A. Thomas, K. Zong, Adv. Mater., **12** (2000) 222.
25. P. Audebert, G. Bidan, J. Electroanal., Chem., **190** (1985) 129.
26. A. Mertz, R. Schrop, R. Schwartz, Adv. Mater., **6** (1992) 409.
27. M. G. Cross, N. J. Morse, R. J. Mortimer, D. R. Rosseinsky, D. J. Simmonds, D. Walton, J. Electroanal. Chem., 189 (1985) 389.
28. F. M. Gray, "Solid Polymer Electrolytes; Fundamentals and Technological Applications", VCH Publishers, inc.,New York (1991).
29. ZHU, J. Poly. Sciences, **39** (2001) 1246.
30. A. Noda, M. Watanabe, Electrochem. Acta, **45** (2000) 1265.
31. N. Cowlam, A. Gibaud, G. Ungar, T. H. Ritchardson, P. V. Wright, Y. Zeng, J. Mater. Chem., **10** (2000) 69.
32. F. Chia, G. Ungar, P. V. Wright, Y. Zeng Chem. Commun., (2000), 1459.
33. R. J. Neat, PhD Thesis, Leicester Polytechnic (1988).
34. H. Cheradame, A Gandini, J. F. Le Nest, Br. Polym. J., **20** (1988) 253.
35. J. R. MacCallum, A. S. Tomlin, C. A. Vincent, Eur. Polym. J., **22** (1986) 787.
36. W. L. Archer, R. D. Armstrong, Electrochim. Acta, **25** (1980) 1689.
37. C. A. Vincent, Prog. Solid State Chem., **17** (1987) 145.
38. R. J. Latham, S. E. Rowlands, W. S. Schlindwein, Solid State Ionics, **147** (2002) 243.
39. P. Mustarelli, Solid State Ionics, **135** (2000) 81.

Chapter 4

1. C Kittel, "Introduction to Solid State Physics", 7th Ed., New York; John Wiley and sons, (1996).
2. D. B. and G. B. Beard, "Quantum Mechanics; Principles and Application", Boston; Allyn and Bacon, (1970).
3. G. Sposito, "Principles of Quantum Mechanics", New York; John Wiley and sons, (1970).
4. D. De Cogan, "Solid State Devices", Macmillan Educational Ltd., 1st Ed., (1987) 93.
5. T. E. Jenkins, "Semiconductor Science", Prentice Hall, New York 1st Ed.,(1995) 74, 175.
6. G. Burns, "Solid State physics; International Ed.", Academic Press, Inc., Harcourt Brace Publishers, Boston, (1985) Chapt. 10.
7. H. F. Hameka, "Quantum Mechanics", New York; John Wiley and sons, (1981).
8. B. Unal, "Optical, Electrical and Structural Properties of Nanostructured Silicon and Silicon-Germanium Alloys", PhD thesis De Montfort University, Leicester (1998).
9. A. Madan, M. P. Shaw, "The Physics and Applications of Amorphous Semiconductors", (1988).
10. A. Uhlir, Bell Syst. Tech. J., **35** (1956) 333.
11. V. Labunov, I. Baranov and V. Bodranenko, Thin Solid Films, **64** (1979) 479
12. Y. Watanabe, Y. Arita, T. Yokoyama, Y. Igarashi, J. Electrochem. Soc., **122** (1975) 1351
13 H. Unno, K. Immai and S. Muramoto, J. Electrochem. Soc., **134** 645 (1987).
14 K. Barla, G. Bomchil, R. Herino and J. F. Pfister, J. Cryst. Growth, **68** (1984) 721.
15 D. R. Turner, J. Electrochem. Soc., **105** (1958) 402.
16 V. Lehmann, J. Willer, SS Tech., **1** (1995) 99.
17 R. L. Smith, S. D. Collins, J. Appl. Phys., **71** (1992) R1.
18 G. S. Popkirov, R. N. Schindler, Rev. Sci. Instum., **63** (1992) 5366.
19 V. Lehmann, U. Gossel, Appl. Phys. Lett., 58 (1991) 856.

20 V. Lehmann and J. Willer, Solid State Tech., **1** (1995) 99.
L.M. Peter, D.J. Blackwood and S. Pons, Phys. Rev. lett., **62** (1987) 308.
21 P. Gupta, A.C. Dillon, A.S. Bracker and S.M. George, Surf. Sci. **245** (1991) 360.
22 J. Sarathy, S. Shih, K. Jung, C. Tsai, K. H. Li, D. L. Kwong, J. C. Campbel, S. Yan, A. J. Bard, Appl. Phys. Lett., **60** (1992) 1532.
23 R. J. Archer, J. Phys. Chem. Solids, **14** (1960) 104.
24 R. W. Fathauer, T. George, A Ksendzov, R.P. Vasquez, Appl. Phys. Lett., **60** (1992) 995.
25 A. J. Steckl, J. Xu, H.C. Mogul, S. Morgen, Appl. Phys. Lett., **62** (1993) 1982.
26 D. Dimova-Malinoskva, M. Sendova-Vassileva, N. Tzenov, M. Kamenova, Thin Solid Films, **297** (1997) 9.
27 D. R. Turner, J. Electrochem. Soc., **107** (1960) 810.

Chapter 5

1. V.S. Bagotzky, "Fundamentals of Electrochemistry", Plenum Press, London and New York, 1993.
2. P. J. Mahonet, J. Power Sources, **91** (2000) 68.
3. G.S. Popkirov and R.N. Schindler, Rev. Sci. Instum., **63** (1992) 5366.
4. P.A. Christensen, A. Hamnet, "Techniques and Mechanisms in Electrochemistry", Blackie Academic & Proffessional, an imprint of Chapman and Hall, Glasgow, 1994.
5. A.J.Bard, L.R.Faulkner, "Electrochemical Methods Fundamentals and Applications", John Harwood and Sons, Chichester, 1980.
6. V.S. Bagotzky, "Fundamentals of Electrochemistry", Plenum Press, London and New York, 1993.
7. Z.Galus, "Fundamentals of Electrochemical Analysis, second (revised) edition", Ellis Horwood limited, Chichester, 1994.
8. W. G. Pell, B. E. Conway, N. Marincic, J. Electroanal. Chem., **491** (2000) 9.

Chapter 6

1. G. Woods, "The ICI Polyurethanes Book; 2nd Ed.", Wiley and sons, New York (1990).
2. H. Ohno, M. Tsuchida, K. Tsunemi, Electrochim. Acta., **28** (1983) 59.
3. R. G. Linford, "Electrochemical Science and Technology of Polymers-2", Elsevier, New York, (1990).
4. P. G. Bruce, C. A. Vincent, Faraday Discuss. Chem. Soc., 88 (1989) 43.
5. P. G. Bruce, C. A. Vincent, Solid State Ionics, 40/41 (1990) 607.
6. F. M. Gray, "Solid Polymer Electrolytes; Fundamentals and Technological Applications", VCH Publishers, Inc., New York (1991).
7. Perkin and Elmer instruction manual.
8. P. W. Atkins, "Physical Chemisrty; 6th Ed.", Oxford University Press, Oxford, (1998).
9. R. Idris, "Studies of Physical Properties of Novel Lithium Polymer Electrolytes", PhD thesis De Montfort University, Leicester (2001).

Chapter 7

1. B.E. Conway, V. Birss, J. Wojtowicz, J. Power Sources, **66** (1997) 1.
2. B.E. Conway, J. Electrochem. Soc., **138** (1991) 1539.
3. A. Rudge, S. Gottesfeld, J. Power Sources, **47** (1994) 89.
4. X. Lui, T. Momma, N. Nojima, T. Osaka, J. Electrochem. Soc., **146** (1999) 1724.
5. S.A. Hashmi, R.J. Latham, R.G. Linford, W.S. Schlindwein, Polymer International, **47** (1998) 28.

Chapter 8

1. V. Lehmann and J. Willer, Solid State Technology, **1**, (1995) 99.
2. T. Tada, Appl. Phys. Let., **70** (1997) 2538.
3. D.C. Grahame, Chem. Rev., **47** (1947) 441.
4. C. Owen, Final Year Project Report, De Montfort University, Leicester (2000).

Chapter 9

1. F. M. Gray, "Solid Polymer Electrolytes; Fundamentals and Technological Applications", VCH Publishers, Inc., New York (1991).
2. S. Deki, A. Kajinami, M. Mizuhata, P. Periasamy, T. Fujieda, Y. Saito, T. sakai, M. Shikano, K. Tatsumi, Solid State Ionics, **126** (1999) 285.
3. R. Idris, "Studies of Physical Properties of Novel Lithium Polymer Electrolytes", PhD thesis De Montfort University, Leicester (2001).
4. S.A. Hashmi, R.J. Latham, R.G. Linford, W.S. Schlindwein, Polymer International, **47** (1998) 28.
5. X. Lui, T. Momma, N. Nojima, T. Osaka, J. Electrochem. Soc., **146** (1999) 1724.
6. T. Tada, Appl. Phys. Let., **70**, 2538 (1997).